

# <sup>1</sup> Progress on Perovskite Materials and Solar Cells with Mixed Cations and Halide Anions

<sup>3</sup> Luis K. Ono,<sup>‡</sup> Emilio J. Juarez-Perez,<sup>‡</sup> and Yabing Qi\*<sup>†</sup>

<sup>4</sup> Energy Materials and Surface Sciences Unit (EMSS), Okinawa Institute of Science and Technology Graduate University (OIST),  
<sup>5</sup> 1919-1 Tancha Onna-son, Okinawa 904-0495, Japan



**ABSTRACT:** Organic–inorganic halide perovskite materials (e.g., MAPbI<sub>3</sub>, FAPbI<sub>3</sub>, etc.; where MA = CH<sub>3</sub>NH<sub>3</sub><sup>+</sup>, FA = CH(NH<sub>2</sub>)<sub>2</sub><sup>+</sup>) have been studied intensively for photovoltaic applications. Major concerns for the commercialization of perovskite photovoltaic technology to take off include lead toxicity, long-term stability, hysteresis, and optimal bandgap. Therefore, there is still need for further exploration of alternative candidates. Elemental composition engineering of MAPbI<sub>3</sub> and FAPbI<sub>3</sub> has been proposed to address the above concerns. Among the best six certified power conversion efficiencies reported by National Renewable Energy Laboratory on perovskite-based solar cells, five are based on mixed perovskites (e.g., MAPbI<sub>1-x</sub>Br<sub>x</sub>, FA<sub>0.85</sub>MA<sub>0.15</sub>PbI<sub>2.55</sub>Br<sub>0.45</sub>, Cs<sub>0.1</sub>FA<sub>0.75</sub>MA<sub>0.15</sub>PbI<sub>2.49</sub>Br<sub>0.51</sub>). In this paper, we review the recent progress on the synthesis and fundamental aspects of mixed cation and halide perovskites correlating with device performance, long-term stability, and hysteresis. In the outlook, we outline the future research directions based on the reported results as well as related topics that warrant further investigation.

**KEYWORDS:** perovskite, solar cell, mixed cations, mixed halides, stability, hysteresis

## 1. INTRODUCTION

Organic–inorganic halide perovskite materials (hereinafter denoted as “perovskites”) continue to attract worldwide attention, shown by a rapid increase in the number of publications per year (Figure 1a).<sup>1</sup> CH<sub>3</sub>NH<sub>3</sub>PbI<sub>3</sub> and CH<sub>3</sub>NH<sub>3</sub>PbBr<sub>3</sub> perovskites were first incorporated as light harvesters in liquid dye-sensitized solar cells in 2009 by Kojima et al.<sup>2</sup> In 2012, a significant breakthrough was made with the introduction of all solid-state CH<sub>3</sub>NH<sub>3</sub>PbI<sub>3</sub> perovskite solar cells by Kim et al.<sup>3</sup> Since then, perovskite solar cells have been under the spotlight with a cluster of fundamental scientific discoveries<sup>4–39</sup> as well as breakthroughs in solar-to-electricity power conversion efficiencies (PCEs).<sup>40</sup> The highest certified efficiency of 22.1% as of today is only a few percent points shy of that of the best single-crystalline silicon solar cells.<sup>40–43</sup> Perovskite solar cells are considered as the most promising candidate for the next generation high efficiency solar cell technology that is compatible with low-cost, low-temperature processing, flexible substrates, and large-area (module) fabrication processes.<sup>4,10,23,25,44–58</sup>

Highly efficient perovskite solar cells are composed of 36 perovskites that have an ABX<sub>3</sub> three-dimensional (3D) 37 structure and are commonly composed of an organic/inorganic 38 monovalent cation, A = (methylammonium (MA), CH<sub>3</sub>NH<sub>3</sub><sup>+</sup>; 39 formamidinium (FA), CH(NH<sub>2</sub>)<sub>2</sub><sup>+</sup>; Cs<sup>+</sup>; Rb<sup>+</sup>), a divalent metal 40 cation, B = (Pb<sup>2+</sup>; Sn<sup>2+</sup>), and halide anion motif X<sub>3</sub> = (I<sup>-</sup>; Br<sup>-</sup>; 41 Cl<sup>-</sup>). Pristine methylammonium lead iodide perovskite 42 (MAPbI<sub>3</sub>) has been intensively used as light harvesting material 43 from earlier times of perovskite solar cell developments.<sup>2,3,42,43,59</sup> Perovskite compositions with single ions 44 occupying each of A, B, and X sites (e.g., MAPbI<sub>3</sub>, FAPbI<sub>3</sub>, 45 etc.) are hereinafter denoted as “simple perovskites” and has 46 been intensively studied (Figure 1a). In earlier studies, 47 perovskites with mixed halides including minute quantities of 48 Cl<sup>-</sup> in the X<sub>3</sub> motif of MAPbI<sub>3</sub> (i.e., MAPbI<sub>3-x</sub>Cl<sub>x</sub>) were 49 employed,<sup>60,61</sup> and currently there is still a high predominance 50 of employing high contents of iodine-based perovskite 51 of employing high contents of iodine-based perovskite 52

**Received:** May 9, 2017

**Accepted:** July 6, 2017

**Published:** July 6, 2017

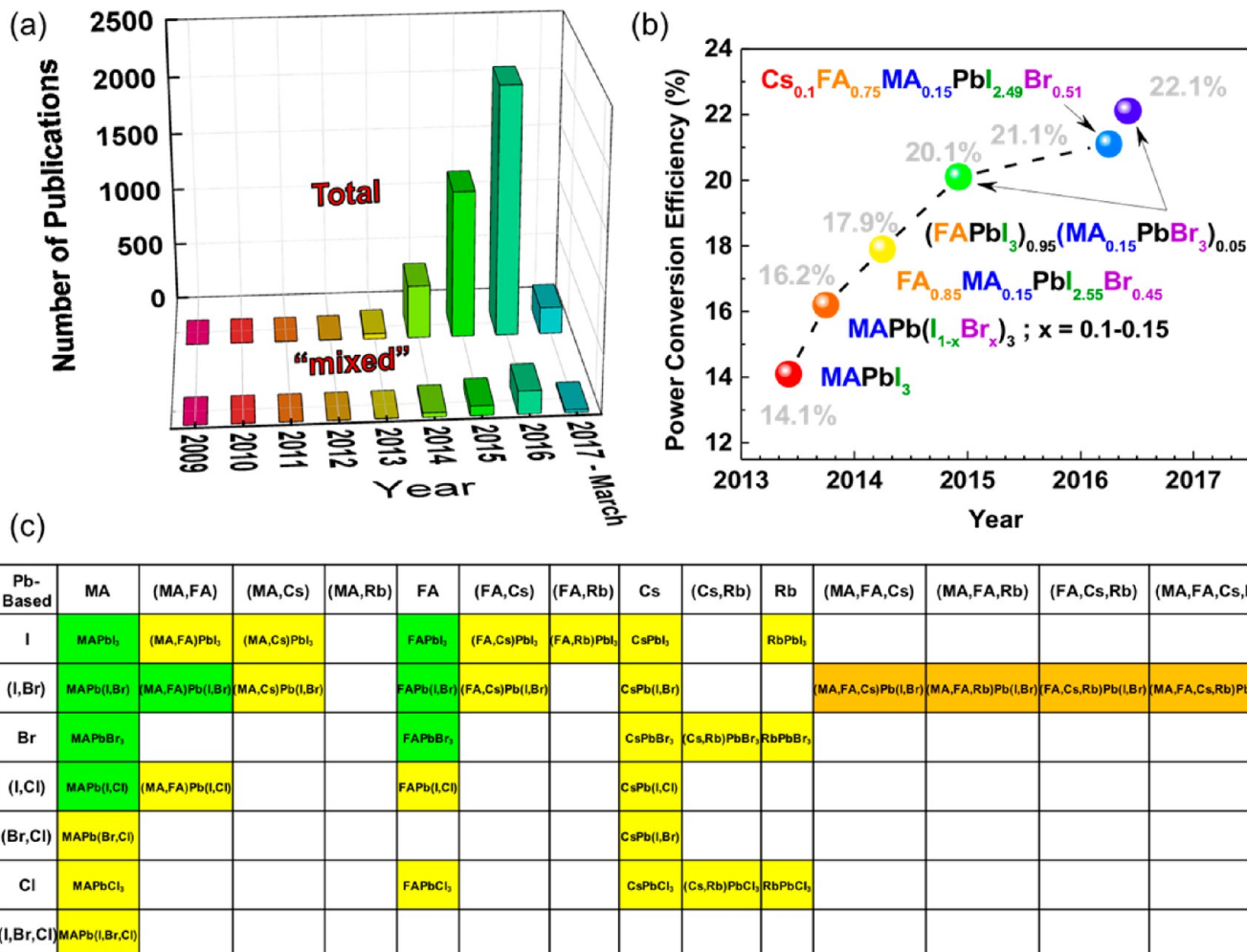


**Figure 1.** (a) Number of publications retrieved from Web of Science (Thomson Reuters) as a function of the year using the following search keywords: “perovskite” AND “solar” AND “cell” (AND “mixed”).<sup>1</sup> (b) Best research perovskite solar cells efficiencies certified by NREL.<sup>40</sup> For each of certified efficiencies, the chemical compositions of mixed perovskites are specified. (c) matrix of several simple and mixed cations and mixed halides Pb-based perovskites generated by the permutation of A = (MA,FA,Cs,Rb) and X = (I,Br,Cl). The perovskite compositions marked in yellow are documented in the literature. The green ones correspond to widely studied in the literature due to suitability for optoelectronic applications. The orange ones are the ones receiving great attention. Finally, the white boxes are perovskite compositions not still explored.

53 deposition recipes for photovoltaic applications.<sup>13,24–26</sup> In fact,  
 54 except for the first certified efficiency record reported for hybrid  
 55 perovskite research cells using phase pure  $\text{MAPbI}_3$ ,<sup>59</sup> the  
 56 following subsequent five National Renewable Energy Labo-  
 57 ratory (NREL) records with publicly disclosed information  
 58 used A and/or X site mixed hybrid perovskites<sup>62–66</sup> (herein-  
 59 after denoted as “mixed perovskites”), see Figure 1b. However,  
 60 based on Figure 1a, the fraction of the number of publications  
 61 employing mixed perovskites with respect to the total number  
 62 are still relatively low, ~9% in 2016 and ~10% as of April 15th,  
 63 2017.<sup>1</sup> A question naturally arises whether the future trends for  
 64 perovskite photovoltaic technology should be focused on mixed  
 65 perovskites. In this review, we outline systematically the  
 66 benefits to employ mixed cations and halides in perovskite  
 67 materials. For example, we will highlight the following  
 68 advantages: (i) higher performance, (ii) increased stability,  
 69 (iii) enhanced carriers charge transport, (iv) enabling band gap  
 70 tuning, (v) less pronounced hysteresis, (vi) a thorough  
 71 understanding of fundamental aspects of Pb-based mixed  
 72 cations and halides may lead to alternative Pb-free perovskites  
 73 by rational designs. In this review, only the Pb-based mixed  
 74 cations and halides perovskites are to be covered based on the

fact that substantial knowledge has been accumulated with 75  
 several congruent conclusions for Pb-based mixed cations and 76  
 halides perovskites. In Figure 1c, we marked the Pb-based pure 77  
 and mixed cations and halides perovskites that have been 78  
 reported in the literature. The color coding signifies: (yellow,- 79  
 green,orange) = reported in the literature; green = widely 80  
 studied composition; orange = receiving attention recently; 81  
 white = not reported composition. Following our survey 82  
 (Figure 1c) and aiming a comprehensive description of mixed 83  
 cations and mixed halides perovskites, we start with the 84  
 description of the simpler systems of mixed A cations ( $\text{FA}/$  85  
 $\text{MA}\text{PbI}_3$ ,  $(\text{MA/Cs})\text{PbI}_3$ ,  $(\text{FA/Cs})\text{PbI}_3$ ,  $(\text{FA/Rb})\text{PbI}_3$  perov- 86  
 skites (section 2) and the mixed X halides  $\text{MAPb}(\text{I/Cl})$ ,<sup>87</sup>  
 $\text{FAPb}(\text{I/Cl})$ ,  $\text{MAPb}(\text{I/Br})$ ,  $\text{FAPb}(\text{I/Br})$ ,  $\text{MAPb}(\text{Br/Cl})$ ,<sup>88</sup>  
 $\text{MAPb}(\text{I/Br/Cl})$ ,  $\text{CsPb}(\text{I/Br})$ ,  $\text{CsPb}(\text{Br/Cl})$ ,  $\text{CsPb}(\text{I/Cl})$  per- 89  
 ovskites (section 3). Based on important concepts described in 90  
 sections 2 and 3, the more complex systems of simultaneously 91  
 mixed A and mixed X ( $(\text{MA/Cs})\text{Pb}(\text{I/Br})$ ,  $(\text{FA/MA})\text{Pb}(\text{I/Br})$ ,<sup>92</sup>  
 $(\text{FA/MA})\text{Pb}(\text{I/Cl})$ ,  $(\text{FA/Cs})\text{Pb}(\text{I/Br})$ ,  $(\text{Cs/FA/MA})\text{Pb}(\text{I/Br})$ ,<sup>93</sup>  
 $(\text{Rb/FA/MA})\text{Pb}(\text{I/Br})$ ,  $(\text{Rb/Cs/FA})\text{Pb}(\text{I/Br})$ ,  $(\text{Rb/Cs/FA/}$ <sup>94</sup>  
 $\text{MA})\text{Pb}(\text{I/Br})$  perovskites are described in section 4.<sup>95</sup>

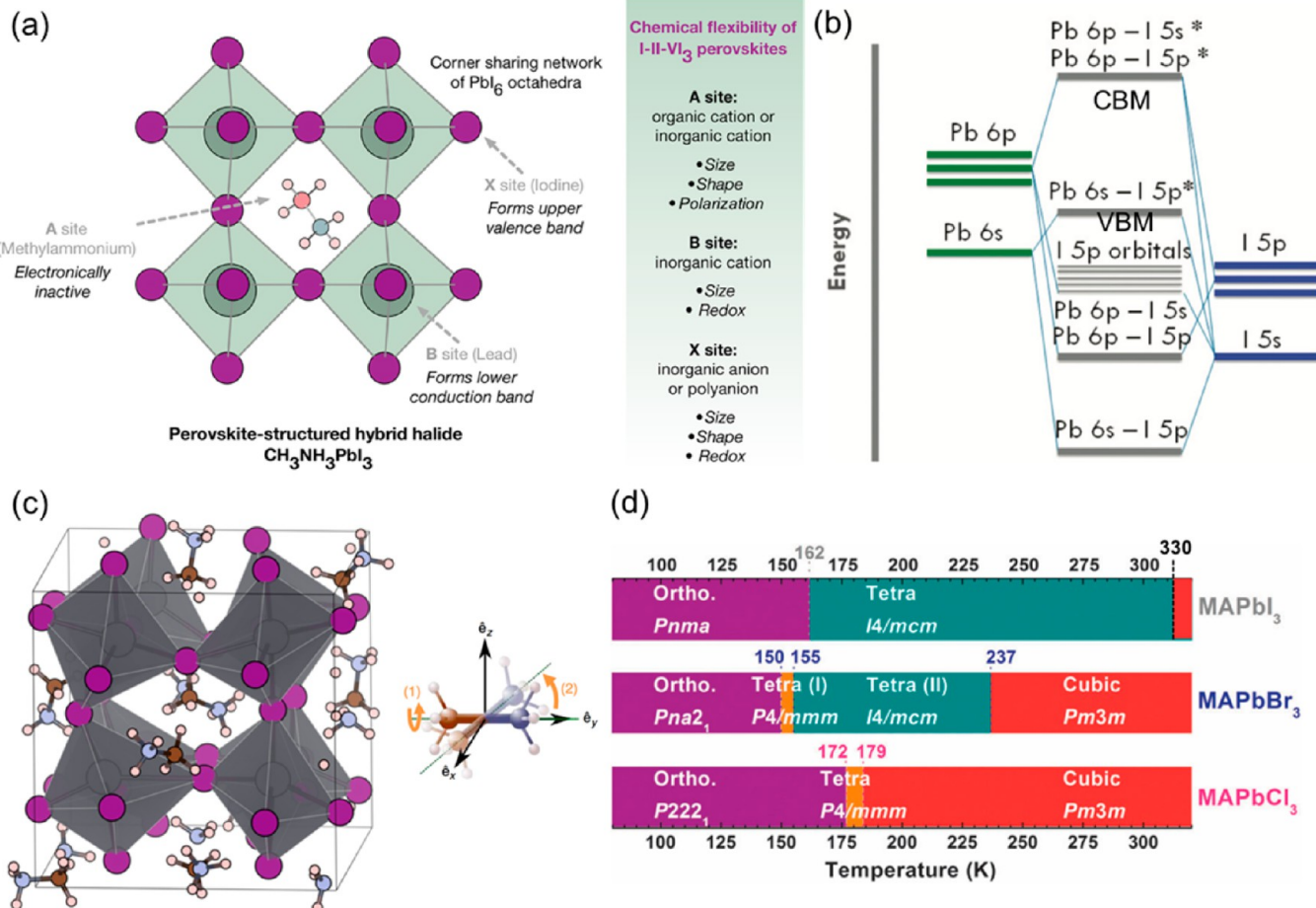


**Figure 2.** (a) Illustration of a  $\text{CH}_3\text{NH}_3\text{PbI}_3$  perovskite structure with A, B, and X lattice sites. The redox chemistry of ions influence the valence and conduction band energies and orbital composition. Reprinted with permission from ref 67. Copyright 2015 American Chemical Society. (b) Illustration of energy bands in  $\text{CH}_3\text{NH}_3\text{PbI}_3$  relative to isolated p and s atomic orbital energies of Pb and I. The  $\text{CH}_3\text{NH}_3^+$  cation does not introduce states at the band edge. Reprinted with permission from ref 68. Copyright 2014 The Royal Society of Chemistry. (c) Dynamics of  $\text{CH}_3\text{NH}_3^+$  cations generating distortions in the  $\text{PbI}_6$  octahedra. Reprinted with permission from refs 69 and 70. Copyright 2015 American Chemical Society and Copyright 2015 Nature Publishing Group. (d) Summary of  $\text{CH}_3\text{NH}_3\text{PbX}_3$ -based (X = I, Br, Cl) perovskites and space groups adopted as a function of temperature. Reprinted with permission from ref 71. Copyright 2016 The Royal Society of Chemistry.

Before starting to describe more complex mixed cation perovskite systems [e.g.,  $(\text{Rb}/\text{Cs}/\text{MA}/\text{FA})\text{Pb}(\text{I}/\text{Br})$  or  $(\text{MA}/\text{FA})\text{Pb}(\text{I}/\text{Br})$ ], we briefly outline our current understanding on structure–property relationship of simple perovskite systems (e.g.,  $\text{MAPbI}_3$  and  $\text{FAPbI}_3$ ) and then gradually add one element (cation or halide) at a time and introduce the new properties of the material induced by the addition of this new element.  $\text{MAPbI}_3$  is the most widely studied hybrid halide perovskite for photovoltaic applications<sup>13,24–26,72</sup> and therefore its fundamental properties were investigated most thoroughly.<sup>12,14,67,73–82</sup> At room temperature, the Goldschmidt's tolerance factor ( $t$ ) of  $\text{MAPbI}_3$  is 0.91<sup>83,84</sup> with ionic radii of  $\text{Pb}^{2+} = 0.132 \text{ nm}$ ,  $\text{I}^- = 0.206 \text{ nm}$ , and  $\text{MA}^+ = 0.18 \text{ nm}^7$  suggesting the tetragonal phase, which was confirmed experimentally by  $\text{MAPbI}_3$  single crystal X-ray diffraction (XRD) data.<sup>7,9</sup> It was reported that the  $\text{PbI}_6$  octahedra in  $\text{MAPbI}_3$  are corner connected and the  $\text{MA}^+$  cations are filled in the octahedral interstices (Figure 2a).<sup>67</sup> According to density functional theory (DFT) calculations, the ions within the inorganic  $\text{PbI}_6$  octahedra have electronic configuration of Pb:  $5d^{10}6s^26p^0$  and I:  $5p^6$ . The Pb  $6s6p$ –I  $5p$  interactions are responsible for chemical bonding in  $\text{PbI}_6$  octahedra and generation of two bands: the valence band maximum (VBM) is formed of an antibonding ( $\sigma^*$ ) Pb  $6s$ –I  $5p$

interactions, while the conduction band minimum (CBM) is formed of empty Pb  $6p$  orbitals<sup>73</sup> and/or from Pb  $6p$ –I  $5p$  interactions (Figure 2b).<sup>68,72,85–87</sup> The  $\text{MA}^+$  molecular units form bonding ( $\sigma$ ) states deep (5 eV below Fermi level) in the VBM and they do not hybridize with the  $\text{PbI}_6$  octahedra near CBM or VBM. Therefore, the  $\text{MA}^+$  cations were proposed to do not contribute directly toward the band structure, but play a major role providing structural stability by charge compensation within the  $\text{PbI}_6$  octahedra based largely on electrostatic (van der Waals) interactions.<sup>15,26,74</sup> Because of this lack of electronic interaction between  $\text{MA}^+$  and  $\text{PbI}_6^{4-}$ , free carriers in  $\text{MAPbI}_3$  are likely to diffuse along the corner shared  $\text{PbI}_6$  chains in the crystal lattice.<sup>88,89</sup> The VBM electrons that are photoexcited to CBM empty states determine the band gap ( $E_g$ ) (Figure 2b).<sup>85</sup> A wide range of  $E_g$  values between 1.5 and 1.61 eV have been reported for  $\text{MAPbI}_3$ <sup>14,15,80,90</sup> with the  $E_g$  values generally higher for polycrystalline films possibly due to quantum confinement.<sup>7,90</sup> Because the optimal  $E_g$  for a single-junction solar cell is between 1.1 and 1.4 eV on the basis of the Shockley–Queisser limit,<sup>91</sup> efforts have been made to modify the  $\text{MAPbI}_3$  structure.<sup>14,15</sup>

In addition, material instabilities have been widely reported.<sup>28,29,92,93</sup> It has been proposed that perovskites have

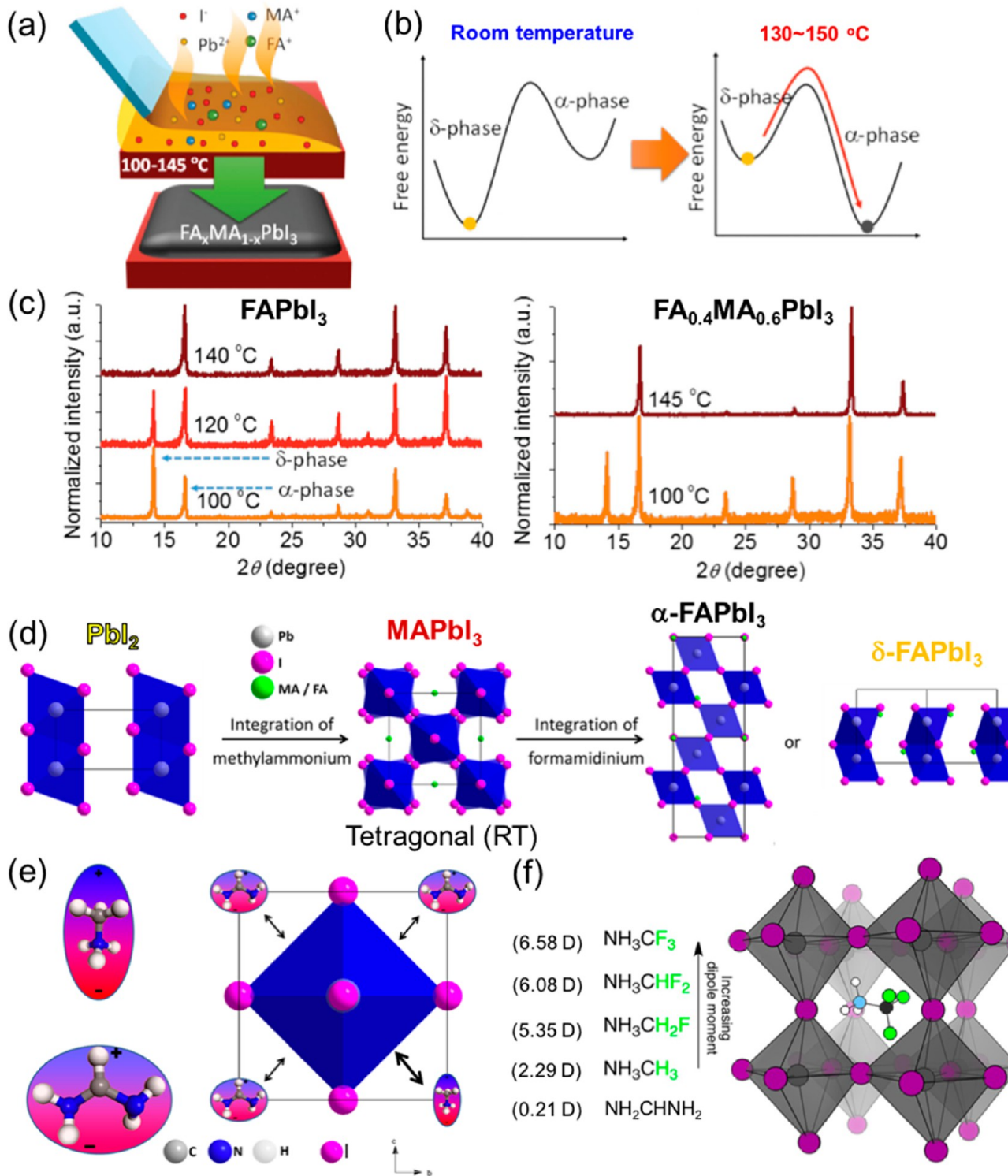


**Figure 3.** (a) Illustration of  $\text{MA}_{0.6}\text{FA}_{0.4}\text{PbI}_3$  perovskite film formation by doctor-blade method. (b) Schematic diagrams of free energy versus  $\alpha$ -phase and  $\delta$ -phase of  $\text{FAPbI}_3$  and  $\text{MA}_x\text{FA}_{1-x}\text{PbI}_3$  perovskites. (c) XRD patterns for  $\text{FAPbI}_3$  and  $\text{MA}_x\text{FA}_{1-x}\text{PbI}_3$  perovskites as a function of annealing temperature. The reflection at  $2\theta = 12^\circ$  and  $14^\circ$  are correlated to  $\delta$ - and  $\alpha$ -phase of  $\text{FAPbI}_3$ , respectively. Reprinted with permission from ref 111. Copyright 2016 WILEY-VCH Verlag GmbH & Co. KGaA, Weinheim. (d) Crystal structures of  $\text{PbI}_2$  where  $\text{PbI}_6$  octahedra are connected via shared plane of three iodide ions. Incorporation of MA leads the layered octahedra to form a 3D  $\text{MAPbI}_3$  network in tetragonal phase by reducing the number of shared iodide ions from three to one. Incorporation of <20% FA to  $\text{MAPbI}_3$  leads the unit cell to expand while maintaining the tetragonal phase. With FA/MA > 80% in the  $\text{MAPbI}_3$  structure, the tetragonal phase collapses and the trigonal phase of  $\alpha\text{-FAPbI}_3$  is formed (3D network). However, at room temperature, the hexagonal phase of  $\delta\text{-FAPbI}_3$  can also be formed. (e) Schematic illustration of the mechanism for the  $\text{MA}_x\text{FA}_{1-x}\text{PbI}_3$  stabilization based on the dipole moments of cations. Reprinted with permission from ref 106. Copyright 2015 American Chemical Society. (f) Theoretically calculated dipole moments for selected cations. Reprinted with permission from ref 114. Copyright 2014 American Chemical Society.

**Table 1.** Summary of Perovskite Solar Cell Performances Employing Mixed Cations and/or Halide Perovskites<sup>a,b</sup>

Solar cell architecture	Perovskite thickness (nm)	$E_g$ (eV)	Electrode active area (cm <sup>2</sup> )	$J_{sc}$ (mA/cm <sup>2</sup> )	$V_{oc}$ (V)	FF (%)	PCE (%)	Hysteresis	Stability	ref.
FTO/c-TiO <sub>2</sub> /mp-TiO <sub>2</sub> /MA <sub>0.6</sub> FA <sub>0.4</sub> PbI <sub>3</sub> /spiro/Au	~300 nm	1.53	0.285	18.15	1.027	71.5	13.4	—	Storage in air; ~25 °C and RH < 60%; 120 days.	102
ITO/PEDOT:PSS/MA <sub>0.6</sub> FA <sub>0.4</sub> PbI <sub>3</sub> /PC61BM/C <sub>60</sub> /Ag	~300 nm	— <sup>c</sup>	0.4	18.95	0.943	73.1	13.0	Hysteresis present.	—	109
FTO/c-TiO <sub>2</sub> /[MAPbI <sub>3</sub> ](FAPbI <sub>3</sub> )/Au [No HTL]	—	1.53–1.54	0.09	9.58	0.77	54	4.0	—	—	103
FTO/c-TiO <sub>2</sub> /[MA <sub>0.13</sub> FA <sub>0.87</sub> PbI <sub>3</sub> ]/spiro/Au	—	1.52 ± 0.02	0.0831	15.7	1	56	8.73	—	—	106
FTO/c-TiO <sub>2</sub> /mp-TiO <sub>2</sub> /MA <sub>0.6</sub> FA <sub>0.4</sub> PbI <sub>3</sub> /spiro/Au	— <sup>c</sup>	0.16	20.87	0.975	69.97	14.23	MA <sub>0.6</sub> FA <sub>0.4</sub> shows small hysteresis; Other compositions show hysteresis.	Storage in air and dark; RH < 60%; 120 days.	104	
ITO/PTAA/[MA <sub>0.6</sub> FA <sub>0.4</sub> PbI <sub>3</sub> ]/ICBA/C <sub>60</sub> /BCP/Cu [Doctor blade]	— <sup>c</sup>	1.55	—	23	1.03	77	18.3	Small hysteresis.	Storage in air; ~25 °C and RH 20%–60%; 30 days.	111
ITO/PEDOT:PSS/[MA <sub>0.6</sub> FA <sub>0.4</sub> PbI <sub>3</sub> ]/PC <sub>60</sub> BM/Ag	—	—	0.1	20.96 ± 0.14	0.979 ± 0.016	64.7 ± 1.2	13.28 ± 0.37	Small hysteresis.	—	110
FTO/c-TiO <sub>2</sub> /mp-TiO <sub>2</sub> /MA <sub>x</sub> FA <sub>1-x</sub> PbI <sub>3</sub> /WO <sub>3</sub> /Ag [CVD]	—	1.57	0.2	20.85	1.04	73.15	15.86	Negligible hysteresis.	Storage in air; 30 days.	112
FTO/ZnO/MA <sub>0.6</sub> FA <sub>0.4</sub> PbI <sub>3</sub> /spiro/Ag	~315	—	0.045	22.39	0.984	60.66	13.4	Hysteresis present.	Storage in N <sub>2</sub> ; 21 days.	105
FTO/c-TiO <sub>2</sub> /C60/MA <sub>0.6</sub> FA <sub>0.4</sub> PbI <sub>3</sub> /spiro/Au [LP-VASP]	~340	1.55	0.09	22.51	1.00	73.56	16.48	Small hysteresis.	Storage in N <sub>2</sub> ; 288 h.	113
FTO/c-TiO <sub>2</sub> /mp-TiO <sub>2</sub> /MA <sub>0.25</sub> FA <sub>0.75</sub> PbI <sub>3</sub> /spiro/Ag	~300	~1.545	—	21.10	1.03	71.38	15.51	Hysteresis present.	—	107
FTO/c-TiO <sub>2</sub> /[MA <sub>0.7</sub> FA <sub>0.3</sub> PbI <sub>3</sub> ]/spiro/Ag	—	—	22.03	1.03	75	17.02	Hysteresis present.	—	108	
ITO/PEDOT:PSS/[MA <sub>0.9</sub> C <sub>60</sub> <sub>0.1</sub> PbI <sub>3</sub> ]/PC60BM/Al	38 ± 9	1.54	0.13	10.10	1.05	73	7.68	—	Storage in air; ~20 °C and RH 11%; 42.5 h.	115
FTO/c-TiO <sub>2</sub> /mp-TiO <sub>2</sub> /MA <sub>0.91</sub> Cs <sub>0.09</sub> PbI <sub>3</sub> /spiro/Au	~400	— <sup>c</sup>	0.09	22.57	1.06	76	18.1	Hysteresis present.	Storage in air; ~85 °C; 1 h.	116
FTO/c-TiO <sub>2</sub> /Cs <sub>0.1</sub> FA <sub>0.9</sub> PbI <sub>3</sub> /spiro/Ag or Au	— <sup>c</sup>	1.55	0.125	23.5	1.06	66.3	16.5 <sup>d</sup>	Hysteresis present.	Test 1: Exposure to white light; Sample temperature ~60 °C; RH < 50%. Test 2: Storage in dark; 25 °C, RH 85%.	100
FTO/c-TiO <sub>2</sub> /Cs <sub>0.15</sub> FA <sub>0.85</sub> PbI <sub>3</sub> /spiro/Ag	—	1.52	—	20.39	1.06	74	16.1 <sup>d</sup>	Hysteresis present.	Storage in a desiccator and dark; RH 1.5%; 350 h.	101
FTO/c-TiO <sub>2</sub> /mp-TiO <sub>2</sub> /Cs <sub>0.2</sub> FA <sub>0.8</sub> PbI <sub>3</sub> /spiro/Au	—	1.56	0.16	21.5	1.017	70.1	15.69	—	Storage in air; 1000 h.	117
FTO/c-SnO <sub>2</sub> /C60-SAM/Cs <sub>0.2</sub> FA <sub>0.8</sub> PbI <sub>3</sub> /spiro/Au	~435	— <sup>c</sup>	0.08	21.73 ± 0.51	1.03 ± 0.02	72.37 ± 1.18	16.18 ± 0.50 <sup>d</sup>	Hysteresis present.	Storage in a drybox under room light; 10 days.	118
FTO/c-SnO <sub>2</sub> /C60-SAM/Cs <sub>0.2</sub> FA <sub>0.8</sub> PbI <sub>3</sub> + 0.5 mol % Pb(SCN) <sub>2</sub> /spiro/Au	— <sup>c</sup>	—	21.94 ± 0.31	1.06 ± 0.01	77.77 ± 1.51	18.16 ± 0.54 <sup>d</sup>	[Reverse]	Hysteresis present.	Storage in air; ~25 °C and RH ~ 40%; 4 h.	119
FTO/c-TiO <sub>2</sub> /Cs <sub>x</sub> FA <sub>1-x</sub> PbI <sub>3</sub> /spiro/Ag (x not determined)	— <sup>c</sup>	0.12	20.4	1.09	74	16.4	—	—	—	120
FTO/NiO/Cs <sub>0.15</sub> FA <sub>0.85</sub> PbI <sub>3</sub> /PC61BM/IFEN-Br/Ag	— <sup>c</sup>	0.09	20.81	1.035	71.4	15.38	—	—	Storage in air; ~25 °C and RH ~ 55%; 1000 h.	121
FTO/c-TiO <sub>2</sub> /mp-TiO <sub>2</sub> /Rb <sub>0.05</sub> FA <sub>0.95</sub> PbI <sub>3</sub> /spiro/Au	~480 (capping layer)	1.53	—	23.93	1.07	67	17.16	Smaller hysteresis compared to FAPbI <sub>3</sub> .	Storage in air; ~25 °C and RH ~ 55%; 4 weeks.	122
FTO/c-TiO <sub>2</sub> /mp-TiO <sub>2</sub> /Rb <sub>0.05</sub> FA <sub>0.95</sub> PbI <sub>3</sub> /spiro/Au	—	— <sup>c</sup>	0.65	23.8	1.03	65.9	16.2	—	—	—

Table 1. continued

Solar cell architecture	Perovskite thickness (nm)	$E_g$ (eV)	Electrode active area (cm <sup>2</sup> )	$J_{sc}$ (mA/cm <sup>2</sup> )	$V_{oc}$ (V)	FF (%)	PCE (%)	Hysteresis	Stability	ref.
FTO/c-TiO <sub>2</sub> /mp-TiO <sub>2</sub> / Cs <sub>0.2</sub> FA <sub>0.8</sub> PbI <sub>2.84</sub> Br <sub>0.16</sub> /spiro/Au	—	1.58	0.16	21.9	1.073	74.2	17.35	—	Storage in air; 1000 h.	117
FTO/c-TiO <sub>2</sub> /mp-TiO <sub>2</sub> /(MAP- bI <sub>3</sub> ) <sub>1-x</sub> (C <sub>x</sub> PbBr <sub>3</sub> ) <sub>x</sub> /spiro/Au	360	— <sup>c</sup>	0.09	20.9 ± 0.42	1.07 ± 0.01	71 ± 2	15.9 ± 0.52	Small hysteresis	(1) Degradation test of unencapsulated devices under UV light (365 nm, 364 mW/cm <sup>2</sup> ) (2) Stability of unencapsulated devices in ambient air (25 °C, 20–30% RH) 2000 h aging test.	123
FTO/Nb-TiO <sub>2</sub> /FA <sub>0.84</sub> MA <sub>0.16</sub> Pb(I <sub>0.8</sub> Br <sub>0.16</sub> )/ spiro/Au	~500	— <sup>c</sup>	0.12	23.4	1.006	74	17.6	—	Storage in air (~50% RH, 23 °C) without encapsulation for 1000 h.	124
FTO/c-TiO <sub>2</sub> /mp-TiO <sub>2</sub> /FAPbI <sub>3</sub> -MABr/spiro/ Au	~450	—	0.096	22.17	1.07	67.38	15.98	Small hysteresis	Storage in air (~50% RH, 23 °C) without encapsulation for 1000 h.	125
ITO/PEDOT:PSS/(FAP- bI <sub>3</sub> ) <sub>0.8</sub> (MAPbBr <sub>3</sub> ) <sub>0.2</sub> /C60/BCP/Ag	~280 <sup>c</sup>	—	0.48	22.14	1.04	63.38	14.59	—	—	126
FTO/c-TiO <sub>2</sub> /mp-TiO <sub>2</sub> /(FAPbI <sub>3</sub> ) <sub>0.85</sub> Pb (MABr <sub>3</sub> ) <sub>0.15</sub> /spiro/Au	mp-TiO <sub>2</sub> with PVSK in- filtrated (~200 nm) + capping layer (~650 nm)	1.57– 1.58	0.126	22.5	1.13	69	17.6	Yes	—	127
FTO/c-TiO <sub>2</sub> /mp-TiO <sub>2</sub> /(FA/MA)Pb(I <sub>Br</sub> ) <sub>3</sub> / spiro/Au	—	0.36	21	1.01	69	14.5	Small hysteresis	ISOS-O <sub>2</sub> protocol for 1000 h.	128	
ITO/PEDOT:PSS/(FAP- bI <sub>3</sub> ) <sub>0.8</sub> (MAPbBr <sub>3</sub> ) <sub>0.2</sub> /C60/BCP/Ag	— <sup>c</sup>	0.1	20.1 ± 0.5	0.87 ± 0.01	66.4 ± 1.2	11.8 ± 0.20	Small hysteresis	—	—	129
FTO/c-TiO <sub>2</sub> /mp-TiO <sub>2</sub> /(FA/MA)Pb(I <sub>Br</sub> ) <sub>3</sub> / spiro/Au PbI <sub>2</sub> :FAI = 1.05 (PbI <sub>2</sub> excess)	~400 <sup>c</sup>	1.6	0.16	24.6	1.16	73	20.8	No hysteresis	Sealed cells using epoxy and stored in a desiccator in dark for 1 month.	130
FTO/c-TiO <sub>2</sub> /mp-TiO <sub>2</sub> /(FA <sub>1-x</sub> MA <sub>x</sub> ) <sub>0.8</sub> Pb (I <sub>5/6</sub> Br <sub>1/6</sub> )/spiro/Au	~400 <sup>c</sup>	1.64	0.16	23.7	1.14	76	20.67	Hysteresis varies accord- ing to composition.	—	90
ITO/PEDOT:PSS/(MA <sub>0.80</sub> FA <sub>0.20</sub> )PbI <sub>3-y</sub> Cl <sub>y</sub> / PC61BM/C60/LiF/Ag	~280	1.58	0.11	21.55 ± 0.55	1.10 ± 0.01	75 ± 2	17.45	No hysteresis when MA <sub>0.8</sub> FA <sub>0.20</sub> PbI <sub>3-y</sub> Cl <sub>y</sub> is annealed below 110 °C.	—	131
FTO/SnO <sub>2</sub> /PC60BM/FA <sub>0.83</sub> C <sub>5</sub> <sub>0.17</sub> Pb (I <sub>0.6</sub> Br <sub>0.4</sub> ) <sub>3</sub> /spiro/Ag	— <sup>c</sup>	1.74	0.0919	19.4	1.2	75.1	17.1	—	—	132
ITO/NiO/FA <sub>0.83</sub> C <sub>5</sub> <sub>0.17</sub> Pb(I <sub>0.6</sub> Br <sub>0.4</sub> ) <sub>3</sub> /LiF/ PC60BM/SnO <sub>2</sub> /ZTO/TTO/LiF/Ag <sub>8</sub>	— <sup>c</sup>	1.63	0.715	19.5	1.19	67.8	14.7	—	single-junction perovskite device with no addi- tional encapsulation during 1000 h of continuous maximum-power-point tracking	133
FTO/SnO <sub>2</sub> /C60/C <sub>5</sub> <sub>0.17</sub> FA <sub>0.83</sub> Pb(I <sub>0.6</sub> Br <sub>0.4</sub> ) <sub>3</sub> / spiro/Au	—	—	0.0919	23	1.06	75	18.3	—	Aged under full AM1.5 spectrum at $V_{oc}$ in air without UV filter.	134
FTO/c-TiO <sub>2</sub> /mp-TiO <sub>2</sub> / Cs <sub>0.2</sub> FA <sub>0.8</sub> PbI <sub>2.84</sub> Br <sub>0.16</sub> /spiro/Au	—	1.49	0.16	21.9	1.073	74.2	17.35	—	Storage in air; 1000 h.	117
FTO/c-TiO <sub>2</sub> /mp-TiO <sub>2</sub> / Cs <sub>0.05</sub> (FA <sub>0.83</sub> MA <sub>0.17</sub> ) <sub>0.95</sub> Pb(I <sub>0.83</sub> Br <sub>0.17</sub> ) <sub>3</sub> / spiro/Au	~500 <sup>c</sup>	1.6 <sup>c</sup>	0.16	22.69 ± 0.75	1.132 ± 0.025	74.8 ± 1.8	19.2 ± 0.91	Yes	Under constant illumination and maximum power tracking for 250 h; Cells held at room temper- ature.	65
FTO/c-TiO <sub>2</sub> /mp-TiO <sub>2</sub> /Cs <sub>0.8</sub> FA <sub>0.2</sub> MA <sub>0.01</sub> Pb (I <sub>0.83</sub> Br <sub>0.17</sub> ) <sub>3</sub> /spiro/Au	~500	— <sup>c</sup>	0.16	21.5	1.155	73	18.1	Yes	300 h storage; dry air and in dark.	135
FTO/SnO <sub>2</sub> /Cs <sub>0.1</sub> FA <sub>0.83</sub> MA <sub>0.01</sub> Pb(I <sub>0.83</sub> Br <sub>0.17</sub> ) <sub>3</sub> / spiro/Au	— <sup>c</sup>	0.16	22.86 ± 0.37	1.123 ± 0.011	69.6 ± 1.9	17.68 ± 0.91	Yes	Exhibit some degree of hysteresis	(1) Under continuous light illumination; cells kept under ambient conditions (40–50% RH, 25 °C).	136
FTO/c-TiO <sub>2</sub> /mp-TiO <sub>2</sub> / Rb <sub>x</sub> (FAPbI <sub>3</sub> ) <sub>1-x</sub> (MAPbBr <sub>3</sub> ) <sub>y</sub> /PTAA/Au 15% PbI <sub>2</sub> excess S% RbI doping	— <sup>c</sup>	—	—	—	—	—	—	—	—	—

Table 1. continued

Solar cell architecture	Perovskite thickness (nm)	$E_g$ (eV)	Electrode active area ( $\text{cm}^2$ )	$J_{sc}$ ( $\text{mA}/\text{cm}^2$ )	$V_{oc}$ (V)	FF (%)	PCE (%)	Hysteresis	Stability	ref.
FTO/c-TiO <sub>2</sub> /mp-TiO <sub>2</sub> / Rb <sub>0.05</sub> FA <sub>0.8</sub> MA <sub>0.15</sub> Pb <sub>0.25</sub> Br <sub>0.45</sub> /spiro/Au	—	— <sup>c</sup>	0.5	22.5	1.168	74.7	19.6	—	(2) Steady-state efficiency tracking maximum power point under N <sub>2</sub> environment. Storage in air; ~25 °C, and RH ~55%; 4 weeks.	122
FTO/c-TiO <sub>2</sub> /mp-TiO <sub>2</sub> /Rb <sub>0.05</sub> C <sub>80</sub> <sub>10</sub> FA <sub>0.85</sub> Pb <sub>(I<sub>0.83</sub>Br<sub>0.17</sub>)<sub>3</sub></sub> /spiro/Au	—	—	0.16	22.3	1.157	75	19.3	Yes	—	137
FTO/c-TiO <sub>2</sub> /mp-TiO <sub>2</sub> / Rb <sub>0.05</sub> C <sub>80</sub> <sub>10</sub> (FA <sub>0.83</sub> MA <sub>0.17</sub> ) <sub>0.90</sub> Pb(I <sub>0.83</sub> Br <sub>0.17</sub> ) <sub>3</sub> / PTAA/Au	~500	1.63	0.16	22.8	1.180	81	21.8	Yes	Device aged for 500 h at 85 °C under continuous full illumination and maximum power tracking in a nitrogen atmosphere.	—
FTO/c-TiO <sub>2</sub> /mp-TiO <sub>2</sub> / Rb <sub>0.05</sub> (MA <sub>0.6</sub> C <sub>80</sub> <sub>0.4</sub> ) <sub>0.25</sub> Pb <sub>0.2</sub> Br/PTAA/Au	—	— <sup>c</sup>	0.5	>20 <sup>c</sup>	>1.15 <sup>c</sup>	—	17.4 (steady state power)	—	(2) 12 h-light/dark cycles.	—
FTO/c-TiO <sub>2</sub> /mp-TiO <sub>2</sub> /Rb(S%) in FA <sub>0.75</sub> (MA <sub>0.6</sub> C <sub>80</sub> <sub>0.4</sub> ) <sub>0.25</sub> Pb <sub>0.2</sub> Br/PTAA/Au	mp-TiO <sub>2</sub> with PVSK infiltrated (~180 nm) + capping layer (~400 nm)	1.73	0.1764	18.3	>1.1 <sup>c</sup>	— <sup>c</sup>	17.4 (steady state power)	Negligible	(1) Light stability for 12 h under continuous 1 sun illumination and applied maximum power point voltage in N <sub>2</sub> environment with (controlled 25 °C). (2) 12 h-light/dark cycles.	138

<sup>a</sup>Perovskite thickness, bandgap ( $E_g$ ), electrode active area, solar cell parameters of short-circuit current ( $J_{sc}$ ), open-circuit voltage ( $V_{oc}$ ), fill factor (FF), and power conversion efficiency (PCE) are indicated. Additional notes on hysteresis and stability are indicated. <sup>b</sup>Abbreviations: FTO = indium tin oxide; FTOTPD = poly(*N,N'*-bis(4-butylphenyl)-*N,N'*-bis(phenyl)benzidine); c-TiO<sub>2</sub> = compact layered TiO<sub>2</sub>; spiro-MeOTAD = 2,7,7,7-tetrakis(*N,N*-di-*p*-methoxyphenylamine)-9,9'-spirobifluorene; PTAA = poly[bis(4-phenyl)(2,4,6-trimethylphenyl)amine]; PEDOT:PSS = poly(3,4-ethylenedioxythiophene):poly(styrene sulfonate); ICBA = indene-C60 bisadduct; BCP = 2,9-dimethyl-4,7-diphenyl-1,10-phenanthroline; PC60BM = [6,6]-phenyl-C60 butyric acid methyl ester; PC61BM = [6,6]-phenyl C61 butyric acid methyl ester; PFN-Br = poly[(9,9-bis(3'-(*N,N*-dimethyl)-*N*-ethylammonium)propyl)-2,7-fluorene)-*alt*-2,7-(9,9-diethylfluorene)] dibromide. C60-SAM = fullerene-self-assembled-monolayer. Pb(SCN)<sub>2</sub> = lead(II) thiocyanate. PFN-Br = poly[(9,9-bis(3'-(*N,N*-dimethyl)-*N*-ethylammonium)propyl)-2,7-fluorene)-*alt*-2,7-(9,9-diethylfluorene)] dibromide. ZTO = zinc tin oxide. <sup>c</sup>Thickness and absorption measured, but values not explicitly stated. <sup>d</sup>Averaged values based on forward and reverse scans reported.

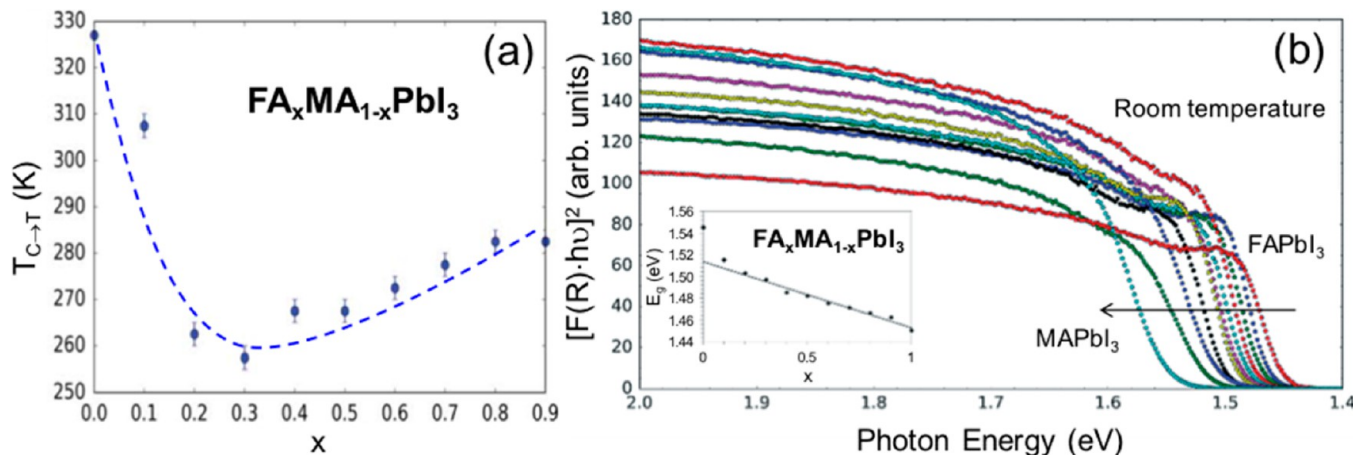


**Figure 4.** (a) Phase transition temperatures from cubic to tetragonal ( $T_{C \rightarrow T}$ ) and (b) Tauc plots of UV–vis reflectance spectra measured at room temperature and (inset) extracted band gap ( $E_g$ ) of  $FA_xMA_{1-x}PbI_3$  ( $0 \leq x \leq 1$ ) perovskites. Reprinted with permission from ref 83. Copyright 2016 The Royal Society of Chemistry.

an inherently “soft” structure (“plastic crystals”<sup>94</sup>) and therefore several dynamical phenomena characterized by different time scales exist in perovskites (from femtosecond up to minutes) influencing strongly on the overall optoelectronic properties (e.g., energy levels, bandgap, balanced/imbalanced charge transport, etc.) of perovskites (Figure 2c).<sup>69,70,95–97</sup> Furthermore,  $MAPbI_3$  undergoes a phase transition from the tetragonal to cubic phase at  $\sim 54$  °C (Figure 2d), a temperature that is of relevance during typical solar cell operation.<sup>9,49</sup> Therefore, it is imperative to develop perovskites insensitive to composition instabilities under stress conditions for solar cell operation. For certification, solar modules must operate successfully in the temperature range between  $-40$  and  $+85$  °C.<sup>98</sup> In contrast to  $MAPbI_3$ ,  $FAPbI_3$  was reported to be free from phase transition between a wide temperature range from  $25$  to  $150$  °C.<sup>99,100</sup> Chemical compositional engineering<sup>63</sup> (or alloying<sup>8,101</sup>) was shown to be an effective strategy (e.g., substitution of  $MA^+$  by other cations such as  $FA^+$ ,  $Cs^+$ ,  $Rb^+$ , Figure 1c) to further enhance the optoelectronic properties of  $MAPbI_3$  as evidenced by reported certified efficiencies (Figure 1b).<sup>5,7,90</sup>

## 2. MIXED A CATIONS

**2.1. Binary ( $FA/MA$ ) $PbI_3$  System.** Perturbing the A cation size can influence the optical properties by deforming the  $BX_6$  octahedron network. A larger (e.g.,  $FA^+ = 0.19\text{--}0.22$  nm) or smaller (e.g.,  $Cs^+ = 0.167$  nm,  $Rb^+ = 0.152$  nm) cation causes the lattice to expand or contract leading to the change of  $B-X$  bond length, which has been shown to influence  $E_g$ . Pellet et al. reported the first mixed A cation describing the bandgap tunability of  $MA_xFA_{1-x}PbI_3$ -based solar cells by varying the ratio of MA to FA.<sup>102</sup> The MA/FA mixed perovskites were synthesized by dipping the predeposited  $PbI_2$  with premixed  $MA_xFA_{1-x}I$  solution in isopropanol. They showed that the  $MA_{0.6}FA_{0.4}PbI_3$  composition resulted in the best PCE of 13.4% (Table 1) with the absorption edge extending up to  $\sim 810$  nm ( $E_g \sim 1.53$  eV), which was also similar to the pure  $FAPbI_3$  perovskite. Later several works have been published showing better  $MA_xFA_{1-x}PbI_3$  film quality (higher film coverage, fewer pin-holes, higher crystal quality, larger grain sizes, smaller roughness within the grains, and alternative selective contacts),<sup>103–108</sup> employing inverted structure,<sup>109,110</sup> and using perovskite deposition techniques other than spin-coating (Table 1),<sup>111–113</sup> such as doctor blading (Figure 3a),<sup>111</sup>

chemical vapor deposition (CVD),<sup>112</sup> and low-pressure vapor-assisted solution process (LP-VASP)<sup>113</sup> (Table 1). Based on Table 1, among optimized MA/FA ratios, there is a consensus that  $MA_{0.6}FA_{0.4}PbI_3$  composition results in the best PCE as high as 18.3%.<sup>111</sup> Deng et al.<sup>111</sup> employed additionally Cu as the top electrode in their devices and observed high device performances. Chen et al.<sup>113</sup> reported devices with larger active area of  $1\text{ cm}^2$  generating PCE of 8%, while their smaller cells ( $0.09\text{ cm}^2$ ) generated PCE of 16.48%.

The highest PCE for  $MAPbI_3$  solar cells in a standard device architecture was reported to reach  $\sim 20\%$ ,<sup>139,140</sup> whereas in an inverted structure, the highest PCE of 18.1% was reported.<sup>141</sup> Up to now, employing complex strategies (e.g., solvent-engineering,  $HPbI_3$  precursor, organic-cation displacement), the best PCE reported for  $FAPbI_3$  perovskite solar cells reached 13.5–18%, which is somehow lower than the  $MAPbI_3$ -based ones.<sup>64,99,142–144</sup> Because of the larger ionic radius of  $FA^+$  compared to  $MA^+$ ,  $FAPbI_3$  perovskites are expected to have a smaller  $E_g$  (1.47 to 1.55 eV depending on the fabrication methods<sup>145</sup>) compared to  $MAPbI_3$ .<sup>99,143,146,147</sup> As the consequence, higher PCE would be expected for  $FAPbI_3$  solar cells as light harvesting range extends further into the near-infrared. Comparative works have shown that the short-circuit current ( $J_{sc}$ ) of  $FAPbI_3$  devices is higher than that of  $MAPbI_3$ , confirming the ability of extended light-absorption of  $FAPbI_3$  perovskites. The main loss in PCE comes from the poor fill factor (FF).<sup>143,148</sup> Several studies proposed that there is a fundamental limitation associated with the phase instability of the pure  $FAPbI_3$  in ambient conditions (either in the form of polycrystalline film<sup>8,63,106,149</sup> or single crystal<sup>150</sup>). As a matter of fact,  $FAPbI_3$  possess two polymorphs (Figure 3b–d).<sup>8,82,106,119,149–151</sup>  $FAPbI_3$  crystallizes at room temperature as (i) photoinactive nonperovskite, hexagonal  $\delta$ - $FAPbI_3$  perovskite (“delta or yellow phase”, space group  $P6_3mc$ <sup>82</sup>) formed from face-sharing  $PbI_6$  octahedra (Figure 3d), and (ii) photoactive trigonal  $\alpha$ - $FAPbI_3$  perovskite (“alpha or black phase”, space group  $P3m1$ <sup>82</sup> or  $Pm\bar{3}m$ <sup>149</sup>) formed at higher temperatures,  $\sim 125\text{--}165$  °C (Figure 3d).<sup>65,82,101,111,121</sup> Similar polymorphism was reported for  $\alpha,\delta$ - $CsPbI_3$  system.<sup>65,121</sup> After  $\alpha$ - $FAPbI_3$  is formed, a slow phase transformation to  $\delta$ - $FAPbI_3$  is reported when kept at room temperature, which leads to unstable device operation.<sup>8,111</sup> It is interesting to note that the incorporation of  $MA^+$  into  $FAPbI_3$  structure results in a much

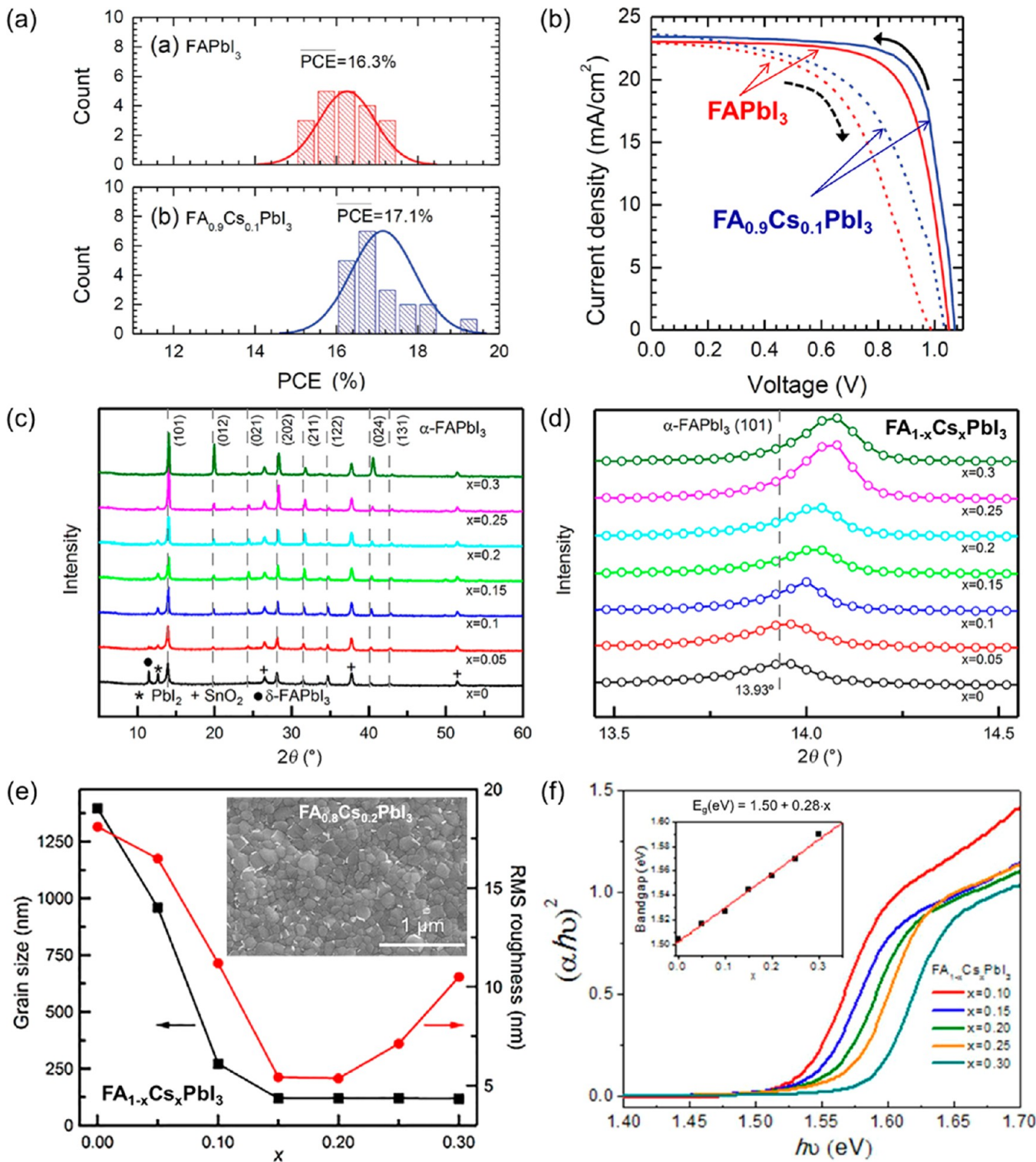


**Figure 5.** (a) Statistical distribution of perovskite solar cell PCE based on FAPbI<sub>3</sub> (red) and FA<sub>1-x</sub>Cs<sub>x</sub>PbI<sub>3</sub> (blue) and (b) *J*–*V* curves of the best performing devices for FAPbI<sub>3</sub> (red) and FA<sub>1-x</sub>Cs<sub>x</sub>PbI<sub>3</sub> (blue) at reverse scans (solid lines) and forward scans (dotted lines). Reprinted with permission from ref 100. Copyright 2015 WILEY-VCH Verlag GmbH & Co. KGaA, Weinheim. (c,d) XRD patterns and (e) grain size and surface RMS roughness of FA<sub>1-x</sub>Cs<sub>x</sub>PbI<sub>3</sub> with x = 0 to 0.30. Reprinted with permission from ref 118. Copyright 2016 WILEY-VCH Verlag GmbH & Co. KGaA, Weinheim. (f) Tauc plots and extracted band gaps (E<sub>g</sub> inset) for FA<sub>1-x</sub>Cs<sub>x</sub>PbI<sub>3</sub> with x = 0 to 0.30. Reprinted with permission from ref 101. Copyright 2015 American Chemical Society.

more stable MA<sub>x</sub>FA<sub>1-x</sub>PbI<sub>3</sub> perovskite structure,<sup>83,152,153</sup> its origins of which were further investigated by Binek et al.<sup>106</sup> It has been proposed that the incorporation of a smaller cations (MA<sup>+</sup>) with a large dipole moment exhibits stronger interaction

with the PbI<sub>6</sub> octahedra, which stabilizes the 3D arrangement of α-FAPbI<sub>3</sub> with little lattice shrinkage or changes in the optical properties (Figure 3e). MA<sup>+</sup> has a dipole moment ten times higher than that of FA<sup>+</sup> (Figure 3f).<sup>114</sup> Similarly, based on DFT

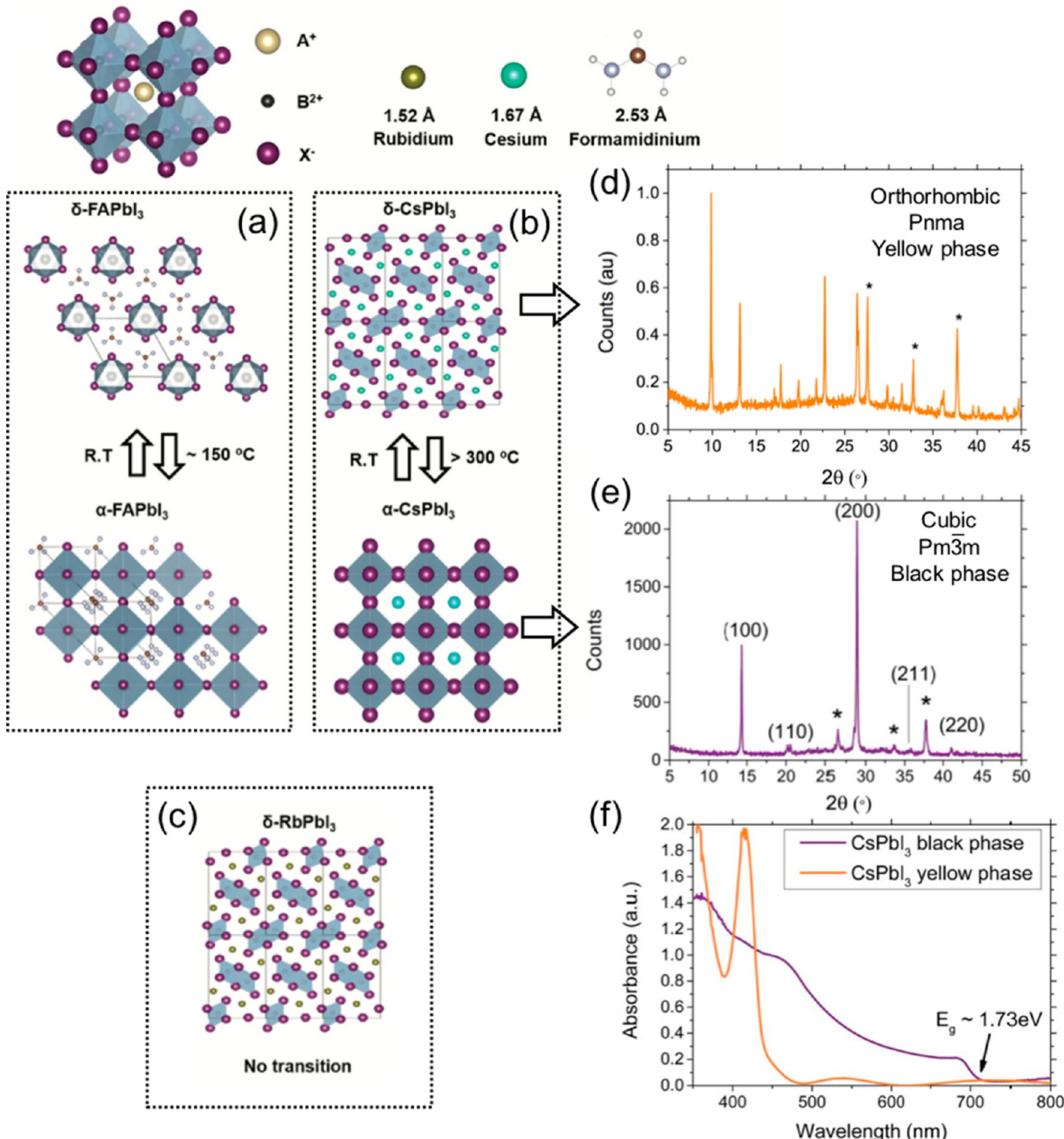


**Figure 6.** Illustration of  $\text{ABX}_3$  perovskite crystal structure and possible candidates for the A-site cation ( $\text{FA}^+$ ,  $\text{Cs}^+$ ,  $\text{Rb}^+$ ) with corresponding ionic radius. (a) Schematic representations of the polymorphs in (b)  $\alpha,\delta\text{-FAPbI}_3$  and (c)  $\alpha,\delta\text{-CsPbI}_3$  perovskites. The  $\alpha \rightarrow \delta$  phase transitions for  $\text{CsPbI}_3$  is much higher than in  $\text{FAPbI}_3$ . At room temperature, the  $\delta$ -phases are preferentially stabilized. Reprinted with permission from ref 121. Copyright 2017 WILEY-VCH Verlag GmbH & Co. KGaA, Weinheim. (d) XRD of  $\text{CsPbI}_3$  thin film in yellow phase and (e) black phase. Peaks with \* correspond to the FTO substrate. (f) Absorbance spectra of black and yellow phases of  $\text{CsPbI}_3$  thin films. The measurements were done in air, with the black phase perovskite coated with poly methyl methacrylate (PMMA) to minimize transformation into the yellow phase. Reprinted with permission from ref 155. Copyright 2015 The Royal Society of Chemistry.

calculations El-Mellouhi et al.<sup>154</sup> proposed that  $\text{CH}_3\text{PH}_3^+$ ,  $\text{CH}_3\text{SH}_2^+$ , and  $\text{SH}_3^+$  cations could also result in stronger cohesion between  $\text{PbI}_6$  octahedra and A cation within the crystal and attain enhanced stability while maintaining a suitable bandgap for solar cell applications. As described later

in section 2.3,  $\text{Cs}^+$  that has no dipole moment also helps stabilize the  $\alpha\text{-FAPbI}_3$  phase. The transition from tetragonal  $\text{MAPbI}_3$  to trigonal  $\alpha\text{-FAPbI}_3$  is observed when the  $\text{FA}^+/\text{MA}^+$  ratio in the structure is  $> 80\%$ .<sup>106</sup> The phase transition behavior as a function of  $\text{FA}_x\text{MA}_{1-x}\text{PbI}_3$  ( $0 \leq x \leq 1$ ) composition and

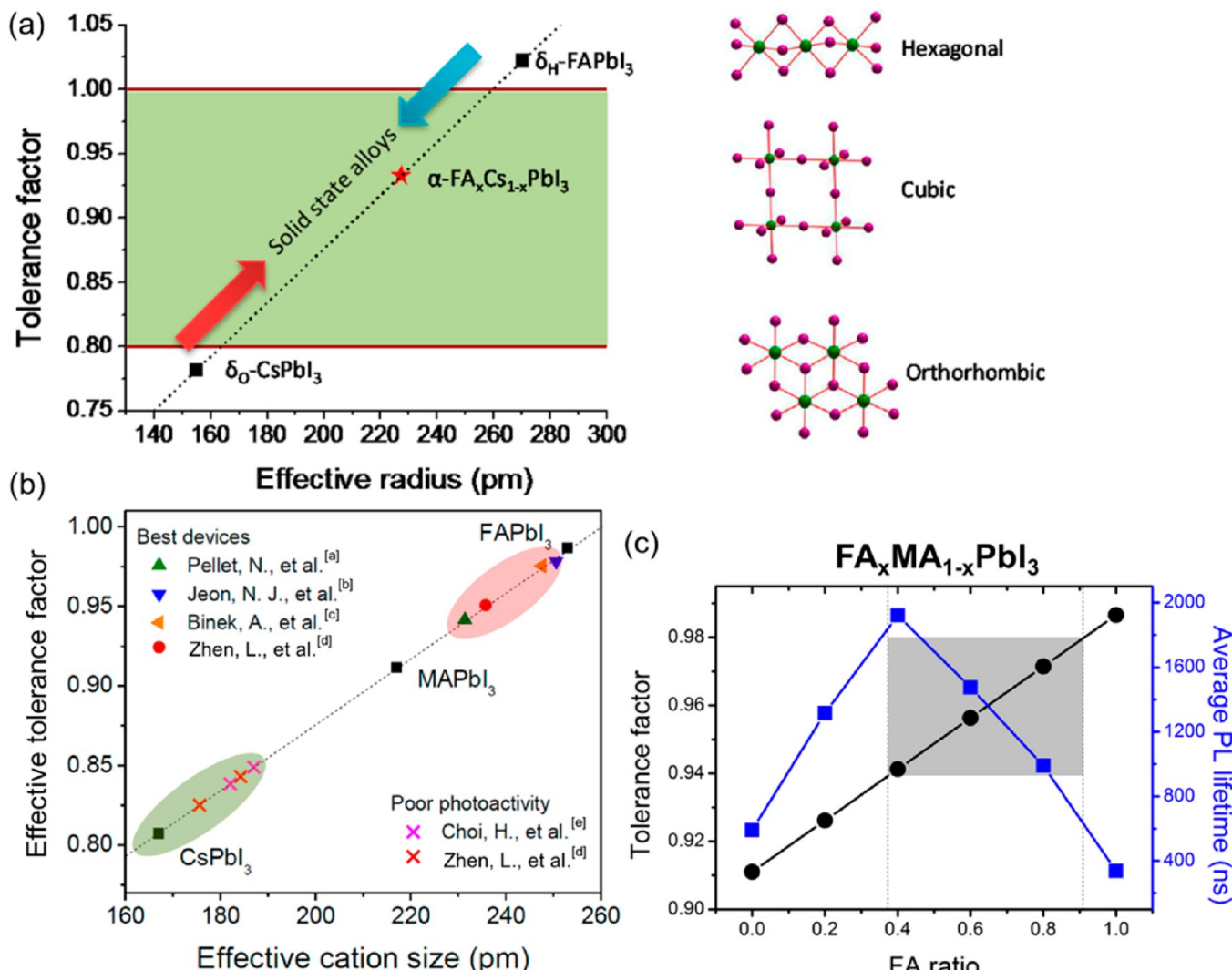


**Figure 7.** (a) Goldschmidt tolerance factor as empirical index for predicting stable perovskite crystal structure. Tolerance factor between 0.8 and 1.0 (green area) is favorable for cubic perovskite structure, and larger (>1) or smaller (<0.8) values generate nonperovskite structures. (b) Summary of the effective tolerance factors of different mixed perovskite alloys from the literature. [a]  $\text{MA}_{0.6}\text{FA}_{0.4}\text{PbI}_3$ ,<sup>[102]</sup> [b]  $(\text{FAPbI}_3)_{1-x}(\text{MAPbBr}_3)_x$  ( $x = 0.15$ ),<sup>[63]</sup> [c]  $\text{MA}_{0.13}\text{FA}_{0.87}\text{PbI}_3$ ,<sup>[106]</sup> [d]  $\text{Cs}_{0.15}\text{FA}_{0.85}\text{PbI}_3$ ,<sup>[101]</sup> [e]  $\text{MA}_{0.9}\text{Cs}_{0.1}\text{PbI}_3$ ,<sup>[115]</sup> Reprinted with permission from ref 101. Copyright 2016 American Chemical Society. (c) Correlation between Goldschmidt tolerance factor (black circles) and PL (blue squares) of the mixed cation  $\text{FA}_x\text{MA}_{1-x}\text{PbI}_3$  perovskites. Reprinted with permission from ref 152. Copyright 2016 American Chemical Society.

temperature ( $150 \text{ K} \leq T \leq 300 \text{ K}$ ) was investigated experimentally by Weber et al.<sup>83</sup> At 300 K, the  $\text{FA}_x\text{MA}_{1-x}\text{PbI}_3$  with  $0.2 \leq x \leq 1$  composition revealed a cubic structure with unit cell dimensions of  $\sim 6.3 \text{ \AA}$ . However, the tetragonal phase was observed for  $\text{MAPbI}_3$  ( $x = 0$ ) and  $\text{FA}_{0.1}\text{MA}_{0.9}\text{PbI}_3$  ( $x = 0.1$ ) perovskites. Their summary data (Figure 4a) extracted from variable temperature single crystal XRD measurements show a nonmonotonic behavior of the phase transition temperatures from cubic to tetragonal ( $T_{\text{C} \rightarrow \text{T}}$ ). Starting from  $x = 0$  ( $\text{MAPbI}_3$ ) showing  $T_{\text{C} \rightarrow \text{T}} \sim 327 \text{ K}$ ,  $T_{\text{C} \rightarrow \text{T}}$  decreased sharply reaching  $\sim 257 \text{ K}$  at  $x = 0.3$ . Subsequent increase in the FA ( $0.3 \leq x \leq 0.9$ ) content leads to a slow steady increase in  $T_{\text{C} \rightarrow \text{T}} \sim 298 \text{ K}$  at  $x = 0.9$  (Figure 4a). UV-vis measurements on  $\text{FA}_x\text{MA}_{1-x}\text{PbI}_3$  ( $0 \leq x \leq 1$ ) revealed a linear decrease in the optical band gap with increase in the FA content from  $0.2 \leq x \leq 1$  (Figure 4b), corresponding to the range of compositions adopting the cubic unit cell at room temperature.  $\text{MAPbI}_3$  ( $x = 0$ ) and  $\text{FA}_{0.1}\text{MA}_{0.9}\text{PbI}_3$  ( $x = 0.1$ ) showed deviation from the linear

trend due to the tetragonal structure stabilized at room temperature.<sup>262</sup>

**2.2. Binary (MA/Cs)PbI<sub>3</sub> System.** To the best of our knowledge, there are only two reports about the (MA/Cs)PbI<sub>3</sub> system. The first study was conducted by Choi et al.,<sup>115</sup> in which they optimized  $\text{Cs}_x\text{MA}_{1-x}\text{PbI}_3$  devices with  $x = 0.1$  (inverted structure: ITO/PEDOT:PSS/Cs<sub>0.1</sub>MA<sub>0.9</sub>PbI<sub>3</sub>/PCBM/Al) achieved a PCE of 7.68%. The second study was performed by Niu et al.,<sup>116</sup> reporting a higher efficiency (reverse scan) of 18.1% in their optimized  $\text{Cs}_x\text{MA}_{1-x}\text{PbI}_3$  devices with  $x = 0.09$  (regular structure: FTO/c-TiO<sub>2</sub>/mp-TiO<sub>2</sub>/Cs<sub>0.09</sub>MA<sub>0.91</sub>PbI<sub>3</sub>/Spiro-MeOTAD/Au) (Table 1). When the PCEs of  $\text{Cs}_x\text{MA}_{1-x}\text{PbI}_3$  devices are compared to their individual reference cells, i.e.,  $\text{MAPbI}_3$ , both studies observed increase of  $\sim 20\%$ <sup>115</sup> and  $\sim 15\%$ ,<sup>116</sup> respectively. Although, the phase transitions for (MA/Cs)PbI<sub>3</sub> system were not studied, Niu et al.<sup>116</sup> showed better thermal stability of  $\text{Cs}_x\text{MA}_{1-x}\text{PbI}_3$  with  $x = 0.09$  and  $x = 0.20$  than that of  $\text{MAPbI}_3$ . Contrary to MA<sup>+</sup> (section 2.1), which has a large dipole moment, Cs<sup>+</sup>

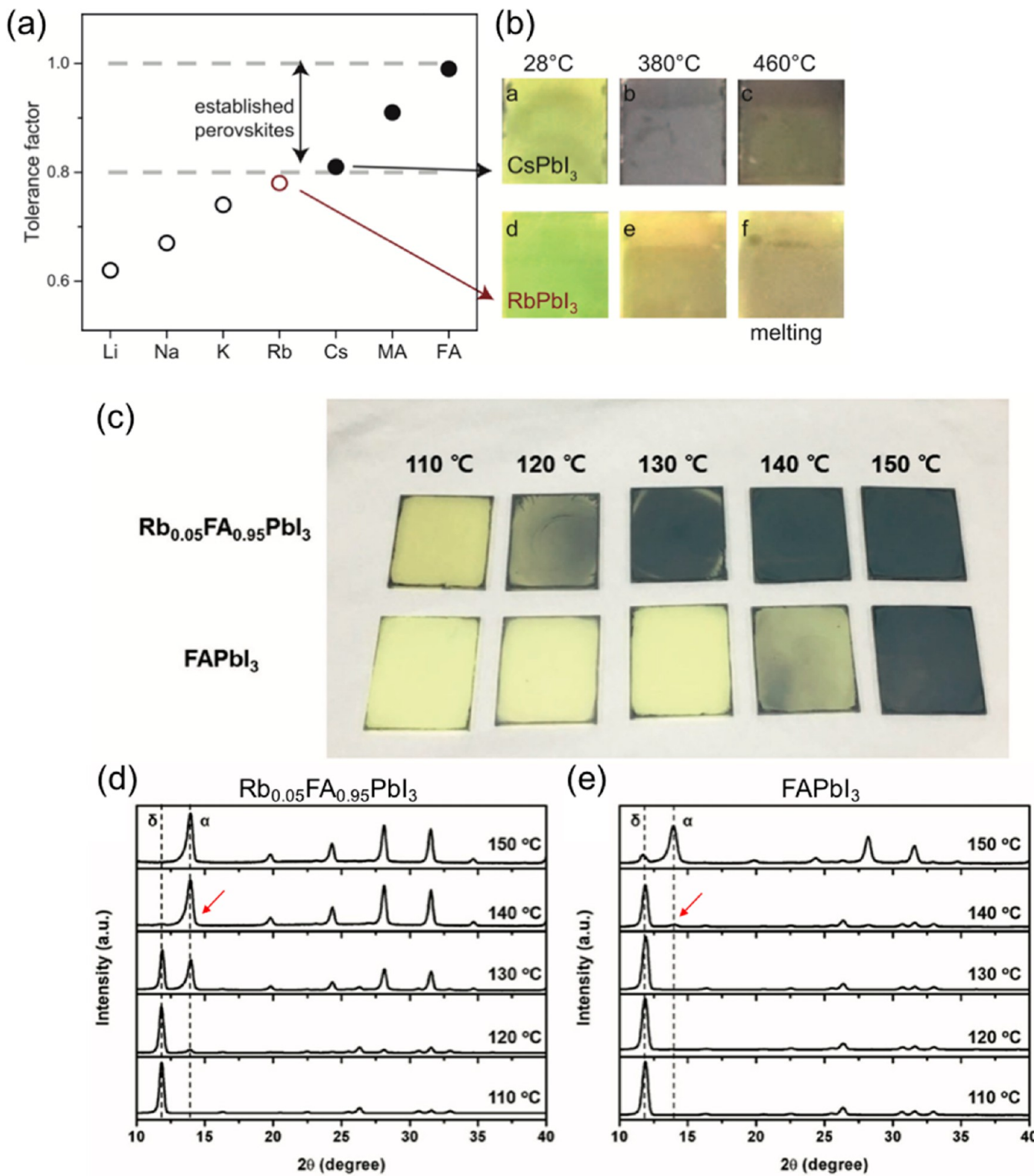


**Figure 8.** (a) Goldschmidt tolerance factor of  $\text{APbI}_3$  ( $\text{A} = \text{Li}, \text{Na}, \text{K}, \text{Rb}, \text{Cs}, \text{MA}, \text{FA}$ ) perovskites. Empirically, perovskites with a tolerance factor between 0.8 and 1.0 (dashed lines) show a photoactive black phase (solid circles) as opposed to nonphotoactive phases (open circles). Rb (red open circle) is very close to this limit. (b)  $\text{CsPbI}_3$  and  $\text{RbPbI}_3$  at 28, 380, and 460 °C. Irreversible melting occurs at 460 °C.  $\text{RbPbI}_3$  never shows a black phase. Reprinted with permission from ref 137. Copyright 2016 American Association for the Advancement of Science (AAAS). (c) Photographs and XRD patterns of (d)  $\text{Rb}_{0.05}\text{FA}_{0.95}\text{PbI}_3$  and (e)  $\text{FAPbI}_3$  films after heating at specified temperatures for 5 min. Diffraction peaks corresponding to  $\alpha$ - and  $\delta$ - $\text{FAPbI}_3$  are indicated. Reprinted with permission from ref 121. Copyright 2016 WILEY-VCH Verlag GmbH & Co. KGaA, Weinheim.

281 cation (ionic radius = 0.167–0.181 nm) has no dipole moment,  
282 therefore it would be interesting to study the fundamental  
283 aspects of stabilization of MA/Cs and FA/Cs combinatorial  
284 systems.

**2.3. Binary (FA/Cs) $\text{PbI}_3$  System.** The number of reports 285 on (FA/Cs) $\text{PbI}_3$  system is also scarce (Table 1).<sup>100,101,118–120</sup> 286 In all these studies, similar to the  $\text{Cs}_x\text{MA}_{1-x}\text{PbI}_3$  case, it is 287 noticed that  $\text{Cs}_x\text{FA}_{1-x}\text{PbI}_3$  with Cs quantities in the range of  $x$  288

289 = 0.1 to 0.2 shows some enhancement in PCEs when compared  
 290 to pure FAPbI<sub>3</sub> (Table 1, Figure 5a). These enhancements in  
 291 PCEs can go as high as ~5%,<sup>100</sup> ~13%,<sup>101</sup> ~16%.<sup>118</sup> Hysteresis  
 292 phenomena (Figure 5b) are present in all these studies  
 293 employing devices with a standard structure of (i) FTO/c-  
 294 TiO<sub>2</sub>/Cs<sub>x</sub>FA<sub>1-x</sub>PbI<sub>3</sub>/spiro-MeOTAD/Au (or Ag)<sup>100,101,119</sup> and  
 295 (ii) FTO/c-SnO<sub>2</sub>/C60-SAM/Cs<sub>0.2</sub>FA<sub>0.8</sub>PbI<sub>3</sub>/spiro-MeOTAD/  
 296 Au.<sup>118</sup> Encapsulated Cs<sub>x</sub>MA<sub>1-x</sub>PbI<sub>3</sub> devices were reported to  
 297 show some promises regarding long-term stability tests under  
 298 continuous white light illumination (250 h)<sup>100</sup> or unencapsu-  
 299 lated devices under storage at low relative humidity (~15%) for  
 300 350 h.<sup>101</sup> Lee et al.<sup>100</sup> proposed that partial substitution of FA<sup>+</sup>  
 301 by Cs<sup>+</sup> leads to the contraction of the cuboctahedral volume  
 302 (Figure 5c,d), and consequently enhances the interactions  
 303 between FA<sup>+</sup> and iodine. Calculated lattice parameters of  
 304 Cs<sub>x</sub>MA<sub>1-x</sub>PbI<sub>3</sub> vary from ~6.363 Å ( $x = 0$ ) down to ~6.310 Å  
 305 ( $x = 0.25$ ).<sup>101</sup> Full width at half-maximum (fwhm) was reported  
 306 to broaden with increasing Cs content (Figure 5d), which was  
 307 correlated with a decrease in grain size (Figure 5e).<sup>100,118</sup> An  
 308 exception is observed in the work by Li et al.<sup>101</sup> who observed  
 309 enhancement in grain size as a function of Cs addition.  
 310 Nevertheless, proposed additional strategies such as the use of  
 311 Pb(SCN)<sub>2</sub> additive<sup>118</sup> and microstructure-mediated  $\delta \rightarrow \alpha$  phase  
 312 transformation methods<sup>119</sup> in perovskite film formation help  
 313 further enlarge grain sizes. The lattice contraction of  
 314 Cs<sub>x</sub>MA<sub>1-x</sub>PbI<sub>3</sub> with increasing Cs concentration (Figure 5d)  
 315 leads to increase in  $E_g$  (Figure 5f) from ~1.50 eV ( $x = 0$ ) up to  
 316 ~1.59 eV ( $x = 0.3$ ) resulting in lower  $J_{sc}$  (and consequently  
 317 diminishing PCEs).<sup>100,101,118,119</sup>

318 Similar to the  $\alpha,\delta$ -FAPbI<sub>3</sub> perovskite (Figure 3b), CsPbI<sub>3</sub> also  
 319 shows the polymorphism; however, the  $\alpha \rightarrow \delta$  phase transition  
 320 temperature is much higher (>300 °C) than in the FAPbI<sub>3</sub> case  
 321 (Figure 6a). Although the black  $\alpha$ -CsPbI<sub>3</sub> has  $E_g$  of ~1.67 to  
 322 ~1.73 eV (Figure 6f),<sup>82,155</sup> solar cells based on CsPbI<sub>3</sub> have  
 323 exhibited low PCEs (<2.9%),<sup>115,155,156</sup> which was attributed to  
 324 the structural instability, i.e., favorable  $\alpha \rightarrow \delta$  phase trans-  
 325 formation at room temperature (Figure 6b,d,e).<sup>155,157</sup> Typical  
 326  $E_g$  for the yellow  $\delta$ -CsPbI<sub>3</sub> is ~2.82 eV (Figure 6f).<sup>155</sup> Despite  
 327 these complex behaviors of FAPbI<sub>3</sub>, CsPbI<sub>3</sub> and predominance  
 328 of  $\delta$ -phases at room temperature, it is interesting to note that  
 329 mixing small quantities of Cs with FA substantially enhances  
 330 the stability of Cs<sub>x</sub>FA<sub>1-x</sub>PbI<sub>3</sub>.<sup>100,101,118,119</sup> For example, the  $\delta \rightarrow$   
 331  $\alpha$  phase transformation in FAPbI<sub>3</sub> that occurs at ~125–165 °C  
 332 (Figure 6a)<sup>65,82,101,111,121</sup> can be lowered down to room  
 333 temperature when Cs/FA ratio of 45 at. % is incorporated in  
 334 the Cs<sub>x</sub>FA<sub>1-x</sub>PbI<sub>3</sub>.<sup>101</sup> This decrease of phase transition  
 335 temperature suggests that the stability of black phase  $\alpha$ -  
 336 FAPbI<sub>3</sub> can be stabilized even at room temperature, which is  
 337 important for solar cell applications.<sup>101</sup> An explanation for the  
 338 enhanced stability of Cs<sub>x</sub>MA<sub>1-x</sub>PbI<sub>3</sub> perovskites was proposed  
 339 by Li et al.<sup>101</sup> based on the empirical Goldschmidt tolerance  
 340 factor ( $t$ ).<sup>158–160</sup> For a composition of A<sub>x</sub>B<sub>1-x</sub>PbI<sub>3</sub>, the effective  
 341 tolerance factor ( $t_{\text{effective}}$ ) is given by (eq 1). The atomic-ratio  
 342 weighted average of two different cations is used as the  
 343 estimated effective cation size ( $r_{\text{effective}}$ ) as shown in (eq 2).

$$t_{\text{effective}} = \frac{r_{\text{effective}} + r_I^-}{\sqrt{2} (r_{\text{Pb}^{2+}} + r_I^-)} \quad (1)$$

$$r_{\text{effective}} = xr_{\text{A}^+} + (1 - x)r_{\text{B}^+} \quad (2)$$

344 (Cs/FA)PbI<sub>3</sub> perovskite materials tend to form  $\delta$ -phase  
 345 orthorhombic perovskite structure (e.g.,  $\delta_{\text{O}}$ -CsPbI<sub>3</sub>) for  $t < 0.8$ ,  
 346 a cubic structure for  $0.8 < t < 1$  (e.g., Cs<sub>x</sub>FA<sub>1-x</sub>PbI<sub>3</sub>), and a

hexagonal nonperovskite structure for  $t > 1$  (e.g.,  $\delta_{\text{H}}$ -FAPbI<sub>3</sub>)<sup>349</sup>  
 350 (Figure 7a).<sup>101</sup> Alloying FAPbI<sub>3</sub> with a high  $t$  value and CsPbI<sub>3</sub><sup>350</sup> f7  
 351 with a low  $t$  value,  $t_{\text{effective}}$  can be tuned to be between 0.8 and 351  
 352 1.0 in Cs<sub>x</sub>MA<sub>1-x</sub>PbI<sub>3</sub> perovskites, which favors a stable 352  
 353 perovskite structure. This concept was extended to other 353  
 354 alloy systems to verify its validity (Figure 7b).<sup>101</sup> For the 354  
 355 different alloy compositions reported (see Figure 7b), [a] 355  
 356 MA<sub>0.6</sub>FA<sub>0.4</sub>PbI<sub>3</sub>,<sup>102</sup> [b] (FAPbI<sub>3</sub>)<sub>1-x</sub>(MAPbBr<sub>3</sub>)<sub>x</sub> ( $x = 0.15$ ),<sup>63</sup>  
 357 [c] MA<sub>0.13</sub>FA<sub>0.87</sub>PbI<sub>3</sub>,<sup>106</sup> [d] Cs<sub>0.15</sub>FA<sub>0.85</sub>PbI<sub>3</sub>,<sup>101</sup> [e] 357  
 358 MA<sub>0.9</sub>Cs<sub>0.1</sub>PbI<sub>3</sub>,<sup>115</sup> the best performing devices are for perov- 358  
 359 skites with  $t_{\text{effective}}$  around 0.94–0.98 (red circle).<sup>101</sup> On the 359  
 360 other hand, poor-photoactive mixed perovskites assemble at the 360  
 361 low tolerance factor region with  $t < 0.85$  (green area).<sup>101</sup> In 361  
 362 summary, Li et al.<sup>101</sup> proposed that  $t_{\text{effective}}$  (eqs 1 and 2) can be 362  
 363 a simpler figure of merit to roughly predict stable structures of 363  
 364 mixed perovskite alloys. Furthermore, they extracted that  $t_{\text{effective}}$  364  
 365 of approximately 0.95 but not exceeding 1 is good for 365  
 366 maintaining a cubic perovskite structure. However, an  $t_{\text{effective}}$  366  
 367 lower than 0.85 would cause too much distortion in the lattice 367  
 368 leading easily to nonperovskite structures.<sup>101</sup> Returning to the 368  
 369 (MA/FA)PbI<sub>3</sub> system, Dai et al.<sup>152</sup> found that all mixed 369  
 370 FA<sub>x</sub>MA<sub>1-x</sub>PbI<sub>3</sub> nanorods presented longer photoluminescence 370  
 371 (PL) lifetimes than the pure FAPbI<sub>3</sub> and MAPbI<sub>3</sub> nanorods, 371  
 372 (blue squares, Figure 7c). The longer PL lifetimes at the 372  
 373 composition around FA<sub>0.4</sub>MA<sub>0.6</sub>PbI<sub>3</sub> (Figure 7c) was correlated 373  
 374 with a lower density of defects and consequently resulting in 374  
 375 high performance.<sup>102,104,105,107–113</sup> Based on PL measurements,<sup>375</sup>  
 376 Dai et al.<sup>152</sup> identified that the FA/MA molar ratio region in the 376  
 377 range of 37.5–91% would lead to high performing solar cells 377  
 378 (gray area, Figure 7c).<sup>378</sup>

379 **2.4. Binary (FA/Rb)PbI<sub>3</sub> System.** Recently, Rb<sup>+</sup> cation,<sup>379</sup>  
 380 which has an even smaller ionic radius of 0.152 nm than Cs<sup>+</sup><sup>380</sup>  
 381 (Figure 6), has also received attention due to the viability of 381  
 382 enhancing further both the efficiency and stability of Rb-mixed 382  
 383 perovskite solar cells.<sup>121,122,137</sup> Due to the intrinsic non- 383  
 384 perovskite structure of  $\delta$ -RbPbI<sub>3</sub> (Figure 6c and 8a,b), it has 384 f8  
 385 been rarely investigated as a light harvesting material for 385  
 386 perovskite solar cell.<sup>121,122,137,157</sup> In fact, RbPbI<sub>3</sub> is known to 386  
 387 have only the  $\delta$ -phase ( $E_g \sim 2.7$ –3.1 eV)<sup>121,161–163</sup> and the  $\alpha$ - 387  
 388 phase has not been reported.<sup>121,122,137,157,164</sup> As shown by 388  
 389 heating experiments of RbPbI<sub>3</sub> films at different temperatures 389  
 390 (Figure 8b), RbPbI<sub>3</sub> at 28 °C is yellow; upon heating to 380 °C 390  
 391 still the yellow color persists in RbPbI<sub>3</sub> while CsPbI<sub>3</sub> (as 391  
 392 comparison) has transformed to its black  $\alpha$ -CsPbI<sub>3</sub>. Further 392  
 393 heating up to 460 °C causes eventually both RbPbI<sub>3</sub> and 393  
 394 CsPbI<sub>3</sub> to melt, and RbPbI<sub>3</sub> does not show a black phase 394  
 395 (Figure 8b).<sup>121,137</sup>

396 The (FA/Rb)PbI<sub>3</sub> system was studied systematically and 396  
 397 independently by Park et al.<sup>121</sup> and Zhang et al.<sup>122</sup> Both studies 397  
 398 report that only a small Rb quantity ( $x \leq 0.05$ ) can be 398  
 399 incorporated into the Rb<sub>x</sub>FA<sub>1-x</sub>PbI<sub>3</sub> perovskite lattice, other- 399  
 400 wise phase segregation will occur. As shown in Figure 8c, the 400  
 401 formation of the black  $\alpha$ -phase Rb<sub>0.05</sub>FA<sub>0.95</sub>PbI<sub>3</sub> started at 120 401  
 402 °C, whereas for FAPbI<sub>3</sub> started at a higher temperature of 140 402  
 403 °C and completely darkened at 150 °C. XRD patterns of 403  
 404 Rb<sub>0.05</sub>FA<sub>0.95</sub>PbI<sub>3</sub> (Figure 8d) and FAPbI<sub>3</sub> (Figure 8e) confirms a 404  
 405 slightly lower transition temperature for the Rb<sub>0.05</sub>FA<sub>0.95</sub>PbI<sub>3</sub> 405  
 406 compared to FAPbI<sub>3</sub>.<sup>121,122</sup> Further differential scanning 406  
 407 calorimetry (DSC) results also confirmed a temperature 407  
 408 difference of ~10 °C when probing the  $\delta \rightarrow \alpha$  phase transitions 408  
 409 of Rb<sub>0.05</sub>FA<sub>0.95</sub>PbI<sub>3</sub> and FAPbI<sub>3</sub>.<sup>121</sup> Park et al.<sup>121</sup> described that 409  
 410 the area under the transition peak in DSC curve is indicative of 410  
 411 enthalpy of transition ( $\Delta H$ ). The area of the peak 411

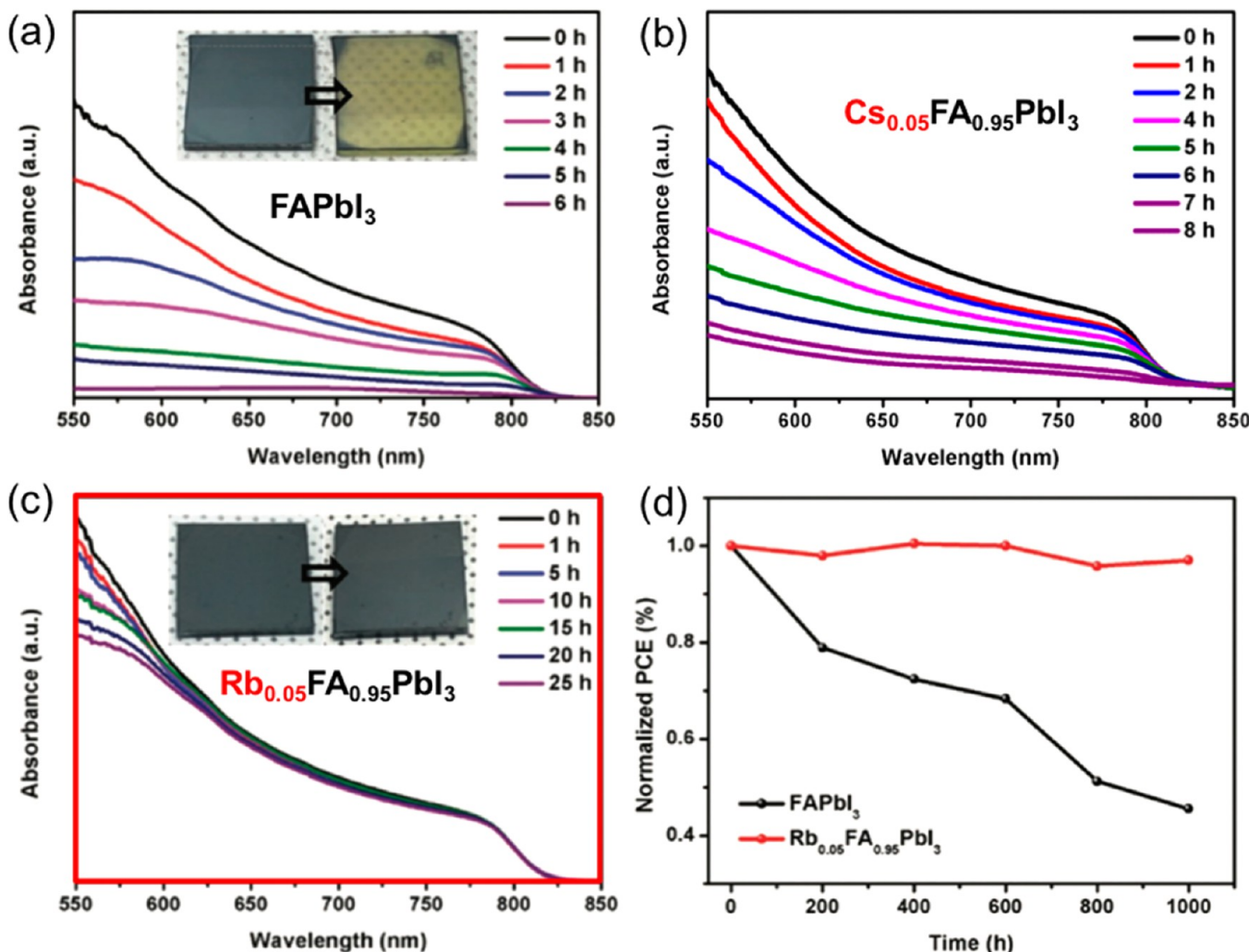


**Figure 9.** Stability tests (85% RH, 25 °C, and dark) of (a) FAPbI<sub>3</sub>, (b) Cs<sub>0.05</sub>FA<sub>0.95</sub>PbI<sub>3</sub>, and (c) Rb<sub>0.05</sub>FA<sub>0.95</sub>PbI<sub>3</sub> perovskite films monitored by the changes in absorbance as a function of time. The enhanced stability of Rb<sub>0.05</sub>FA<sub>0.95</sub>PbI<sub>3</sub> films is highlighted from this comparison experiments. (d) Comparison of the stability of FAPbI<sub>3</sub> and Rb<sub>0.05</sub>FA<sub>0.95</sub>PbI<sub>3</sub>-based unencapsulated devices kept under ambient conditions (average 55% RH) and in the dark. Reprinted with permission from ref 121. Copyright 2017 WILEY-VCH Verlag GmbH & Co. KGaA, Weinheim.

corresponding to the perovskite  $\delta \rightarrow \alpha$  phase transition was observed to be smaller for Rb<sub>0.05</sub>FA<sub>0.95</sub>PbI<sub>3</sub> than FAPbI<sub>3</sub>, indicating that perovskite transition to  $\alpha$ -phase is more favorable when Rb is present in FAPbI<sub>3</sub>. It was also reported that the  $\delta \rightarrow \alpha$  phase transformation kinetics of Rb<sub>0.05</sub>FA<sub>0.95</sub>PbI<sub>3</sub> is faster ( $\sim 60$  s) than FAPbI<sub>3</sub> ( $\sim 4$  min).<sup>121</sup> Park et al.<sup>121</sup> and Zhang et al.<sup>122</sup> showed that perovskite devices based on Rb<sub>0.05</sub>FA<sub>0.95</sub>PbI<sub>3</sub> when compared to FAPbI<sub>3</sub> devices, outperformed in PCE from 11.1%  $\rightarrow$  16.15% (on average) and 14.9%  $\rightarrow$  16.2%, respectively. More importantly, the superior enhanced stability against moisture of Rb-mixed perovskites (Figure 9) was highlighted in these two works.<sup>121,122</sup> Figure 9a,b,c shows the absorbance change with time for FAPbI<sub>3</sub>, Cs<sub>0.05</sub>FAPbI<sub>3</sub>, and Rb<sub>0.05</sub>FA<sub>0.95</sub>PbI<sub>3</sub> films kept in a sealed box at 85% RH and 25 °C.<sup>121</sup> In the case of FAPbI<sub>3</sub>, the film degraded after 6 h indicated by the formation of  $\delta$ -phase and/or PbI<sub>2</sub> (Figure 9a). Slightly better stability can be inferred when Cs is incorporated forming Cs<sub>0.05</sub>FAPbI<sub>3</sub> (Figure 9b). However, no obvious changes in the absorbance onset ( $\sim 800$  nm) can be observed for Rb<sub>0.05</sub>FA<sub>0.95</sub>PbI<sub>3</sub> films even after 25 h air exposure (Figure 9c). Cs<sup>+</sup> and Rb<sup>+</sup> cations have chemically and electrostatically similar properties if not equal

because they belong to the same alkali metal group. The stability properties in Cs<sub>0.05</sub>FAPbI<sub>3</sub>, and Rb<sub>0.05</sub>FA<sub>0.95</sub>PbI<sub>3</sub> perovskites are mainly dictated by the small differences in the ionic radius for hexacoordinated Cs<sup>+</sup> (0.167 nm) and Rb<sup>+</sup> (0.152 nm). This ionic radius difference is not significant, and it is remarkable the enhanced stability of Rb<sub>0.05</sub>FA<sub>0.95</sub>PbI<sub>3</sub> compared to that of Cs<sub>0.05</sub>FA<sub>0.95</sub>PbI<sub>3</sub> (Figure 9b,c). Park et al.<sup>121</sup> and Zhang et al.<sup>122</sup> also compared the long-term stabilities ( $\sim 1$  month) of complete devices (FTO/c-TiO<sub>2</sub>/mp-TiO<sub>2</sub>/Rb<sub>0.05</sub>FA<sub>0.95</sub>PbI<sub>3</sub>/Spiro-MeOTAD/Au) evaluating under ambient air storage conditions without any encapsulation. Rb<sub>0.05</sub>FA<sub>0.95</sub>PbI<sub>3</sub>-based solar cells maintained a PCE  $> 97\%$ <sup>121</sup> and  $> 90\%$ <sup>122</sup> of their initial efficiencies corresponding to the fresh devices.<sup>447</sup>

Yi et al.<sup>117</sup> proposed that the stability of Cs<sub>x</sub>FA<sub>1-x</sub>PbI<sub>3</sub> perovskites could be rationalized based on the structural and thermodynamics arguments of internal energy variation ( $\Delta E$ ) and entropic gains ( $\Delta S$ , mixing entropy concept) (Figure 10a). They calculated the free energies,  $\Delta F = \Delta E - T \cdot \Delta S$  (black squares, Figure 10a), of Cs<sub>x</sub>FA<sub>1-x</sub>PbI<sub>3</sub> with  $\delta$ -,  $\beta$ -,  $\alpha$ -phases considering different Cs contents ( $0 \leq x \leq 1$ ). A range in Cs composition was identified to lead to  $\Delta F < 0$  (black squares,

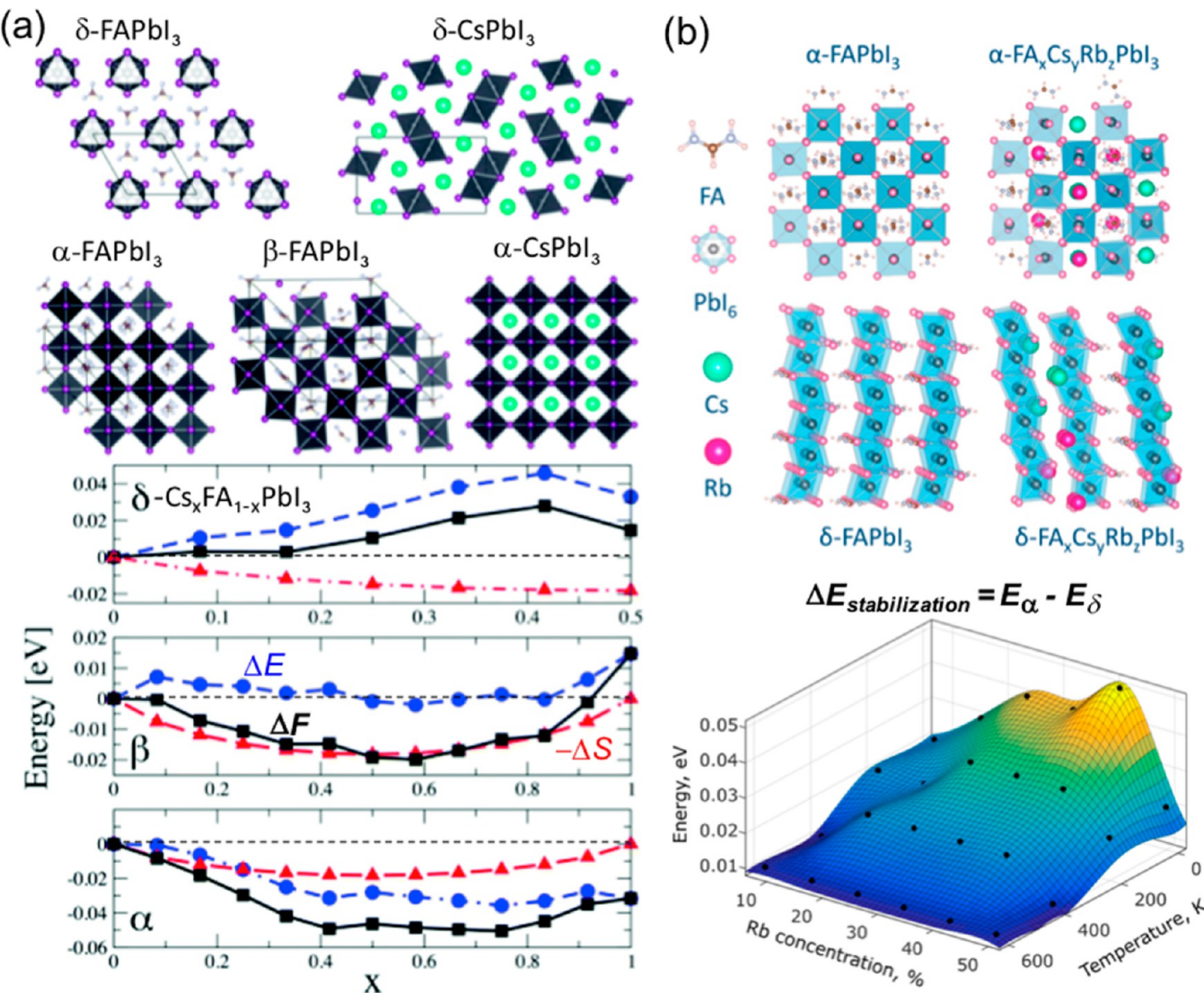


**Figure 10.** (a) Crystal structure of various polymorphs of  $\text{FAPbI}_3$  and  $\text{CsPbI}_3$ . The stability of  $\text{Cs}_x\text{FA}_{1-x}\text{PbI}_3$  was rationalized based on structural and thermodynamic arguments. Variation of internal energy  $\Delta E$  (blue circles), mixing entropy contribution  $-\Delta S$  (red triangles), and free energy  $\Delta F = \Delta E - T\Delta S$  (black squares).  $\Delta F < 0$  (below the dashed lines) signifies stability is observed. Reprinted with permission from ref 117. Copyright 2016 The Royal Society of Chemistry. (b) Structures of pure  $\text{FAPbI}_3$  and mixed  $\text{FA}_x\text{Cs}_y\text{Rb}_z\text{PbI}_3$  in  $\alpha$ - and  $\delta$ -phases. Reprinted with permission from ref 157. Copyright 2017 American Chemical Society.

Figure 10a), which signifies stable configuration. The stabilization energy was calculated to be in the order of 0.05 eV ( $\sim 2k_B T$  at room temperature) and 0.02 eV ( $\sim 0.8k_B T$ ) per stoichiometric unit for  $\alpha$ - and  $\beta$ -phases, respectively. Based on this model, the  $\delta \rightarrow \alpha$  or  $\beta$  transition temperature is reduced by  $\sim 200$ – $300$  K when going from pure  $\text{FAPbI}_3$  to the mixed  $\text{Cs}_x\text{FA}_{1-x}\text{PbI}_3$  perovskites. In a follow-up work, Syzgantseva et al.<sup>157</sup> have recently performed additional computational study comparing the influences of  $\text{MA}^+$ ,  $\text{Cs}^+$ ,  $\text{Rb}^+$  cation substitutions on the stabilization energies of  $\text{FAPbI}_3$  perovskite (Figure 10b) based on the same arguments described by Yi et al.<sup>117</sup> The relative stabilization energies ( $\Delta E_{\text{stabilization}} = E_\alpha - E_\delta$ , Figure 10b) of  $\alpha$ - ( $E_\alpha$ ) with respect to  $\delta$ -phase ( $E_\delta$ ) were determined using simulations of a series of  $\alpha$  and  $\delta$  structures, in which  $\text{FA}^+$  cations were successively substituted by  $\text{MA}^+$ ,  $\text{Cs}^+$ , and  $\text{Rb}^+$ .  $\text{Cs}^+$  and  $\text{Rb}^+$  were shown to be more efficient in stabilizing the perovskite than  $\text{MA}^+$  based on the balance of  $\Delta E$  and  $\Delta S$ .<sup>117,157</sup> The introduction of  $\text{Cs}^+$  and/or  $\text{Rb}^+$  thermodynamically favors

the formation of new perovskite phases, bringing the system into a new equilibrium state.<sup>157</sup>

To achieve a systematic understanding of the influences of mixing halides in the  $\text{ABX}_3$  structure, in the next section we will first describe simpler systems constraining the A cation to single elements ( $\text{MA}^+$ ,  $\text{FA}^+$ , or  $\text{Cs}^+$ ) and allowing to vary halide part ( $\text{I}/\text{Br}$ ,  $\text{I}/\text{Cl}$ , or  $\text{I}/\text{Br}/\text{Cl}$ ) in the X site.

### 3. MIXED X HALIDE ANIONS

A handful number of reviews described and summarized the new optoelectronic properties of mixed perovskites when mixed halide ions are incorporated in perovskites.<sup>5,7,8,14,15,24,26</sup> Below we present the current views of the structure–property relationship based on a survey of recently published papers summarized for  $\text{MAPb}(\text{I}/\text{Cl})$ ,  $\text{FAPb}(\text{I}/\text{Cl})$ ,  $\text{MAPb}(\text{I}/\text{Br})$ ,  $\text{FAPb}(\text{I}/\text{Br})$ ,  $\text{MAPb}(\text{Br}/\text{Cl})$ ,  $\text{CsPb}(\text{I}/\text{Br})$ ,  $\text{CsPb}(\text{Br}/\text{Cl})$ ,  $\text{CsPb}(\text{I}/\text{Cl})$ ,  $\text{MAPb}(\text{I}/\text{Br}/\text{Cl})$ .

**3.1. Binary  $\text{MAPb}(\text{I}/\text{Cl})$  and  $\text{FAPb}(\text{I}/\text{Cl})$  Systems.** The  $\text{MAPb}(\text{I}/\text{Cl})$  material system is by far one of the most studied

**Table 2. Summary of Experimental Conditions for MAPbI<sub>3-x</sub>Cl<sub>x</sub> Synthesis Methods and Experimental Technique and Measurement Conditions Extracted from References 60, 165–199, 209<sup>a</sup>**

ref. (Year)	Sample structure	MAPbI <sub>3-x</sub> Cl <sub>x</sub> fabrication environmental conditions	Experimental techniques	Measurement environmental conditions	Cl detected?	Main conclusions
165 (2017) ITO/PEDOT:PSS PVSK	MAPbI <sub>3-x</sub> Cl <sub>x</sub> fabrication method (1) 40 wt % dissolving MAI and PbCl <sub>2</sub> in 3:1 molar ratio in DMF.	N <sub>2</sub> glovebox	TOF-SIMS	Vacuum	Yes	(1) MAPbCl <sub>3</sub> forms as intermediate phase during crystallization. (2) After completion of PVSK crystallization some Cl detected by TOF-SIMS. (3) Cl is majorly located at the interface and within the underlying PEDOT:PS.
166 (2016) FTO/c-TiO <sub>2</sub> /PVSK	Redissolution and crystal grain growth via spray coating: (1) MAI and PbCl <sub>2</sub> in 3:1 molar ratio dissolved in IPA. (2) Centrifuge. (3) MAPbI <sub>3-x</sub> Cl <sub>x</sub> redissolved in DMF:GBL.	Ambient	XPS	Vacuum	Yes	Atomic ratio of Cl:I ~ 3:97 determined by XPS.
167 (2016) Glass slide	Single-crystalline nanofibers; Stock solutions of (MACl+PbCl <sub>2</sub> /DMF, 0.03 M) and (MAI+PbI <sub>2</sub> /DMF, 0.03 M) at different volume ratios.	—	EDX, XRD, UV-vis, PL	—	Yes	(1) EDX analysis showed compositions of MAPb-Cl <sub>0.27</sub> I <sub>2.73</sub> , MAPbCl <sub>0.55</sub> I <sub>2.45</sub> , MAPbCl <sub>0.7</sub> I <sub>0.25</sub> . (2) 3D crystal structure for MAPbI <sub>3-x</sub> Cl <sub>x</sub> proposed. (1) EDX showed Cl:I ~ 0.61.
168 (2016) FTO/c-TiO <sub>2</sub> /mp-TiO <sub>2</sub> /PVSK	Vapor-assisted solution deposition: 1 M PbI <sub>2</sub> in DMF spin coated and substrate heated at 110 °C (15 min); PbI <sub>2</sub> film placed 2 mm above MACl source in an oven; Postannealing at 70 °C (30 min).	—	EDX, XRD	—	Yes	(2) XRD showed MAPbCl <sub>3</sub> phase. (3) Assuming 4% Cl incorporation in MAPbI <sub>3-x</sub> Cl <sub>x</sub> lattice, the ratio of MAPbI <sub>3-x</sub> Cl <sub>x</sub> and MAPbI <sub>3</sub> phases will be ~65:35. This is close to expected reaction: 3MACl + 3PbI <sub>2</sub> → 2MAPbI <sub>3</sub> + MAPbCl <sub>3</sub> .
169 (2015) FTO/c-TiO <sub>2</sub> /PVSK (and) SiN/PVSK	(1) MAI and PbCl <sub>2</sub> in 3:1 molar ratio dissolved in DMF. (2) Postannealing at 95 °C for 0, 15, 60, 90, 120 min in dry air (3 ppm of H <sub>2</sub> O).	—	XANES	He atmosphere	Yes	(1) x = 0.05 ± 0.03 Cl atoms per formula unit (i.e., Pb atom). (2) Cl may be incorporated in the film directly (e.g., substitution or interstitial) or indirectly (e.g., grain boundary or poor crystalline region). (1) Mild annealing (60 °C, 1 h) leads to a MAPbI <sub>3-x</sub> Cl <sub>x</sub> film with Cl-rich (x < 0.3) and Cl-poor phases. (2) Further annealing (110 °C) leads to a homogeneous Cl-poorer (x < 0.06) phase.
170 (2015) ZnS optical prism/ PEDOT:PSS/PVSK	Multicycle spin-coating process: PbI <sub>2</sub> in DMF spin-coated on substrate; MAI/MACl (4:1 molar ratio) in IPA spin-coated on PbI <sub>2</sub> film; Postannealing at different temperatures.	—	PTIR	Under N <sub>2</sub> flow	Yes	(1) As-grown MAPbI <sub>3-x</sub> Cl <sub>x</sub> showed 0.13 at. % Cl. (1) MAPbI <sub>2.9</sub> Cl <sub>0.06</sub> composition determined.
171 (2015) Quartz	Vacuum coevaporation of MAI and PbCl <sub>2</sub> ; Postannealing at 70, 80, 90, 100, 110, 120 °C (1 h) in N <sub>2</sub> glovebox; ~530 nm thickness.	Vacuum	XRD, EDX, UV-vis, PL	—	Yes	(1) Measured n <sub>Cl</sub> /(n <sub>Cl</sub> + n <sub>I</sub> ) mole fraction content in PVSK according to (PbCl <sub>2</sub> /PbI <sub>2</sub> ): 0.012 ± 0.008 (0.10); 0.073 ± 0.012 (0.20); 0.185 ± 0.015 (0.30); 0.220 ± 0.015 (0.40). (2) Band gap varies from 1.54 to 1.59 eV with increasing Cl. (3) XRD shows shifts in (110) and (220) peaks.
172 (2015) c-TiO <sub>2</sub> /PVSK	(1) MAI and PbCl <sub>2</sub> in 3:1 molar ratio dissolved in DMF.	—	Ion chromatography	Films dissolved in DI water and H <sub>2</sub> SO <sub>4</sub> (0.15 M)	Yes	
173 (2015) ITO/PEDOT:PSS PVSK	(2) Postannealing at 120 °C for 45 min. Two-step method: (1) 1.5 M PbCl <sub>2</sub> /PbI <sub>2</sub> dissolved in DMF and spin coated.	Ambient air with 20 °C and 20% RH.	Potentiometric titration method, XRD, UV-vis	Ultrapure water	Yes	

Table 2. continued

ref. (Year)	Sample structure	MAPbI <sub>3-x</sub> Cl <sub>x</sub> fabrication method	Experimental techniques	Measurement environmental conditions	Cl detected?	Main conclusions
174 (2015)	FTO/c-TiO <sub>2</sub> /PVSK	(1) MAI and PbCl <sub>2</sub> in 3:1 molar ratio dissolved in DMF. (2) Postannealing at 90 °C (2.5 h) and then 120 °C (15 min).	N <sub>2</sub> glovebox	HAXPES, FY-PES	Vacuum	Yes  (1) Cl is depleted from top surface.
175 (2015)	FTO/c-TiO <sub>2</sub> /PVSK	Two-step method: (1) PbI <sub>2</sub> in DMF spin coated. MAI/MACl (10:1 in weight) dissolved in IPA spin coated on top of dry PbI <sub>2</sub> film. (2) PbI <sub>2</sub> in DMF spin coated. MACl dissolved in IPA spin coated on top of dry PbI <sub>2</sub> film. Both films annealed in air at 135 °C.	Dry air (Dew Point of -70 °C)	XRD, XPS	—	Yes  (2) Upper limit on the amount of Cl in MAPbI <sub>3-x</sub> Cl <sub>x</sub> : $x < 0.07$ and $x < 0.40$ to depths of ~10 and ~26 nm, respectively. (3) High Cl concentration ( $x > 0.40$ ) deep in the film and near PVSK/TiO <sub>2</sub> interface. (1) Cl incorporation improve carrier transport across heterojunction interfaces, rather than within perovskite crystal. (2) XRD showed ~0.5% difference of the unit cell volume. (3) Very weak Cl 2p signal in XPS; Cl has negligible impact on the original crystal structure. (1) MAPbI <sub>3-x</sub> Cl <sub>x</sub> with maximum of $x = 0.15$ determined based on lattice volume. (3) XPS and EDX did not show Cl. (4) Small Cl amount incorporated in the crystal lattice; Most of Cl resides at grain boundary or interface with substrate.
176 (2014)	Glass/PVSK (for optical and structural determination) (and) Si/TiO <sub>2</sub> (for GIWAXS)	(1) MAI and PbCl <sub>2</sub> in 3:1 molar ratio dissolved in DMF. (2) Postannealing at 95 and 100 °C for various times.	PVSK preparation in glovebox. Post annealing in air and N <sub>2</sub> for comparison.	GIWAXS, in situ XRD, XPS, XRF, EDX, UV-vis	In situ XRD in ambient; XPS and EDX in vacuum; UV-vis in glovebox	Yes  (1) MAPbI <sub>3</sub> with maximum of $x = 0.15$ determined by XRF. (3) XPS and EDX did not show Cl. (4) Small Cl amount incorporated in the crystal lattice; Most of Cl resides at grain boundary or interface with substrate.
177 (2015)	FTO/c-TiO <sub>2</sub> /PVSK	Two-step method: (1) 1 M PbI <sub>2</sub> in DMF. (2) Substrate dipping into MACl + MAI dissolved in IPA.	—	KPFM	—	Yes  Larger band-bending at grain boundaries with Cl incorporation.
178 (2015)	ITO/PEDOT:PSS/ PVSK	Layer-by-layer growth; PbCl <sub>2</sub> thermally evaporated in vacuum; Dipping in MAI solution (IPA); Similarly a second PbCl <sub>2</sub> thermally evaporated on MAPbI <sub>3-x</sub> Cl <sub>x</sub> and dipped into MAI solution. These cycles are repeated until desired film thickness is attained.	—	XPS	Vacuum	Yes  (1) Cl atomic ratio was 8.39%. The ratio above is much higher than that of solution-cast counterpart (1.4%).
179 (2014)	FTO/c-TiO <sub>2</sub> /PVSK	(1) 1.5 wt % dissolving MAI and PbCl <sub>2</sub> in 3:1 molar ratio in DME. N <sub>2</sub> atmosphere (2) Postannealing at 100 °C for 1 h. (3) ~15 nm thickness.	—	AR-XPS	Vacuum	Yes  Chloride located at TiO <sub>2</sub> /PVSK
180 (2014)	Soda lime glass/PVSK	Vacuum coevaporation of MAI and PbCl <sub>2</sub> .	Vacuum	In situ XRD, EDX	Vacuum	Yes  (1) There exists a miscibility gap for MAPbI <sub>3</sub> and MAPbCl <sub>3</sub> in the $0.5 < x < 0.95$ regime for MAPb(I <sub>x</sub> Cl <sub>1-x</sub> ) <sub>3</sub> . (2) Cl incorporation stabilizes the cubic phase of MAPbI <sub>3</sub> at room temperature. (1) Cl content in the film is minuscule, but detected by XPS (~1 at. %) and TGA (~1.3 at. %). (2) EDX did not detect Cl.
181 (2015)	FTO/c-TiO <sub>2</sub> /PVSK	(1) 0.88 M PbCl <sub>2</sub> + 2.64 M MAI. (2) 0.88 M PbI <sub>2</sub> + 0.88 M MAI + 0.88 M MACl. (3) Films were dried at 70 °C (10 min) and annealed at 100 °C (45 min).	Glove box	TGA, XPS, EDX	TGA in N <sub>2</sub> flow (40 mL/min) and ~10 mg of PVSK, XPS and EDX in vacuum	Yes  (1) EDX shows tetragonal $I4/mcm$ structure.

Table 2. continued

ref. (Year)	Sample structure	MAPbI <sub>3-x</sub> Cl <sub>x</sub> fabrication method	Experimental techniques	Measurement environmental conditions	Cl detected?	Main conclusions
182 (2014)	FTO/PVSK	MAI and PbCl <sub>2</sub> in 3:1 molar ratio dissolved in DMF; Postannealing at 100 °C (50 min).	N <sub>2</sub> glovebox	XPS depth profile (Ar sputtering), EDX	Yes	(1) Very weak Cl signal in XPS of ~1% Cl detected for the top 20 nm. (2) EDX probed Cl content of 0.7 at. %. There is a note that detection limit of EDX setup is ~1 at. %.
183 (2014)	ITO/PEDOT:PSS/ PVSK	MAI and PbCl <sub>2</sub> in 3:1 molar ratio dissolved in DMF; Postannealing at 90 °C (2 h).	—	XPS	Yes	(1) Cl/(Cl + I) ~ 2.2% detected by XPS. (2) XRD shows similar diffraction pattern to MAPbI <sub>3</sub> ; therefore, only small fraction of Cl can be incorporated.
184 (2014)	ITO/TiO <sub>2</sub> /PVSK	22.5–60 wt % MAI and PbCl <sub>2</sub> in 3:1 molar ratio dissolved in DMSO; Postannealing at 100 °C (50 min).	N <sub>2</sub> glovebox (<1 ppm of O <sub>2</sub> and H <sub>2</sub> O)	XPS	Yes	XPS on the 60 wt % precursor concentration, showed atomic composition of C:N:Pb:I:Cl = 1.04:1.1:0.5:2.02:0.99.
185 (2013)	Glass slide (and) FTO/c-TiO <sub>2</sub> /mp- TiO <sub>2</sub> /PVSK	(1) 20 wt % MAI and PbCl <sub>2</sub> (3:1 molar ratio) dissolved in DMF; Postannealing at 100 °C (45 min).  (2) 20 wt % MACl and PbI <sub>2</sub> (1:1 molar ratio) dissolved in DMF; Postannealing at 100 °C (10 min).	Spin coating in N <sub>2</sub> flux	EDX	Yes	(1) Reliable values of the Cl content not achieved as the amplitude of Cl-related signal was observed to decrease during the measurement. (2) Based on DFT, Cl incorporation is allowed at low concentrations (below 3–4%) in MAPbI <sub>3</sub> . MAPbI <sub>2</sub> Cl had I/Cl ratio ~2:1.
60 (2012)	FTO/c-TiO <sub>2</sub> /mp- TiO <sub>2</sub> (or Al <sub>2</sub> O <sub>3</sub> )/ PVSK	MAI and PbCl <sub>2</sub> in 3:1 molar ratio dissolved in DMF; Postannealing at 100 °C for 45 min.	Ambient air	EDX	Yes	(1) Cl can be incorporated into precursor film in the form of PbICl or PbCl <sub>2</sub> and it was found in the final PVSK film in MAPb <sub>3-x</sub> Cl <sub>x</sub> , PbI <sub>2</sub> Cl, or PbCl <sub>3</sub> . (2) No evidence for MAPbI <sub>3-x</sub> Cl <sub>x</sub> phase observed. (3) MAPbI <sub>3-x</sub> Cl <sub>x</sub> phase is relatively unstable or possess higher formation energy.
186 (2017)	FTO/c-TiO <sub>2</sub> / PC61BM/PVSK	1 M PbCl <sub>2</sub> :PbI <sub>2</sub> (molar ratios of 0:1, 1:3, 11: 3:1)	N <sub>2</sub> glovebox (RH < 10%)	—	No	(1) Cl can be incorporated into precursor film in the form of PbICl or PbCl <sub>2</sub> and it was found in the final PVSK film in MAPb <sub>3-x</sub> Cl <sub>x</sub> , PbI <sub>2</sub> Cl, or PbCl <sub>3</sub> . (2) No evidence for MAPbI <sub>3-x</sub> Cl <sub>x</sub> phase observed. (3) MAPbI <sub>3-x</sub> Cl <sub>x</sub> phase is relatively unstable or possess higher formation energy.
R						
187 (2017)	FTO/c-TiO <sub>2</sub> /PVSK	MAI and PbCl <sub>2</sub> in 3:1 molar ratio dissolved in DMF; Postannealing at 100 °C (110 min).	Glove box	XRD, UV-vis, XPS	—	XPS shows negligible amount of Cl in fully annealed films.
188 (2016)	Glass	PbI <sub>2</sub> and PbCl <sub>2</sub> dissolved in DMSO spin coated on glass and loaded in XRD stage.	He atmosphere	In situ XRD, TOF-SIMS	In situ XRD in He TOF-SIMS	(1) In the presence of reactive I <sup>-</sup> ions, neither Br <sup>-</sup> nor Cl <sup>-</sup> can be incorporated into the perovskite crystal lattice. (2) TOF-SIMS mapping revealed that Cl <sup>-</sup> resides in the grain boundaries, possibly in the form of amorphous Cl <sup>-</sup> -based compounds.
		MAI powder dispersed around the film and sample stage controllably heated.				(1) Initially, the film crystallizes in MAPbCl <sub>3</sub> and is fully converted to MAPbI <sub>3</sub> after a certain time under heating. (2) Below detection limits of XPS.
189 (2016)	FTO/c-TiO <sub>2</sub> /PVSK	MAI and PbCl <sub>2</sub> in 3:1 molar ratio dissolved in DMF; Postannealing at 90 °C (2 h), 100 °C (10 min), 130 °C (5 min).	—	in situ XRD	N <sub>2</sub> atmosphere	No
209 (2016)	MAPb(Cl) single crystal	Supporting info in ref209.	—	XRD, XPS, TOF-SIMS	—	No
190 (2015)	ITO	(1) Sequential vacuum evaporation of MAI (15 nm) and then PbCl <sub>2</sub> . (2) coevaporation.	Vacuum	In situ XPS	Vacuum	No
191 (2015)	FTO/c-TiO <sub>2</sub> /PVSK	(1) PbI <sub>2</sub> dissolved in DMF and spin coated. (2) CVD: First reacted with MACl (120 °C, 5 min) and then with MAI at 145 °C, 100 min.	—	XRD, XPS, EDX	XPS and EDX in vacuum.	No

Table 2. continued

ref. (Year)	Sample structure	MAPbI <sub>3-x</sub> Cl <sub>x</sub> fabrication method	Experimental techniques	Measurement environmental conditions	Cl detected?	Main conclusions
192 (2015)	ITO/PEDOT:PSS/ PVSK	MAI and PbCl <sub>2</sub> in 3:1 molar ratio dissolved in DMF; Postannealing at 60 °C (2 h).	Postannealing in vacuum and glo- vebox	XPS	Vacuum	No
193 (2014)	FTO/c-TiO <sub>2</sub> /PVSK	(1) Two-step: PbI <sub>2</sub> ; MAI:MACI (95:5 wt %) in IPA. (2) Two-step: PbCl <sub>2</sub> ; MAI in IPA. (3) One-step: PbCl <sub>2</sub> :MAI = 1:3	—	STEM-EDS	Vacuum	No
194 (2014)	ITO/PEDOT:PSS/ PVSK	Several (Table S2 in ref 194) dissolved in DMF; Postannealing at 90 °C for 2–3 h.	N <sub>2</sub> glovebox	TEM, SAED, EDX, XPS	No (below detection limit)	(1) EDX showed I:Pb ~3 at. % ratio. (2) Cl was below detection limit of EDX (~0.1 at. %). (3) Presence of Cl impacts on the microstructure and orientation of PVSK films. (4) SAED patterns indexed to tetragonal MAPbI <sub>3</sub> . (1) No signs of Cl in XPS. (2) EDX showed no Cl (or is below detection limit, <1% mol).
195 (2014)	FTO/c-TiO <sub>2</sub> /PVSK	MAI and PbCl <sub>2</sub> in 3:1 molar ratio dissolved in DMF; Postannealing at 120 °C (30–60 min).	Ambient atmos- phere	EDX, XPS	Vacuum	No
196 (2014)	Glass/mp-TiO <sub>2</sub> / PVSK	MAI and PbCl <sub>2</sub> in 3:1 molar ratio dissolved in DMF and DMSO mixed in 7:3 by volume; Postannealing at 140 °C (30 min) in dry air box (RH < 10%); Samples dried in vacuum ( $5 \times 10^{-5}$ Torr, 1 h)	Dry air box (RH < 10%)	XRD	Room temperature in air; RH 30– 50%; 4 h measure- ment.	No
197 (2014)	FTO/c-TiO <sub>2</sub> /mp- TiO <sub>2</sub> /PVSK	PbI <sub>2</sub> , MAI dissolved in DMF with molar ratio of 1:1;x (x varies from 0 to 2; max dissolvable x is ~2.8); Postannealing at 100 °C (5–45 min).	Ambient air	EDX	Vacuum	No
198 (2014)	FTO/c-TiO <sub>2</sub> /PVSK	Two-step: PbI <sub>2</sub> in DMF; Spin coating (>200 nm film thickness); MAI and MACI dissolved in IPA. Substrate immersed.	—	EELS, EDX, XPS	Vacuum	No
199 (2014)	FTO/mp-TiO <sub>2</sub> /PVSK	MAI and PbCl <sub>2</sub> in 3:1 molar ratio dissolved in DMF; Postannealing at different temperatures (60–200 °C) and times (20 to 0.17 h)	Ambient air	XRD	Ambient	No

<sup>a</sup>Abbreviations: See Table 1. PVSK = “MAPbI<sub>3-x</sub>Cl<sub>x</sub>”; DMF = *NN'*-dimethylformamide; GBL =  $\gamma$ -butyrolactone; IPA = 2-propanol; XPS = X-ray photoelectron spectroscopy; AR-XPS = angle-resolved XPS; hard XPS (HAXPES); fluorescence yield X-ray absorption spectroscopy (FY-XAS); TOF-SIMS = time-of-flight secondary ion mass spectrometry; GI-XRD = glazing-incidence X-ray diffraction; XANES = X-ray absorption near edge structure; EDS/EDX = energy-dispersive X-ray spectroscopy; XRF = X-ray fluorescence spectroscopy; GWAXS = grazing-incidence wide-angle X-ray scattering, TEM = transmission electron microscopy, SAED = select area electron diffractogram, KPFM = Kelvin probe force microscopy, PTIR = photothermal-induced resonance; TGA = thermogravimetric analysis, PL = photoluminescence, STEM-EDS = scanning transmission electron microscopy EDS. EELS = electron energy loss spectroscopy.

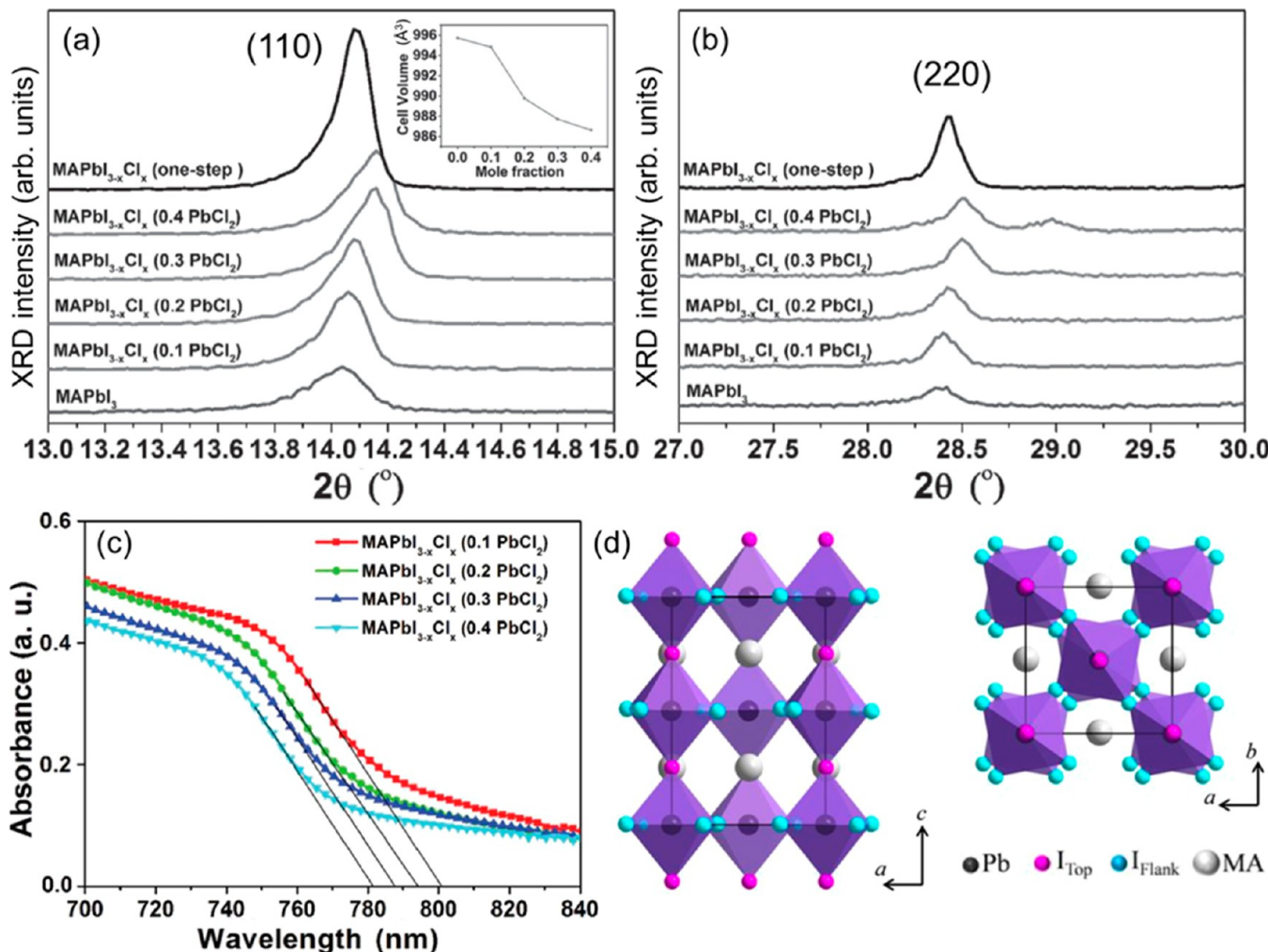


**Figure 11.** XRD pattern of (a) (110) and (b) (220) lattice planes of MAPbI<sub>3-x</sub>Cl<sub>x</sub> perovskites with different PbCl<sub>2</sub> mole fractions by a two-step method. MAPbI<sub>3-x</sub>Cl<sub>x</sub> perovskites formed by one-step method and pure-phase MAPbI<sub>3</sub> are shown as comparison. (c) UV-vis of MAPbI<sub>3-x</sub>Cl<sub>x</sub> perovskites with different PbCl<sub>2</sub> mole fractions by a two-step method. Reprinted with permission from ref 173. Copyright 2017 WILEY-VCH Verlag GmbH & Co. KGaA, Weinheim. (d) Proposed schematic representation of tetragonal crystal structure of MAPbI<sub>3-x</sub>Cl<sub>x</sub> where Cl atoms partly substituted I at I<sub>flank</sub> (blue) positions forming different contents of  $x$ . Reprinted with permission from ref 167. Copyright 2017 WILEY-VCH Verlag GmbH & Co. KGaA, Weinheim.

491 binary mixed perovskite.<sup>60,61,165–200</sup> From earlier re-  
 492 ports,<sup>2,3,21,47,201,202</sup> PbI<sub>2</sub> and MAI precursors are employed  
 493 for the synthesis of MAPbI<sub>3</sub>. Furthermore, if one-step method  
 494 is employed, generally equimolar ratio of PbI<sub>2</sub>:MAI (i.e., 1:1) is  
 495 used. Lee et al.<sup>60</sup> reported the first deposition approach  
 496 employing PbCl<sub>2</sub> and 3-fold excess of MAI (i.e., 1:3). The  
 497 dissolution of PbCl<sub>2</sub> in *N,N*-dimethylformamide (DMF) is  
 498 difficult when the MAI:PbCl<sub>2</sub> molar ratio is lower than  
 499 3:1.<sup>194,195</sup> Although Cl incorporation has been reported to  
 500 improve optoelectronic properties (e.g., diffusion lengths for  
 501 electron and holes of ~130 and ~90–105 nm in MAPbI<sub>3</sub>,  
 502 increases by 10 times in MAPbI<sub>3-x</sub>Cl<sub>x</sub>, ~1069 and ~1213 nm,  
 503 respectively),<sup>200,203</sup> the controversial question whether Cl can  
 504 in fact be incorporated into the crystal lattice of MAPbI<sub>3</sub> is still  
 505 not completely settled. Reviews on this topic can be found in  
 506 refs.<sup>8,14,15,169,204</sup> The reported studies show contradicting results  
 507 regarding detection or absence of Cl in MAPbI<sub>3-x</sub>Cl<sub>x</sub> perovskite  
 508 (Table 2). From a total of thirty seven studies surveyed by us  
 509 (Table 2), we find that twenty two confirmed the presence of  
 510 Cl in MAPbI<sub>3-x</sub>Cl<sub>x</sub> based on an extensive number of analytical  
 511 tools such as X-ray photoelectron spectroscopy

(XPS),<sup>166,175,178,181,183,184</sup> angle-resolved XPS (AR-XPS),<sup>179</sup> XPS depth-profile,<sup>182</sup> hard XPS (HAXPES),<sup>174</sup> fluorescence yield X-ray absorption spectroscopy (FY-XAS),<sup>174</sup> time-of-flight secondary ion mass spectrometry (TOF-SIMS), in situ XRD,<sup>180</sup> glazing-incidence XRD (GIXRD),<sup>165</sup> X-ray absorption near edge structure (XANES),<sup>169</sup> energy-dispersive X-ray spectroscopy (EDX or EDS),<sup>167,168,171,182,185</sup> X-ray fluorescence spectroscopy (XRF),<sup>176</sup> grazing-incidence wide-angle X-ray scattering (GIWAXS), select area electron diffractogram (SAED), photothermal-induced resonance (PTIR),<sup>170</sup> Kelvin probe force microscopy (KPFM),<sup>177</sup> thermogravimetric analysis (TGA),<sup>181</sup> ion chromatography,<sup>172</sup> potentiometric titration.<sup>173</sup> However, there are also at least 15 studies arriving at the conclusion that Cl is absent in the final perovskite films or is below the detection limit of the instruments (e.g., EDX detection limit is 0.1–1 at. %<sup>194,195,197</sup> or ~1000 ppm<sup>193</sup> and XPS detection limit is 0.1 at. %<sup>190</sup>). It has been argued that (1) as a result of the larger difference in ionic radii, Cl incorporation yields low miscibility with iodine;<sup>15,176,185</sup> (2) the MAPbI<sub>3-x</sub>Cl<sub>x</sub> phase is metastable or possess higher formation energies;<sup>186</sup> (3) PbCl<sub>2</sub> is the least

533 soluble Pb-halide in DMF that may lead to  $\text{PbCl}_2$  534 particles;<sup>194,195</sup> (4) experimental evidence that Cl were found 535 at the perovskite/substrate interface (i.e., the affinity of Cl to 536  $\text{TiO}_2$ <sup>169,176,179</sup> and PEDOT:PSS<sup>165</sup> is high) and/or grain 537 boundaries;<sup>169,170,176,177</sup> (5) the postannealing step ( $100^\circ\text{C}$ , 538 45 min) leads to sublimation of Cl in the form of 539  $\text{MACl}$ ;<sup>55,181,182,192,199</sup> (6)  $\text{MAPbI}_{3-x}\text{Cl}_x$  and  $\text{MAPbI}_3$  perov- 540 skites show very similar UV-vis and XRD patterns indicating 541 no or a very small amount of Cl can be incorpo- 542 rated;<sup>15,60,186,191,197–199</sup> (7) crystallization (crystallographic 543 texture, crystalline orientation) and morphological (polycrystal- 544 line grain structure) improvements instead of Cl-incorpo- 545 ration.<sup>167,182,194,195,205</sup>

In Table 2, we compare the relevant parameters such as sample conditions (sample preparation method and environment, sample structure, perovskite thicknesses) as well as technical aspects of measurement conditions (vacuum versus ambient pressure and/or under inert gas environment). We find that the different results from these studies may stem from (1) the various sample preparation conditions, for instance, vapor-based techniques (e.g., vacuum codeposition, vapor-assisted solution deposition at ambient, chemical vapor deposition) versus solution methods (one-step and two-step methods; use of  $\text{MACl}$  or  $\text{PbCl}_2$  as source for Cl) and (2) the influence of excitation probes and environment during measurements. Zhao and Zhu<sup>197</sup> showed that Cl can be incorporated in  $\text{MAPbI}_3$  employing  $\text{MACl}$  precursor by controlling the annealing time ( $\sim 20$  min). On the contrary, Chen et al.<sup>175</sup> reported that it is difficult to incorporate Cl using the  $\text{MACl}$  precursor.  $\text{PbCl}_2$  was proposed to be a better way to introduce Cl. Li et al.<sup>173</sup> employed a two-step dipping method for the fabrication of  $\text{MAPbI}_{3-x}\text{Cl}_x$  films, which were deposited on PEDOT:PSS. The  $\text{PbCl}_2:\text{PbI}_2$  with various mole fractions were dissolved at  $85^\circ\text{C}$  in DMF and spin coated on PEDOT:PSS films (after the solutions were cooled to room temperature). The substrates were then dipped into a preheated MAI solution ( $70^\circ\text{C}$ , 60 s) dissolved in 2-propanol. Finally, the substrates were postannealed at a temperature of  $75^\circ\text{C}$  for 20 min. It is noticed that in several works large variations in the postannealing temperature is employed for the perovskite crystallization, for example in the one-step method, 9 0 – 1 2 0  $^\circ\text{C}$  for 4 5 – 1 2 0 min.<sup>60,165,169,172,176,179,181,182,184,185,189,195,199</sup> The fine-tuning of annealing temperature and time will play a major role for the delicate incorporation of Cl into the perovskite crystal lattice. The XRD data on  $\text{MAPbI}_{3-x}\text{Cl}_x$  films using the two-step method by Li et al.<sup>173</sup> show that the (110) and (220) diffraction peaks shift as a  $\text{PbCl}_2$  concentration increases (Figure 11a,b). Although the shift is small, it is above the instrumental sensitivity and not negligible. They performed further XRD data fitting extracting the lattice parameters and unit cell volumes (inset in Figure 11a). In addition, the XRD pattern shows that the Cl-content in perovskites prepared by the two-step dipping method is higher than the ones fabricated by the one-step method. Furthermore, no (110) diffraction peak ( $15.68^\circ$ ) related to  $\text{MAPbCl}_3$  was found indicating no phase segregation occurring (Figure 11a,b).<sup>173,186,196</sup> The UV-vis of perovskite films show the shift of absorption edge toward a shorter wavelength with increasing  $\text{PbCl}_2:\text{PbI}_2$  mole fraction (Figure 11c) corroborating with XRD on solid-solution formation. Zhang et al.<sup>167</sup> synthesized single-crystalline nanofibers (NFs) of  $\text{MAPbI}_{3-x}\text{Cl}_x$  perovskites in the tetragonal phase at room temperature with the Cl-content between  $0 \leq x \leq 0.75$ . Furthermore, based on SAED patterns it was suggested that I ions are not substituted by Cl ions along the [001] direction of single-crystalline NFs, but the Cl incorporation takes place along the [100] or [010] directions, i.e., within the crystal ab-plane (Figure 11d). In other words, Cl-inclusion occurred along the [001] direction (apical positions) because of high intensity of (110) diffraction planes observed for  $\text{MAPbI}_{3-x}\text{Cl}_x$  perovskites.<sup>15,206–208</sup> Pistor et al.<sup>180</sup> and Luo et al.<sup>171</sup> synthesized  $\text{MAPbI}_{3-x}\text{Cl}_x$  perovskites under vacuum conditions by coevaporation of MAI and  $\text{PbCl}_2$  sources. Interestingly, upon subsequent postannealing treatments, they observed that a phase transition from tetragonal to a cubic phase (space group  $Pm\bar{3}m$  with lattice constant of  $6.276 \text{ \AA}$ ) takes place in  $\text{MAPbI}_{3-x}\text{Cl}_x$  perovskites, which was also reported to be stabilized after the cooling at room temperature. As comparison,  $\text{MAPbCl}_3$  adopts a cubic structure at room temperature (Figure 2d). More recently, a recipe for the synthesis of single crystal  $\text{MAPb(I/Cl)}$  was reported by Lian et al.<sup>209</sup> and their TOF-SIMS measurements confirmed the trace amount of Cl in the  $\text{MAPb(I/Cl)}$  bulk film.

The second possible scenario for the discrepancies in the reports could lie on the technical aspects of the measurement conditions. Most of chemical analytical tools (XPS, EDX, TOF-SIMS, etc.) require high vacuum under which volatile species contained in perovskite films can desorb.<sup>174</sup> Furthermore, the situation can be more drastic when perovskite films are exposed to a probing beam (e-beam, UV, X-ray, etc.) that may lead to beam-induced artifacts during measurement. Colella et al.<sup>185</sup> mentioned that reliable values of Cl concentration could not be achieved as the amplitude of the Cl-related signal was observed to decrease during the measurement in EDX. Starr et al.<sup>174</sup> emphasized the importance of employing nondestructive techniques (e.g., HAXPS and FY-XAS) to guarantee that the measurement itself will not modify the original chemical composition of the perovskite samples. Based on the extensive analytical measurements (Table 2), our current understanding is that the incorporation of Cl ions into the perovskite crystal lattice is viable only in a small quantity (<1 at. %), but sufficient to induce new material properties.<sup>173</sup> Alternatively, Cl-based additives may be another way to facilitate Cl-incorporation into the perovskite lattice.  $\text{HCl}$ ,<sup>210–212</sup>  $\text{NH}_4\text{Cl}$ ,<sup>213</sup>  $\text{CaCl}_2$ ,<sup>214</sup> tetraphenylphosphonium chloride (TPPCl),<sup>215</sup> and butylphosphonic acid 4-ammonium chloride (4-ABPACl)<sup>216</sup> additives were reported to play an important role in the formation of high quality films as well as enhancement of device stability; however, the question whether chloride ions enter the perovskite crystal lattice is still under debate.<sup>217</sup>

To our knowledge, there are only two reports focusing on the  $\text{FAPb(I/Cl)}$  system.<sup>218,219</sup> Lv et al.<sup>218</sup> employed the one-step method by mixing  $\text{PbCl}_2$  and FAI in a molar ratio of 1:3 in DMF followed by stirring at  $60^\circ\text{C}$  for 30 min. The solution was spin coated on FTO/c-TiO<sub>2</sub>/mp-TiO<sub>2</sub>, and the  $\text{FAPbI}_{3-x}\text{Cl}_x$  films were formed by postannealing in an oven at a temperature ranging from 120 to  $170^\circ\text{C}$  for 30 min. Based on XRD data, annealing at  $140^\circ\text{C}$  generated  $\text{FAPbI}_{3-x}\text{Cl}_x$  perovskite in the tetragonal phase (space group  $P3m1$ ,  $a = b = 8.977(7) \text{ \AA}$ ,  $c = 10.890(2) \text{ \AA}$ ). A slight c lattice parameter contraction of  $\sim 1.1\%$  compared to the  $\text{FAPbI}_3$  perovskite ( $a = 9.000(8) \text{ \AA}$ ,  $c = 11.012(2) \text{ \AA}$ ) was attributed to the partial substitution of  $\text{Cl}^-$  into the perovskite structure. EDX was also employed to estimate the chlorine content, but it was barely detectable.<sup>218</sup> Wang et al.<sup>219</sup> employed  $\text{NH}_4\text{Cl}$ ,  $\text{MACl}$ , and  $\text{FACl}$  additives to suppress the formation of yellow  $\delta$ -phase

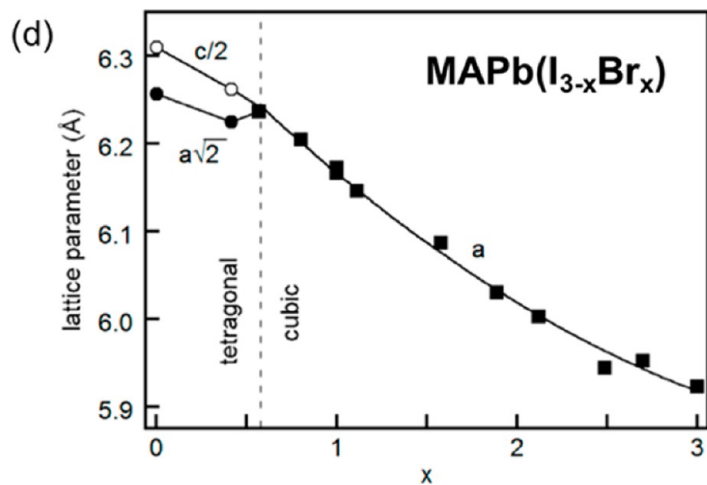
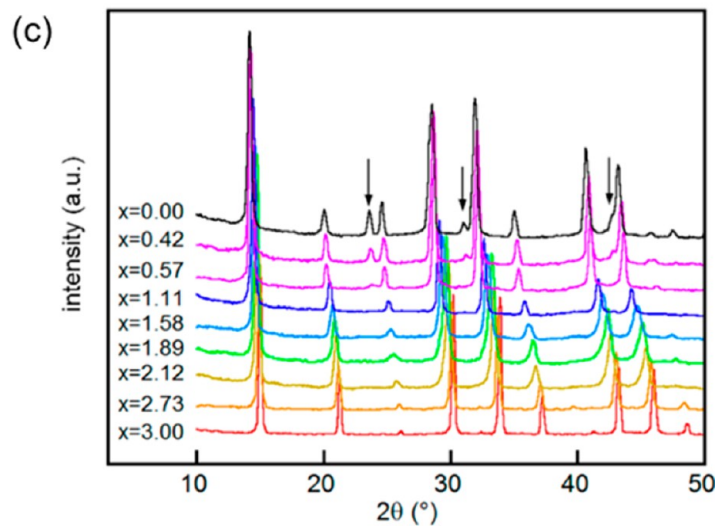
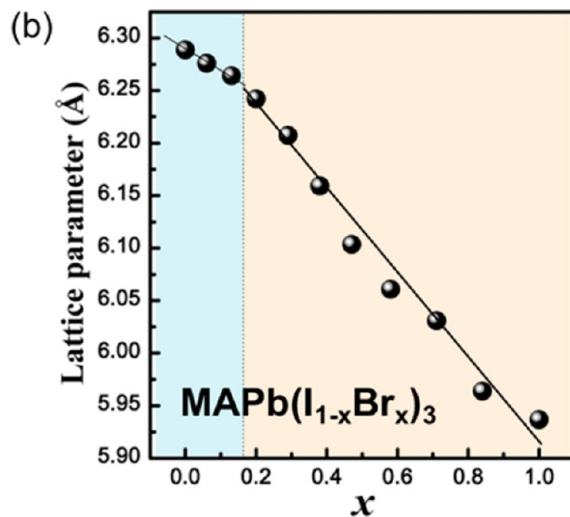
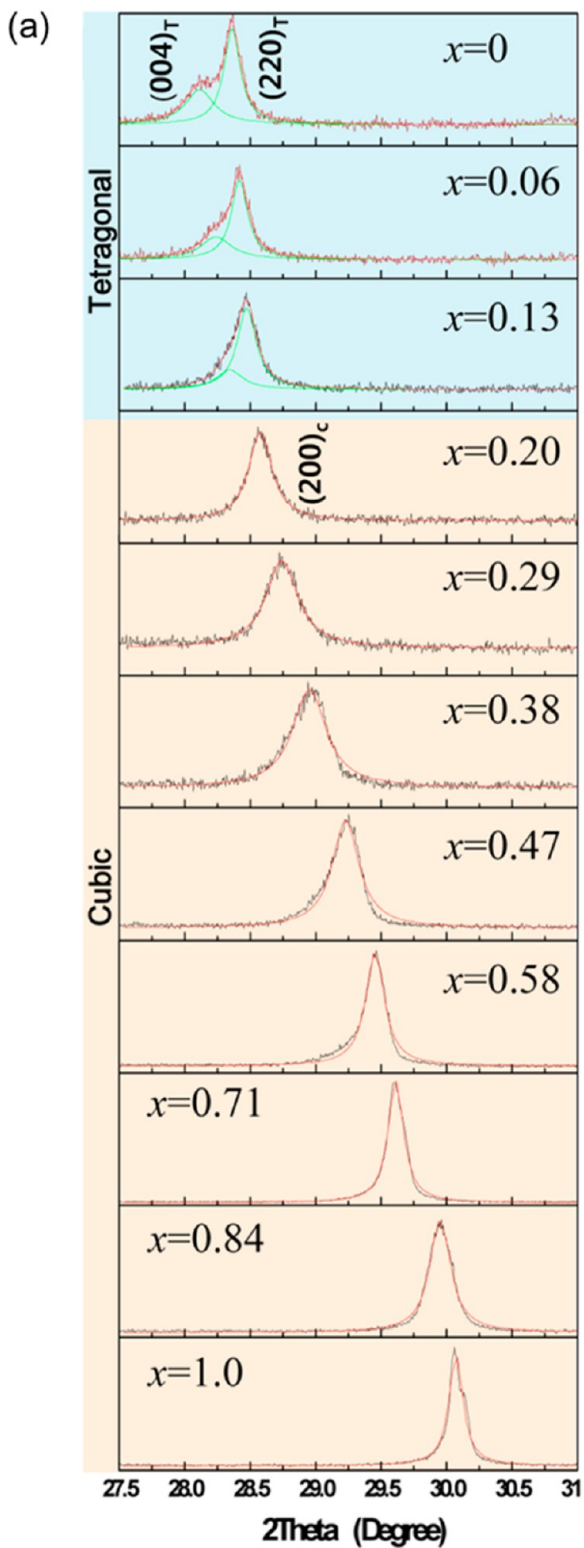


**Figure 12.** (a) Narrow-range XRD pattern of  $\text{MAPb}(\text{I}/\text{Br})$  perovskites with varying Br:I molar ratio concentrations magnified in the region of the tetragonal  $(004)_T$  and  $(220)_T$  and cubic  $(200)_C$  peaks. (b) Lattice constants of pseudocubic or cubic as a function of Br:I molar ratio concentrations. (c) Wide-range XRD pattern of  $\text{MAPb}(\text{I}/\text{Br})$  perovskites and (d) extracted lattice parameters. (a,b) Reprinted with permission from ref 220. Copyright 2013 American Chemical Society. (c,d) Reprinted with permission from ref 226. Copyright 2015 American Chemical Society.

FAPbI<sub>3</sub>. It has been proposed that suppressing the formation of  $\delta$ -FAPbI<sub>3</sub> phase at all stages of the formation of FAPbI<sub>3</sub> on mp-TiO<sub>2</sub> is essential for achieving high-purity black  $\alpha$ -FAPbI<sub>3</sub> perovskite phase.

### 3.2. Binary $\text{MAPb}(\text{I}/\text{Br})$ and $\text{FAPb}(\text{I}/\text{Br})$ Systems.

Contrary to the  $\text{MAPb}(\text{I}/\text{Cl})$  material system described in section 3.1, the substitution of I<sup>-</sup> by Br<sup>-</sup> ions has been widely demonstrated and to effectively tune the band gap of

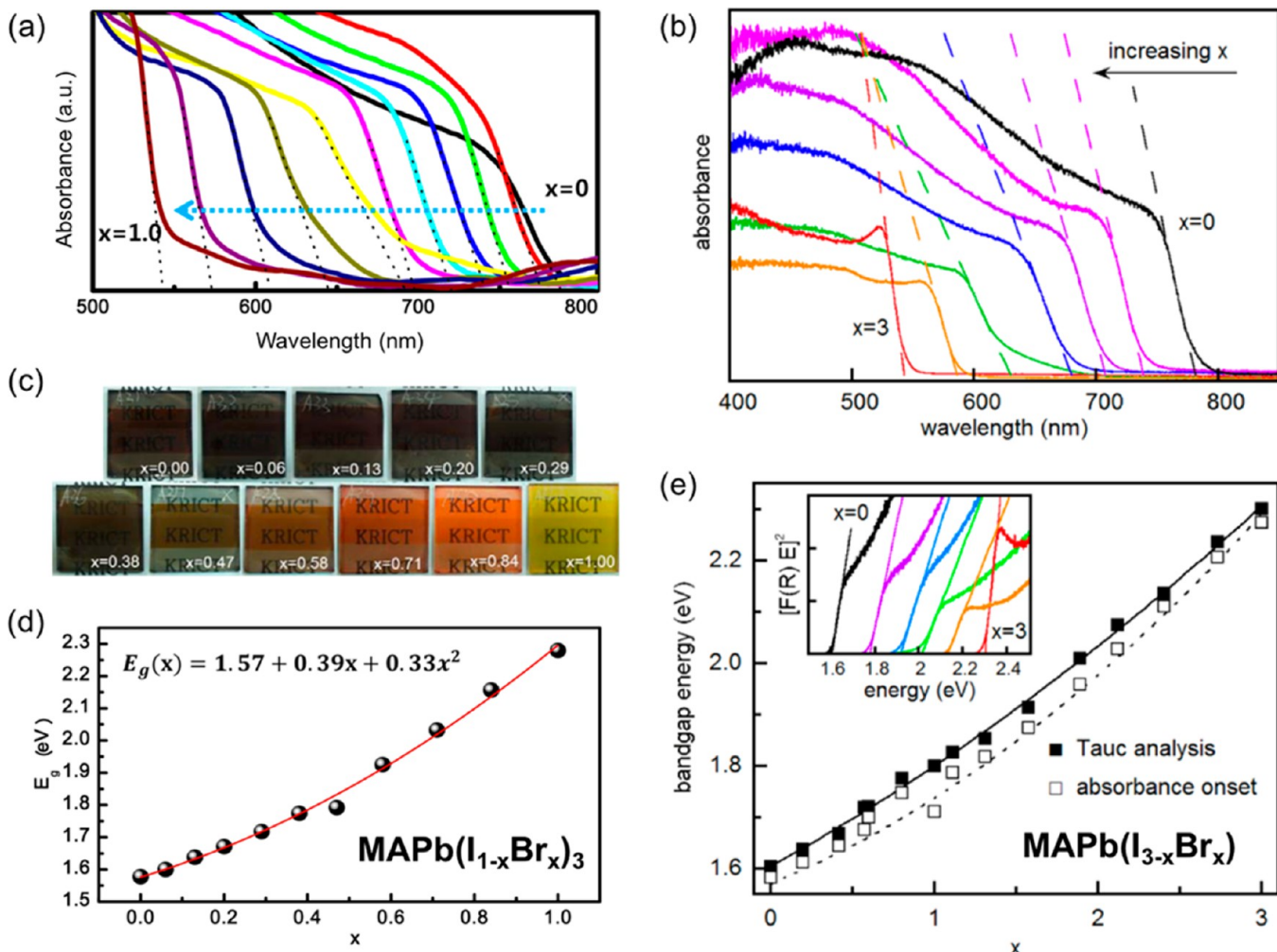


**Figure 13.** (a,b) UV-vis absorbance spectra of MAPb(I/Br) perovskites with varying Br:I molar ratio concentrations. (c) Photographs of MAPb(I/Br) perovskite films. (d,e) Band gap energies as a function of Br:I concentrations extracted from the absorbance onsets and Tauc analysis. Inset in (e) shows representative Tauc plots used to determine  $E_g$ . (a,c,d) Reprinted with permission from ref 220. Copyright 2013 American Chemical Society. (b,e) Reprinted with permission from ref 226. Copyright 2015 American Chemical Society.

perovskites.<sup>220</sup> The photovoltaic properties of mixed MAP-  
668 bl<sub>3-x</sub>Br<sub>x</sub> were first demonstrated by Noh et al.<sup>220</sup> reporting an  
669 efficiency of 12.3%. Jeon et al.<sup>62</sup> achieved a certified PCE of  
670 16.2% (Figure 1b) by the solvent-engineering method, which  
671 enables the deposition of uniform and dense perovskite films of  
672 MAPbI<sub>3-x</sub>Br<sub>x</sub> ( $x = 0.10\text{--}0.15$ ). Later alternative deposition  
673 methods such as vacuum deposition,<sup>221</sup> low-pressure vapor-<sup>222</sup>  
674 assisted solution (LP-VASP),<sup>222</sup> and printing<sup>223</sup> have been  
675 demonstrated. In the work by Noh et al.,<sup>220</sup> the Br content  
676 (<10%) gave the best initial efficiency due to a lower band gap,  
677 but higher Br contents (>20%) provided a better high-humidity  
678 shelf life stability (RH 55%). This was correlated with a  
679 tetragonal to pseudocubic structural transition (at  $x = 0.13$ )  
680 arising from a higher  $t$  factor due to the smaller ionic radius of  
681 Br (Figure 12). Mixed perovskites composed of two different  
682 perovskite crystals with similar lattice constants follow the  
683 Vegard's law. According to this law, a linear dependence of the  
684 lattice parameter with composition is expected, in the absence  
685 of strong electronic effects.<sup>220,224\text{--}228</sup> Fedeli et al.<sup>226</sup> claimed  
686 that in the cubic regime ( $x \geq 0.57$ , MAPbI<sub>3-x</sub>Br<sub>x</sub>), a small  
687 deviation from the Vegard's law was observed indicating  
688 additional interactions in the mixed-halogens (Figure 12d).  
689 Furthermore, a blue-shift of the absorption edge, i.e., increase in

band gap following a quadratic function of the Br content was  
690 extracted from absorbance onsets,  $E_g(x) = 1.57 + 0.39x + 0.33x^2$  (eV)  
691 by Noh et al.<sup>220</sup> (Figure 13a,c,d). Fedeli et al.<sup>226</sup> emphasized that slight variations (a few tens of meV) in  $E_g$   
692 values are obtained when derived from the Tauc analysis and  
693 compared to  $E_g$  values extracted from the absorbance onset  
694 (Figure 13b). The  $E_g(x)$  expression that is independent of the  
695 film properties (thickness, surface roughness related scattering)  
696 was derived based on Tauc plots (Figure 13e):  
697

$$E_g(x) = E_{I3} + (E_{Br3} - E_{I3} - b)\frac{x}{3} + b\left(\frac{x}{3}\right)^2 \quad (3)$$

where  $E_{I3}$  and  $E_{Br3}$  are the bandgaps of MAPbI<sub>3</sub> (1.604 eV) and  
700 MAPbBr<sub>3</sub> (2.307 eV), respectively, and  $b$  (0.175 eV) is the so-  
701 called bowing parameter that accounts for the effects of  
702 composition disorder on the conduction and valence band  
703 edges. Based on the low  $b$  value extracted, the authors  
704 concluded that compositional disorder is low in MAPb(I/Br)  
705 perovskites (Figure 14a). Based on DFT calculations, Mosconi  
706 et al.<sup>206</sup> proposed that Br can occupy both apical and equatorial  
707 positions in the PbX<sub>6</sub> octahedra. Based on combined first-  
708 principles total energy calculations with statistical mechanical  
709 treatments (evoking the energy and entropy of mixing), Brivio  
710

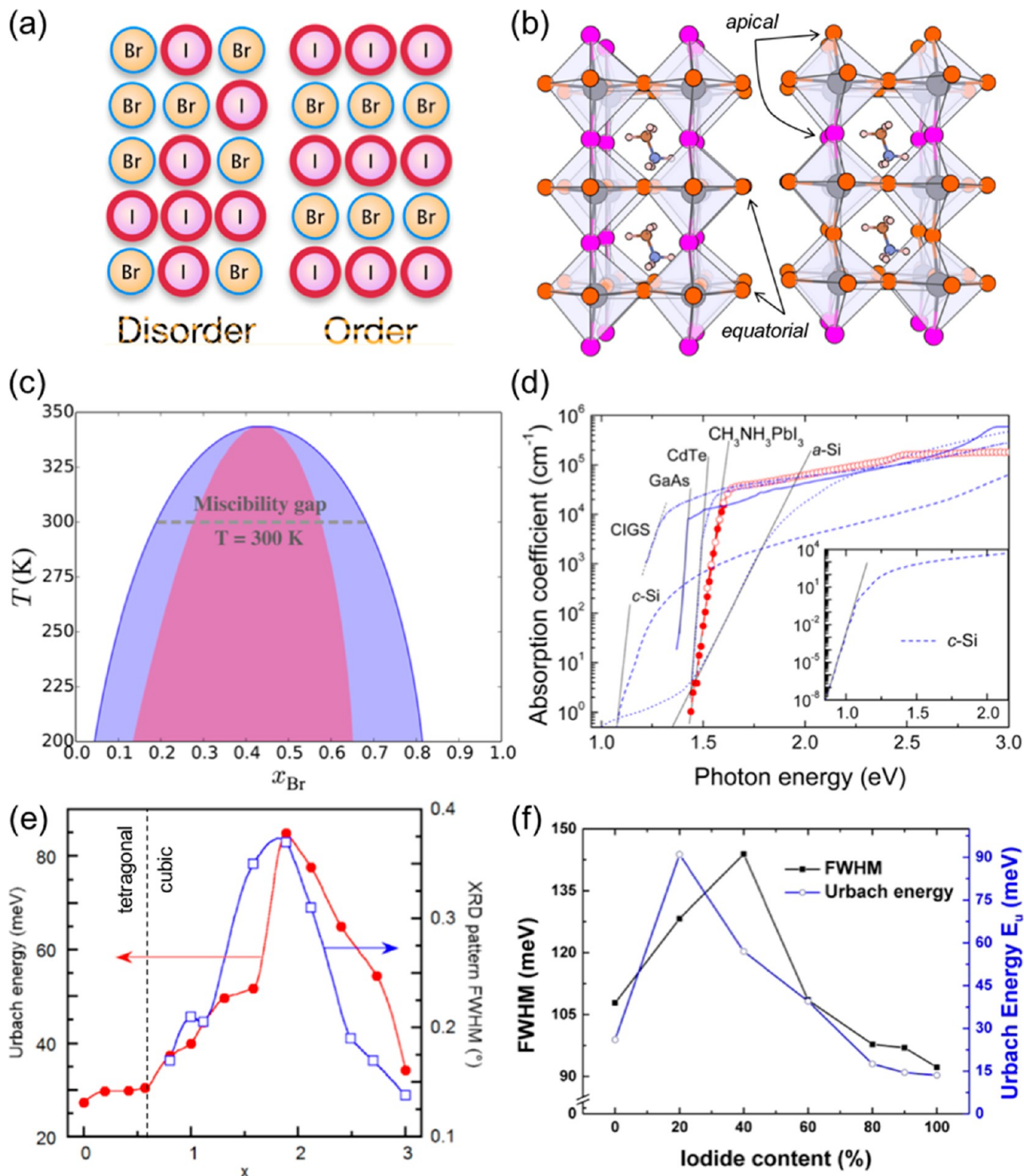


**Figure 14.** (a) Schematic illustration of disordered and ordered systems in MAPb(I/Br). (b) Identified stable ordered structures for MAPbI<sub>3</sub> and MAPbI<sub>1/2</sub>Br<sub>5/2</sub> (layered with iodine at the apical positions) that minimize internal strain arising from the size mismatch between I and Br. (c) Calculated phase diagram of MAPb(I<sub>1-x</sub>Br<sub>x</sub>)<sub>3</sub> alloy. Purple and pink lines are binodal and spinodal lines, respectively. The dashed horizontal line corresponds to miscibility gap at room temperature. Thermodynamically stable alloy can be formed only in the white region. Reprinted with permission from ref 229. Copyright 2016 American Chemical Society. (d) Effective absorption coefficient of MAPbI<sub>3</sub> perovskite compared with other technologically relevant photovoltaic materials, amorphous-silicon (a-Si), GaAs, CIGS, CdTe, and crystalline silicone (c-Si), all corresponding to room temperature measurements. For each material, the slope of the Urbach tail is shown. The inset shows the data for c-Si down to low absorption values. Reprinted with permission from ref 230. Copyright 2014 American Chemical Society. (e) Urbach energy and fwhm of the XRD pattern in the cubic phase composition range as a function of Br:I molar ratios in MAPb(I/Br) perovskites. Reprinted with permission from ref 226. Copyright 2014 American Chemical Society. (f) Urbach energy and fwhm of the PL peak as a function of iodine concentration in MAPb(I/Br) perovskites. Reprinted with permission from ref 231. Copyright 2014 American Chemical Society.

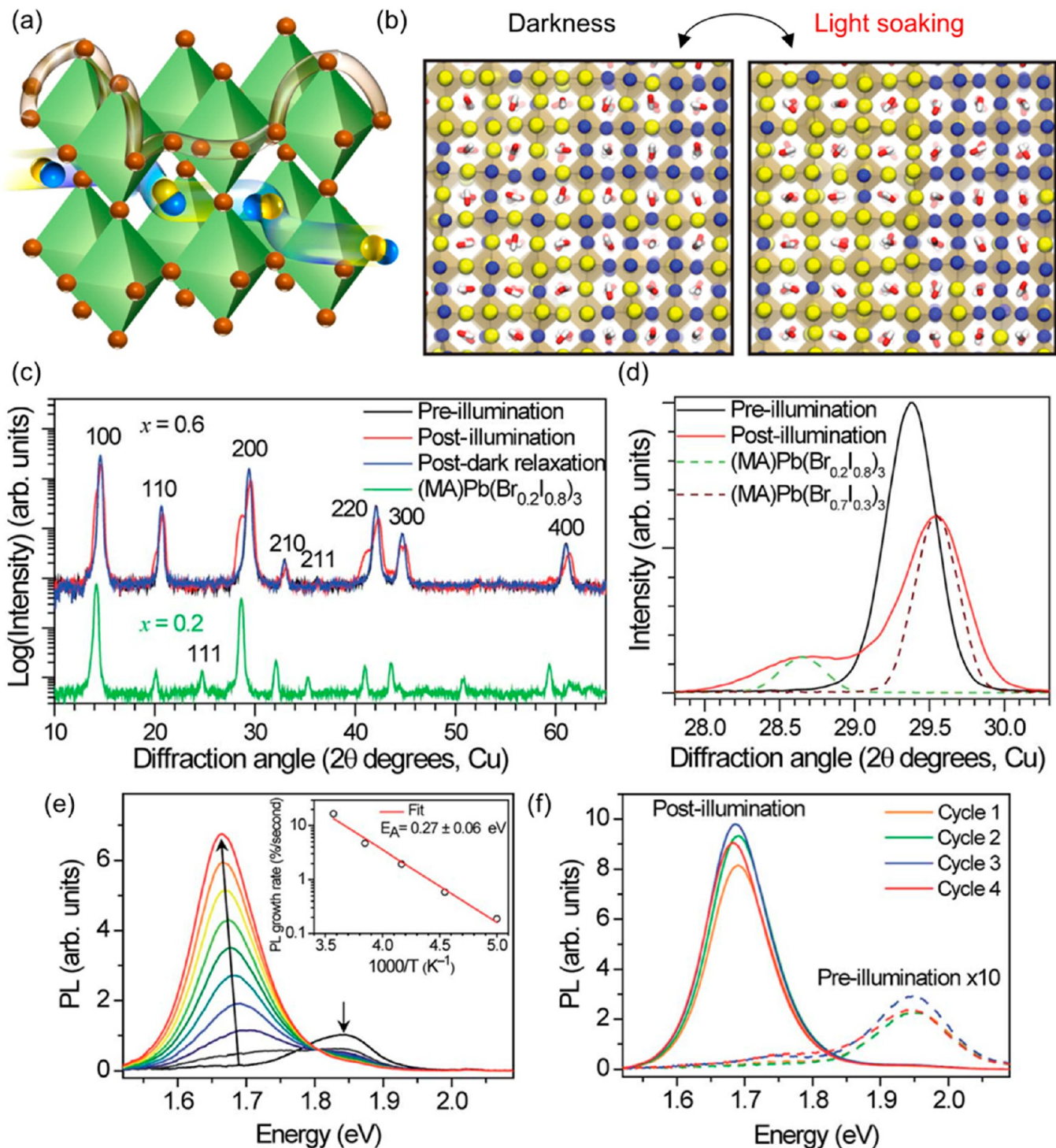


**Figure 15.** (a) Illustration of proposed migration path of  $\text{I}^-$  ions along the  $\text{I}^-\text{-I}^-$  edge of the  $\text{PbI}_6$  octahedra in  $\text{MAPbI}_3$ .  $\text{MA}^+$  migration was also corroborated experimentally. Reprinted with permission from ref 232. Copyright 2016 American Chemical Society. (b) Schematic illustration of phase separation (Light soaking) and reversibility (darkness) in  $\text{MAPb}(\text{I}/\text{Br})$  system, where yellow and blue spheres represent  $\text{I}^-$  and  $\text{Br}^-$ , respectively; the red and white pill shapes represent  $\text{MA}$ . Reprinted with permission from ref 233. Copyright 2017 American Chemical Society. (c) XRD pattern of  $\text{MAPbBr}_{0.6}\text{I}_{0.4}$  film before (black) and after (red) white-light soaking ( $\sim 50 \text{ mW/cm}^2$ ;  $\sim 0.5 \text{ sun}$ ) for 5 min, and subsequently after 2 h in the dark (blue). XRD of  $\text{MAPbBr}_{0.2}\text{I}_{0.8}$  (green) is shown for comparison. (d) (200) XRD peak of  $\text{MAPbBr}_{0.6}\text{I}_{0.4}$  film before (black) and after (red) white-light soaking ( $\sim 50 \text{ mW/cm}^2$ ) for 5 min. XRD of  $\text{MAPbBr}_{0.2}\text{I}_{0.8}$  (dashed green) and  $\text{MAPbBr}_{0.7}\text{I}_{0.3}$  (dashed brown) are shown for comparison. (e) PL spectra of  $\text{MAPbBr}_{0.6}\text{I}_{0.4}$  film over 45 s in 5 s increments under 475 nm, 15  $\text{mW/cm}^2$  at 300 K. Inset shows temperature dependence of initial PL growth rate. (f) PL spectra of  $\text{MAPbBr}_{0.6}\text{I}_{0.4}$  film after sequential cycles of illumination (475 nm, 15  $\text{mW/cm}^2$ ) for 2 min followed by 5 min in the dark. Reprinted with permission from ref 234. Copyright 2015 The Royal Society of Chemistry.

711 et al.<sup>229</sup> identified the two most stable configurations  
712 corresponding to ordered structures of  $\text{MAPbIBr}_2$  and

MAPb $\text{I}_{1/2}\text{Br}_{5/2}$  (Figure 14b). Both structures were formed  
713 with iodine ions located at the apical locations. Furthermore,  
714

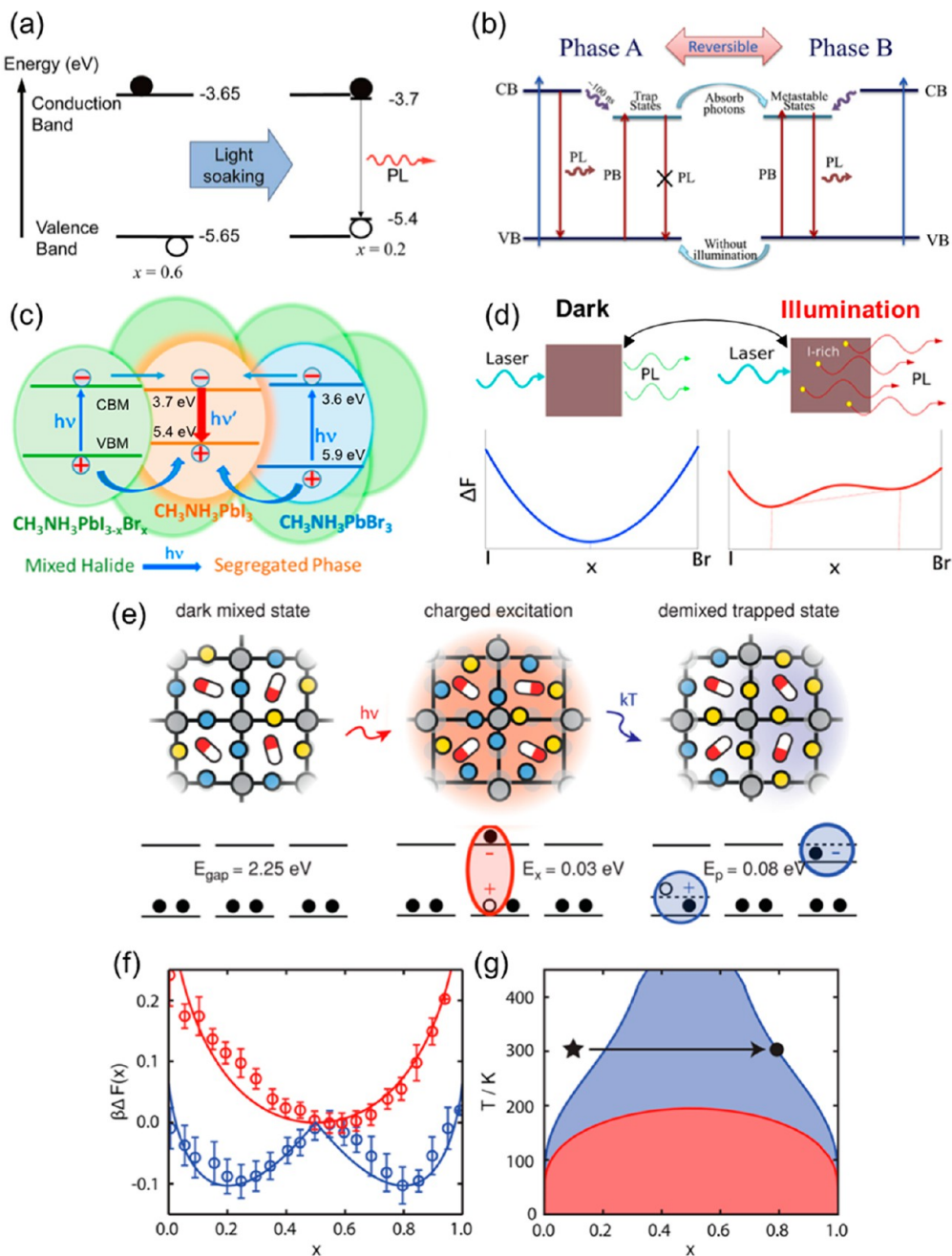


**Figure 16.** (a) Illustration of proposed mechanism for photoinduced trap states formation within the band gap in MAPbBr<sub>0.4</sub>I<sub>0.6</sub>. Photogenerated holes or excitons are hypothesized to stabilize the formation of iodine-rich domains (e.g., MAPb(Br<sub>0.2</sub>I<sub>0.8</sub>)<sub>3</sub>) that dominate PL. Reprinted with permission from ref 234. Copyright 2015 The Royal Society of Chemistry. (b) Illustration for the proposed two-step mechanism for light induced segregation: initial photon absorption will generate trap states in the band gap after 100 ns; these traps have lifetime of 1  $\mu$ s (Phase A). If subsequent coming photons are absorbed by these traps, it transforms to a metastable state (Phase B), which behave as new energy band and can lead to PL emission. Reprinted with permission from ref 235. Copyright 2016 Elsevier Ltd. (c) Illustration of MAPb(I/Br) with each of the domains (iodide- and bromide-rich) having characteristic conduction band minimum (CBM) and valence band maximum (VBM) values will lead to iodide-rich domains to serve as sinks for the photogenerated charge carriers. Reprinted with permission from ref 236. Copyright 2016 American Chemical Society. (d) Schematic Helmholz free-energy ( $\Delta F$ ) curves in light and in dark predicting phase segregation. The red vertical dashed lines show that the lowest attainable free energy in light occurs when the material segregates into I-rich and Br-rich phases, whereas the blue dashed line shows that the lowest energy corresponds when the material remains in a single phase in dark. Reprinted with permission from ref 237. Copyright 2016 American Chemical Society. (e) Photoinduced polaron trapping and associated energy scales. Yellow and blue spheres represent I<sup>-</sup> and Br<sup>-</sup>, respectively; the red and white pill shapes represent MA. Lead atoms represented by gray circles. (f) Free energies per unit cell for MAPb(I<sub>x</sub>Br<sub>1-x</sub>)<sub>3</sub> with varying composition in the ground (red) and photoexcited (blue) states, computed from MD simulations (circles) and mean field theory (solid lines). (g) Temperature-composition phase diagram in the ground (red) and photoexcited state (blue). Areas beneath the red and blue coexisting curves indicate demixed states. The arrow through the phase diagram from initial state (star) to demixed state (circle) correspond to experimental observation for MAPb(I<sub>0.1</sub>Br<sub>0.9</sub>)<sub>3</sub>. Reprinted with permission from ref 233. Copyright 2017 American Chemical Society.

715 based on the Helmholtz free energy variation, a phase diagram  
716 of MAPb(I/Br) was constructed predicting that (i) there is a  
717 critical temperature of  $\sim 343$  K, above which the solid solution  
718 is stable for any Br/I composition; (ii) at 300 K, the alloy is not  
719 stable against a phase separation in  $\text{MAPbI}_3$  and  $\text{MAPbBr}_3$  in  
720 the range of compositions between  $0.19 < x < 0.68$  (miscibility  
721 gap). The lattice constant mismatch ( $\sim 6\%$ ) between  $\text{MAPbI}_3$ ,  
722 and  $\text{MAPbBr}_3$  was associated with the instability of isostructural  
723 solid solutions.<sup>229</sup>

724 Further investigations regarding disorder dependence on Br:I  
725 ratio were conducted by analyzing the exponential decay of the  
726 sub-band gap absorbance, commonly described by the empirical  
727 Urbach rule,  $A \propto \exp(E/E_0)$ , where  $A$  is absorbance,  $E$  photon  
728 energy, and  $E_0$  the characteristic Urbach energy representing  
729 the width of the exponential Urbach tail (Figure 14d).<sup>226,230,231</sup>

730 Despite the fact that there is no theoretical derivation for the  
731 Urbach rule, a general consensus exists that the Urbach tail in  
732 crystalline semiconductors is related to the static (structural  
733 disorder) and/or dynamic (phonon) disorder, that arises from  
734 lattice point defects, dislocations, strain, deviation from ideal  
735 stoichiometry, and grains.<sup>226,230,231</sup> Pure  $\text{MAPbI}_3$  and  $\text{MAPbBr}_3$   
736 perovskites were determined to have sharp absorption edges  
737 with low Urbach energy of  $\sim 15\text{--}27$  meV and  $\sim 23\text{--}34$  meV,  
738 respectively.<sup>226,230,231</sup> Compared with other semiconductors  
739 (Figure 14d), the Urbach energy of  $\text{MAPbI}_3$  is close to the  
740 value of GaAs (monocrystalline direct band gap semi-  
741 conductor). Crystalline Si (c-Si) shows also a similar slope  
742 below its bandgap, but because of its indirect band gap, it  
743 occurs at much a lower value and shows signatures related to  
744 phonon-assisted absorption (inset in Figure 14d). The disorder  
745 evaluated on  $\text{MAPbI}_{3-x}\text{Br}_x$  perovskites through the Urbach  
746 energy showed larger values reaching a maxima of  $\sim 85$  meV  
747 ( $\text{MAPbI}_{1.12}\text{Br}_{1.88}$ , Figure 14e)<sup>226</sup> and  $\sim 90$  meV ( $\text{MAPbI}_{1.2}\text{Br}_{1.8}$ ,  
748 Figure 14f).<sup>231</sup> Interestingly, the dependence of  $x$  with these  
749 Urbach energies was closely related to grain-size domains  
750 (Figure 14e), and it was suggested that the sub-band gap  
751 absorption is due to defect states localized at the grain  
752 boundaries.<sup>226</sup> It was also shown that the fwhm of the  
753 photoluminescence (PL) peaks are correlated with the Urbach  
754 energies (Figure 14f). This observation indicates that  
755 absorption and emission arise from similar states.<sup>231</sup> Also, the  
756 larger PL fwhm and Urbach energy with iodine concentrations  
757 of 20–40% (Figure 14f) was observed to correlate with shorter  
758 lifetimes observed in transient PL.<sup>231</sup>

759 Although under storage conditions the MAPb(I/Br) system  
760 exhibits enhanced stability, it has been reported that dynamical  
761 processes (e.g., material degradation and phase segregation)  
762 takes place when exposed to light. Misra et al.<sup>227</sup> performed  
763 photochemical stability tests of encapsulated films of  
764  $\text{MAPbI}_{3-x}\text{Br}_x$  ( $x = 0.11, 0.16, 0.22, 1$ ) under accelerated  
765 stressing conditions using concentrated sunlight (100 suns).  
766 They observed that  $\text{MAPbBr}_3$  was the most stable composition  
767 exhibiting no degradation, whereas increasing iodine incorpo-  
768 ration leads to accelerated photochemical degradation yielding  
769  $\text{PbI}_2$  as a final remaining product. No degradation was recorded  
770 for  $\text{MAPbI}_{3-x}\text{Br}_x$  under shelf-storage conditions, and degra-  
771 dation was observed to occur only under illumination conditions.  
772 Currently, it is widely accepted that ion migration is one of the  
773 causes for the anomalous photocurrent hysteresis phenomena  
774 (Figure 15a).<sup>232,238,239</sup> In addition, there are also concerns that  
775 ion migration is closely correlated with inherent instability  
776 issues in perovskite solar cells. For example, Hoke et al.<sup>234</sup>  
777 reported first on the occurrence of a serious phase segregation

778 in  $\text{MAPb}(\text{I}/\text{Br})$  films under illumination (coined as Hoke  
779 effect<sup>237,240</sup>). The initially homogeneous  $\text{MAPb}(\text{Br},\text{I}_{1-x})_3$  ( $0.2 < x < 0.9$ )  
780 perovskite films were observed to undergo photoexcited phase-separation into two phases, one iodine-rich  
781 and the other bromide-rich domain in the same film (Figure 15b), as corroborated by the peak splitting probed in  
782 XRD (Figure 15c,d) and PL (Figure 15e,f) measurements. As shown in Figure 15d, when the  $\text{MAPb}(\text{Br}_{0.6}\text{I}_{0.4})_3$  film was illuminated with white light, the original diffraction pattern splits into two peaks, suggesting formation of phases with larger and smaller lattice constants. More interestingly, when allowed to relax in dark, the XRD pattern returned to its original, single phase state. Additional, PL (Figure 15f) and absorption spectra acquired before and after light soaking confirmed this reversibility (Figure 15b). Temperature dependence (200–300 K) was performed to verify that phase segregation occurs solely due to illumination and not from temperature increase during illumination (Figure 15e). Although phase segregation (disappearance of the original peak and rise of new lower-energy peak) was observed at the lowest temperature of 200 K, the time scale for the changes varied widely. The changes occurred in  $\sim 1$  min at 300 K, whereas at 200 K the phase segregation took  $\sim 1$  h to complete. The Arrhenius plot behavior (inset in Figure 15e) was observed for this phase segregation, where an activation energy of  $\sim 0.3$  eV was extracted. Interestingly, this value is similar to halide ion migration activation energies reported previously, supporting further that ionic transport plays a major role in perovskite solar cells (Figure 15a,b).<sup>232,234,237</sup> It is emphasized that even without light illumination, the PL peak position was observed to shift in  $\text{MAPbBr}_{1.2}\text{I}_{1.8}$  films from 1.68 to 1.94 eV after 2 weeks storage under dark and inert environment.<sup>231</sup> This was attributed to a slow, but spontaneous room temperature phase segregation within the miscibility gap (Figure 14c).<sup>229</sup>

812 A number of reports proposed the microscopic origins for the phase-segregation phenomena.<sup>74,233–237,240</sup> Hoke et al. proposed that the existence of initial iodide-rich domains (nucleation points) in as prepared MAPb(I/Br) samples stabilizes hole accumulation upon illumination (Figure 16a). These accumulation of unbalanced charges (holes) provide further driving enthalpy for halide segregation growing further the iodide-rich domain sizes (Figure 15d,e). Yang et al. employed PL and photomodulation (PM) spectroscopy to study the  $\text{MAPbBr}_{1.7}\text{I}_{1.3}$  films. Using continuous wave (CW) or 10 ns pulsed laser with high repetition rates, they observed that the initial PL  $\sim 640$  nm ( $\sim 1.94$  eV) peak position shifted to a longer wavelength of  $\sim 750$  nm ( $\sim 1.65$  eV) after illumination.<sup>235</sup> Interestingly, with the same 10 ns pulsed laser, but using lower repetition rates (<500 Hz), no matter what the intensity of excitation light is, PL did not show shift in peak position. Based on CW pump probe spectroscopy and transient dynamics, Yang et al. proposed a two-step process: initial photon absorption will generate trap states within the band gap, but these traps will not lead to PL emission; these traps have lifetime of  $1\ \mu\text{s}$  (Phase A). If subsequent incident photons are absorbed by these traps within the lifetime, it transforms to a long-lived ( $\sim\text{ms}$ ) “metastable” state (Phase B), which behaves as new energy band and can lead to PL emission (Figure 16b). These polar states (later identified as polaronic states<sup>233</sup>) were hypothesized to locally drive ion migration. Yoon et al. proposed that MAPb(I/Br) with each of the domains (iodide- and bromide-rich) having characteristic conduction band minimum (CBM) and valence band maximum (VBM) values

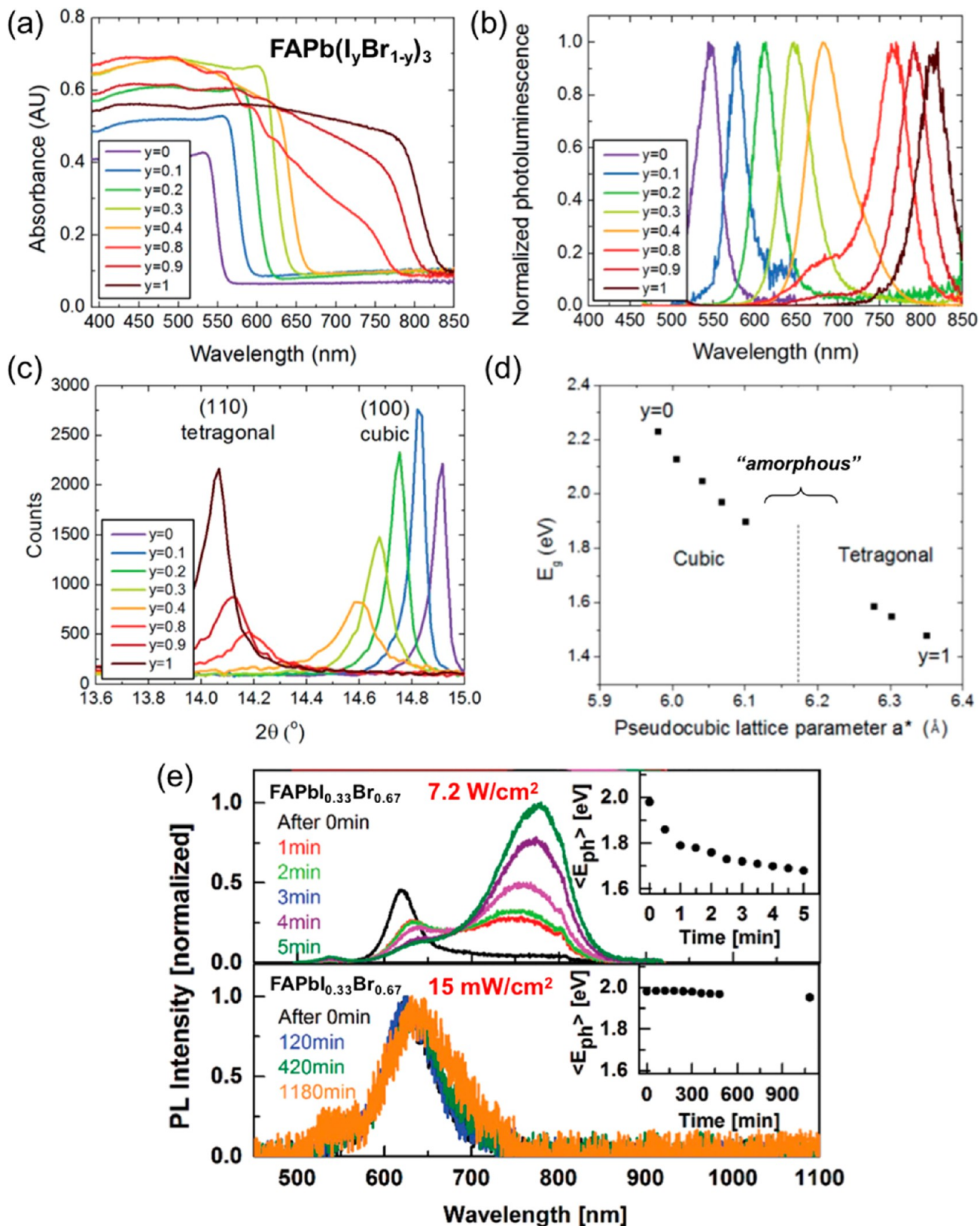


**Figure 17.** (a) UV–vis absorbance, (b) steady-state PL spectra, (c) XRD of  $\text{FAPbI}_x\text{Br}_{3-x}$  perovskites with varying  $x$  composition. (d) Variation of band gap as a function of pseudocubic lattice parameter extracted from XRD data. Reprinted with permission from ref 147. Copyright 2014 The Royal Society of Chemistry. (e) PL spectra of  $\text{FAPb}(\text{Br}_{0.67}\text{I}_{0.33})_3$  film over 5 min of continuous illumination following excitation at 400 nm with intensity of 7.2  $\text{W}/\text{cm}^2$  and 15  $\text{mW}/\text{cm}^2$ . Inset: Change of the average photon energy ( $E_{\text{ph}}$ ) as a function of time. Reprinted with permission from ref 242. Copyright 2015 WILEY-VCH Verlag GmbH & Co. KGaA, Weinheim.

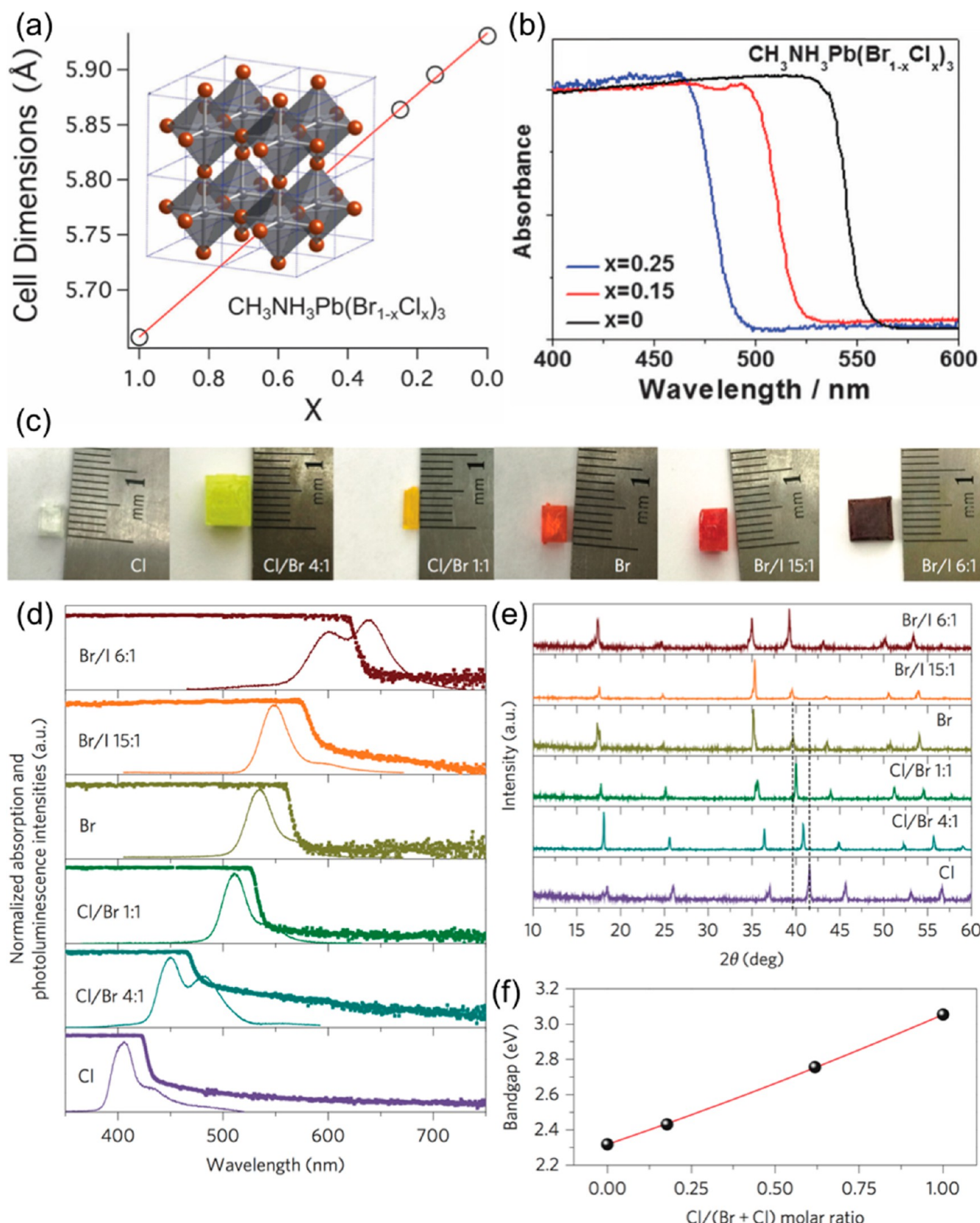


**Figure 18.** (a) Single crystal XRD cell dimensions and (b) UV-vis absorption spectra for  $\text{MAPb}(\text{Br}_{1-x}\text{Cl}_x)_3$  ( $x = 0, 0.15, 0.25$ ). Reprinted with permission from ref 247. Copyright 2015 The Royal Society of Chemistry. (c) Photographs of  $\text{MAPb}(\text{Br}/\text{Cl})$  and  $\text{MAPb}(\text{Br}/\text{I})$  mixed halide perovskite single crystals with different halide compositions. (d) Absorption and PL spectra. (e) Powder XRD. (f) Crystal band gap extracted from PL as a function of  $\text{Cl}/(\text{Cl} + \text{Br})$  molar ratio derived from XRD. Reprinted with permission from ref 246. Copyright 2015 Nature Publishing Group.

will lead to iodide-rich domains to serve as charge recombination sites and thus contribute to the observed PL emission (Figure 16c). Slotcavage et al.<sup>237</sup> discussed the thermodynamic origins of observed light-induced phase segregation (Figure 16d). Bischak et al.<sup>233</sup> performed combined cathodoluminescence (CL) mapping to visualize the spatial segregation into iodide- and bromide-rich domains. After prolonged illumination, small clusters enriched in iodide were observed to localize near grain boundaries. Their molecular dynamics (MD) simulations were able to demonstrate that photoinduced phase separation arises when charged excitations generate enough lattice strain to destabilize the solid solution, favoring phase-segregation. Their findings show that upon light absorption weakly bound electron–hole pair (binding energy  $\sim 0.03$  eV) quickly dissociates into free carriers (Figure 16e). Due to the ionic nature of the perovskite, these charges deform the surrounding lattice through electron–phonon coupling. The charge and the lattice deformation field that surrounds together form a polaron that was predicted to have an average size of 8 nm and binding energy of  $E_p = 0.08$  eV (Figure 16e).<sup>233</sup> This polaron-induced lattice distortion changes the magnitude of the free energy as a function of bromide content from one with one minimum (in dark, red curve in Figure 16f) to another with two minima (under illumination, blue curve in Figure 16f). They also determined a full temperature–composition phase diagram for both ground- and photoexcited states (Figure 16g). This graph shows that for MAPb(I<sub>0.1</sub>Br<sub>0.9</sub>)<sub>3</sub> film (star symbol in Figure 16g), temperature variation over a range of 50 K was insufficient to induce demixing, but does increase the demixing rate under light illumination (circle in Figure 16g). Their model suggests that naturally occurring small variations in perovskite composition that exists before illumination will yield iodide-rich domains that has a reduced band gap. Therefore, perovskite compositional homogeneity seems to be one of the determining factors that will favor stability.<sup>233,237,240</sup> It has been shown that photoinduced phase segregation is minimized in highly crystalline perovskites.<sup>241</sup> Similarly, mixed halide FAPbI<sub>3-x</sub>Br<sub>x</sub> perovskites were also synthesized with  $x$  varying from 0 to 1.<sup>147,242</sup> Interestingly, both reports described that they were unable to form crystalline phases of FAPb(I<sub>1-x</sub>Br<sub>x</sub>)<sub>3</sub> perovskites with bromide contents in the range  $0.3 < x < 0.5$ , as it was apparent from the absence of significant UV–vis, PL, and XRD data (Figure 17a–d). The term “amorphous”<sup>242</sup> was used implying that the crystalline order is too short in the length scale detectable by XRD (Figure 17d).<sup>147</sup> Fundamental origins for this amorphous regime have not been fully clarified. Phase segregation phenomena in iodide- and bromide-rich domains were also reported for the FAPb(I/Br) system.<sup>234</sup> Rehman et al.<sup>242</sup> reported that the intensity of the laser excitation spot played a major role in producing phase segregation (Figure 17e). The PL emission of FAPb(Br<sub>0.67</sub>I<sub>0.33</sub>)<sub>3</sub> films recorded for laser excitation with an intensity of 7.2 W/cm<sup>2</sup> following 5 min of continuous illumination showed the gradual decrease and shift of the 620 nm ( $\sim 2$  eV) to a new dominant low-energy PL feature at  $\sim 785$  nm (1.58 eV). On the other hand, when an identical FAPb(Br<sub>0.67</sub>I<sub>0.33</sub>)<sub>3</sub> film was illuminated at the same wavelength (400 nm) with lower laser intensity of 15 mW/cm<sup>2</sup>, no changes in PL spectra were observed even after 1180 min ( $\sim 20$  h) exposure (Figure 17e). Compared to the MAPb(I/Br) system, it was reported that light intensity as low as 1.2 mW/cm<sup>2</sup> with continuous illumination (10 min) can induce phase segregation.<sup>235</sup> Because photovoltaic devices are typically tested under

AM1.5 conditions (100 mW/cm<sup>2</sup>), strategies to make both MAPb(I/Br) and FAPb(I/Br) systems resilient to phase segregation phenomena is needed.

**3.3. Binary MAPb(Br/Cl) System.** Contrary to the MAPb(I/Cl) system described in section 3.1, Cl was confirmed to coexist with I in the MAPb(Br/Cl) system.<sup>243–249</sup> Theoretical calculations determining the phase transitions of temperature–halide compositions showed a relatively low demixing critical temperature for MAPb(Br/Cl) system ( $\sim 140$  K), which was similar to that of MAPb(Br/I) system ( $\sim 190$  K).<sup>233</sup> In comparison, for the MAPb(I/Cl) system, the determined critical solution temperature of  $\sim 1800$  K was well above room temperature, explaining why this mixture is unstable.<sup>233</sup> The larger difference in ionic radii, Cl<sup>-</sup> (1.67 Å) < Br<sup>-</sup> (1.84 Å) < I<sup>-</sup> (2.07 Å)<sup>250</sup> and the higher degree of ionic character is explained as origin for the “easy” miscibility between (Cl/Br) and (Br/I) system, but not for the (Cl/I) system.<sup>15,233,250</sup> This is also reinforced by the fact that growth of halide mixed MAPbBr<sub>3-x</sub>Cl<sub>x</sub> and MAPbBr<sub>3-x</sub>I<sub>x</sub> single crystal perovskites is possible in the full range of Br:Cl and Br:I molar ratios confirming halide miscibilities (Figure 18).<sup>17,217,246,247</sup> The single crystals were synthesized from stoichiometric PbBr<sub>2</sub> and [yMCl + (1 - y)MABr] precursor solutions in DMF by Zhang et al.<sup>247</sup> employing the solvothermal method, which is based on inverse solubility (Figure 18a,b). Fang et al.<sup>246</sup> employed the cooling-induced crystallization method to growth mixed halide perovskite single crystals (Figure 18c–f). The authors constructed photodetector devices based on these single crystals with a thickness of  $\sim 1$  mm. The response spectrum could be tuned from blue to red by varying the halide composition of these single crystals. The main advantage lies on the very narrowband fwhm (less than 20 nm) photo-detection.<sup>246</sup> Among the family of mixed halide perovskites, MAPbBr<sub>3-x</sub>Cl<sub>x</sub> has a larger band gap (Figure 18b,d,f) than that of iodine-based perovskites (MAPbI<sub>3-x</sub>Cl<sub>x</sub> and MAPbI<sub>3-x</sub>Br<sub>x</sub>).<sup>217</sup> Therefore, most of works focused on perovskite light-emitting devices where the emission color could be tuned from the red to blue color by modulating the halide composition in the perovskite.<sup>245,246,251–253</sup>

**3.4. Ternary MAPb(I/Br/Cl) System.** A few reports describe the triple halide-mixed MAPb(I/Br/Cl) system.<sup>254–256</sup> Similar to what was discussed in section 3.1, the amount of Cl incorporated seems negligible. Nevertheless, Cl was shown to impact device performance by improving coverage and reducing crystal growth rate.<sup>254–256</sup> On the other hand, Br was observed to influence strongly the band gap of MAPb(I/Br/Cl) system and consequently increase open-circuit voltage ( $V_{oc}$ ). In addition, Br incorporation was reported to stabilize crystal lattice improving lifetime of device. These influences of Br incorporation are similar to what was discussed in section 3.2. We observe that the ternary MAPb(I/Br/Cl) system resembles a linear combination of MAPb(I/Cl) + MAPb(I/Br) systems. Chiang et al.<sup>256</sup> synthesized MAPb(I/Br/Cl) perovskites by a combined hot solution spin-coating and solvent annealing film casting engineering obtaining high quality solid solution films. Their inverted solar cell devices (ITO/PEDOT:PSS/MAPbI<sub>3-x-y</sub>Br<sub>x</sub>Cl<sub>y</sub>/PC<sub>61</sub>BM/Ca/Al) with active areas of 0.1 cm<sup>2</sup> generated  $J_{sc} = 19.25$  mA/cm<sup>2</sup>,  $V_{oc} = 1.10$  V, FF = 78%, PCE = 16.52% (the average efficiency from 34 devices yields a small standard deviation: PCE = 15.61  $\pm$  0.84%). Furthermore, the same authors up-scaled the process and their designed inverted perovskite module composed of 9 cells in series with an active area of each cell equal to 4 mm  $\times$  966

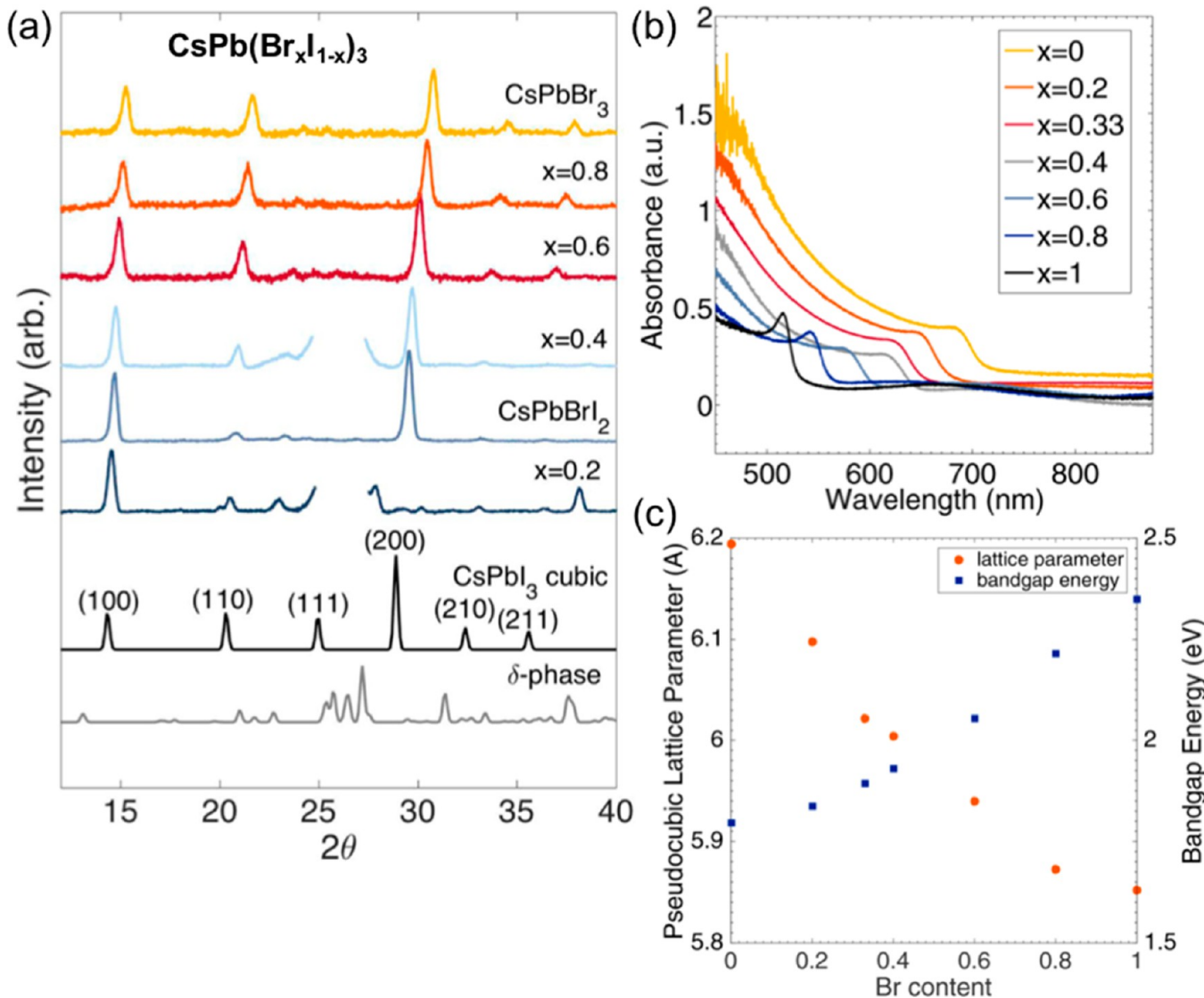


**Figure 19.** (a) XRD and (b) UV–vis absorption spectra for  $\text{CsPb}(\text{Br}_x\text{I}_{1-x})_3$  ( $0 \leq x \leq 1$ ) system. (c) Summary of lattice parameter changes based on the shift of the (100) peak and corresponding changes in the band gap energy extracted from the absorption onset. Reprinted with permission from ref 257. Copyright 2016 American Chemical Society.

70 mm (total active area =  $25.2 \text{ cm}^2$ ) generated  $J_{sc} = 53.5 \text{ mA}$ ,  
 $V_{oc} = 9.05 \text{ V}$  (average per each cell is  $1.06 \text{ V}$ ), FF = 74.4%,  
overall PCE = 14.3%.<sup>256</sup>

**3.5. Binary  $\text{CsPb(I/Br)}$ ,  $\text{CsPb(Br/Cl)}$ , and  $\text{CsPb(I/Cl)}$  Systems.** Recent reports bring additional relevant insights into the  $\text{CsPb(I/Br)}$  system (Figure 19).<sup>98,250,257,258</sup> For example, (i) contrary to the  $\text{MAPb(I/Br)}$  and  $\text{FAPb(I/Br)}$  systems (section 3.2), halide phase-segregation into iodide- and bromide-rich domains (or Hoke effect) was observed to be minimized for  $\text{CsPb}(\text{Br}_x\text{I}_{1-x})_3$  films with low Br concentrations ( $x < 0.4$ ).<sup>257</sup> However, for  $x > 0.4$ , phase separation was reported to occur under illumination ( $\sim 1$  sun). (ii) The  $\text{CsPbI}_2\text{Br}$  in particular, was studied in more details due to its suitable band gap energy for photovoltaic applications.  $\text{CsPbI}_2\text{Br}$  showed enhanced thermal stability when examined at  $200^\circ\text{C}$  in an inert atmosphere<sup>257</sup> and under solar cell operation conditions ( $85^\circ\text{C}$  in air).<sup>98</sup> (iii) The addition of bromide reduces the phase transition temperature. Good thermal stability of  $\text{CsPbIBr}_2$  alloy was also demonstrated at  $200^\circ\text{C}$  in inert atmosphere.<sup>258</sup> The perovskite crystal forms at

$\sim 350^\circ\text{C}$  for  $\text{CsPbI}_3$  and  $\sim 230^\circ\text{C}$  for  $\text{CsPbI}_2\text{Br}$ , meaning a reduction of over  $100^\circ\text{C}$  in the transition temperature.<sup>98</sup> Device configuration of FTO/c-TiO<sub>2</sub>/mp-TiO<sub>2</sub>/ $\text{CsPbI}_2\text{Br}$  ( $\sim 150 \text{ nm}$ )/spiro-MeOTAD/Ag was demonstrated to generate the best efficiency of 9.84%, with  $J_{sc} = 11.89 \text{ mA/cm}^2$ ,  $V_{oc} = 1.11 \text{ V}$ , and FF = 75%.<sup>98</sup> Devices with an inverted structure, ITO/PEDOT:PSS/ $\text{CsPbI}_2\text{Br}$  ( $\sim 150 \text{ nm}$ )/PC60BM/BCP/Al, were shown to generate a PCE of 6.80%,  $J_{sc} = 10.9 \text{ mA/cm}^2$ ,  $V_{oc} = 1.06 \text{ V}$ , and FF = PCE/( $J_{sc} \times V_{oc}$ )  $\sim 59\%$ .<sup>257</sup>

Yin et al.<sup>250</sup> performed DFT calculations together with Monte Carlo simulations to systematically study the structural, electronic and energetic properties of mixed halide  $\text{CsPb(I/Br)}$ ,  $\text{CsPb(Br/Cl)}$ , and  $\text{CsPb(I/Cl)}$  systems. They found that these perovskites exhibit anomalous alloy properties that differ from the conventional semiconductors (e.g.,  $\text{GaAs}_{1-x}\text{Sb}_x$ ). Generally, in conventional isovalent semiconductors, the formation energies are positive mostly attributed to the strain energy (e.g., original ideal A and B bulk materials are stretched or compressed to a new lattice constant of alloy  $\text{A}_{1-x}\text{B}_x$ ). Halide perovskites have strong ionic character, so Coulomb

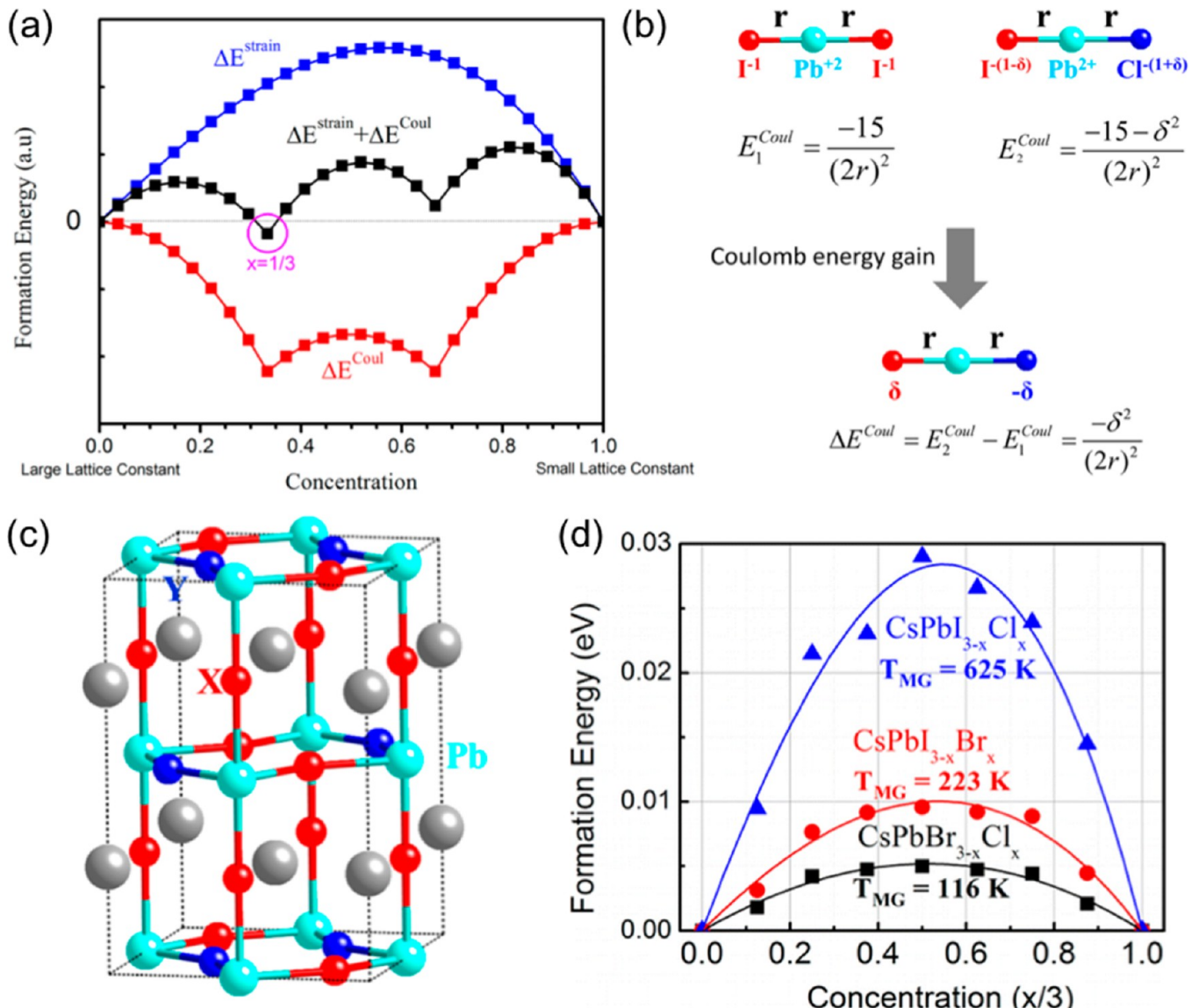


**Figure 20.** (a) Joint effects of strain (favoring demixing) and Coulomb (favoring mixing) energies for describing the formation energies of  $\text{CsPb}(\text{X}_{1-x}\text{Y}_x)_3$  ( $\text{X},\text{Y} = \text{I}, \text{Br}, \text{Cl}$ ). This purely physical models lead the lowest energy at  $x = 1/3$ . (b) Model system ( $\text{I}-\text{Pb}-\text{Cl}$  trimer) shows the Coulomb energy gain process by charge transfer when halides are mixed. (c) Particular stable mixed-halide configuration for  $\text{CsPbX}_{3-x}\text{Y}_x$  ( $\text{X},\text{Y} = \text{I}, \text{Br}, \text{Cl}$ ; atomic size of  $\text{X} > \text{Y}$ ) at  $x = 1$ . (d) Formation energies (per halogen atom) of  $\text{CsPb}(\text{X}_{1-x}\text{Y}_x)_3$  ( $\text{X},\text{Y} = \text{I}, \text{Br}, \text{Cl}$ ) alloys calculated based on special-quasirandom-structures (scattered points). The solid lines are fitting based on the nine different points per halogen atom. The miscibility gap temperatures ( $T_{\text{MG}}$ ) are indicated. Reprinted with permission from ref 250. Copyright 2014 American Chemical Society.

interactions play a major role. The Coulomb energy gain was identified to lower the overall formation energy (i.e., lower the strain energy) favoring certain stable ordered structures (Figure 20c). The authors gave a comprehensive example of a rigid ionic  $\text{I}-\text{Pb}-\text{I}$  trimer model (Figure 20b), where Pb and I have nominal 2+ and 1− oxidation states, respectively. In this case, Pb has Coulomb attraction with two I ions and two I ions have Coulomb repulsion between them, which equilibrates the entire system. Now, when one ion is replaced by a Cl ion, there will be electron transfer between I and Cl because the two ions have different electronegativities. Cl will be  $(1 + \delta)^-$  charged and I will be  $(1 - \delta)^-$  charged. As consequence, the total Coulomb energy (before and after) will be lowered by  $\delta^2/(2r)^2$  (Figure 20b). The schematic shapes of Coulomb energy gain are shown in Figure 20a. The alloy system has the largest Coulomb energy

gain at  $x = 1/3$ . As described at the beginning of section 3.5, experimental reports by Sutton et al.<sup>98</sup> and Beal et al.<sup>250</sup> seem to confirm this prediction, where  $\text{CsPbI}_2\text{Br}$  was demonstrated to show enhanced thermal and air stability. Yin et al.<sup>250</sup> calculated the miscibility gap temperature ( $T_{\text{MG}}$ ), which is defined as critical temperature that alloys can be fully mixed based on special-quasirandom-structures (Figure 20d). MGs of 625, 223, and 116 K were extracted for  $\text{CsPbI}_{3-x}\text{Cl}_x$ ,  $\text{CsPbI}_{3-x}\text{Br}_x$ , and  $\text{CsPbBr}_{3-x}\text{Cl}_x$ , respectively. These indicate that mixed-(Br/I) and (Br/Cl) are easily formed, whereas mixed-(Cl/I) perovskites are difficult to be formed.

#### 4. SIMULTANEOUS MIXED A-CATIONS AND MIXED X-HALIDE ANIONS

In the following sections, we continue to describe the more complex mixed-perovskite systems where the double (MA/

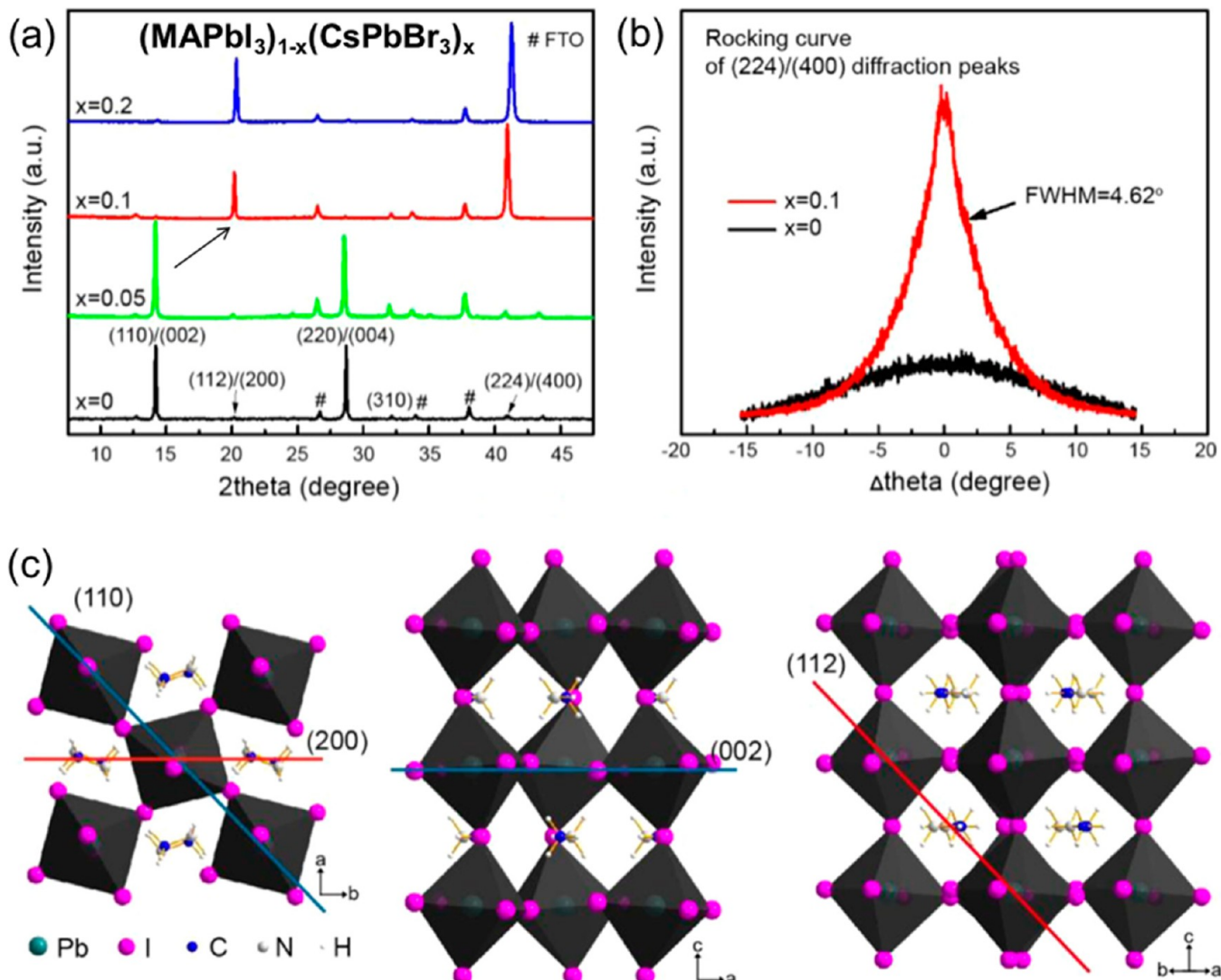


**Figure 21.** (a) XRD patterns of  $(\text{MAPbI}_3)_{1-x}(\text{CsPbBr}_3)_x$  with  $x$  ranging from 0 to 0.2. (b) Rocking curve measurement of (224)/(400) diffraction peaks for  $x = 0$  and 0.1. (c) Schematic illustrations of (110), (002), (112), and (200) perovskite crystal planes. Reprinted with permission from ref 123. Copyright 2016 Elsevier Ltd.

1037 FA),<sup>63,64,90,125–129,136,259</sup> ( $\text{Cs/MA}$ ),<sup>123</sup> ( $\text{Cs/}$   
1038 FA),<sup>117,132–134,260,261</sup> triple ( $\text{Cs/FA/MA}$ ),<sup>65,135,262</sup> and even  
1039 quadrupole ( $\text{Rb/Cs/FA/MA}$ ) mixed cations,<sup>7,137</sup> are generally  
1040 followed by the mixed ( $\text{I/Br}$ ), e.g., ( $\text{Rb/Cs/FA/MA}\text{Pb(I/Br)}$ ).  
1041 These newly developed material systems were reported to show  
1042 even higher stability<sup>137</sup> and efficiencies as shown in the plot of  
1043 certified efficiencies (Figure 1b).

1044 **4.1. (MA/Cs)Pb(I/Br) System.** Niu et al.<sup>123</sup> reported for the  
1045 first time on the synthesis of  $(\text{MAPbI}_3)_{1-x}(\text{CsPbBr}_3)_x$  by a one-  
1046 step method dissolving MAI,  $\text{PbI}_2$ , CsBr,  $\text{PbBr}_2$  precursors in a  
1047 mixed solvent of  $\gamma$ -butyrolactone:DMSO = 7:3 vol %. The  
1048 fabricated solar cells exhibited an optimal performance at  $x =$   
1049 0.1 with an average PCE of  $15.9 \pm 0.52\%$  (Table 1). The best  
1050 cell showed  $J_{sc} = 22.8 \text{ mA/cm}^2$ ,  $V_{oc} = 1.05 \text{ V}$ , FF = 73%, and  
1051 PCE = 17.6%. The stabilized power output (power output  
1052 measurement over time until a steady value is reached) of the  
1053 champion cell exhibited a PCE of 15.7% and photocurrent of  
1054 19.6  $\text{mA/cm}^2$ , which means hysteresis is present. Accelerated  
1055 stability of  $(\text{MAPbI}_3)_{1-x}(\text{CsPbBr}_3)_x$ -based solar cells was  
1056 evaluated under UV irradiation (365 nm, 364  $\text{mW/cm}^2$ )  
1057 without encapsulation. It was mentioned that as  $x$  increased, the

1058 stability was significantly increased. For  $(\text{MAPbI}_3)_{0.9}(\text{CsPbBr}_3)_{0.1}$ , 75% of the initial performance was  
1059 maintained after a total of 150 min irradiation. The same  
1060 authors performed shelf life stability tests of unencapsulated  
1061 ( $\text{MAPbI}_3)_{0.9}(\text{CsPbBr}_3)_{0.1}$  devices in ambient air (dark, 25 °C,  
1062 20–30% RH) and observed that nearly 80% of the initial  
1063 performance was maintained after 500 h.

1064 The same work by Niu et al.<sup>123</sup> touches upon an interesting  
1065 topic whether the photovoltaic efficiency is dependent on the  
1066 facet-orientation in single grains of perovskites. This topic was  
1067 discussed previously by Leblebici et al.<sup>263</sup> Generally,  $\text{MAPbI}_3$   
1068 and  $\text{MAPbI}_{3-x}\text{Cl}_x$  systems exhibit preferred orientation along  
1069  $\langle 110 \rangle$  and/or  $\langle 002 \rangle$  directions (see XRD pattern correspond-  
1070 ing to  $x = 0$  in Figure 21a). Interestingly, the (112) and (200)  
1071 facets increased in intensity substantially with  $(\text{CsPbBr}_3)_x$  ( $x =$   
1072 0.1 and 0.2) concentration (Figure 21a). The orientation of the  
1073 film can be further verified by rocking curve measurements  
1074 (Figure 21b), which provides information on the existence of  
1075 preferential growth axis and its spread on the azimuthal angle.  
1076 For  $x = 0.1$ , (224)/(400) planes were parallel to the substrate  
1077 with an angular spread of  $\pm 4.6^\circ$ ; meanwhile, for  $x = 0$ , no peaks  
1078

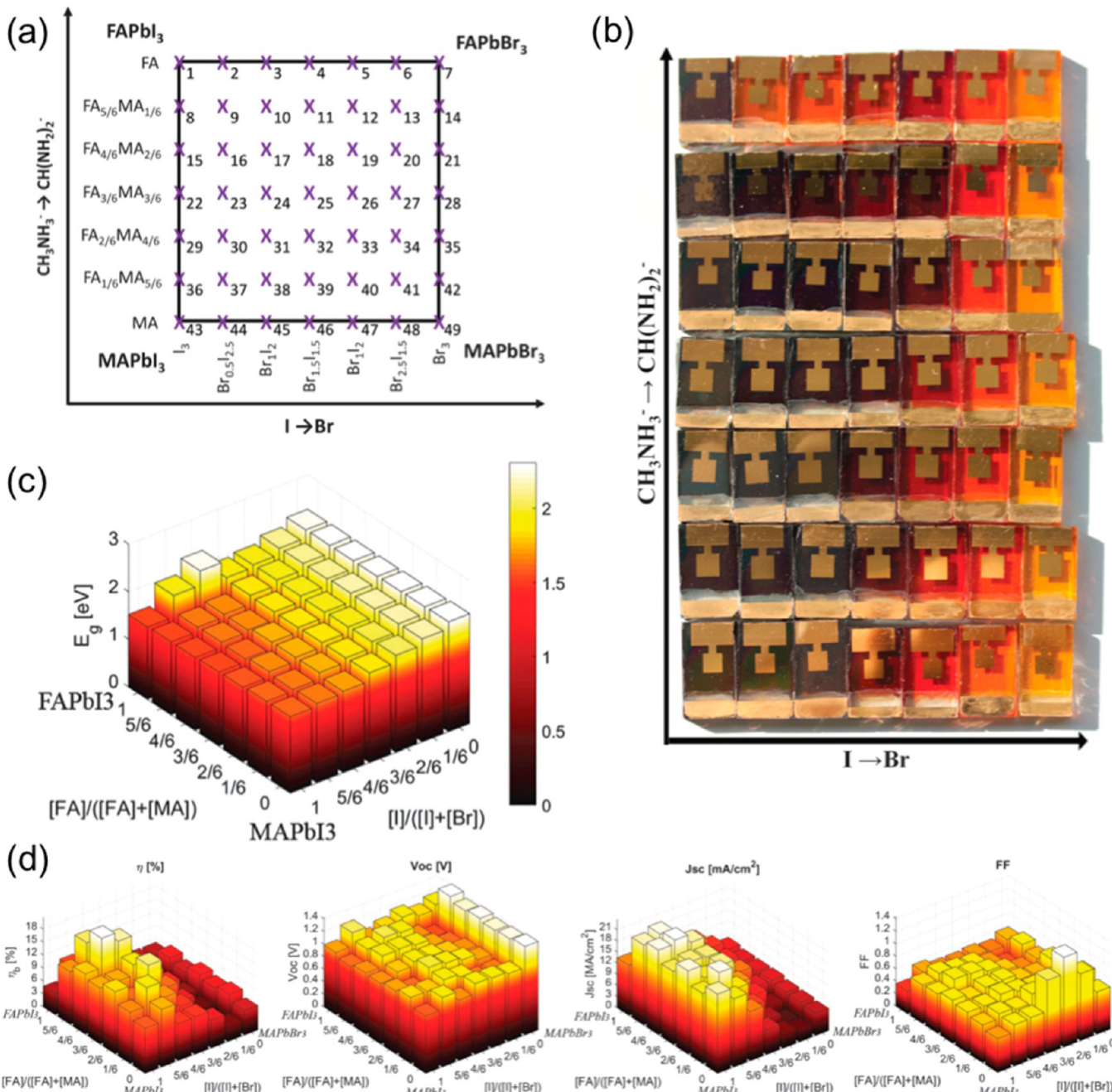


**Figure 22.** (a) Schematic illustration of the compositional matrix and (b) photo of fabricated cells of (FA/MA)Pb(I/Br) system. A total of 49 compositions were mapped. (c) Bar plot of the band gaps in the compositional space explored. (d) Solar cell device parameters for (FA/MA)Pb(I/Br)-based perovskite with different compositions. Reprinted with permission from ref 90. Copyright 2016 The Royal Society of Chemistry.

were observed. When  $x$  is increased to 0.3 and above, new peaks assigned to CsPb<sub>2</sub>Br<sub>5</sub> were observed in XRD, which indicates  $x = 0.2$  is a threshold limit for the full-miscibility in (MAPbI<sub>3</sub>)<sub>1-x</sub>(CsPbBr<sub>3</sub>)<sub>x</sub>. The origin for this preferential orientational growth was further examined employing XPS depth profile and DFT. Results from these measurements showed a heavily Cs-incorporated perovskite preferentially forms at the bottom layer. Based on DFT calculations of the CsPbBr<sub>3</sub> structure, it was shown that (100) ( $\gamma = 0.299$  J/m<sup>2</sup>) and (112) ( $\gamma = 0.314$  J/m<sup>2</sup>) planes showed a lower surface energy than the (110) ( $\gamma = 0.437$  J/m<sup>2</sup>) and (001) ( $\gamma = 0.526$  J/m<sup>2</sup>) planes. Therefore, it was concluded that the heavily Cs-incorporated perovskite at the bottom of the film could initiate

the film growth along the ⟨112⟩/⟨200⟩ directions under thermodynamic control (Figure 21c).

**4.2. (FA/MA)Pb(I/Br) System.** After the initial works by Jeon et al.<sup>63</sup> and Yang et al.,<sup>64</sup> the simultaneous FA/MA-cation mixed and I/Br-halide mixed perovskites are one of the most studied ternary mixed perovskite system for photovoltaic applications (Table 1).<sup>7,90,124–130,259,262,264–266</sup> Out of six, three certified efficiencies reported by NREL is based on this perovskite system (Figure 1b). Jacobsson et al.<sup>90</sup> provided the entire compositional space of MA-FA-Br-I experimentally (Figure 22). In this study, a total of 49 precursor solutions with varying concentrations of PbI<sub>2</sub>, PbBr<sub>2</sub>, MAI, MABr, FAI, and FABr were used for perovskite synthesis (Figure 22a). The

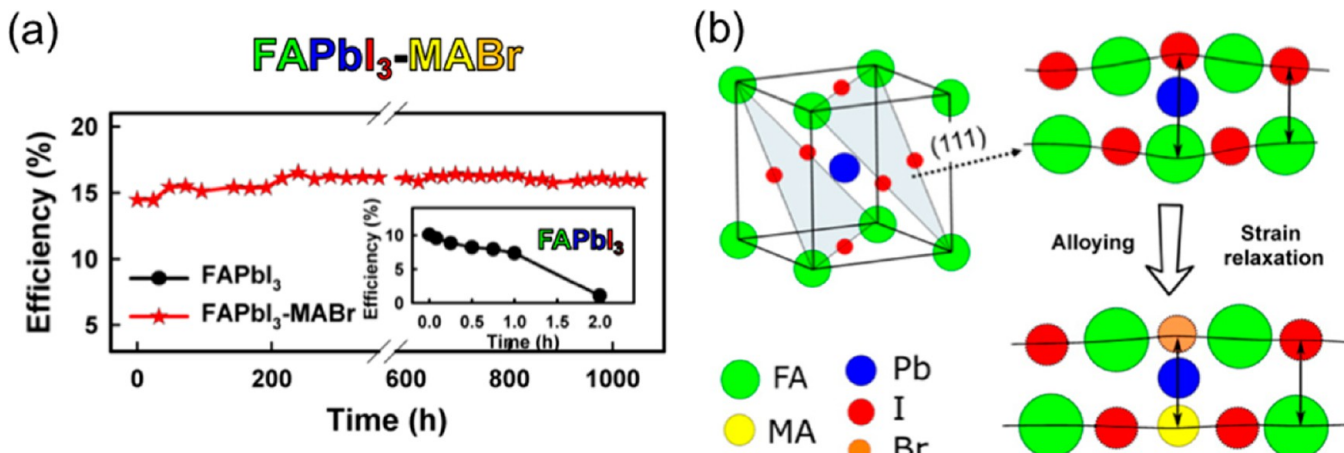


**Figure 23.** (a) Comparative PCEs of FAPbI<sub>3</sub>-MABr- and FAPbI<sub>3</sub>-based perovskite solar cells tested under storage conditions in air (~50% RH, 23 °C) without encapsulation. (b) Schematic illustration of strain relaxation when MABr is alloyed with FAPbI<sub>3</sub>. Reprinted with permission from ref 125. Copyright 2016 American Chemical Society.

1105 films were systematically characterized by UV-vis, PL, XRD  
1106 techniques. Differences in cation and halide compositions lead  
1107 to large variation in the optical appearance of deposited films  
1108 (Figure 22b,c). The distribution of extracted bandgaps in the  
1109 compositional matrix (Figure 22c) was fitted with an empirical  
1110 relation to provide a numerical description of the dependence  
1111 of band gap with respect to MA/FA and Br/I compositions (eq  
1112 4).

$$E_g(x, y) = 1.58 + 0.436x - 0.058y + 0.294x^2 \\ + 0.0199x \cdot y \quad (4)$$

$$x = \frac{[\text{Br}]}{[\text{Br}] + [\text{I}]} \text{ and } y = \frac{[\text{FA}]}{[\text{FA}] + [\text{MA}]}$$

1114 Similar to the description in section 3.2, PL measurements  
1115 revealed also the appearance of more than one peak for films  
1116 with 50% bromide or more, excluding the pure bromide  
1117 perovskites. The authors proposed two explanations, (i)  
1118 perovskites with a high bromide concentration increase the  
1119 density of trap states within the band gap that can act as  
1120 recombination centers and (ii) phase separation with the  
1121 formation of an iodine-rich domains leads to the peak at lower  
1122 photon energies in PL (section 3.2). XRD measurements  
1123 provide valuable experimental observations: (i) iodine-rich pure  
1124 FA-samples (numbers 2 and 3 in Figure 22a,b) deviate from  
1125 others and the dominant phase is not the photoactive  
1126 perovskites; (ii) Disregarding these two compositions and the  
1127 FAPbI<sub>3</sub> composition (due to yellow phase; number 1 in Figure  
1128 22a,b), all other intended perovskites were formed and were  
1129 the dominant phases; (iii) for compositions 1 to 38 (FA-rich  
1130 devices), the experimental XRD data are in line with a cubic  
1131 structure; (iv) it has been proposed that the transition border  
1132 between room temperature tetragonal and cubic structures is  
1133 found around FA<sub>1/6</sub>MA<sub>5/6</sub>PbBr<sub>1</sub>I<sub>2</sub> (number 38). Full solar cell  
1134 devices made with all 49 different compositions showed a  
1135 widespread with efficiencies varying from 2.3% to 20.67%  
1136 (Figure 22d). FA<sub>4/6</sub>MA<sub>2/6</sub>Pb(Br<sub>1</sub>I<sub>5/6</sub>)<sub>3</sub> (number 16) yielded  
1137 the best devices with a top efficiency of 20.67% ( $J_{sc} = 23.7 \text{ mA/cm}^2$ ,  
1138  $V_{oc} = 1.14 \text{ V}$ , FF = 76%, Table 1). This is in agreement  
1139 with other reports reporting high efficiencies around this  
1140 composition.<sup>63,130</sup> Hysteresis was also observed to vary as

1141 mapping the compositional space. Interestingly, a trend can be  
1142 observed that hysteresis is small for devices with a high fraction  
1143 of both iodide and FA, and is higher for bromide- and MA-rich  
1144 devices.<sup>90</sup> Ion migration on time scales from  $10^{-1}$  to  $10^2$  s was  
1145 previously reported to explain hysteresis.<sup>7,259</sup> Several reports  
1146 showed that regardless of solar cell architectures and  
1147 composition in perovskites, halide defects migrate and can  
1148 reversibly accumulate at the interfaces of selective contacts.  
1149 Furthermore, among several types of defects, iodide or bromide  
1150 vacancy generation has been calculated to show the lowest  
1151 formation energies (e.g., defects formed during sample  
1152 preparation, under bias, etc.), with further bromide vacancies  
1153 being favored over iodide.<sup>7,259</sup> Tress et al.<sup>266</sup> reported that  
1154 inverted hysteresis (forward bias scan generates higher PCE  
1155 than backward scan) is particularly pronounced in (FA/  
1156 MA)Pb(I/Br) systems. Zheng et al.<sup>125</sup> fabricated MAPbBr<sub>3</sub>-  
1157 alloyed FAPbI<sub>3</sub> perovskites and solar cells based on these  
1158 materials showed enhanced shelf life stability of more than  
1159 1000 h under ambient air (~50% RH, 23 °C) without  
1160 encapsulation (Figure 23a). Based on XRD, the authors  
1161 proposed a model that  $\alpha$ -FAPbI<sub>3</sub> has an anisotropic strained  
1162 lattice; higher strain in the (111) plane. In contrast,  $\delta$ -FAPbI<sub>3</sub> is  
1163 almost strain free explaining the favored  $\alpha \rightarrow \delta$  phase transition  
1164 at room temperature (section 2.1). They proposed that the  
1165 strain in the (111) plane of  $\alpha$ -phase is the driving force for the  
1166 phase transition to the  $\delta$ -phase (Figure 23b). When MABr is  
1167 incorporated to alloy with FAPbI<sub>3</sub>, the lattice size is reduced  
1168 and strain within the grain is relaxed. In this way, the  
1169 pseudocubic  $\alpha$ -phase is stabilized at room temperature and  
1170 even under humid air. In a recent report, Domanski et al.<sup>259</sup>  
1171 investigated the impacts of cation defects formation and  
1172 migration in the (FAPbI<sub>3</sub>)<sub>1-x</sub>(MAPbBr<sub>3</sub>)<sub>x</sub> perovskite on its  
1173 corresponding solar cell performance and long-term stability  
1174 under operation conditions. Maximum power output was  
1175 monitored for three identically prepared devices (A, B, C in  
1176 Figure 24a). Devices A and B were continuously tracked over  
1177 100 h. These two devices exhibit very different profiles from  
1178 that of device A showing high instability than that of device B.  
1179 Because long-term stability is reflected from a convolution of  
1180 several mechanisms (physicochemical and electrical) taking  
1181 place within the perovskite solar cell, it is not surprising that  
1182 identically prepared devices age differently. However, the  
1183 authors identified that the initial decay in performance  
1184

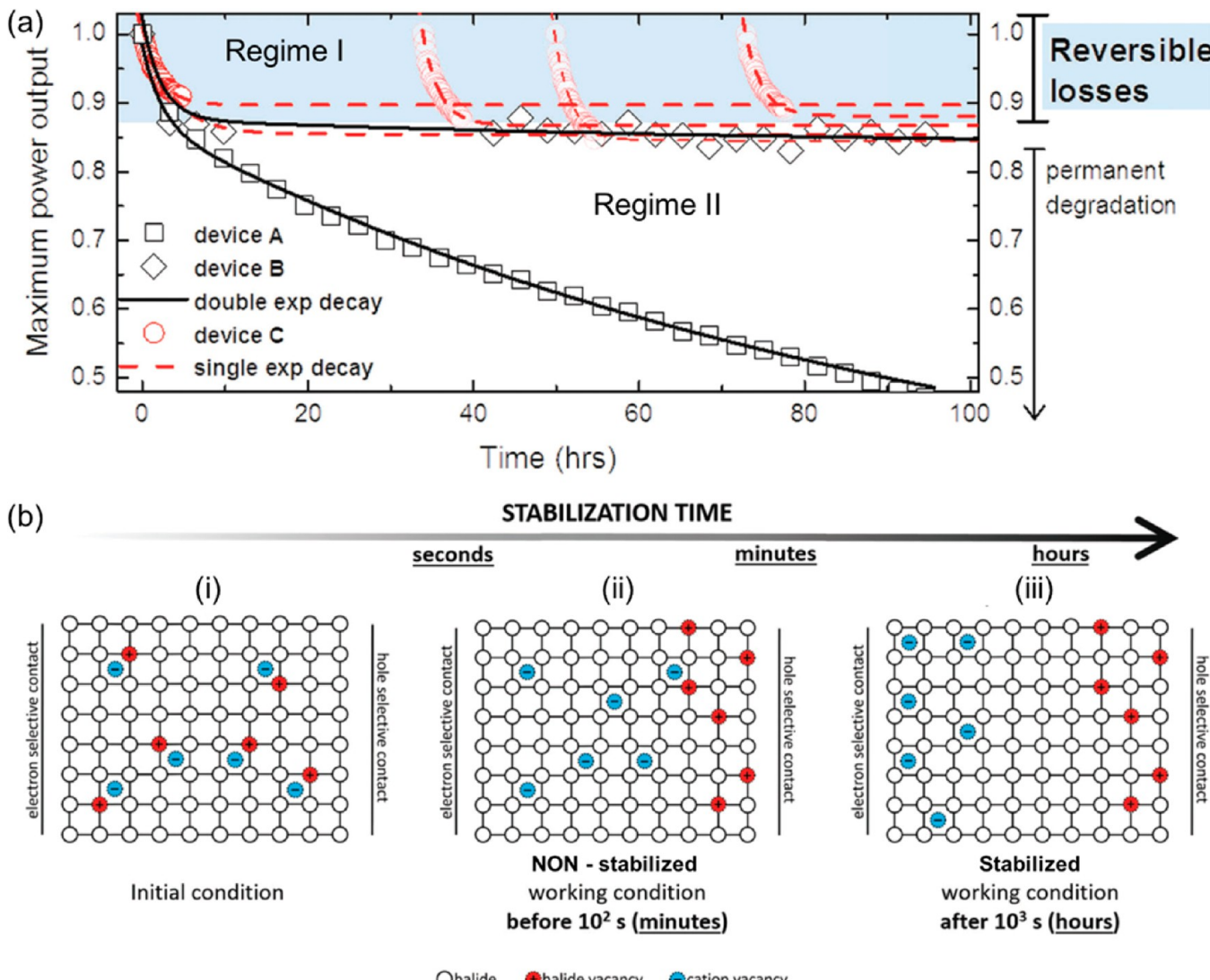


**Figure 24.** (a) Normalized maximum power output ( $V \sim 0.85$  V) tested in  $N_2$  environment for 3 identically prepared perovskite solar cells (devices A, B, C) measured under 1 sun. Devices A and B were continuously tracked for over 100 h. Device C was cyclically tracked 4 times for 5 h and it was left in dark at open circuit between consecutive measurements. (b) Schematic illustration showing the evolution of the ion distribution within the perovskite layer sandwiched between electron and hole selective contacts under working conditions on time scales from seconds to hours (i–iii). Reprinted with permission from ref 259. Copyright 2017 The Royal Society of Chemistry.

designated as regime I (Figure 24a) was unchanged. To isolate regime I from the subsequent degradation (regime II), the maximum power point for device C was stopped after only 5 h and repeated cyclically after resting the devices in dark for a different number of hours. Interestingly, the initial power output at each cycle was similar to the previous cycle, demonstrating that the initial performance losses are fully reversible (regime I) and can be separated from the subsequent permanent degradation (regime II). Degradation related to regime II (HTL, perovskite, top Au electrode related issues) was previously reported.<sup>65,267,268</sup> Followed by a subsequent series of experiments, the authors concluded that migration of cation vacancies form an additional Debye layer at the interface with the electron selective contact, which inhibits charge extraction (Figure 24b). However, when the device is given several hours of rest in dark, the ionic distribution equilibrates to the initial state, which leads to recovery of the initial performance (Regime I, Figure 24b). Migration of cation vacancies was shown to exhibit significantly longer time scales

( $>10^3$  s) than the halide vacancy migration (between  $10^{-1}$  and  $10^{2}$  s, Figure 24b).

**4.3. (FA/MA)Pb(I/Cl) System.** Mixed MA/FA cations and I/Cl halides perovskites with a chemical composition of  $MA_{1-x}FA_xPb(I_{1-y}Cl_y)_3$  were first synthesized by Isikgor et al.<sup>131</sup> These perovskite films were prepared by dissolving  $PbI_2 + PbCl_2$  and MAI + FAI precursors in a cosolvent of GBL/DMSO (3:7 vol. ratio) and low postannealing temperature of 80–110 °C to avoid chlorine species sublimate and/or decompose in the form of  $MACl$  (described in section 3.1). A planar heterojunction perovskite solar cell based on an inverted structure with ITO/PEDOT:PSS/MA<sub>0.80</sub>FA<sub>0.20</sub>PbI<sub>3-y</sub>Cl<sub>y</sub>/PC61BM/C60/LiF/Au generated average  $J_{sc} = 21.55 \pm 0.55$  mA/cm<sup>2</sup>,  $V_{oc} = 1.10 \pm 0.01$  V, FF = 75 ± 2%, and PCE = 17.45% (Table 1). This performance employing MA<sub>0.80</sub>FA<sub>0.20</sub>PbI<sub>3-y</sub>Cl<sub>y</sub> ( $E_g = 1.58$  eV) outperformed the control perovskite solar cells (MAPbI<sub>3</sub>, MAPbI<sub>3-y</sub>Cl<sub>y</sub>, MAPbI<sub>3-y</sub>Br<sub>y</sub>, and MA<sub>1-x</sub>FA<sub>x</sub>PbI<sub>3</sub>). The high photovoltaic performance was attributed mainly to (i) the long charge diffusion length

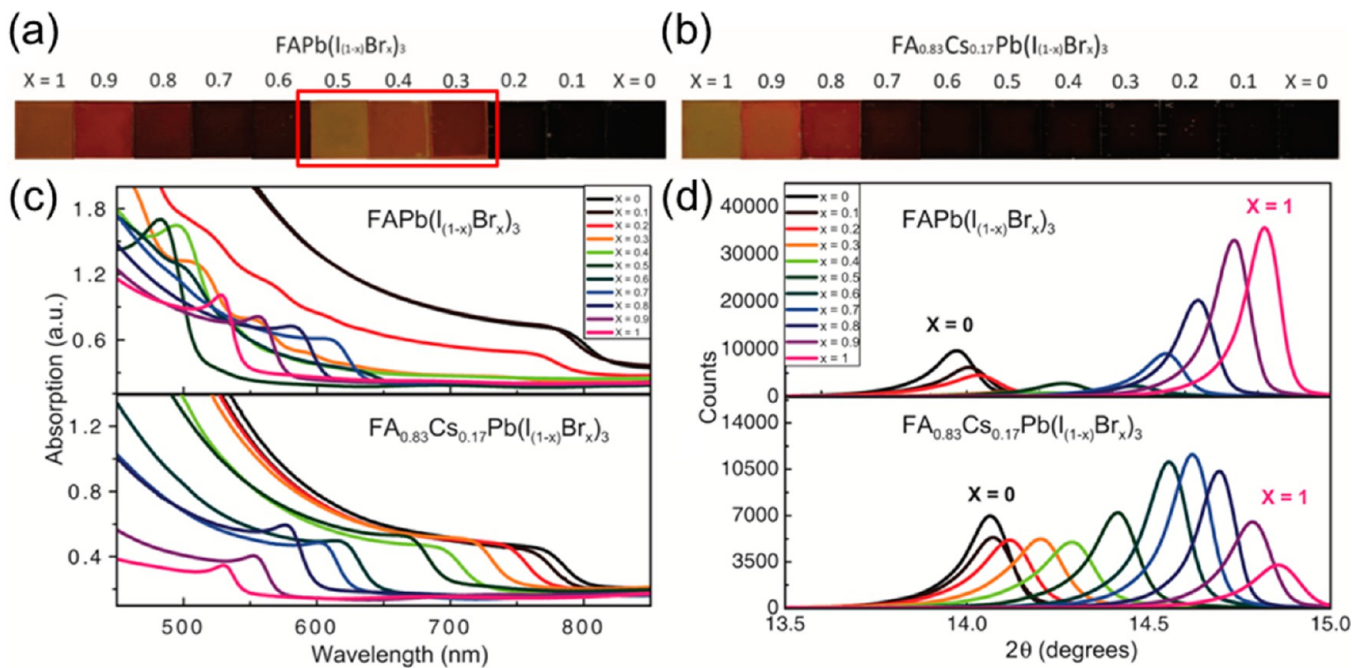


**Figure 25.** Photographs of (a) FAPb(I<sub>1-x</sub>Br<sub>x</sub>)<sub>3</sub> and (b) FA<sub>0.83</sub>Cs<sub>0.17</sub>Pb(I<sub>1-x</sub>Br<sub>x</sub>)<sub>3</sub> perovskite films with Br composition increasing from  $x = 0$  to 1. (c) UV-vis absorbance spectra and (d) XRD patterns of FAPb(I<sub>1-x</sub>Br<sub>x</sub>)<sub>3</sub> and FA<sub>0.83</sub>Cs<sub>0.17</sub>Pb(I<sub>1-x</sub>Br<sub>x</sub>)<sub>3</sub> perovskites. Reprinted with permission from ref 132. Copyright 2016 American Association for the Advancement of Science (AAAS).

1222 induced by mixed organic cations and mixed halides and (ii)  
1223 suppression of the formation of undesirable yellow  $\delta$ -phase of  
1224 FAPbI<sub>3</sub> ( $E_g = 2.8$  eV).

1225 **4.4. (FA/Cs)Pb(I/Br) System.** With the aim to fabricate  
1226 perovskite/silicon tandem solar cells, a number of reports  
1227 synthesized mixed-cations and mixed-halides (i) to achieve high  
1228 stability and (ii) to tune the band gap to an optimal value of  
1229  $\sim 1.75$  eV in order to current-match the top perovskite cell and  
1230 bottom Si cell ( $E_g = 1.1$  eV).<sup>132,133,269</sup> Based on the  
1231 observations reported previously for binary mixed perovskites,  
1232 (i) MAPb(I/Br) (section 3.2) is thermally unstable and suffers  
1233 from halide segregation; (ii) FAPb(I/Br) shows better stability  
1234 regarding halide segregation (section 3.2) and Br concentration  
1235 helps tune the band gap to a desired value ( $\sim 1.75$  eV); (iii)  
1236 FAPb(I<sub>1-x</sub>Br<sub>x</sub>)<sub>3</sub> with  $0.3 < x < 0.6$ , an amorphous unstable  
1237 phase is formed caused by a transition from a trigonal ( $x < 0.3$ )  
1238 and cubic ( $x > 0.5$ ) (Figure 25a); therefore, this composition  
1239 range should be avoided (section 3.2); (iv) mixing small  
1240 quantities of Cs with FA substantially enhances the stability of  
1241 Cs<sub>x</sub>FA<sub>1-x</sub>PbI<sub>3</sub> suppressing halide segregation (section 2.3); (iv)  
1242 the  $\delta \rightarrow \alpha$  phase transformation in FAPbI<sub>3</sub> can be lowered down  
1243 to room temperature when Cs/FA ratio of 45 at. % is  
1244 incorporated in the Cs<sub>x</sub>FA<sub>1-x</sub>PbI<sub>3</sub> (section 2.3), McMeekin et  
1245 al.<sup>132</sup> proposed the first FA<sub>y</sub>Cs<sub>1-y</sub>Pb(I<sub>1-x</sub>Br<sub>x</sub>)<sub>3</sub> system based on  
1246 FAI, CsI, PbBr<sub>2</sub>, and PbI<sub>2</sub> precursors dissolved in DMF  
1247 followed by addition of HI and HBr. Initially, they  
1248 hypothesized that if FA is partially substituted by Cs, the  
1249 structural instability in Br-to-I phase space could be shifted to  
1250 higher energies, and thus achieve a structurally stable mixed  
1251 halide perovskite with a band gap of 1.75 eV. Their trial with  
1252 FA<sub>0.83</sub>Cs<sub>0.17</sub>Pb(I<sub>1-x</sub>Br<sub>x</sub>)<sub>3</sub> showed unexpected results that the  
1253 region of structural instability was not observed (Figure 25b).  
1254 Instead, a continuous series of dark films throughout the entire  
1255 composition range ( $0 \leq x \leq 1$ ) was observed and corroborated  
1256 by UV-vis (Figure 25c) and XRD (Figure 25d) measurements.  
1257 Over the entire of Br-to-I range, FA<sub>0.83</sub>Cs<sub>0.17</sub>Pb(I<sub>0.6</sub>Br<sub>0.4</sub>)<sub>3</sub>

1258 composition was chosen based on the Vergard's law (section 1258  
1259 3.2) leading to the band gap of 1.74 eV. These perovskites 1259  
1260 showed further improved structural stability and resistance to 1260  
1261 halide segregation when compared to MAPb(I<sub>0.6</sub>Br<sub>0.4</sub>)<sub>3</sub> (section 1261  
1262 3.2). Furthermore, under thermal stress conditions at 130 °C, 1262  
1263 FA<sub>0.83</sub>Cs<sub>0.17</sub>Pb(I<sub>1-x</sub>Br<sub>x</sub>)<sub>3</sub> showed superior stability compared to 1263  
1264 MAPb(I<sub>0.6</sub>Br<sub>0.4</sub>).<sup>132</sup> Planar heterojunction perovskite solar cell 1264  
1265 based on an inverted structure with FTO/SnO<sub>2</sub>/PC60BM/ 1265  
1266 FA<sub>0.83</sub>Cs<sub>0.17</sub>Pb(I<sub>0.6</sub>Br<sub>0.4</sub>)<sub>3</sub>/spiro-MeOTAD/Ag generated  $J_{sc} =$  1266  
1267 19.4 mA/cm<sup>2</sup>,  $V_{oc} = 1.2$  V, FF = 75.1%, and PCE = 17.1% 1267  
1268 (Table 1). When combined with a 19% PCE c-Si, the feasibility 1268  
1269 of achieving >25% PC four-terminal tandem cells were 1269  
1270 demonstrated.<sup>132</sup> Employing the same FA<sub>0.83</sub>Cs<sub>0.17</sub>Pb(I<sub>0.6</sub>Br<sub>0.4</sub>)<sub>3</sub> 1270  
1271 perovskite, Busch et al.<sup>133</sup> demonstrated a two-terminal 1 cm<sup>2</sup> 1271  
1272 active area perovskite/tandem solar cell with  $J_{sc} = 18.1$  mA/ 1272  
1273 cm<sup>2</sup>,  $V_{oc} = 1.65$  V, FF = 79%, and PCE = 23.6%. More recently, 1273  
1274 Zhang et al.<sup>269</sup> performed DFT calculations determining three 1274  
1275 sets of  $x$  and  $y$  for FA<sub>y</sub>Cs<sub>1-y</sub>Pb(I<sub>1-x</sub>Br<sub>x</sub>)<sub>3</sub> systems, which have 1275  
1276 band gap around 1.75 eV. In addition, their refractive indices 1276  
1277 and extinction coefficients were also calculated. They found 1277  
1278 that FA<sub>0.89</sub>Cs<sub>0.11</sub>Pb(I<sub>0.56</sub>Br<sub>0.44</sub>)<sub>3</sub>/c-Si tandem solar cells achieved 1278  
1279 the highest PCE among the three sets. The concept of 1279  
1280 perovskite-perovskite tandem cell employing 1280  
1281 FA<sub>0.75</sub>Cs<sub>0.25</sub>Sn<sub>0.5</sub>Pb<sub>0.5</sub>I<sub>3</sub>/FA<sub>0.83</sub>Cs<sub>0.17</sub>Pb(I<sub>0.6</sub>Br<sub>0.4</sub>)<sub>3</sub> with band 1281  
1282 gaps of 1.2 and 1.74 eV, respectively, was demonstrated to 1282  
1283 generate PCE as high as 20.3% in a four-terminal configuration.<sup>1283</sup>

1284 Perovskite single-junction solar cells with regular structure 1284  
1285 (TiO<sub>2</sub> electron transport layer (ETL) and spiro-MeOTAD 1285  
1286 HTL) based on similar FA<sub>0.8</sub>Cs<sub>0.2</sub>PbI<sub>2.84</sub>Br<sub>0.16</sub> composition, 1286  
1287 generated  $J_{sc} = 23.3$  mA/cm<sup>2</sup>,  $V_{oc} = 1.072$  V, FF = 72.3%, and 1287  
1288 PCE = 18.02%. A wider parameter space of the influences of 1288  
1289 mixed-cation and mixed-halide perovskites in Cs<sub>y</sub>FA<sub>1-y</sub>Pb- 1289  
1290 (I<sub>1-x</sub>Br<sub>x</sub>)<sub>3</sub> was studied by Rehman et al.<sup>261</sup> They showed that a 1290  
1291 region for Cs concentration between  $0.10 < y < 0.30$  leads to 1291  
1292 high crystalline quality, long charge-carrier lifetimes, and high 1292  
1293 charge-carrier mobilities. Within the Cs<sub>y</sub>FA<sub>1-y</sub>Pb(I<sub>0.4</sub>Br<sub>0.6</sub>)<sub>3</sub> 1293

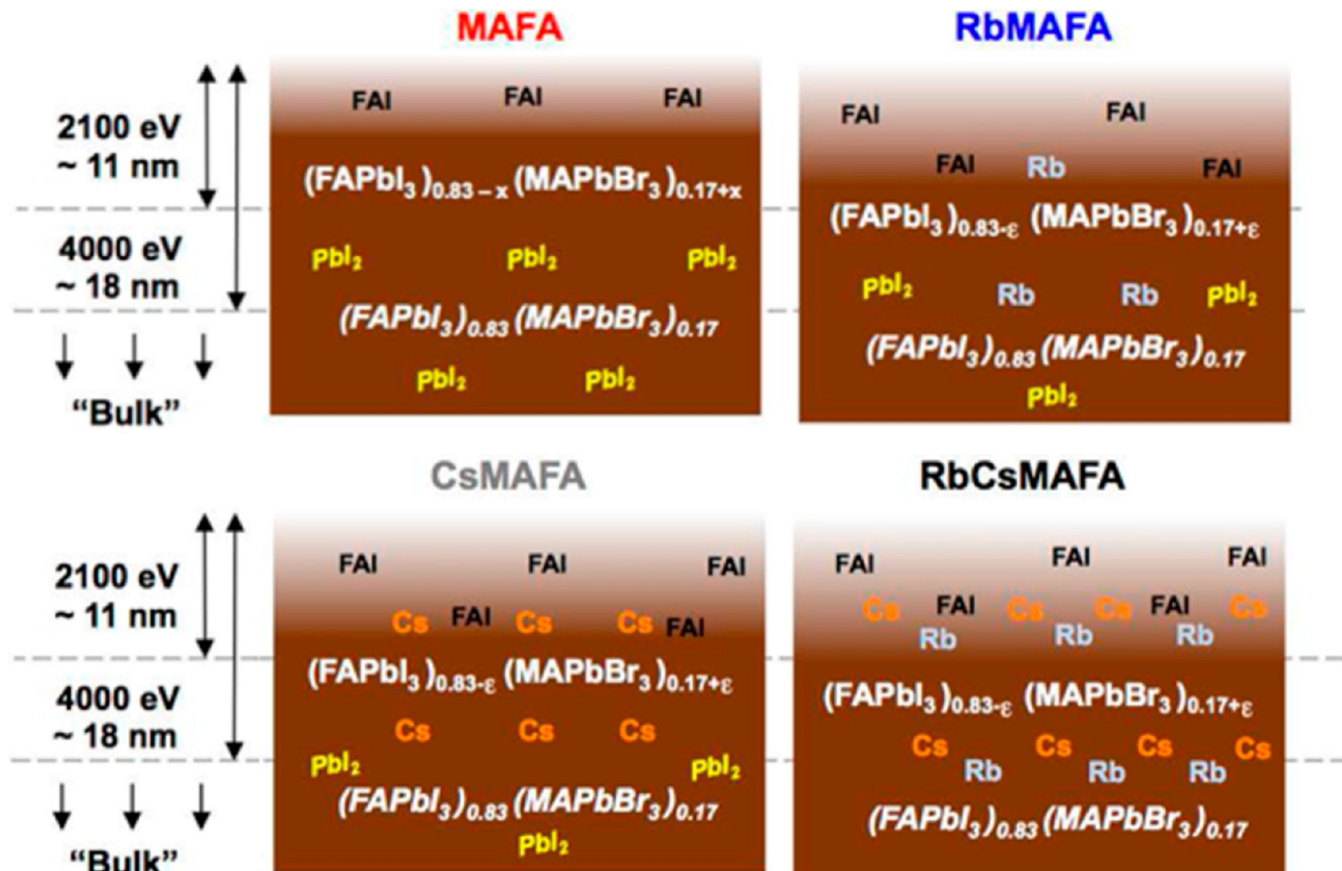


**Figure 26.** Schematic illustration of a depth-dependent chemical composition in MAFA =  $(MA_{0.17}FA_{0.83})Pb(I_{0.83}Br_{0.17})_3$ , 0.1[0.83PbI<sub>2</sub>, 0.17PbBr<sub>2</sub>]; RbMAFA = 0.05RbI[(MA<sub>0.17</sub>FA<sub>0.83</sub>)Pb(I<sub>0.83</sub>Br<sub>0.17</sub>)<sub>3</sub>, 0.1[0.83PbI<sub>2</sub>, 0.17PbBr<sub>2</sub>]]<sub>0.95</sub>; CsMAFA = 0.05CsI[(MA<sub>0.17</sub>FA<sub>0.83</sub>)Pb(I<sub>0.83</sub>Br<sub>0.17</sub>)<sub>3</sub>, 0.1[0.83PbI<sub>2</sub>, 0.17PbBr<sub>2</sub>]]<sub>0.95</sub>; RbCsMAFA = 0.05RbI[0.05CsI[(MA<sub>0.17</sub>FA<sub>0.83</sub>)Pb(I<sub>0.83</sub>Br<sub>0.17</sub>)<sub>3</sub>, 0.1[0.83PbI<sub>2</sub>, 0.17PbBr<sub>2</sub>]]<sub>0.95</sub>]<sub>0.95</sub>. The chemical formulae are based on the precursor solution composition. A nonstoichiometric solution was used in excess of 10 mol % lead precursors leading to the nominal composition of MAFA stated above. Reprinted with permission from ref 270. Copyright 2017 American Chemical Society.

series,  $y = 0.2$  showed the concentration leading the perovskite film exhibiting high charge-carrier mobilities of  $\sim 18 \text{ cm}^2 \cdot \text{V}^{-1} \cdot \text{s}^{-1}$  and charge-carrier lifetimes of  $\sim 80 \text{ ns}$ . They demonstrated a correlation between high crystallinity and suppressed photo-induced halide segregation, i.e., short-range crystalline order or the presence of grain boundaries enables halide segregation by releasing lattice strain energy leading to iodide-rich and bromide-rich domains (section 3.2). Next, the halide-parameter space was investigated for  $Cs_{0.17}FA_{0.83}Pb(I_{1-x}Br_x)_3$ . They showed that once the perovskite contains enough fraction of Cs for the stability, high charge-carrier mobilities and diffusion lengths are obtained across the full I:Br range. Furthermore, the band gap varies linearly with the Vegard's law (section 3.2) across the full I:Br range.<sup>261</sup> Nonencapsulated  $Cs_{0.17}FA_{0.83}Pb(I_{0.6}Br_{0.4})$ -based perovskite solar cells employing *n*-doped C60 as electron extraction layer in a planar heterojunction architecture, showed a 30-fold enhanced air stability compared to MAPbI<sub>3-x</sub>Cl<sub>x</sub>-based devices under full spectrum solar illumination without encapsulation ( $t_{80} \sim 600 \text{ h}$ ); and  $t_{80} > 3420 \text{ h}$  when sealed.<sup>134</sup>

**4.5. (Cs/FA/MA)Pb(I/Br) System.** Based on previous successful reports of Cs incorporation in (MA/Cs)PbI<sub>3</sub> and (FA/Cs)PbI<sub>3</sub> systems (sections 2.2 and 2.3), Saliba et al.<sup>65</sup> (a follow up work from the same group was reported by Matsui et al.<sup>135</sup>) reported on the first triple cation mixed (Cs/FA/MA)Pb(I/Br) system generating stabilized power output of 21.1% that also holds a position in the certified NREL chart

(Figure 1b). The stability of these devices was tested in a nitrogen atmosphere held at room temperature under constant illumination and maximum power tracking for 250 h. The device efficiencies of triple cation perovskites with FTO/c-TiO<sub>2</sub>/mp-TiO<sub>2</sub>/Cs<sub>0.05</sub>(FA<sub>0.83</sub>MA<sub>0.17</sub>)<sub>0.95</sub>Pb(I<sub>0.83</sub>Br<sub>0.17</sub>)<sub>3</sub>/spiro-MeOTAD/Au structure decayed from  $\sim 20\%$  to  $\sim 18\%$  within a few hours (Regime I,<sup>259</sup> section 4.2) and then stayed stable for at least 250 h.

**4.6. (Rb/FA/MA)Pb(I/Br) System.** Duong et al.<sup>136</sup> and Zhang et al.<sup>122</sup> studied the incorporation of Rb in high performing (FAPbI<sub>3</sub>)<sub>1-x</sub>(MAPbBr<sub>3</sub>)<sub>x</sub> mixed perovskites. The motivation for studying this system was that inclusion of a smaller cation of Cs in (FAPbI<sub>3</sub>)<sub>1-x</sub>(MAPbBr<sub>3</sub>)<sub>x</sub> lead to enhanced stability (section 4.5). Therefore, the incorporation of an even smaller cation would be interesting to be tested. The addition of 5% RbI in combination with excess PbI<sub>2</sub> was observed to eliminate the formation of yellow nonperovskite phase and enhance the crystallinity of the films. However, inclusion of more than 10% RbI resulted in the formation of a Rb-rich phase, which was detrimental for the cell performance.<sup>136</sup> A side-by-side comparison of solar cell devices based on Rb<sub>0.05</sub>F<sub>A</sub><sub>0.80</sub>M<sub>A</sub><sub>0.15</sub>P<sub>b</sub>I<sub>2.55</sub>B<sub>r</sub><sub>0.45</sub> and Cs<sub>0.05</sub>F<sub>A</sub><sub>0.80</sub>M<sub>A</sub><sub>0.15</sub>P<sub>b</sub>I<sub>2.55</sub>B<sub>r</sub><sub>0.45</sub> showed very similar performances (PCE  $\sim 19.5\%$ , Table 1).

**4.7. (Rb/Cs/FA)Pb(I/Br) System.** Syzgantseva et al.<sup>157</sup> reported theoretical calculations on the stabilization of FAPbI<sub>3</sub> by Cs/Rb incorporations. Enhanced stabilization of mixed

1348 perovskites was demonstrated when  $\text{Cs}^+$  and  $\text{Rb}^+$  are employed  
 1349 instead of  $\text{MA}^+$ . In addition, the increased phase stability of  $\text{Cs}^+$   
 1350 and  $\text{Rb}^+$  incorporated systems comes with only a slight increase  
 1351 in the band gap. Saliba et al.<sup>137</sup> fabricated systematically  
 1352  $\text{Rb}_{0.05}\text{Cs}_{0.05}\text{FA}_{0.90}\text{Pb}(\text{I}_{0.83}\text{Br}_{0.17})_3^-$ ,  $\text{Rb}_{0.05}\text{Cs}_{0.10}\text{FA}_{0.85}\text{Pb}(\text{I}_{0.83}\text{Br}_{0.17})_3^-$ ,  
 1353 and  $\text{Rb}_{0.10}\text{Cs}_{0.05}\text{FA}_{0.85}\text{Pb}(\text{I}_{0.83}\text{Br}_{0.17})_3^-$ -based solar  
 1354 cells showing efficiencies as high as 18.3%, 19.3%, and 18.7%,  
 1355 respectively (Table 1).

1356 **4.8. (Rb/Cs/FA/MA)Pb(I/Br) System.** Based on their past  
 1357 experience with binary and triply mixed cations ( $\text{RbFA}$ ,  
 1358  $\text{RbCsFA}$ ,  $\text{RbMAFA}$ ), Saliba et al.<sup>137</sup> were able to synthesize  
 1359 the first perovskite containing four simultaneous cations  
 1360 ( $\text{RbCsFAMA}$ ). The concentration of Rb was limited to 5 at.  
 1361 % as they were aware that a higher concentration of Rb will lead  
 1362 to the formation of a Rb-rich phase, which is detrimental for the  
 1363 performance (section 2.4). Devices with the architecture of  
 1364 FTO/c-TiO<sub>2</sub>/mp-TiO<sub>2</sub>/Rb<sub>0.05</sub>Cs<sub>0.05</sub>(FA<sub>0.83</sub>MA<sub>0.17</sub>)<sub>0.90</sub>Pb-  
 1365 ( $\text{I}_{0.83}\text{Br}_{0.17})_3^-$ /PTAA/Au generated stabilized efficiencies of up to  
 1366 21.6% (averaged PCE was 20.2%, Table 1). Furthermore,  
 1367 PTAA was employed as hole transport layer (HTL) and these  
 1368 cells maintained ~95% of their initial performance when tested  
 1369 in N<sub>2</sub> atmosphere, but at elevated temperature of 85 °C for 500  
 1370 h and under operation conditions (full illumination and  
 1371 tracking the maximum power point). Similar high stability  
 1372 was also confirmed by Duong et al.<sup>138</sup> fabricating FTO/c-TiO<sub>2</sub>/  
 1373 mp-TiO<sub>2</sub>/Rb(5%) doped FA<sub>0.75</sub>(MA<sub>0.6</sub>Cs<sub>0.4</sub>)<sub>0.25</sub>PbI<sub>2</sub>Br/PTAA/  
 1374 Au, which generated stabilized power output of ~17.4% (Table  
 1375 1). The long-term high stability under illumination indicates  
 1376 that phase segregation in iodide- and bromide-rich domains  
 1377 phenomena (section 3.2) is significantly suppressed upon this  
 1378 cation engineering strategy.<sup>137,138</sup> The charge transport within  
 1379 the RbCsMAFA perovskite layer is substantially faster than in  
 1380 CsMAFA, which is already much faster than in MAFA leading  
 1381 to the conclusion that Rb incorporation leads to defect-free  
 1382 perovskites.<sup>132</sup>

1383 Although these studies seem to infer a uniform solid solution,  
 1384 there is no clear evidence supporting that these cations are  
 1385 incorporated into the perovskite crystal structure forming a  
 1386 uniform solid solution. Recently, Philippe et al.<sup>270</sup> reported a  
 1387 depth-dependent chemical composition in (Rb/Cs/FA/MA)-  
 1388 Pb(I/Br) perovskite films employing hard X-ray photoelectron  
 1389 spectroscopy (HAXPS, synchrotron radiation source). These  
 1390 results were compared systematically with perovskite materials  
 1391 with two (MA/FA) and three cations (CsMAFA and  
 1392 RbMAFA) to investigate the role of Cs and Rb cations. Two  
 1393 photon energies were employed, with the photon energy of  
 1394 2100 eV to probe the surface of the sample (~11 nm) and the  
 1395 photon energy of 4000 eV to probe deeper (~18 nm; referred  
 1396 as bulk chemical composition). Quantifications were conducted  
 1397 for both photon energies and the I/Pb, Cs/Pb, and Rb/Pb  
 1398 ratios and its interpretation were summarized in Figure 26. For  
 1399 example, the Br/Pb and I/Br ration correspond to the  
 1400 proportion of FA and MA. In the case of MAFA sample that  
 1401 is generally prepared with excess of PbI<sub>2</sub>, HAXPS (4000 eV)  
 1402 confirms that the excessive PbI<sub>2</sub> can be found in the bulk of the  
 1403 material. Upon addition of a third cation ( $\text{Cs}^+$  or  $\text{Rb}^+$ ), less PbI<sub>2</sub>  
 1404 remains in the material. When the probe depth decreases, an  
 1405 increase of Br over Pb was observed indicating a slight bromide  
 1406 enrichment within the surface as compared to bulk as illustrate  
 1407 with  $(\text{MAPbBr}_3)_{0.17+\epsilon}(\text{FAPbI}_3)_{0.83-\epsilon}$ . This slight MAPbBr<sub>3</sub>  
 1408 enrichment in the surface was assigned to the presence of  
 1409 unreacted FAI at the surface and PbI<sub>2</sub> in the bulk leading to  
 1410 deficiency in FAPbI<sub>3</sub>. In the RbMAFA sample, only 2% and 1%

1411 were detected at 4000 and 2100 eV, respectively, suggesting  
 1412 that Rb was mainly located in the bulk, but observed to easily  
 1413 migrate to the surface due to its small ionic radius. For the  
 1414 CsMAFA sample, ~6% detected Cs was found to distribute  
 1415 uniformly at both depths. Interestingly, the RbCsMAFA sample  
 1416 did not correspond to a simple superposition of RbMAFA and  
 1417 CsMAFA samples. Both Cs and Rb distributions were  
 1418 homogeneous over the ~18 nm indicating that Rb<sup>+</sup> and Cs<sup>+</sup>  
 1419 alkali metals act jointly in a way that Cs helps the incorporation  
 1420 of Rb into the perovskite compound.<sup>270</sup> This is also in good  
 1421 agreement with recent theoretical calculations by Syzgantseva  
 1422 et al.<sup>157</sup> reporting that doping by a mixture of Cs and Rb has a  
 1423 synergistic effect on perovskite stabilization.  
 1423

## 5. SUMMARY AND OUTLOOK

1424 The exceptional performance of perovskites as light harvester  
 1425 materials for solar cells are ascribed to excellent material  
 1426 properties such as direct band gap, outstanding high absorption  
 1427 coefficient, abrupt optical band edge, large charge carrier  
 1428 diffusion length and low exciton binding energy. The earlier  
 1429 works focused on MAPbI<sub>3</sub> ( $E_g \sim 1.5\text{--}1.61$  eV, section 1),  $\alpha$ -  
 1430 FAPbI<sub>3</sub> ( $E_g \sim 1.47\text{--}1.55$  eV, section 2.1), and  $\alpha$ -CsPbI<sub>3</sub> ( $E_g \sim$   
 1431 1.67–1.73 eV, section 2.3) with preference for FAPbI<sub>3</sub> because  
 1432 of its smaller band gap. The optimal  $E_g$  for a single-junction  
 1433 solar cell is between 1.1 and 1.4 eV according to the Shockley–  
 1434 Queisser limit<sup>91</sup> and therefore there is still plenty of room for  
 1435 improvement to achieve even higher efficiencies. So far, the  
 1436 highest PCE of pure MAPbI<sub>3</sub>-based solar cell was reported to  
 1437 reach ~18–20%.<sup>139,140</sup> As a comparison, the best PCE reported  
 1438 for pure FAPbI<sub>3</sub>-based perovskite solar cell reached 13.5–  
 1439 18%,<sup>64,99,142–144</sup> which is somewhat lower than MAPbI<sub>3</sub> (see  
 1440 section 2.1 for more details). CsPbI<sub>3</sub>-based perovskite solar cell  
 1441 exhibited limited PCEs of <2.9% (section 2.3).<sup>115,155,156</sup> Despite high efficiencies of MAPbI<sub>3</sub>- and FAPbI<sub>3</sub>-based solar  
 1442 cells, these simple hybrid perovskite materials fail to meet the  
 1443 required long-term stability under working conditions (e.g.,  
 1444 when tracking the maximum power point (MPP) voltage under  
 1445 continuous light illumination), which is the main obstacle for  
 1446 this technology to reach commercialization.  
 1447

1448 The fundamental origins for the major PCE loss during solar  
 1449 cell operation includes (i) thermal, moisture, oxygen, bias, and  
 1450 light induced permanent degradation leading to PbI<sub>2</sub> and I-  
 1451 containing volatile species<sup>28,29,37,92,93,271,272</sup> and (ii) poly-  
 1452 morphism of  $\alpha,\delta$ -FAPbI<sub>3</sub> in ambient conditions (section 2.1  
 1453 and Figure 3b–d). At room temperature, FAPbI<sub>3</sub> preferentially  
 1454 crystallizes to the  $\delta$ -FAPbI<sub>3</sub>, which possess a high  $E_g$  (~2.43  
 1455 eV<sup>151</sup>) and is unsuitable for photovoltaic applications. The  
 1456 photoactive  $\alpha$ -FAPbI<sub>3</sub> is stabilized only at higher temperatures  
 1457 of ~125–165 °C (Figure 3d). Note that phase transition (e.g.,  
 1458 tetragonal to cubic in MAPbI<sub>3</sub>) or polymorphism ( $\alpha$ - to  $\delta$ -  
 1459 phase in FAPbI<sub>3</sub>) is not a permanent degradation phenomenon  
 1460 as they can be recovered reversibly.  
 1460

1461 The most promising approaches to improve degradation and  
 1462 phase/polymorphism stability in perovskite solar cells are the  
 1463 introduction of the mixing of A (binary, tertiary, or even  
 1464 quaternary mixed position) site cations and X site halide anions  
 1465 (I, Br, and Cl anions) (Figure 1b and Table 1), i.e., chemical  
 1466 compositional engineering or alloying.<sup>8,101</sup> In fact, A cation  
 1467 mixed perovskite systems of (FA/MA)PbI<sub>3</sub>, (MA/Cs)PbI<sub>3</sub>,  
 1468 (FA/Cs)PbI<sub>3</sub>, (FA/Rb)PbI<sub>3</sub> (section 2) showed enhanced  
 1469 stability (Figure 8c and Figure 9) as compared to reference cells  
 1470 comprising simple perovskites (MAPbI<sub>3</sub> or FAPbI<sub>3</sub>). At the  
 1471 current stage, it is difficult to pinpoint the binary composition  
 1471

(mixed A cation) that leads to the most enhanced stability. This is because of the various synthesis methods of perovskite films adopted by the different groups that lead to different grain sizes, uneven coverage, pinhole formation, capping layer thickness, variations in stoichiometry (e.g., excessive lead halide or cation), nonuniform spatial distribution of mixed perovskites' constituents, and etc. Furthermore, variations in devices induced by processing imperfections make it difficult to properly identify intrinsic material and device properties when comparing among the individual and independent reports from the various groups (Table 1). In this sense, a universal deposition protocol<sup>262</sup> is desirable that allows side-by-side comparisons from a myriad of different chemical compositions to pinpoint the most promising chemical composition for photovoltaic applications. Fundamental microscopic origins of enhanced stability for (FA/MA)PbI<sub>3</sub><sup>106</sup> (section 2.1) as well as  $t_{\text{effective}}$  (geometric Goldschmidt effective tolerance factor) for (FA/Cs)PbI<sub>3</sub><sup>101</sup> (section 2.3) and thermodynamic considerations for (FA/Cs)PbI<sub>3</sub><sup>117</sup> and (FA/Cs/Rb)PbI<sub>3</sub><sup>157</sup> (section 2.3) were proposed. For the (FA/MA)PbI<sub>3</sub>, the incorporation of MA<sup>+</sup> cations that has a high dipole moment leads to stronger interactions with PbI<sub>6</sub> octahedra and stabilizes the  $\alpha$ -FAPbI<sub>3</sub> without significant lattice shrinkage or changes in the optical properties (Figure 3e).<sup>106</sup> It has been generalized that perovskites with  $t < 0.8$  and  $t > 1$  tend to form the  $\delta$ -phase orthorhombic structure (e.g.,  $\delta_{\text{O}}\text{-CsPbI}_3$ ) and the  $\delta$ -phase hexagonal structure (e.g.,  $\delta_{\text{H}}\text{-FAPbI}_3$ ), respectively.<sup>101</sup> The cubic structure is only preferred for  $0.8 < t < 1$  (Figure 7a). Alloying a high  $t$  FAPbI<sub>3</sub> and low  $t$  CsPbI<sub>3</sub>,  $t_{\text{effective}}$  can be tuned to be between 0.8 and 1.0 in (FA/Cs)PbI<sub>3</sub> perovskites, which favors a stable perovskite structure.<sup>101</sup> Based on theoretical calculations, thermodynamic arguments were used to explain the stability of (FA/Cs)PbI<sub>3</sub><sup>117</sup> and (FA/Cs/Rb)PbI<sub>3</sub><sup>157</sup> perovskite systems. Cs<sup>+</sup> and Rb<sup>+</sup> were predicted to be more efficient in stabilizing the FAPbI<sub>3</sub> perovskite than MA<sup>+</sup> based on the balance of internal energy variation ( $\Delta E$ ), mixing entropy contributions ( $-\Delta S$ ), and free energy  $\Delta F = \Delta E - \Delta S$  (Figure 10). In short, the incorporation of Cs<sup>+</sup> and/or Rb<sup>+</sup> thermodynamically favors the formation of new perovskite phases and brings the system into a new equilibrium state. Systems with mixed X anion halides with A site constrained to a single monovalent cation, MAPb(I/Cl), FAPb(I/Cl), MAPb(I/Br), FAPb(I/Br), MAPb(Br/Cl), MAPb(I/Br/Cl), CsPb(I/Br), CsPb(Br/Cl), CsPb(I/Cl) were reported to show peculiar phenomena (section 3). MAPb(I/Cl) is one of the most studied binary mixed perovskite because of the strong interest from the field trying to answer the question whether Cl can in fact be incorporated into the lattice of MAPbI<sub>3</sub> (section 3.1). It has been proposed that Cl incorporation in FAPbI<sub>3</sub> structure helps stabilize the  $\alpha$ -FAPbI<sub>3</sub> phase; however, further in-depth studies are needed as the reported works are scarce (section 3.1). Synthesis of MAPb(I/Br) system in the full range of Br:I composition ratio was reported by various groups where  $E_g$  can be tuned effectively (section 3.2 and Figure 13). These  $E_g$  values are closely related to the lattice parameter of MAPb(I/Br), which was demonstrated to closely follow the Vegard's law (section 3.2). Only a small deviation from the Vegard's law was observed in the cubic regime (Figure 12) indicating presence of additional interactions in the mixed-halogens.<sup>220,226</sup> Under storage conditions in dark or low light intensity, MAPb(I/Br) with the Br content of ~20% provided enhanced stability even under relative humidity of 55%. This was closely correlated to the tetragonal to pseudocubic phase trans-

formation (Figure 12b,d) arising from the incorporation of smaller ionic radius of Br and consequently leading to a more compact tightly bound structure (higher  $t$  factor). However, when the initially homogeneous MAPb(I/Br) is exposed to light, a phase-separation into two phases, one I-rich domain and the other Br-rich domain form in the same film (Figure 15).<sup>234,237,240</sup> A number of reports proposed the microscopic as well as macroscopic origins based on thermodynamics, energy levels (CBM and VBM), and light-induced generation of lattice strain leading phase-segregation phenomena (see section 3.2 and Figure 16). In comparison, the FAPb(I/Br) system was reported to be more resilient against phase segregation than MAPb(I/Br) system (section 3.2). The XRD analysis of FAPb(I/Br) system in the full range of Br:I composition ratio shows an interesting phenomenon that has an amorphous phase, which a fundamental understanding is still lacking (Figure 17). More interestingly, incorporation of small amounts of Cs was observed to suppress this amorphous phase (section 4.4). Based on the fact that halide perovskites have strong ionic character, Coulomb interactions were also proposed to play a major role (section 3.5 and Figure 20). The interplay of strain (favoring demixing) and Coulomb (favoring mixing) energies describes the formation energies of CsPb(X/Y) with X,Y = I, Br, Cl that as consequence dictates its stability (Figure 20).<sup>250</sup> Based on these fundamental concepts described in sections 1 and 2, the more complex systems of simultaneously mixed A and mixed X (MA/Cs)Pb(I/Br), (FA/MA)Pb(I/Br), (FA/MA)Pb(I/Cl), (FA/Cs)Pb(I/Br), (Cs/FA/MA)Pb(I/Br), (Rb/FA/MA)Pb(I/Br), (Rb/Cs/FA)Pb(I/Br), (Rb/Cs/FA/MA)Pb(I/Br) perovskites were described in section 4. Out of six, five certified efficiencies reported by NREL were based on the (FA/MA)Pb(I/Br) perovskite system (Figure 1b). Enhanced stability under storage conditions was reported for (FA/MA)Pb(I/Br) system (Figure 23a). It was proposed that when MABr is incorporated to alloy with FAPbI<sub>3</sub>, the lattice size is reduced and the strain forces (demixing) within the grain are relaxed. In this way, the pseudocubic  $\alpha$ -phase is stabilized at room temperature and even under humid air (Figure 23b). However, (FA/MA)Pb(I/Br)-based solar cells under operation conditions (tracking the maximum power point), migration of halide vacancies as well as cation vacancies were proposed to take place (Figure 24).<sup>259</sup> Cs incorporation in (FA/Cs)Pb(I/Br) system (section 4.4) was reported to suppress halide segregation (section 2.3) and formation of unstable amorphous phase (Figure 25a). Optimized compositions lead generally to higher  $E_g$  and therefore the (FA/Cs)Pb(I/Br) system was employed as the top cell in the tandem solar cell structure showing high promises (section 4.4).<sup>132,133,269</sup> Reports on ternary (Cs/FA/MA)<sup>65,135,262</sup> and quaternary (Rb/Cs/FA/MA) mixed cations<sup>7,137</sup> have just bought new hopes that a "magical" composition may lead to a stable perovskite with even higher PCE.<sup>84</sup> Thermodynamics must underlie this "magical" composition. The concept of effective tolerance factor (section 2.3) may help as a starting point for identifying thermodynamically stable hybrid mixed cations and mixed halides perovskites. Multicomponent perovskite design to achieve a stable single pure phase can enable a creation of stable structures with optimal transport and optical properties. However, a strict control over the phase composition of mixed perovskites should be ensured at the preparation stage, i.e., mixed perovskite materials should be clean from admixtures of nonperovskite phases (section 3.2).<sup>120,157</sup> Strategies to fabricate perovskite single-crystal-based solar cells were reported in the

1598 literature<sup>17,273–275</sup> and naturally it is of high interest to study  
1599 the optoelectronic properties (e.g., surface and bulk trap  
1600 densities) of mixed halide perovskite single crystals, which has  
1601 significantly different morphological (e.g., grain boundary),  
1602 structural (e.g., perovskite crystal orientation), as well as spatial  
1603 chemical composition distribution compared to polycrystalline  
1604 thin-films of perovskites.<sup>209,246,247</sup>

1605 Energy levels measurements (work function, CBM, and  
1606 VBM) of mixed perovskites and its alignments with adjacent  
1607 selective contact layers (ETL and HTL) are largely missing in  
1608 the literature. To date, only a handful of publications provided  
1609 insights into the energy diagrams, band bending, and interfacial  
1610 dipole concepts studied on simpler MAPbI<sub>3</sub>, MAPbI<sub>3-x</sub>Cl<sub>x</sub>,  
1611 MAPbBr<sub>3</sub>, MAPbBr<sub>3-x</sub>Cl<sub>x</sub>, CsPbBr<sub>3</sub> perovskite systems.<sup>276–288</sup>  
1612 Within perovskite solar cell structures, each underneath  
1613 substrate may have influence on the energy levels of the top  
1614 layer under examination by ultraviolet spectroscopy  
1615 (UPS).<sup>282,289,290</sup> Therefore, precise energy level alignments  
1616 among stacked layers can only be obtained if UPS is performed  
1617 on the individual top layers that are stacked on the actual prior  
1618 layers following device structure. A few studies provided the  
1619 energy-level alignments across all stacked functional layers  
1620 within the perovskite solar cell, e.g., FTO/c-TiO<sub>2</sub> (+mp-TiO<sub>2</sub>)/  
1621 MAPbI<sub>3</sub> (or MAPbI<sub>3-x</sub>Cl<sub>x</sub>)/spiro-MeOTAD/Ag or Au, em-  
1622 ploying KPFM.<sup>291–293</sup> Further studies on the energy level  
1623 alignments of mixed perovskites across all stacked layers are  
1624 expected to bring insights into the correlation with perovskite  
1625 solar cell parameters.<sup>276–288</sup>

1626 Pb-free perovskites are still being investigated inten-  
1627 sively.<sup>294–306</sup> Computational approaches based on the tolerance  
1628 factor (*t*) are generally employed to predict the geometrical  
1629 stability of three-dimensional (3D) ABX<sub>3</sub> perovskite struc-  
1630 tures.<sup>15,160,307</sup> Based on revised ionic radii, which considers  
1631 greater covalency in metal-halide bonds, Travis et al.<sup>160</sup> found  
1632 that only a handful of cations may be successfully placed on the  
1633 B site of iodide-based perovskite: Sn, Yb, Dy, Tm, Sm, Ca, Sr.  
1634 Filip and Giustino<sup>308</sup> and Körbel et al.<sup>309</sup> performed a  
1635 systematic combinatorial search based on DFT over the entire  
1636 periodic table. Starting from over 32 000 possible 3D ABX<sub>3</sub>  
1637 compounds, Körbel et al. found 199 thermodynamically stable  
1638 perovskites in the cubic structure.<sup>309</sup> Considering the E<sub>g</sub> values  
1639 suitable for photovoltaic applications among these 199  
1640 perovskites, all ABX<sub>3</sub> structures with single cation and single  
1641 anion were based on Sn and Ge halide perovskites. The overall  
1642 conclusion from these studies is that Pb plays a key role in the  
1643 optoelectronic properties of 3D ABX<sub>3</sub> perovskites and is unique  
1644 among all single divalent metals in the periodic table. Great  
1645 efforts<sup>306</sup> have been made toward searching for low-dimen-  
1646 sional perovskites with multivalent elements yielding a “3-2-9”  
1647 (or A<sub>3</sub>B<sub>2</sub>X<sub>9</sub>) 2D,<sup>81,310–312</sup> quasi-2D,<sup>313–316</sup> “3-1-5” single-chain,  
1648 “4-1-6” single-octahedron structures, and “2-1-1-6” 3D double  
1649 perovskite structures with compensated charges.<sup>81,296,299,306,317</sup>  
1650 Quasi-2D perovskite solar cells were reported to show  
1651 enhanced moisture stability; however, it is often associated  
1652 with poor photovoltaic properties. In a recent work, Xiao et  
1653 al.<sup>306</sup> compiled reported Pb-free halide perovskites and  
1654 introduced the concept of electronic dimensionality. It was  
1655 proposed that the higher photovoltaic performance is  
1656 intimately associated with the isotropic 3D transport properties  
1657 of photogenerated charges.<sup>313,315,316</sup> In this sense, it explains  
1658 the lower PCE reported for lower-dimensional perovskites as  
1659 absorbers.<sup>306</sup> The chemical composition engineering or alloying  
1660 strategy has been scarcely explored for Pb-free perovskite

systems, and further exploration for a “magical” composition is  
1661 expected to bring subsequent years of key findings for the  
1662 photovoltaic community stimulating further interests of both  
1663 academia (fundamental research) and industry (new technol-  
1664 ogy).  
1665

## AUTHOR INFORMATION

### Corresponding Author

\*Y. B. Qi. E-mail: [Yabing.Qi@OIST.jp](mailto:Yabing.Qi@OIST.jp).

### ORCID

Yabing Qi: [0000-0002-4876-8049](http://orcid.org/0000-0002-4876-8049)

### Author Contributions

<sup>†</sup>These authors contributed equally to this work.

### Author Contributions

Y.B.Q. conceived the idea, initiated, and supervised the work.  
All authors contributed to writing the paper.

### Notes

The authors declare no competing financial interest.

## ACKNOWLEDGMENTS

This work was supported by funding from the Energy Materials  
and Surface Sciences Unit of the Okinawa Institute of Science  
and Technology Graduate University, the OIST Proof of  
Concept (POC) Program, the OIST R&D Cluster Research  
Program, and JSPS KAKENHI Grant Number 15K17925.

## REFERENCES

- (1) Web of Science, Thomson Reuters. <https://webofknowledge.com/> (accessed March 21st, 2017).
- (2) Kojima, A.; Teshima, K.; Shirai, Y.; Miyasaka, T. Organometal Halide Perovskites as Visible-Light Sensitizers for Photovoltaic Cells. *J. Am. Chem. Soc.* **2009**, *131*, 6050–6051.
- (3) Kim, H. S.; Lee, C. R.; Im, J. H.; Lee, K. B.; Moehl, T.; Marchioro, A.; Moon, S. J.; Humphry-Baker, R.; Yum, J. H.; Moser, J. E.; et al. Lead Iodide Perovskite Sensitized All-Solid-State Submicron Thin Film Mesoscopic Solar Cell with Efficiency Exceeding 9%. *Sci. Rep.* **2012**, *2*, 591.
- (4) Bisquert, J.; Qi, Y. B.; Ma, T.; Yan, Y. Advances and Obstacles on Perovskite Solar Cell Research from Material Properties to Photovoltaic Function. *ACS Energy Lett.* **2017**, *2*, 520–523.
- (5) Xu, F.; Zhang, T.; Li, G.; Zhao, Y. Mixed Cation Hybrid Lead Halide Perovskites with Enhanced Performance and Stability. *J. Mater. Chem. A* **2017**, *5*, 11450–11461.
- (6) Ha, S. T.; Su, R.; Xing, J.; Zhang, Q.; Xiong, Q. Metal Halide Perovskite Nanomaterials: Synthesis and Applications. *Chem. Sci.* **2017**, *8*, 2522–2536.
- (7) Correa-Baena, J.-P.; Abate, A.; Saliba, M.; Tress, W.; Jesper Jacobsson, T.; Grätzel, M.; Hagfeldt, A. The Rapid Evolution of Highly Efficient Perovskite Solar Cells. *Energy Environ. Sci.* **2017**, *10*, 710–727.
- (8) Zhou, Y.; Zhou, Z.; Chen, M.; Zong, Y.; Huang, J.; Pang, S.; Padture, N. P. Doping and alloying for improved perovskite solar cells. *J. Mater. Chem. A* **2016**, *4*, 17623–17635.
- (9) Ono, L. K.; Qi, Y. B. Surface and Interface Aspects of Organometal Halide Perovskite Materials and Solar Cells. *J. Phys. Chem. Lett.* **2016**, *7*, 4764–4794.
- (10) Park, N.-G.; Grätzel, M.; Miyasaka, T.; Zhu, K.; Emery, K. Towards stable and commercially available perovskite solar cells. *Nat. Energy* **2016**, *1*, 16152.
- (11) Fan, Z.; Sun, K.; Wang, J. Perovskites for Photovoltaics: A Combined Review of Organic-Inorganic Halide Perovskites and Ferroelectric Oxide Perovskites. *J. Mater. Chem. A* **2015**, *3*, 18809–18828.
- (12) Brenner, T. M.; Egger, D. A.; Kronik, L.; Hodes, G.; Cahen, D. Hybrid Organic–Inorganic Perovskites: Low-Cost Semiconductors

- 1723 with Intriguing Charge-Transport Properties. *Nat. Rev. Mater.* **2016**, *1*,  
1724 15007.
- 1725 (13) Ye, M.; Hong, X.; Zhang, F.; Liu, X. Recent Advancements in  
1726 Perovskite Solar Cells: Flexibility, Stability and Large Scale. *J. Mater.*  
1727 *Chem. A* **2016**, *4*, 6755–6771.
- 1728 (14) Yin, W. J.; Yang, J. H.; Kang, J.; Yan, Y. F.; Wei, S. H. Halide  
1729 Perovskite Materials for Solar Cells: A Theoretical Review. *J. Mater.*  
1730 *Chem. A* **2015**, *3*, 8926–8942.
- 1731 (15) Chen, Q.; De Marco, N.; Yang, Y.; Song, T. B.; Chen, C. C.;  
1732 Zhao, H. X.; Hong, Z. R.; Zhou, H. P.; Yang, Y. Under the Spotlight:  
1733 The Organic-Inorganic Hybrid Halide Perovskite for Optoelectronic  
1734 Applications. *Nano Today* **2015**, *10*, 355–396.
- 1735 (16) Berry, J.; Buonassisi, T.; Egger, D. A.; Hodes, G.; Kronik, L.;  
1736 Loo, Y.-L.; Lubomirsky, I.; Marder, S. R.; Mastai, Y.; Miller, J. S.; et al.  
1737 Hybrid Organic-Inorganic Perovskites (HOIPs): Opportunities and  
1738 Challenges. *Adv. Mater.* **2015**, *27*, 5102–5112.
- 1739 (17) Huang, J.; Shao, Y.; Dong, Q. Organometal Trihalide Perovskite  
1740 Single Crystals: A Next Wave of Materials for 25% Efficiency  
1741 Photovoltaics and Applications Beyond? *J. Phys. Chem. Lett.* **2015**, *6*,  
1742 3218–3227.
- 1743 (18) Christians, J. A.; Manser, J. S.; Kamat, P. V. Multifaceted Excited  
1744 State of  $\text{CH}_3\text{NH}_3\text{PbI}_3$ . Charge Separation, Recombination, and  
1745 Trapping. *J. Phys. Chem. Lett.* **2015**, *6*, 2086–2095.
- 1746 (19) Green, M. A.; Jiang, Y.; Soufiani, A. M.; Ho-Baillie, A. Optical  
1747 Properties of Photovoltaic Organic-Inorganic Lead Halide Perov-  
1748 skites. *J. Phys. Chem. Lett.* **2015**, *6*, 4774–4785.
- 1749 (20) Zheng, F.; Saldana-Greco, D.; Liu, S.; Rappe, A. M. Material  
1750 Innovation in Advancing Organometal Halide Perovskite Function-  
1751 ality. *J. Phys. Chem. Lett.* **2015**, *6*, 4862–4872.
- 1752 (21) Zhou, Y.; Game, O. S.; Pang, S.; Padture, N. P. Microstructures  
1753 of Organometal Trihalide Perovskites for Solar Cells: Their Evolution  
1754 from Solutions and Characterization. *J. Phys. Chem. Lett.* **2015**, *6*,  
1755 4827–4839.
- 1756 (22) Zhu, X. Y.; Podzorov, V. Charge Carriers in Hybrid Organic-  
1757 Inorganic Lead Halide Perovskites Might Be Protected as Large  
1758 Polaron. *J. Phys. Chem. Lett.* **2015**, *6*, 4758–4761.
- 1759 (23) Song, T. B.; Chen, Q.; Zhou, H. P.; Jiang, C. Y.; Wang, H. H.;  
1760 Yang, Y.; Liu, Y. S.; You, J. B.; Yang, Y. Perovskite Solar Cells: Film  
1761 Formation and Properties. *J. Mater. Chem. A* **2015**, *3*, 9032–9050.
- 1762 (24) Luo, S. Q.; Daoud, W. A. Recent Progress in Organic-Inorganic  
1763 Halide Perovskite Solar Cells: Mechanisms and Material Design. *J.*  
1764 *Mater. Chem. A* **2015**, *3*, 8992–9010.
- 1765 (25) Kazim, S.; Nazeeruddin, M. K.; Grätzel, M.; Ahmad, S.  
1766 Perovskite as Light Harvester: A Game Changer in Photovoltaics.  
1767 *Angew. Chem., Int. Ed.* **2014**, *53*, 2812–2824.
- 1768 (26) Gao, P.; Grätzel, M.; Nazeeruddin, M. K. Organohalide Lead  
1769 Perovskites for Photovoltaic Applications. *Energy Environ. Sci.* **2014**, *7*,  
1770 2448–2463.
- 1771 (27) Lee, M. V.; Raga, S. R.; Kato, Y.; Leyden, M. R.; Ono, L. K.;  
1772 Wang, S.; Qi, Y. Transamidation of Dimethylformamide during  
1773 Alkylammonium Lead Triiodide Film Formation for Perovskite Solar  
1774 Cells. *J. Mater. Res.* **2017**, *32*, 45–55.
- 1775 (28) Wang, S.; Jiang, Y.; Juarez-Perez, E. J.; Ono, L. K.; Qi, Y. B.  
1776 Accelerated Degradation of Methylammonium Lead Iodide Perov-  
1777 skites Induced by Exposure to Iodine Vapour. *Nat. Energy* **2016**, *2*,  
1778 16195.
- 1779 (29) Juarez-Perez, E. J.; Hawash, Z.; Raga, S. R.; Ono, L. K.; Qi, Y. B.  
1780 Thermal Degradation of  $\text{CH}_3\text{NH}_3\text{PbI}_3$  Perovskite into  $\text{NH}_3$  and  $\text{CH}_3\text{I}$   
1781 Gases Observed by Coupled Thermogravimetry-Mass Spectrometry  
1782 Analysis. *Energy Environ. Sci.* **2016**, *9*, 3406–3410.
- 1783 (30) Jung, M.-C.; Qi, Y. B. Dopant Interdiffusion Effects in n-i-p  
1784 Structured Spiro-OMeTAD Hole Transport Layer of Organometal  
1785 Halide Perovskite Solar Cells. *Org. Electron.* **2016**, *31*, 71–76.
- 1786 (31) Jung, M.-C.; Lee, Y. M.; Lee, H.-K.; Park, J.; Raga, S. R.; Ono, L.  
1787 K.; Wang, S.; Leyden, M. R.; Yu, B. D.; Hong, S.; et al. The Presence  
1788 of  $\text{CH}_3\text{NH}_2$  Neutral Species in Organometal Halide Perovskite Films.  
1789 *Appl. Phys. Lett.* **2016**, *108*, 073901.
- 1790 (32) Juarez-Perez, E. J.; Leyden, M. R.; Wang, S.; Ono, L. K.;  
1791 Hawash, Z.; Qi, Y. B. Role of the Dopants on the Morphological and  
Transport Properties of Spiro-MeOTAD Hole Transport Layer. *Chem. Mater.* **2016**, *28*, 5702–5709.
- (33) Hawash, Z.; Ono, L. K.; Qi, Y. B. Moisture and Oxygen Enhance Conductivity of LiTFSI-Doped Spiro-MeOTAD Hole Transport Layer in Perovskite Solar Cells. *Adv. Mater. Interfaces* **2016**, *3*, 1600117.
- (34) Ohmann, R.; Ono, L. K.; Kim, H.-S.; Lin, H.; Lee, M. V.; Li, Y.; Park, N.-G.; Qi, Y. B. Real-Space Imaging of the Atomic Structure of Organic-Inorganic Perovskite. *J. Am. Chem. Soc.* **2015**, *137*, 16049–16054.
- (35) Ono, L. K.; Raga, S. R.; Remeika, M.; Winchester, A. J.; Gabe, A.; Qi, Y. B. Pinhole-Free Hole Transport Layers Significantly Improve the Stability of  $\text{MAPbI}_3$ -Based Perovskite Solar Cells Under Operating Conditions. *J. Mater. Chem. A* **2015**, *3*, 15451–15456.
- (36) Hawash, Z.; Ono, L. K.; Raga, S. R.; Lee, M. V.; Qi, Y. B. Air-Exposure Induced Dopant Redistribution and Energy Level Shifts in Spin-Coated Spiro-MeOTAD Films. *Chem. Mater.* **2015**, *27*, 562–569.
- (37) Kato, Y.; Ono, L. K.; Lee, M. V.; Wang, S. H.; Raga, S. R.; Qi, Y. B. Silver Iodide Formation in Methyl Ammonium Lead Iodide Perovskite Solar Cells with Silver Top Electrodes. *Adv. Mater. Interfaces* **2015**, *2*, 1500195.
- (38) Ono, L. K.; Raga, S. R.; Wang, S.; Kato, Y.; Qi, Y. B. Temperature-Dependent Hysteresis Effects in Perovskite-Based Solar Cells. *J. Mater. Chem. A* **2015**, *3*, 9074–9080.
- (39) Ono, L. K.; Schulz, P.; Endres, J. J.; Nikiforov, G. O.; Kato, Y.; Kahn, A.; Qi, Y. B. Air-Exposure-Induced Gas-Molecule Incorporation into Spiro-MeOTAD Films. *J. Phys. Chem. Lett.* **2014**, *5*, 1374–1379.
- (40) National Renewable Energy Laboratory (NREL). Research Cell Efficiency Records. [http://www.nrel.gov/ncpv/images/efficiency\\_chart.jpg](http://www.nrel.gov/ncpv/images/efficiency_chart.jpg) (accessed March 21st, 2017).
- (41) Green, M. A.; Ho-Baillie, A.; Snaith, H. J. The Emergence of Perovskite Solar Cells. *Nat. Photonics* **2014**, *8*, 506–514.
- (42) Park, N. G. Organometal Perovskite Light Absorbers Toward a 20% Efficiency Low-Cost Solid-State Mesoscopic Solar Cell. *J. Phys. Chem. Lett.* **2013**, *4*, 2423–2429.
- (43) Snaith, H. J. Perovskites: The Emergence of a New Era for Low-Cost, High-Efficiency Solar Cells. *J. Phys. Chem. Lett.* **2013**, *4*, 3623–3630.
- (44) Seo, J.; Noh, J. H.; Seok, S. I. Rational Strategies for Efficient Perovskite Solar Cells. *Acc. Chem. Res.* **2016**, *49*, 562–572.
- (45) Acik, M.; Darling, S. B. Graphene in Perovskite Solar Cells: Device Design, Characterization and Implementation. *J. Mater. Chem. A* **2016**, *4*, 6185–6235.
- (46) Docampo, P.; Bein, T. A Long-Term View on Perovskite Optoelectronics. *Acc. Chem. Res.* **2016**, *49*, 339–346.
- (47) Ono, L. K.; Leyden, M. R.; Wang, S.; Qi, Y. B. Organometal Halide Perovskite Thin Films and Solar Cells by Vapor Deposition. *J. Mater. Chem. A* **2016**, *4*, 6693–6713.
- (48) Remeika, M.; Raga, S. R.; Zhang, S.; Qi, Y. B. Transferrable Optimization of Spray-Coated  $\text{PbI}_2$  Films for Perovskite Solar Cell Fabrication. *J. Mater. Chem. A* **2017**, *5*, 5709–5718.
- (49) Leyden, M. R.; Jiang, Y.; Qi, Y. B. Chemical Vapor Deposition Grown Formamidinium Perovskite Solar Modules with High Steady State Power and Thermal Stability. *J. Mater. Chem. A* **2016**, *4*, 13125–13132.
- (50) Raga, S. R.; Ono, L. K.; Qi, Y. B. Rapid Perovskite Formation by  $\text{CH}_3\text{NH}_2$  Gas-Induced Intercalation and Reaction of  $\text{PbI}_2$ . *J. Mater. Chem. A* **2016**, *4*, 2494–2500.
- (51) Raga, S. R.; Qi, Y. The Effect of Impurities on the Impedance Spectroscopy Response of  $\text{CH}_3\text{NH}_3\text{PbI}_3$  Perovskite Solar Cells. *J. Phys. Chem. C* **2016**, *120*, 28519–28526.
- (52) Jiang, Y.; Juarez-Perez, E. J.; Ge, Q.; Wang, S.; Leyden, M. R.; Ono, L. K.; Raga, S. R.; Hu, J.; Qi, Y. Post-Annealing of  $\text{MAPbI}_3$  Perovskite Films with Methylamine for Efficient Perovskite Solar Cells. *Mater. Horiz.* **2016**, *3*, 548–555.
- (53) Jung, M.-C.; Raga, S. R.; Qi, Y. B. Properties and Solar Cell Applications of Pb-Free Perovskite Films Formed by Vapor Deposition. *RSC Adv.* **2016**, *6*, 2819–2825.

- 1860 (54) Leyden, M. R.; Lee, M. V.; Raga, S. R.; Qi, Y. B. Large  
1861 Formamidinium Lead Trihalide Perovskite Solar Cells Using Chemical  
1862 Vapor Deposition with High Reproducibility and Tunable Chlorine  
1863 Concentrations. *J. Mater. Chem. A* **2015**, *3*, 16097–16103.  
1864 (55) Raga, S. R.; Jung, M.-C.; Lee, M. V.; Leyden, M. R.; Kato, Y.; Qi,  
1865 Y. B. Influence of Air Annealing on High Efficiency Planar Structure  
1866 Perovskite Solar Cells. *Chem. Mater.* **2015**, *27*, 1597–1603.  
1867 (56) Wang, S.; Ono, L. K.; Leyden, M. R.; Kato, Y.; Raga, S. R.; Lee,  
1868 M. V.; Qi, Y. B. Smooth Perovskite Thin Films and Efficient Perovskite  
1869 Solar Cells Prepared by the Hybrid Deposition Method. *J. Mater.*  
1870 *Chem. A* **2015**, *3*, 14631–14641.  
1871 (57) Leyden, M. R.; Ono, L. K.; Raga, S. R.; Kato, Y.; Wang, S. H.;  
1872 Qi, Y. B. High Performance Perovskite Solar Cells by Hybrid Chemical  
1873 Vapor Deposition. *J. Mater. Chem. A* **2014**, *2*, 18742–18745.  
1874 (58) Ono, L. K.; Wang, S.; Kato, Y.; Raga, S. R.; Qi, Y. B. Semi-  
1875 Transparent Perovskite Films with Centimeter-scale Superior  
1876 Uniformity by the Hybrid Deposition Method. *Energy Environ. Sci.*  
1877 **2014**, *7*, 3989–3993.  
1878 (59) Burschka, J.; Pellet, N.; Moon, S. J.; Humphry-Baker, R.; Gao,  
1879 P.; Nazeeruddin, M. K.; Grätzel, M. Sequential Deposition as a Route  
1880 to High-Performance Perovskite-Sensitized Solar Cells. *Nature* **2013**,  
1881 *499*, 316–319.  
1882 (60) Lee, M. M.; Teuscher, J.; Miyasaka, T.; Murakami, T. N.; Snaith,  
1883 H. J. Efficient Hybrid Solar Cells Based on Meso-Superstructured  
1884 Organometal Halide Perovskites. *Science* **2012**, *338*, 643–647.  
1885 (61) Liu, M. Z.; Johnston, M. B.; Snaith, H. J. Efficient Planar  
1886 Heterojunction Perovskite Solar Cells by Vapour Deposition. *Nature*  
1887 **2013**, *501*, 395–398.  
1888 (62) Jeon, N. J.; Noh, J. H.; Kim, Y. C.; Yang, W. S.; Ryu, S.; Seok, S.  
1889 I. Solvent Engineering for High-Performance Inorganic–Organic  
1890 Hybrid Perovskite Solar Cells. *Nat. Mater.* **2014**, *13*, 897–903.  
1891 (63) Jeon, N. J.; Noh, J. H.; Yang, W. S.; Kim, Y. C.; Ryu, S.; Seo, J.;  
1892 Seok, S. I. Compositional Engineering of Perovskite Materials for  
1893 High-Performance Solar Cells. *Nature* **2015**, *517*, 476–480.  
1894 (64) Yang, W. S.; Noh, J. H.; Jeon, N. J.; Kim, Y. C.; Ryu, S.; Seo, J.;  
1895 Seok, S. I. High-Performance Photovoltaic Perovskite Layers  
1896 Fabricated through Intramolecular Exchange. *Science* **2015**, *348*,  
1897 1234–1237.  
1898 (65) Saliba, M.; Matsui, T.; Seo, J.-Y.; Domanski, K.; Correa-Baena,  
1899 J.-P.; Nazeeruddin, M. K.; Zakeeruddin, S. M.; Tress, W.; Abate, A.;  
1900 Hagfeldt, A.; et al. Cesium-Containing Triple Cation Perovskite Solar  
1901 Cells: Improved Stability, Reproducibility and High Efficiency. *Energy*  
1902 *Environ. Sci.* **2016**, *9*, 1989–1997.  
1903 (66) Green, M. A.; Emery, K.; Hishikawa, Y.; Warta, W.; Dunlop, E.  
1904 D. Solar cell efficiency tables (version 48). *Prog. Photovoltaics* **2016**, *24*,  
1905 905–913.  
1906 (67) Walsh, A. Principles of Chemical Bonding and Band Gap  
1907 Engineering in Hybrid Organic–Inorganic Halide Perovskites. *J. Phys.*  
1908 *Chem. C* **2015**, *119*, 5755–5760.  
1909 (68) Wang, B.; Xiao, X.; Chen, T. Perovskite Photovoltaics: A High-  
1910 Efficiency Newcomer to the Solar Cell Family. *Nanoscale* **2014**, *6*,  
1911 12287–12297.  
1912 (69) Bakulin, A. A.; Selig, O.; Bakker, H. J.; Rezus, Y. L. A.; Müller,  
1913 C.; Glaser, T.; Lovrinicic, R.; Sun, Z.; Chen, Z.; Walsh, A.; et al. Real-  
1914 Time Observation of Organic Cation Reorientation in Methylammo-  
1915 nium Lead Iodide Perovskites. *J. Phys. Chem. Lett.* **2015**, *6*, 3663–  
1916 3669.  
1917 (70) Leguy, A. M. A.; Frost, J. M.; McMahon, A. P.; Sakai, V. G.;  
1918 Kochelmann, W.; Law, C.; Li, X.; Foglia, F.; Walsh, A.; O'Regan, B. C.;  
1919 et al. The Dynamics of Methylammonium Ions in Hybrid Organic-  
1920 Inorganic Perovskite Solar Cells. *Nat. Commun.* **2015**, *6*, 7124.  
1921 (71) Leguy, A. M. A.; Goni, A. R.; Frost, J. M.; Skelton, J.; Brivio, F.;  
1922 Rodriguez-Martinez, X.; Weber, O. J.; Pallipurath, A.; Alonso, M. I.;  
1923 Campoy-Quiles, M.; et al. Dynamic Disorder, Phonon Lifetimes, and  
1924 the Assignment of Modes to the Vibrational Spectra of Methyl-  
1925 ammonium Lead Halide Perovskites. *Phys. Chem. Chem. Phys.* **2016**,  
1926 *18*, 27051–27066.  
1927 (72) Miyasaka, T. Perovskite Photovoltaics: Rare Functions of Organo Lead Halide in Solar Cells and Optoelectronic Devices. *Chem. Lett.* **2015**, *44*, 720–729.  
1928 (73) Brivio, F.; Walker, A. B.; Walsh, A. Structural and Electronic Properties of Hybrid Perovskites for High-Efficiency Thin-Film Photovoltaics from First-Principles. *APL Mater.* **2013**, *1*, 042111.  
1929 (74) Brivio, F.; Butler, K. T.; Walsh, A.; van Schilfgaarde, M. Relativistic Quasiparticle Self-Consistent Electronic Structure of Hybrid Halide Perovskite Photovoltaic Absorbers. *Phys. Rev. B: Condens. Matter Mater. Phys.* **2014**, *89*, 155204.  
1930 (75) De Angelis, F. Modeling Materials and Processes in Hybrid/Organic Photovoltaics: From Dye-Sensitized to Perovskite Solar Cells. *Acc. Chem. Res.* **2014**, *47*, 3349–3360.  
1931 (76) Umari, P.; Mosconi, E.; De Angelis, F. Relativistic GW calculations on  $\text{CH}_3\text{NH}_3\text{PbI}_3$  and  $\text{CH}_3\text{NH}_3\text{SnI}_3$  Perovskites for Solar Cell Applications. *Sci. Rep.* **2015**, *4*, 4467.  
1932 (77) Quarti, C.; Mosconi, E.; De Angelis, F. Interplay of Orientational Order and Electronic Structure in Methylammonium Lead Iodide: Implications for Solar Cell Operation. *Chem. Mater.* **2014**, *26*, 6557–6569.  
1933 (78) Etienne, T.; Mosconi, E.; De Angelis, F. Dynamical Origin of the Rashba Effect in Organohalide Lead Perovskites: A Key to Suppressed Carrier Recombination in Perovskite Solar Cells? *J. Phys. Chem. Lett.* **2016**, *7*, 1638–1645.  
1934 (79) Quarti, C.; De Angelis, F.; Beljonne, D. Influence of Surface Termination on the Energy Level Alignment at the  $\text{CH}_3\text{NH}_3\text{PbI}_3$ /C60 Interface. *Chem. Mater.* **2017**, *29*, 958–968.  
1935 (80) Shirayama, M.; Kadokawa, H.; Miyadera, T.; Sugita, T.; Tamakoshi, M.; Kato, M.; Fujiseki, T.; Murata, D.; Hara, S.; Murakami, T. N.; et al. Optical Transitions in Hybrid Perovskite Solar Cells: Ellipsometry, Density Functional Theory, and Quantum Efficiency Analyses for  $\text{CH}_3\text{NH}_3\text{PbI}_3$ . *Phys. Rev. Appl.* **2016**, *5*, 014012.  
1936 (81) Saparov, B.; Mitzi, D. B. Organic–Inorganic Perovskites: Structural Versatility for Functional Materials Design. *Chem. Rev.* **2016**, *116*, 4558–4596.  
1937 (82) Stoumpos, C. C.; Malliakas, C. D.; Kanatzidis, M. G. Semiconducting Tin and Lead Iodide Perovskites with Organic Cations: Phase Transitions, High Mobilities, and Near-Infrared Photoluminescent Properties. *Inorg. Chem.* **2013**, *52*, 9019–9038.  
1938 (83) Weber, O. J.; Charles, B.; Weller, M. T. Phase Behaviour and Composition in the Formamidinium-Methylammonium Hybrid Lead Iodide Perovskite Solid Solution. *J. Mater. Chem. A* **2016**, *4*, 15375–15382.  
1939 (84) Nagabhushana, G. P.; Shivaramaiah, R.; Navrotsky, A. Direct Calorimetric Verification of Thermodynamic Instability of Lead Halide Hybrid Perovskites. *Proc. Natl. Acad. Sci. U. S. A.* **2016**, *113*, 7717–7721.  
1940 (85) Brandt, R. E.; Stevanovic, V.; Ginley, D. S.; Buonassisi, T. Identifying Defect-Tolerant Semiconductors with High Minority-Carrier Lifetimes: Beyond Hybrid Lead Halide Perovskites. *MRS Commun.* **2015**, *5*, 265–275.  
1941 (86) Umebayashi, T.; Asai, K.; Kondo, T.; Nakao, A. Electronic Structures of Lead Iodide Based Low-Dimensional Crystals. *Phys. Rev. B: Condens. Matter Mater. Phys.* **2003**, *67*, 155405.  
1942 (87) Lee, J.-H.; Bristowe, N. C.; Lee, J. H.; Lee, S.-H.; Bristowe, P. D.; Cheetham, A. K.; Jang, H. M. Resolving the Physical Origin of Octahedral Tilting in Halide Perovskites. *Chem. Mater.* **2016**, *28*, 4259–4266.  
1943 (88) Yin, W.-J.; Shi, T.; Yan, Y. Unique Properties of Halide Perovskites as Possible Origins of the Superior Solar Cell Performance. *Adv. Mater.* **2014**, *26*, 4653–4658.  
1944 (89) Yin, W.-J.; Shi, T.; Yan, Y. Unusual Defect Physics in  $\text{CH}_3\text{NH}_3\text{PbI}_3$  Perovskite Solar Cell Absorber. *Appl. Phys. Lett.* **2014**, *104*, 063903.  
1945 (90) Jacobsson, T. J.; Correa-Baena, J.-P.; Pazoki, M.; Saliba, M.; Schenck, K.; Grätzel, M.; Hagfeldt, A. Exploration of the Compositional Space for Mixed Lead Halogen Perovskites for High Efficiency Solar Cells. *Energy Environ. Sci.* **2016**, *9*, 1706–1724.  
1946 (91) Jacobsson, T. J.; Correa-Baena, J.-P.; Pazoki, M.; Saliba, M.; Schenck, K.; Grätzel, M.; Hagfeldt, A. Exploration of the Compositional Space for Mixed Lead Halogen Perovskites for High Efficiency Solar Cells. *Energy Environ. Sci.* **2016**, *9*, 1706–1724.  
1947 (92) Jacobsson, T. J.; Correa-Baena, J.-P.; Pazoki, M.; Saliba, M.; Schenck, K.; Grätzel, M.; Hagfeldt, A. Exploration of the Compositional Space for Mixed Lead Halogen Perovskites for High Efficiency Solar Cells. *Energy Environ. Sci.* **2016**, *9*, 1706–1724.  
1948 (93) Jacobsson, T. J.; Correa-Baena, J.-P.; Pazoki, M.; Saliba, M.; Schenck, K.; Grätzel, M.; Hagfeldt, A. Exploration of the Compositional Space for Mixed Lead Halogen Perovskites for High Efficiency Solar Cells. *Energy Environ. Sci.* **2016**, *9*, 1706–1724.  
1949 (94) Jacobsson, T. J.; Correa-Baena, J.-P.; Pazoki, M.; Saliba, M.; Schenck, K.; Grätzel, M.; Hagfeldt, A. Exploration of the Compositional Space for Mixed Lead Halogen Perovskites for High Efficiency Solar Cells. *Energy Environ. Sci.* **2016**, *9*, 1706–1724.  
1950 (95) Jacobsson, T. J.; Correa-Baena, J.-P.; Pazoki, M.; Saliba, M.; Schenck, K.; Grätzel, M.; Hagfeldt, A. Exploration of the Compositional Space for Mixed Lead Halogen Perovskites for High Efficiency Solar Cells. *Energy Environ. Sci.* **2016**, *9*, 1706–1724.  
1951 (96) Jacobsson, T. J.; Correa-Baena, J.-P.; Pazoki, M.; Saliba, M.; Schenck, K.; Grätzel, M.; Hagfeldt, A. Exploration of the Compositional Space for Mixed Lead Halogen Perovskites for High Efficiency Solar Cells. *Energy Environ. Sci.* **2016**, *9*, 1706–1724.  
1952 (97) Jacobsson, T. J.; Correa-Baena, J.-P.; Pazoki, M.; Saliba, M.; Schenck, K.; Grätzel, M.; Hagfeldt, A. Exploration of the Compositional Space for Mixed Lead Halogen Perovskites for High Efficiency Solar Cells. *Energy Environ. Sci.* **2016**, *9*, 1706–1724.  
1953 (98) Jacobsson, T. J.; Correa-Baena, J.-P.; Pazoki, M.; Saliba, M.; Schenck, K.; Grätzel, M.; Hagfeldt, A. Exploration of the Compositional Space for Mixed Lead Halogen Perovskites for High Efficiency Solar Cells. *Energy Environ. Sci.* **2016**, *9*, 1706–1724.  
1954 (99) Jacobsson, T. J.; Correa-Baena, J.-P.; Pazoki, M.; Saliba, M.; Schenck, K.; Grätzel, M.; Hagfeldt, A. Exploration of the Compositional Space for Mixed Lead Halogen Perovskites for High Efficiency Solar Cells. *Energy Environ. Sci.* **2016**, *9*, 1706–1724.  
1955 (100) Jacobsson, T. J.; Correa-Baena, J.-P.; Pazoki, M.; Saliba, M.; Schenck, K.; Grätzel, M.; Hagfeldt, A. Exploration of the Compositional Space for Mixed Lead Halogen Perovskites for High Efficiency Solar Cells. *Energy Environ. Sci.* **2016**, *9*, 1706–1724.  
1956 (101) Jacobsson, T. J.; Correa-Baena, J.-P.; Pazoki, M.; Saliba, M.; Schenck, K.; Grätzel, M.; Hagfeldt, A. Exploration of the Compositional Space for Mixed Lead Halogen Perovskites for High Efficiency Solar Cells. *Energy Environ. Sci.* **2016**, *9*, 1706–1724.  
1957 (102) Jacobsson, T. J.; Correa-Baena, J.-P.; Pazoki, M.; Saliba, M.; Schenck, K.; Grätzel, M.; Hagfeldt, A. Exploration of the Compositional Space for Mixed Lead Halogen Perovskites for High Efficiency Solar Cells. *Energy Environ. Sci.* **2016**, *9*, 1706–1724.  
1958 (103) Jacobsson, T. J.; Correa-Baena, J.-P.; Pazoki, M.; Saliba, M.; Schenck, K.; Grätzel, M.; Hagfeldt, A. Exploration of the Compositional Space for Mixed Lead Halogen Perovskites for High Efficiency Solar Cells. *Energy Environ. Sci.* **2016**, *9*, 1706–1724.  
1959 (104) Jacobsson, T. J.; Correa-Baena, J.-P.; Pazoki, M.; Saliba, M.; Schenck, K.; Grätzel, M.; Hagfeldt, A. Exploration of the Compositional Space for Mixed Lead Halogen Perovskites for High Efficiency Solar Cells. *Energy Environ. Sci.* **2016**, *9*, 1706–1724.  
1960 (105) Jacobsson, T. J.; Correa-Baena, J.-P.; Pazoki, M.; Saliba, M.; Schenck, K.; Grätzel, M.; Hagfeldt, A. Exploration of the Compositional Space for Mixed Lead Halogen Perovskites for High Efficiency Solar Cells. *Energy Environ. Sci.* **2016**, *9*, 1706–1724.  
1961 (106) Jacobsson, T. J.; Correa-Baena, J.-P.; Pazoki, M.; Saliba, M.; Schenck, K.; Grätzel, M.; Hagfeldt, A. Exploration of the Compositional Space for Mixed Lead Halogen Perovskites for High Efficiency Solar Cells. *Energy Environ. Sci.* **2016**, *9*, 1706–1724.  
1962 (107) Jacobsson, T. J.; Correa-Baena, J.-P.; Pazoki, M.; Saliba, M.; Schenck, K.; Grätzel, M.; Hagfeldt, A. Exploration of the Compositional Space for Mixed Lead Halogen Perovskites for High Efficiency Solar Cells. *Energy Environ. Sci.* **2016**, *9*, 1706–1724.  
1963 (108) Jacobsson, T. J.; Correa-Baena, J.-P.; Pazoki, M.; Saliba, M.; Schenck, K.; Grätzel, M.; Hagfeldt, A. Exploration of the Compositional Space for Mixed Lead Halogen Perovskites for High Efficiency Solar Cells. *Energy Environ. Sci.* **2016**, *9*, 1706–1724.  
1964 (109) Jacobsson, T. J.; Correa-Baena, J.-P.; Pazoki, M.; Saliba, M.; Schenck, K.; Grätzel, M.; Hagfeldt, A. Exploration of the Compositional Space for Mixed Lead Halogen Perovskites for High Efficiency Solar Cells. *Energy Environ. Sci.* **2016**, *9*, 1706–1724.  
1965 (110) Jacobsson, T. J.; Correa-Baena, J.-P.; Pazoki, M.; Saliba, M.; Schenck, K.; Grätzel, M.; Hagfeldt, A. Exploration of the Compositional Space for Mixed Lead Halogen Perovskites for High Efficiency Solar Cells. *Energy Environ. Sci.* **2016**, *9*, 1706–1724.  
1966 (111) Jacobsson, T. J.; Correa-Baena, J.-P.; Pazoki, M.; Saliba, M.; Schenck, K.; Grätzel, M.; Hagfeldt, A. Exploration of the Compositional Space for Mixed Lead Halogen Perovskites for High Efficiency Solar Cells. *Energy Environ. Sci.* **2016**, *9*, 1706–1724.  
1967 (112) Jacobsson, T. J.; Correa-Baena, J.-P.; Pazoki, M.; Saliba, M.; Schenck, K.; Grätzel, M.; Hagfeldt, A. Exploration of the Compositional Space for Mixed Lead Halogen Perovskites for High Efficiency Solar Cells. *Energy Environ. Sci.* **2016**, *9*, 1706–1724.  
1968 (113) Jacobsson, T. J.; Correa-Baena, J.-P.; Pazoki, M.; Saliba, M.; Schenck, K.; Grätzel, M.; Hagfeldt, A. Exploration of the Compositional Space for Mixed Lead Halogen Perovskites for High Efficiency Solar Cells. *Energy Environ. Sci.* **2016**, *9*, 1706–1724.  
1969 (114) Jacobsson, T. J.; Correa-Baena, J.-P.; Pazoki, M.; Saliba, M.; Schenck, K.; Grätzel, M.; Hagfeldt, A. Exploration of the Compositional Space for Mixed Lead Halogen Perovskites for High Efficiency Solar Cells. *Energy Environ. Sci.* **2016**, *9*, 1706–1724.  
1970 (115) Jacobsson, T. J.; Correa-Baena, J.-P.; Pazoki, M.; Saliba, M.; Schenck, K.; Grätzel, M.; Hagfeldt, A. Exploration of the Compositional Space for Mixed Lead Halogen Perovskites for High Efficiency Solar Cells. *Energy Environ. Sci.* **2016**, *9*, 1706–1724.  
1971 (116) Jacobsson, T. J.; Correa-Baena, J.-P.; Pazoki, M.; Saliba, M.; Schenck, K.; Grätzel, M.; Hagfeldt, A. Exploration of the Compositional Space for Mixed Lead Halogen Perovskites for High Efficiency Solar Cells. *Energy Environ. Sci.* **2016**, *9*, 1706–1724.  
1972 (117) Jacobsson, T. J.; Correa-Baena, J.-P.; Pazoki, M.; Saliba, M.; Schenck, K.; Grätzel, M.; Hagfeldt, A. Exploration of the Compositional Space for Mixed Lead Halogen Perovskites for High Efficiency Solar Cells. *Energy Environ. Sci.* **2016**, *9*, 1706–1724.  
1973 (118) Jacobsson, T. J.; Correa-Baena, J.-P.; Pazoki, M.; Saliba, M.; Schenck, K.; Grätzel, M.; Hagfeldt, A. Exploration of the Compositional Space for Mixed Lead Halogen Perovskites for High Efficiency Solar Cells. *Energy Environ. Sci.* **2016**, *9*, 1706–1724.  
1974 (119) Jacobsson, T. J.; Correa-Baena, J.-P.; Pazoki, M.; Saliba, M.; Schenck, K.; Grätzel, M.; Hagfeldt, A. Exploration of the Compositional Space for Mixed Lead Halogen Perovskites for High Efficiency Solar Cells. *Energy Environ. Sci.* **2016**, *9*, 1706–1724.  
1975 (120) Jacobsson, T. J.; Correa-Baena, J.-P.; Pazoki, M.; Saliba, M.; Schenck, K.; Grätzel, M.; Hagfeldt, A. Exploration of the Compositional Space for Mixed Lead Halogen Perovskites for High Efficiency Solar Cells. *Energy Environ. Sci.* **2016**, *9*, 1706–1724.  
1976 (121) Jacobsson, T. J.; Correa-Baena, J.-P.; Pazoki, M.; Saliba, M.; Schenck, K.; Grätzel, M.; Hagfeldt, A. Exploration of the Compositional Space for Mixed Lead Halogen Perovskites for High Efficiency Solar Cells. *Energy Environ. Sci.* **2016**, *9*, 1706–1724.  
1977 (122) Jacobsson, T. J.; Correa-Baena, J.-P.; Pazoki, M.; Saliba, M.; Schenck, K.; Grätzel, M.; Hagfeldt, A. Exploration of the Compositional Space for Mixed Lead Halogen Perovskites for High Efficiency Solar Cells. *Energy Environ. Sci.* **2016**, *9*, 1706–1724.  
1978 (123) Jacobsson, T. J.; Correa-Baena, J.-P.; Pazoki, M.; Saliba, M.; Schenck, K.; Grätzel, M.; Hagfeldt, A. Exploration of the Compositional Space for Mixed Lead Halogen Perovskites for High Efficiency Solar Cells. *Energy Environ. Sci.* **2016**, *9*, 1706–1724.  
1979 (124) Jacobsson, T. J.; Correa-Baena, J.-P.; Pazoki, M.; Saliba, M.; Schenck, K.; Grätzel, M.; Hagfeldt, A. Exploration of the Compositional Space for Mixed Lead Halogen Perovskites for High Efficiency Solar Cells. *Energy Environ. Sci.* **2016**, *9*, 1706–1724.  
1980 (125) Jacobsson, T. J.; Correa-Baena, J.-P.; Pazoki, M.; Saliba, M.; Schenck, K.; Grätzel, M.; Hagfeldt, A. Exploration of the Compositional Space for Mixed Lead Halogen Perovskites for High Efficiency Solar Cells. *Energy Environ. Sci.* **2016**, *9*, 1706–1724.  
1981 (126) Jacobsson, T. J.; Correa-Baena, J.-P.; Pazoki, M.; Saliba, M.; Schenck, K.; Grätzel, M.; Hagfeldt, A. Exploration of the Compositional Space for Mixed Lead Halogen Perovskites for High Efficiency Solar Cells. *Energy Environ. Sci.* **2016**, *9*, 1706–1724.  
1982 (127) Jacobsson, T. J.; Correa-Baena, J.-P.; Pazoki, M.; Saliba, M.; Schenck, K.; Grätzel, M.; Hagfeldt, A. Exploration of the Compositional Space for Mixed Lead Halogen Perovskites for High Efficiency Solar Cells. *Energy Environ. Sci.* **2016**, *9*, 1706–1724.  
1983 (128) Jacobsson, T. J.; Correa-Baena, J.-P.; Pazoki, M.; Saliba, M.; Schenck, K.; Grätzel, M.; Hagfeldt, A. Exploration of the Compositional Space for Mixed Lead Halogen Perovskites for High Efficiency Solar Cells. *Energy Environ. Sci.* **2016**, *9*, 1706–1724.  
1984 (129) Jacobsson, T. J.; Correa-Baena, J.-P.; Pazoki, M.; Saliba, M.; Schenck, K.; Grätzel, M.; Hagfeldt, A. Exploration of the Compositional Space for Mixed Lead Halogen Perovskites for High Efficiency Solar Cells. *Energy Environ. Sci.* **2016**, *9*, 1706–1724.  
1985 (130) Jacobsson, T. J.; Correa-Baena, J.-P.; Pazoki, M.; Saliba, M.; Schenck, K.; Grätzel, M.; Hagfeldt, A. Exploration of the Compositional Space for Mixed Lead Halogen Perovskites for High Efficiency Solar Cells. *Energy Environ. Sci.* **2016**, *9*, 1706–1724.  
1986 (131) Jacobsson, T. J.; Correa-Baena, J.-P.; Pazoki, M.; Saliba, M.; Schenck, K.; Grätzel, M.; Hagfeldt, A. Exploration of the Compositional Space for Mixed Lead Halogen Perovskites for High Efficiency Solar Cells. *Energy Environ. Sci.* **2016**, *9*, 1706–1724.  
1987 (132) Jacobsson, T. J.; Correa-Baena, J.-P.; Pazoki, M.; Saliba, M.; Schenck, K.; Grätzel, M.; Hagfeldt, A. Exploration of the Compositional Space for Mixed Lead Halogen Perovskites for High Efficiency Solar Cells. *Energy Environ. Sci.* **2016**, *9*, 1706–1724.  
1988 (133) Jacobsson, T. J.; Correa-Baena, J.-P.; Pazoki, M.; Saliba, M.; Schenck, K.; Grätzel, M.; Hagfeldt, A. Exploration of the Compositional Space for Mixed Lead Halogen Perovskites for High Efficiency Solar Cells. *Energy Environ. Sci.* **2016**, *9*, 1706–1724.  
1989 (134) Jacobsson, T. J.; Correa-Baena, J.-P.; Pazoki, M.; Saliba, M.; Schenck, K.; Grätzel, M.; Hagfeldt, A. Exploration of the Compositional Space for Mixed Lead Halogen Perovskites for High Efficiency Solar Cells. *Energy Environ. Sci.* **2016**, *9*, 1706–1724.  
1990 (135) Jacobsson, T. J.; Correa-Baena, J.-P.; Pazoki, M.; Saliba, M.; Schenck, K.; Grätzel, M.; Hagfeldt, A. Exploration of the Compositional Space for Mixed Lead Halogen Perovskites for High Efficiency Solar Cells. *Energy Environ. Sci.* **2016**, *9*, 1706–1724.  
1991 (136) Jacobsson, T. J.; Correa-Baena, J.-P.; Pazoki, M.; Saliba, M.; Schenck, K.; Grätzel, M.; Hagfeldt, A. Exploration of the Compositional Space for Mixed Lead Halogen Perovskites for High Efficiency Solar Cells. *Energy Environ. Sci.* **2016**, *9*, 1706–1724.  
1992 (137) Jacobsson, T. J.; Correa-Baena, J.-P.; Pazoki, M.; Saliba, M.; Schenck, K.; Grätzel, M.; Hagfeldt, A. Exploration of the Compositional Space for Mixed Lead Halogen Perovskites for High Efficiency Solar Cells. *Energy Environ. Sci.* **2016**, *9*, 1706–1724.  
1993 (138) Jacobsson, T. J.; Correa-Baena, J.-P.; Pazoki, M.; Saliba, M.; Schenck, K.; Grätzel, M.; Hagfeldt, A. Exploration of the Compositional Space for Mixed Lead Halogen Perovskites for High Efficiency Solar Cells. *Energy Environ. Sci.* **2016**, *9*, 1706–1724.  
1994 (139) Jacobsson, T. J.; Correa-Baena, J.-P.; Pazoki, M.; Saliba, M.; Schenck, K.; Grätzel, M.; Hagfeldt, A. Exploration of the Compositional Space for Mixed Lead Halogen Perovskites for High Efficiency Solar Cells. *Energy Environ. Sci.* **2016**, *9*, 1706–1724.  
1995 (140) Jacobsson, T. J.; Correa-Baena, J.-P.; Pazoki, M.; Saliba, M.; Schenck, K.; Grätzel, M.; Hagfeldt, A. Exploration of the Compositional Space for Mixed Lead Halogen Perovskites for High Efficiency Solar Cells. *Energy Environ. Sci.* **2016**, *9*, 1706–1724.  
1996 (141) Jacobsson, T. J.; Correa-Baena, J.-P.; Pazoki, M.; Saliba, M.; Schenck, K.; Grätzel, M.; Hagfeldt, A. Exploration of the Compositional Space for Mixed Lead Halogen Perovskites for High Efficiency Solar Cells. *Energy Environ. Sci.* **2016**, *9*, 1706–1724.  
1997 (142) Jacobsson, T. J.; Correa-Baena, J.-P.; Pazoki, M.; Saliba, M.; Schenck, K.; Grätzel, M.; Hagfeldt, A. Exploration of the Compositional Space for Mixed Lead Halogen Perovskites for High Efficiency Solar Cells. *Energy Environ. Sci.* **2016**, *9*, 1706–1724.  
1998 (143) Jacobsson, T. J.; Correa-Baena, J.-P.; Pazoki, M.; Saliba, M.; Schenck, K.; Grätzel, M.; Hagfeldt, A. Exploration of the Compositional Space for Mixed Lead Halogen Perovskites for High Efficiency Solar Cells. *Energy Environ. Sci.* **2016**, *9*, 1706–1724.  
1999 (144) Jacobsson, T. J.; Correa-Baena, J.-P.; Pazoki, M.; Saliba, M.; Schenck, K.; Grätzel, M.; Hagfeldt, A. Exploration of the Compositional Space for Mixed Lead Halogen Perovskites for High Efficiency Solar Cells. *Energy Environ. Sci.* **2016**, *9*, 1706–1724.  
2000 (145) Jacobsson, T. J.; Correa-Baena, J.-P.; Pazoki, M.; Saliba, M.; Schenck, K.; Grätzel, M.; Hagfeldt, A. Exploration of the Compositional Space for Mixed Lead Halogen Perovskites for High Efficiency Solar Cells. *Energy Environ. Sci.* **2016**, *9*, 1706–1724.  
2001 (146) Jacobsson, T. J.; Correa-Baena, J.-P.; Pazoki, M.; Saliba, M.; Schenck, K.; Grätzel, M.; Hagfeldt, A. Exploration of the Compositional Space for Mixed Lead Halogen Perovskites for High Efficiency Solar Cells. *Energy Environ. Sci.* **2016**, *9*, 1706–1724.  
2002 (147) Jacobsson, T. J.; Correa-Baena, J.-P.; Pazoki, M.; Saliba, M.; Schenck, K.; Grätzel, M.; Hagfeldt, A. Exploration of the Compositional Space for Mixed Lead Halogen Perovskites for High Efficiency Solar Cells. *Energy Environ. Sci.* **2016**, *9*, 1706–1724.  
2003 (148) Jacobsson, T. J.; Correa-Baena, J.-P.; Pazoki, M.; Saliba, M.; Schenck, K.; Grätzel, M.; Hagfeldt, A. Exploration of the Compositional Space for Mixed Lead Halogen Perovskites for High Efficiency Solar Cells. *Energy Environ. Sci.* **2016**, *9*, 1706–1724.  
2004 (149) Jacobsson, T. J.; Correa-Baena, J.-P.; Pazoki, M.; Saliba, M.; Schenck, K.; Grätzel, M.; Hagfeldt, A. Exploration of the Compositional Space for Mixed Lead Halogen Perovskites for High Efficiency Solar Cells. *Energy Environ. Sci.* **2016**, *9*, 1706–1724.  
2005 (150) Jacobsson, T. J.; Correa-Baena, J.-P.; Pazoki, M.; Saliba, M.; Schenck, K.; Grätzel, M.; Hagfeldt, A. Exploration of the Compositional Space for Mixed Lead Halogen Perovskites for High Efficiency Solar Cells. *Energy Environ. Sci.* **2016**, *9*, 1706–1724.  
20

- 1995 (91) Shockley, W.; Queisser, H. J. Detailed Balance Limit of 1996 Efficiency of P-N Junction Solar Cells. *J. Appl. Phys.* **1961**, *32*, 510–1997 519.
- 1998 (92) Berhe, T. A.; Su, W.-N.; Chen, C.-H.; Pan, C.-J.; Cheng, J.-H.; 1999 Chen, H.-M.; Tsai, M.-C.; Chen, L.-Y.; Dubale, A. A.; Hwang, B.-J. 2000 Organometal Halide Perovskite Solar Cells: Degradation and Stability. *Energy Environ. Sci.* **2016**, *9*, 323–356.
- 2002 (93) Xu, T.; Chen, L.; Guo, Z.; Ma, T. Strategic Improvement of The 2003 Long-Term Stability of Perovskite Materials and Perovskite Solar 2004 Cells. *Phys. Chem. Chem. Phys.* **2016**, *18*, 27026–27050.
- 2005 (94) Carignano, M. A.; Saeed, Y.; Aravindh, S. A.; Roqan, I. S.; Even, 2006 J.; Katan, C. A Close Examination of the Structure and Dynamics of 2007  $\text{HC}(\text{NH}_2)_2\text{PbI}_3$  by MD Simulations and Group Theory. *Phys. Chem. 2008 Chem. Phys.* **2016**, *18*, 27109–27118.
- 2009 (95) Hakamata, T.; Shimamura, K.; Shimojo, F.; Kalia, R. K.; 2010 Nakano, A.; Vashishta, P. The Nature of Free-Carrier Transport in 2011 Organometal Halide Perovskites. *Sci. Rep.* **2016**, *6*, 19599.
- 2012 (96) Beecher, A. N.; Semonin, O. E.; Skelton, J. M.; Frost, J. M.; 2013 Terban, M. W.; Zhai, H.; Alatas, A.; Owen, J. S.; Walsh, A.; Billinge, S. 2014 J. L. Direct Observation of Dynamic Symmetry Breaking above Room 2015 Temperature in Methylammonium Lead Iodide Perovskite. *ACS 2016 Energy Lett.* **2016**, *1*, 880–887.
- 2017 (97) Bergmann, V. W.; Guo, Y.; Tanaka, H.; Hermes, I. M.; Li, D.; 2018 Klasen, A.; Bretschneider, S. A.; Nakamura, E.; Berger, R.; Weber, S. A. 2019 L. Local Time-Dependent Charging in a Perovskite Solar Cell. *ACS 2020 Appl. Mater. Interfaces* **2016**, *8*, 19402–19409.
- 2021 (98) Sutton, R. J.; Eperon, G. E.; Miranda, L.; Parrott, E. S.; Kamino, 2022 B. A.; Patel, J. B.; Hörrnner, M. T.; Johnston, M. B.; Haghighirad, A. 2023 A.; Moore, D. T.; et al. Bandgap-Tunable Cesium Lead Halide 2024 Perovskites with High Thermal Stability for Efficient Solar Cells. *Adv. 2025 Energy Mater.* **2016**, *6*, 1502458.
- 2026 (99) Lee, J.-W.; Seol, D.-J.; Cho, A.-N.; Park, N.-G. High-Efficiency 2027 Perovskite Solar Cells Based on the Black Polymorph of  $\text{HC}-\text{PbI}_3$ . *Adv. Mater.* **2014**, *26*, 4991–4998.
- 2029 (100) Lee, J.-W.; Kim, D.-H.; Kim, H.-S.; Seo, S.-W.; Cho, S. M.; 2030 Park, N.-G. Formamidinium and Cesium Hybridization for Photo- and 2031 Moisture-Stable Perovskite Solar Cell. *Adv. Energy Mater.* **2015**, *5*, 2032 1501310.
- 2033 (101) Li, Z.; Yang, M.; Park, J.-S.; Wei, S.-H.; Berry, J. J.; Zhu, K. 2034 Stabilizing Perovskite Structures by Tuning Tolerance Factor: 2035 Formation of Formamidinium and Cesium Lead Iodide Solid-State 2036 Alloys. *Chem. Mater.* **2016**, *28*, 284–292.
- 2037 (102) Pellet, N.; Gao, P.; Gregori, G.; Yang, T.-Y.; Nazeeruddin, M. 2038 K.; Maier, J.; Grätzel, M. Mixed-Organic-Cation Perovskite Photo- 2039 voltaics for Enhanced Solar-Light Harvesting. *Angew. Chem., Int. Ed.* 2040 **2014**, *53*, 3151–3157.
- 2041 (103) Aharon, S.; Dymshits, A.; Rotem, A.; Etgar, L. Temperature 2042 Dependence of Hole Conductor Free Formamidinium Lead Iodide 2043 Perovskite Based Solar Cells. *J. Mater. Chem. A* **2015**, *3*, 9171–9178.
- 2044 (104) Salado, M.; Calio, L.; Berger, R.; Kazim, S.; Ahmad, S. 2045 Influence of the Mixed Organic Cation Ratio in Lead Iodide Based 2046 Perovskite on the Performance of Solar Cells. *Phys. Chem. Chem. Phys.* 2047 **2016**, *18*, 27148–27157.
- 2048 (105) Mahmud, M. A.; Elumalai, N. K.; Upama, M. B.; Wang, D.; 2049 Wright, M.; Chan, K. H.; Xu, C.; Haque, F.; Uddin, A. Single Vs Mixed 2050 Organic Cation for Low Temperature Processed Perovskite Solar 2051 Cells. *Electrochim. Acta* **2016**, *222*, 1510–1521.
- 2052 (106) Binek, A.; Hanusch, F. C.; Docampo, P.; Bein, T. Stabilization 2053 of the Trigonal High-Temperature Phase of Formamidinium Lead 2054 Iodide. *J. Phys. Chem. Lett.* **2015**, *6*, 1249–1253.
- 2055 (107) Ji, F.; Wang, L.; Pang, S.; Gao, P.; Xu, H.; Xie, G.; Zhang, J.; 2056 Cui, G. A Balanced Cation Exchange Reaction Toward Highly 2057 Uniform and Pure Phase  $\text{FA}_{1-x}\text{MA}_x\text{PbI}_3$  Perovskite Films. *J. Mater. 2058 Chem. A* **2016**, *4*, 14437–14443.
- 2059 (108) Li, G.; Zhang, T.; Guo, N.; Xu, F.; Qian, X.; Zhao, Y. Ion- 2060 Exchange-Induced 2D–3D Conversion of  $\text{HMA}_{1-x}\text{FA}_x\text{PbI}_3\text{Cl}$  Perov- 2061 skite into a High-Quality  $\text{MA}_{1-x}\text{FA}_x\text{PbI}_3$  Perovskite. *Angew. Chem., Int.* 2062 *Ed.* **2016**, *55*, 13460–13464.
- (109) Liu, J.; Shirai, Y.; Yang, X.; Yue, Y.; Chen, W.; Wu, Y.; Islam, A.; Han, L. High-Quality Mixed-Organic-Cation Perovskites from a Phase-Pure Non-stoichiometric Intermediate  $(\text{FAI})_{1-x}\text{PbI}_2$  for Solar Cells. *Adv. Mater.* **2015**, *27*, 4918–4923.
- (110) Chen, C.-C.; Chang, S. H.; Chen, L.-C.; Kao, F.-S.; Cheng, H.-M.; Yeh, S.-C.; Chen, C.-T.; Wu, W.-T.; Tseng, Z.-L.; Chuang, C. L.; et al. Improving the Efficiency of Inverted Mixed-Organic-Cation Perovskite Absorber based Photovoltaics by Tailoring the Surface Roughness of PEDOT: PSS Thin Film. *Sol. Energy* **2016**, *134*, 445–451.
- (111) Deng, Y.; Dong, Q.; Bi, C.; Yuan, Y.; Huang, J. Air-Stable, Efficient Mixed-Cation Perovskite Solar Cells with Cu Electrode by Scalable Fabrication of Active Layer. *Adv. Energy Mater.* **2016**, *6*, 1600372.
- (112) Kim, J.; Kim, H. P.; Teridi, M. A. M.; Yusoff, A. R. b. M.; Jang, J. Bandgap Tuning of Mixed Organic Cation Utilizing Chemical Vapor Deposition Process. *Sci. Rep.* **2016**, *6*, 37378.
- (113) Chen, J.; Xu, J.; Xiao, L.; Zhang, B.; Dai, S.; Yao, J. Mixed-Organic-Cation  $(\text{FA})_x(\text{MA})_{1-x}\text{PbI}_3$  Planar Perovskite Solar Cells with 16.48% Efficiency via a Low-Pressure Vapor-Assisted Solution Process. *ACS Appl. Mater. Interfaces* **2017**, *9*, 2449–2458.
- (114) Frost, J. M.; Butler, K. T.; Brivio, F.; Hendon, C. H.; van Schilfgaarde, M.; Walsh, A. Atomistic Origins of High-Performance in Hybrid Halide Perovskite Solar Cells. *Nano Lett.* **2014**, *14*, 2584–2590.
- (115) Choi, H.; Jeong, J.; Kim, H.-B.; Kim, S.; Walker, B.; Kim, G.-H.; Kim, J. Y. Cesium-Doped Methylammonium Lead Iodide Perovskite Light Absorber for Hybrid Solar Cells. *Nano Energy* **2014**, *7*, 80–85.
- (116) Niu, G.; Li, W.; Li, J.; Liang, X.; Wang, L. Enhancement of Thermal Stability for Perovskite Solar Cells through Cesium Doping. *RSC Adv.* **2017**, *7*, 17473–17479.
- (117) Yi, C.; Luo, J.; Meloni, S.; Boziki, A.; Ashari-Astani, N.; Grätzel, C.; Zakeeruddin, S. M.; Rothlisberger, U.; Grätzel, M. Entropic Stabilization of Mixed A-Cation  $\text{ABX}_3$  Metal Halide Perovskites for High Performance Perovskite Solar Cells. *Energy Environ. Sci.* **2016**, *9*, 656–662.
- (118) Yu, Y.; Wang, C.; Grice, C. R.; Shrestha, N.; Chen, J.; Zhao, D.; Liao, W.; Cimaroli, A. J.; Roland, P. J.; Ellingson, R. J.; et al. Improving the Performance of Formamidinium and Cesium Lead Triiodide Perovskite Solar Cells using Lead Thiocyanate Additives. *ChemSusChem* **2016**, *9*, 3288–3297.
- (119) Liu, T.; Zong, Y.; Zhou, Y.; Yang, M.; Li, Z.; Game, O. S.; Zhu, K.; Zhu, R.; Gong, Q.; Padture, N. P. High-Performance Formamidinium-Based Perovskite Solar Cells via Microstructure-Mediated  $\delta$ -to- $\alpha$  Phase Transformation. *Chem. Mater.* **2017**, *29*, 3246–3250.
- (120) Huang, J.; Xu, P.; Liu, J.; You, X.-Z. Sequential Introduction of Cations Deriving Large-Grain  $\text{Cs}_x\text{FA}_{1-x}\text{PbI}_3$  Thin Film for Planar Hybrid Solar Cells: Insight into Phase-Segregation and Thermal-Healing Behavior. *Small* **2017**, *13*, 1603225.
- (121) Park, Y. H.; Jeong, I.; Bae, S.; Son, H. J.; Lee, P.; Lee, J.; Lee, C.-H.; Ko, M. J. Inorganic Rubidium Cation as an Enhancer for Photovoltaic Performance and Moisture Stability of  $\text{HC}(\text{NH}_2)_2\text{PbI}_3$  Perovskite Solar Cells. *Adv. Funct. Mater.* **2017**, *27*, 1605988.
- (122) Zhang, M.; Yun, J. S.; Ma, Q.; Zheng, J.; Lau, C. F. J.; Deng, X.; Kim, J.; Kim, D.; Seidel, J.; Green, M. A.; et al. High-Efficiency Rubidium-Incorporated Perovskite Solar Cells by Gas Quenching. *ACS Energy Lett.* **2017**, *2*, 438–444.
- (123) Niu, G.; Yu, H.; Li, J.; Wang, D.; Wang, L. Controlled Orientation of Perovskite Films Through Mixed Cations Toward High Performance Perovskite Solar Cells. *Nano Energy* **2016**, *27*, 87–94.
- (124) Chen, B.-X.; Li, W.-G.; Rao, H.-S.; Xu, Y.-F.; Kuang, D.-B.; Su, C.-Y. Large-Grained Perovskite Films via  $\text{FA}_x\text{MA}_{1-x}\text{Pb}(\text{I}_x\text{Br}_{1-x})_3$  Single Crystal Precursor for Efficient Solar Cells. *Nano Energy* **2017**, *34*, 264–270.
- (125) Zheng, X.; Wu, C.; Jha, S. K.; Li, Z.; Zhu, K.; Priya, S. Improved Phase Stability of Formamidinium Lead Triiodide Perovskite by Strain Relaxation. *ACS Energy Lett.* **2016**, *1*, 1014–1020.

- 2132 (126) Chen, L. C.; Tseng, Z. L.; Huang, J. K. A Study of Inverted-  
2133 Type Perovskite Solar Cells with Various Composition Ratios of  
2134 ( $\text{FAPbI}_3$ )<sub>(1-x)</sub>( $\text{MAPbBr}_3$ )<sub>x</sub> *Nanomaterials* **2016**, *6*, 183.
- 2135 (127) Sveinbjörnsson, K.; Aitola, K.; Zhang, J.; Johansson, M. B.;  
2136 Zhang, X.; Correa-Baena, J.-P.; Hagfeldt, A.; Boschloo, G.; Johansson,  
2137 E. M. J. Ambient Air-Processed Mixed-Ion Perovskites for High-  
2138 Efficiency Solar Cells. *J. Mater. Chem. A* **2016**, *4*, 16536–16545.
- 2139 (128) Reyna, Y.; Salado, M.; Kazim, S.; Pérez-Tomas, A.; Ahmad, S.;  
2140 Lira-Cantu, M. Performance and Stability of Mixed FAP-  
2141  $\text{bl}_{3(0.85)}\text{MAPbBr}_{3(0.15)}$  Halide Perovskite Solar Cells Under Outdoor  
2142 Conditions and the Effect of Low Light Irradiation. *Nano Energy* **2016**,  
2143 *30*, 570–579.
- 2144 (129) Chen, L.-C.; Wu, J.-R.; Tseng, Z.-L.; Chen, C.-C.; Chang, S.;  
2145 Huang, J.-K.; Lee, K.-L.; Cheng, H.-M. Annealing Effect on  
2146 ( $\text{FAPbI}_3$ )<sub>1-x</sub>( $\text{MAPbBr}_3$ )<sub>x</sub> Perovskite Films in Inverted-Type Perovskite  
2147 Solar Cells. *Materials* **2016**, *9*, 747.
- 2148 (130) Bi, D.; Tress, W.; Dar, M. I.; Gao, P.; Luo, J.; Renévier, C.;  
2149 Schenk, K.; Abate, A.; Giordano, F.; Correa Baena, J.-P.; et al. Efficient  
2150 Luminescent Solar Cells Based on Tailored Mixed-Cation Perovskites.  
2151 *Sci. Adv.* **2016**, *2*, e1501170.
- 2152 (131) Isikgor, F. H.; Li, B.; Zhu, H.; Xu, Q.; Ouyang, J. High  
2153 Performance Planar Perovskite Solar Cells With A Perovskite Of  
2154 Mixed Organic Cations And Mixed Halides,  $\text{MA}_{1-x}\text{FA}_x\text{PbI}_{3-y}\text{Cl}_y$ . *J.*  
2155 *Mater. Chem. A* **2016**, *4*, 12543–12553.
- 2156 (132) McMeekin, D. P.; Sadoughi, G.; Rehman, W.; Eperon, G. E.;  
2157 Saliba, M.; Hörantner, M. T.; Haghhighirad, A.; Sakai, N.; Korte, L.;  
2158 Rech, B.; et al. A Mixed-Cation Lead Mixed-Halide Perovskite  
2159 Absorber for Tandem Solar Cells. *Science* **2016**, *351*, 151–155.
- 2160 (133) Bush, K. A.; Palmstrom, A. F.; Yu, Z. J.; Boccard, M.;  
2161 Cheacharoen, R.; Mailoa, J. P.; McMeekin, D. P.; Hoye, R. L. Z.; Bailie,  
2162 C. D.; Leijtens, T.; et al. 23.6%-Efficient Monolithic Perovskite/Silicon  
2163 Tandem Solar Cells with Improved Stability. *Nat. Energy* **2017**, *2*,  
2164 17009.
- 2165 (134) Wang, Z.; McMeekin, D. P.; Sakai, N.; van Reenen, S.;  
2166 Wojciechowski, K.; Patel, J. B.; Johnston, M. B.; Snaith, H. J. Efficient  
2167 and Air-Stable Mixed-Cation Lead Mixed-Halide Perovskite Solar  
2168 Cells with n-Doped Organic Electron Extraction Layers. *Adv. Mater.*  
2169 **2017**, *29*, 1604186.
- 2170 (135) Matsui, T.; Seo, J.-Y.; Saliba, M.; Zakeeruddin, S. M.; Grätzel,  
2171 M. Room-Temperature Formation of Highly Crystalline Multication  
2172 Perovskites for Efficient, Low-Cost Solar Cells. *Adv. Mater.* **2017**, *29*,  
2173 1606258.
- 2174 (136) Duong, T.; Mulmudi, H. K.; Shen, H.; Wu, Y.; Barugkin, C.;  
2175 Mayon, Y. O.; Nguyen, H. T.; Macdonald, D.; Peng, J.; Lockrey, M.;  
2176 et al. Structural Engineering Using Rubidium Iodide as a Dopant  
2177 Under Excess Lead Iodide Conditions for High Efficiency and Stable  
2178 Perovskites. *Nano Energy* **2016**, *30*, 330–340.
- 2179 (137) Saliba, M.; Matsui, T.; Domanski, K.; Seo, J. Y.; Ummadisingu,  
2180 A.; Zakeeruddin, S. M.; Correa-Baena, J. P.; Tress, W. R.; Abate, A.;  
2181 Hagfeldt, A.; et al. Incorporation of Rubidium Cations Into Perovskite  
2182 Solar Cells Improves Photovoltaic Performance. *Science* **2016**, *354*,  
2183 206–209.
- 2184 (138) Duong, T.; Wu, Y.; Shen, H.; Peng, J.; Fu, X.; Jacobs, D.;  
2185 Wang, E.-C.; Kho, T. C.; Fong, K. C.; Stocks, M.; et al. Rubidium  
2186 Multication Perovskite with Optimized Bandgap for Perovskite-Silicon  
2187 Tandem with over 26% Efficiency. *Adv. Energy Mater.* **2017**, *7*,  
2188 1700228.
- 2189 (139) Son, D.-Y.; Lee, J.-W.; Choi, Y. J.; Jang, I.-H.; Lee, S.; Yoo, P.  
2190 J.; Shin, H.; Ahn, N.; Choi, M.; Kim, D.; et al. Self-Formed Grain  
2191 Boundary Healing Layer for Highly Efficient  $\text{CH}_3\text{NH}_3\text{PbI}_3$  Perovskite  
2192 Solar Cells. *Nat. Energy* **2016**, *1*, 16081.
- 2193 (140) Momblona, C.; Gil-Escríg, L.; Bandiello, E.; Hutter, E. M.;  
2194 Sessolo, M.; Lederer, K.; Blochwitz-Nimoth, J.; Bolink, H. J. Efficient  
2195 Vacuum Deposited p-i-n and n-i-p Perovskite Solar Cells Employing  
2196 Doped Charge Transport Layers. *Energy Environ. Sci.* **2016**, *9*, 3456–  
2197 3463.
- 2198 (141) Wu, C.-G.; Chiang, C.-H.; Tseng, Z.-L.; Nazeeruddin, M. K.;  
2199 Hagfeldt, A.; Grätzel, M. High efficiency stable inverted perovskite  
solar cells without current hysteresis. *Energy Environ. Sci.* **2015**, *8*, 2200  
2725–2733.
- 2200 (142) Wang, F.; Yu, H.; Xu, H.; Zhao, N.  $\text{HPbI}_3$ : A New Precursor  
2201 Compound for Highly Efficient Solution-Processed Perovskite Solar  
2202 Cells. *Adv. Funct. Mater.* **2015**, *25*, 1120–1126.
- 2203 (143) Zhou, Y.; Yang, M.; Pang, S.; Zhu, K.; Padture, N. P. Exceptional  
2204 Morphology-Preserving Evolution of Formamidinium Lead Triiodide  
2205 Perovskite Thin Films via Organic-Cation Displacement. *J. Am. Chem. Soc.* **2016**, *138*, 5535–5538.
- 2206 (144) Pool, V. L.; Dou, B.; Van Campen, D. G.; Klein-Stockert, T. R.;  
2207 Barnes, F. S.; Shaheen, S. E.; Ahmad, M. I.; van Hest, M. F. A. M.;  
2208 Toney, M. F. Thermal engineering of FAPbI<sub>3</sub> perovskite material via  
2209 radiative thermal annealing and in situ XRD. *Nat. Commun.* **2017**, *8*,  
2210 14075.
- 2211 (145) Lee, J.-W.; Kim, H.-S.; Park, N.-G. APbI<sub>3</sub> (A =  $\text{CH}_3\text{NH}_3$  and  
2212  $\text{HC}(\text{NH}_2)_2$ ) Perovskite Solar Cells: From Sensitization to Planar  
2213 Heterojunction. In *Organic-Inorganic Halide Perovskite Photovoltaics*,  
2214 From Fundamentals to Device Architectures; Park, N.-G., Miyasaka, T.,  
2215 Grätzel, M., Eds.; Springer International Publishing: Switzerland, 2016;  
2216 pp 223–253.
- 2217 (146) Amat, A.; Mosconi, E.; Ronca, E.; Quart, C.; Umari, P.;  
2218 Nazeeruddin, M. K.; Grätzel, M.; De Angelis, F. Cation-Induced Band-  
2219 Gap Tuning in Organohalide Perovskites: Interplay of Spin–Orbit  
2220 Coupling and Octahedra Tilting. *Nano Lett.* **2014**, *14*, 3608–3616.
- 2221 (147) Eperon, G. E.; Stranks, S. D.; Menelaou, C.; Johnston, M. B.;  
2222 Herz, L. M.; Snaith, H. J. Formamidinium Lead Trihalide: A Broadly  
2223 Tunable Perovskite for Efficient Planar Heterojunction Solar Cells.  
2224 *Energy Environ. Sci.* **2014**, *7*, 982–988.
- 2225 (148) Zhang, T.; Meng, X.; Bai, Y.; Xiao, S.; Hu, C.; Yang, Y.; Chen,  
2226 H.; Yang, S. Profiling the Organic Cation-Dependent Degradation of  
2227 Organolead Halide Perovskite Solar Cells. *J. Mater. Chem. A* **2017**, *5*,  
2228 1103–1111.
- 2229 (149) Weller, M. T.; Weber, O. J.; Frost, J. M.; Walsh, A. Cubic  
2230 Perovskite Structure of Black Formamidinium Lead Iodide,  $\alpha$ -  
2231  $[\text{HC}(\text{NH}_2)_2]\text{PbI}_3$ , at 298 K. *J. Phys. Chem. Lett.* **2015**, *6*, 3209–3212.
- 2232 (150) Han, Q.; Bae, S.-H.; Sun, P.; Hsieh, Y.-T.; Yang, Y.; Rim, Y. S.;  
2233 Zhao, H.; Chen, Q.; Shi, W.; Li, G.; et al. Single Crystal  
2234 Formamidinium Lead Iodide (FAPbI<sub>3</sub>): Insight into the Structural,  
2235 Optical, and Electrical Properties. *Adv. Mater.* **2016**, *28*, 2253–2258.
- 2236 (151) Ma, F.; Li, J.; Li, W.; Lin, N.; Wang, L.; Qiao, J. Stable alpha/  
2237 delta Phase Junction of Formamidinium Lead Iodide Perovskites for  
2238 Enhanced Near-Infrared Emission. *Chem. Sci.* **2017**, *8*, 800–805.
- 2239 (152) Dai, J.; Fu, Y.; Manger, L. H.; Rea, M. T.; Hwang, L.;  
2240 Goldsmith, R. H.; Jin, S. Carrier Decay Properties of Mixed Cation  
2241 Formamidinium–Methylammonium Lead Iodide Perovskite  
2242  $[\text{HC}(\text{NH}_2)_2]_{1-x}[\text{CH}_3\text{NH}_3]_x\text{PbI}_3$  Nanorods. *J. Phys. Chem. Lett.* **2016**, *7*,  
2243 5036–5043.
- 2244 (153) Slimi, B.; Mollar, M.; Assaker, I. B.; Kriaa, I.; Chtourou, R.;  
2245 Marí, B. Perovskite FA<sub>1-x</sub>MA<sub>x</sub>PbI<sub>3</sub> for Solar Cells: Films Formation and  
2246 Properties. *Energy Procedia* **2016**, *102*, 87–95.
- 2247 (154) El-Mellouhi, F.; Bentria, E. T.; Rashkeev, S. N.; Kais, S.;  
2248 Alharbi, F. H. Enhancing Intrinsic Stability of Hybrid Perovskite Solar  
2249 Cell by Strong, yet Balanced, Electronic Coupling. *Sci. Rep.* **2016**, *6*,  
2250 30305.
- 2251 (155) Eperon, G. E.; Paterno, G. M.; Sutton, R. J.; Zampetti, A.;  
2252 Haghhighirad, A. A.; Cacialli, F.; Snaith, H. J. Inorganic Caesium Lead  
2253 Iodide Perovskite Solar Cells. *J. Mater. Chem. A* **2015**, *3*, 19688–  
2254 19695.
- 2255 (156) Chen, Z.; Wang, J. J.; Ren, Y.; Yu, C.; Shum, K. Schottky Solar  
2256 Cells Based on CsSnI<sub>3</sub> Thin-Films. *Appl. Phys. Lett.* **2012**, *101*, 093901.
- 2257 (157) Syzgantseva, O. A.; Saliba, M.; Grätzel, M.; Rothlisberger, U.  
2258 Stabilization of the Perovskite Phase of Formamidinium Lead  
2259 Triiodide by Methylammonium, Cs, and/or Rb Doping. *J. Phys. Chem. Lett.* **2017**, *8*, 1191–1196.
- 2260 (158) Kieslich, G.; Sun, S.; Cheetham, A. K. Solid-State Principles  
2261 Applied to Organic-Inorganic Perovskites: New Tricks for an Old Dog.  
2262 *Chem. Sci.* **2014**, *5*, 4712–4715.

- 2267 (159) Kieslich, G.; Sun, S.; Cheetham, A. K. An extended Tolerance  
2268 Factor approach for organic-inorganic perovskites. *Chem. Sci.* **2015**, *6*,  
2269 3430–3433.
- 2270 (160) Travis, W.; Glover, E. N. K.; Bronstein, H.; Scanlon, D. O.;  
2271 Palgrave, R. G. On the Application of the Tolerance Factor to  
2272 Inorganic and Hybrid Halide Perovskites: A Revised System. *Chem.  
2273 Sci.* **2016**, *7*, 4548–4556.
- 2274 (161) Brigoch, J.; Lehner, A. J.; Chabiny, M.; Seshadri, R. Ab Initio  
2275 Calculations of Band Gaps and Absolute Band Positions of  
2276 Polymorphs of  $\text{RbPbI}_3$  and  $\text{CsPbI}_3$ : Implications for Main-Group  
2277 Halide Perovskite Photovoltaics. *J. Phys. Chem. C* **2014**, *118*, 27721–  
2278 27727.
- 2279 (162) Jishi, R. A.; Ta, O. B.; Sharif, A. A. Modeling of Lead Halide  
2280 Perovskites for Photovoltaic Applications. *J. Phys. Chem. C* **2014**, *118*,  
2281 28344–28349.
- 2282 (163) Yunakova, O. N.; Miloslavskii, V. K.; Kovalenko, E. N. Exciton  
2283 Absorption Spectrum of Thin  $(\text{KI})_{1-x}(\text{PbI}_2)_x$  Films. *Funct. Mater.*  
2284 **2013**, *20*, 59–63.
- 2285 (164) Trots, D. M.; Myagkota, S. V. High-Temperature Structural  
2286 Evolution of Caesium and Rubidium Triiodoplumbates. *J. Phys. Chem.  
2287 Solids* **2008**, *69*, 2520–2526.
- 2288 (165) Ralaizarisoa, M.; Busby, Y.; Frisch, J.; Salzmann, I.; Pireaux, J.-J.;  
2289 Koch, N. Correlation of Annealing Time with Crystal Structure,  
2290 Composition, and Electronic Properties of  $\text{CH}_3\text{NH}_3\text{PbI}_{3-x}\text{Cl}_x$  Mixed-  
2291 Halide Perovskite Films. *Phys. Chem. Chem. Phys.* **2017**, *19*, 828–836.
- 2292 (166) Heo, J. H.; Lee, M. H.; Jang, M. H.; Im, S. H. Highly Efficient  
2293  $\text{CH}_3\text{NH}_3\text{PbI}_{3-x}\text{Cl}_x$  Mixed Halide Perovskite Solar Cells Prepared by  
2294 Re-Dissolution and Crystal Grain Growth via Spray Coating. *J. Mater.  
2295 Chem. A* **2016**, *4*, 17636–17642.
- 2296 (167) Zhang, H.; Liao, Q.; Wang, X.; Hu, K.; Yao, J.; Fu, H. Controlled Substitution of Chlorine for Iodine in Single-Crystal  
2297 Nanofibers of Mixed Perovskite  $\text{MAPbI}_{3-x}\text{Cl}_x$ . *Small* **2016**, *12*, 3780–  
2299 3787.
- 2300 (168) Sedighi, R.; Tajabadi, F.; Shahbazi, S.; Gholipour, S.;  
2301 Taghavinia, N. Mixed-Halide  $\text{CH}_3\text{NH}_3\text{PbI}_{3-x}\text{X}_x$  ( $\text{X} = \text{Cl}, \text{Br}, \text{I}$ )  
2302 Perovskites: Vapor-Assisted Solution Deposition and Application as  
2303 Solar Cell Absorbers. *ChemPhysChem* **2016**, *17*, 2382–2388.
- 2304 (169) Pool, V. L.; Gold-Parker, A.; McGehee, M. D.; Toney, M. F.  
2305 Chlorine in  $\text{PbCl}_2$ -Derived Hybrid-Perovskite Solar Absorbers. *Chem.  
2306 Mater.* **2015**, *27*, 7240–7243.
- 2307 (170) Chae, J.; Dong, Q.; Huang, J.; Centrone, A. Chloride  
2308 Incorporation Process in  $\text{CH}_3\text{NH}_3\text{PbI}_{3-x}\text{Cl}_x$  Perovskites via Nanoscale  
2309 Bandgap Maps. *Nano Lett.* **2015**, *15*, 8114–8121.
- 2310 (171) Luo, D.; Yu, L.; Wang, H.; Zou, T.; Luo, L.; Liu, Z.; Lu, Z.  
2311 Cubic Structure of the Mixed Halide Perovskite  $\text{CH}_3\text{NH}_3\text{PbI}_{3-x}\text{Cl}_x$  via  
2312 Thermal Annealing. *RSC Adv.* **2015**, *5*, 85480–85485.
- 2313 (172) Cojocaru, L.; Uchida, S.; Jena, A. K.; Miyasaka, T.; Nakazaki, J.;  
2314 Kubo, T.; Segawa, H. Determination of Chloride Content in Planar  
2315  $\text{CH}_3\text{NH}_3\text{PbI}_{3-x}\text{Cl}_x$  Solar Cells by Chemical Analysis. *Chem. Lett.* **2015**,  
2316 *44*, 1089–1091.
- 2317 (173) Li, Y.; Sun, W.; Yan, W.; Ye, S.; Peng, H.; Liu, Z.; Bian, Z.;  
2318 Huang, C. High-Performance Planar Solar Cells Based On  
2319  $\text{CH}_3\text{NH}_3\text{PbI}_{3-x}\text{Cl}_x$  Perovskites with Determined Chlorine Mole  
2320 Fraction. *Adv. Funct. Mater.* **2015**, *25*, 4867–4873.
- 2321 (174) Starr, D. E.; Sadoughi, G.; Handick, E.; Wilks, R. G.; Alsmeyer,  
2322 J. H.; Kohler, L.; Gorgoi, M.; Snaith, H. J.; Bar, M. Direct Observation  
2323 of an Inhomogeneous Chlorine Distribution in  $\text{CH}_3\text{NH}_3\text{PbI}_{3-x}\text{Cl}_x$   
2324 Layers: Surface Depletion and Interface Enrichment. *Energy Environ.  
2325 Sci.* **2015**, *8*, 1609–1615.
- 2326 (175) Chen, Q.; Zhou, H.; Fang, Y.; Stieg, A. Z.; Song, T.-B.; Wang,  
2327 H.-H.; Xu, X.; Liu, Y.; Lu, S.; You, J.; et al. The Optoelectronic Role of  
2328 Chlorine In  $\text{CH}_3\text{NH}_3\text{PbI}_3(\text{Cl})$ -Based Perovskite Solar Cells. *Nat.  
2329 Commun.* **2015**, *6*, 7269.
- 2330 (176) Unger, E. L.; Bowring, A. R.; Tassone, C. J.; Pool, V. L.; Gold-  
2331 Parker, A.; Checharoen, R.; Stone, K. H.; Hoke, E. T.; Toney, M. F.;  
2332 McGehee, M. D. Chloride in Lead Chloride-Derived Organo-Metal  
2333 Halides for Perovskite-Absorber Solar Cells. *Chem. Mater.* **2014**, *26*,  
2334 7158–7165.
- 177) Jiang, M.; Wu, J.; Lan, F.; Tao, Q.; Gao, D.; Li, G. Enhancing  
2335 the Performance of Planar Organo-Lead Halide Perovskite Solar Cells  
2336 by Using a Mixed Halide Source. *J. Mater. Chem. A* **2015**, *3*, 963–967. 2337  
(178) Chen, Y.; Chen, T.; Dai, L. Layer-by-Layer Growth of  
2338  $\text{CH}_3\text{NH}_3\text{PbI}_{3-x}\text{Cl}_x$  for Highly Efficient Planar Heterojunction Perov-  
2339 skite Solar Cells. *Adv. Mater.* **2015**, *27*, 1053–1059. 2340  
(179) Colella, S.; Mosconi, E.; Pellegrino, G.; Alberti, A.; Guerra, V.  
2341 L. P.; Masi, S.; Listorti, A.; Rizzo, A.; Condorelli, G. G.; De Angelis, F.;  
2342 et al. Elusive Presence of Chloride in Mixed Halide Perovskite Solar  
2343 Cells. *J. Phys. Chem. Lett.* **2014**, *5*, 3532–3538. 2344  
(180) Pistor, P.; Borchert, J.; Fränzel, W.; Csuk, R.; Scheer, R.  
2345 Monitoring the Phase Formation of Coevaporated Lead Halide  
2346 Perovskite Thin Films by in Situ X-ray Diffraction. *J. Phys. Chem. Lett.*  
2347 **2014**, *5*, 3308–3312. 2348  
(181) Yantara, N.; Yanan, F.; Shi, C.; Dewi, H. A.; Boix, P. P.;  
2349 Mhaisalkar, S. G.; Mathews, N. Unravelling the Effects of Cl Addition  
2350 in Single Step  $\text{CH}_3\text{NH}_3\text{PbI}_3$  Perovskite Solar Cells. *Chem. Mater.*  
2351 **2015**, *27*, 2309–2314. 2352  
(182) Yu, H.; Wang, F.; Xie, F.; Li, W.; Chen, J.; Zhao, N. The Role  
2353 of Chlorine in the Formation Process of “ $\text{CH}_3\text{NH}_3\text{PbI}_{3-x}\text{Cl}_x$ ”  
2354 Perovskite. *Adv. Funct. Mater.* **2014**, *24*, 7102–7108. 2355  
(183) You, J.; Hong, Z.; Yang, Y.; Chen, Q.; Cai, M.; Song, T.-B.;  
2356 Chen, C.-C.; Lu, S.; Liu, Y.; Zhou, H.; et al. Low-Temperature  
2357 Solution-Processed Perovskite Solar Cells with High Efficiency and  
2358 Flexibility. *ACS Nano* **2014**, *8*, 1674–1680. 2359  
(184) Conings, B.; Baeten, L.; De Dobbelaere, C.; D’Haen, J.; Manca,  
2360 J.; Boyen, H. G. Perovskite-Based Hybrid Solar Cells Exceeding 10%  
2361 Efficiency with High Reproducibility Using a Thin Film Sandwich  
2362 Approach. *Adv. Mater.* **2014**, *26*, 2041–2046. 2363  
(185) Colella, S.; Mosconi, E.; Fedeli, P.; Listorti, A.; Gazza, F.;  
2364 Orlando, F.; Ferro, P.; Besagni, T.; Rizzo, A.; Calestani, G.; et al.  
2365  $\text{MAPbI}_{3-x}\text{Cl}_x$  Mixed Halide Perovskite for Hybrid Solar Cells: The Role  
2366 of Chloride as Dopant on the Transport and Structural Properties.  
2367 *Chem. Mater.* **2013**, *25*, 4613–4618. 2368  
(186) Fan, L.; Ding, Y.; Luo, J. S.; Shi, B.; Yao, X.; Wei, C. C.; Zhang,  
2369 D. K.; Wang, G. C.; Sheng, Y.; Chen, Y. F.; et al. Elucidating the Role  
2370 of Chlorine in Perovskite Solar Cells. *J. Mater. Chem. A* **2017**, *5*, 7423–  
2371 7432. 2372  
(187) Zhang, X.; Liu, C.; Ma, Y.; Shen, Y.; Li, H.; Chen, R.; Mai, Y.  
2373 Study on the Role of Additional Ions in  $\text{CH}_3\text{NH}_3\text{PbI}_{3-x}\text{Cl}_x$  Planar  
2374 Solar Cells. *Sol. Energy* **2017**, *148*, 70–77. 2375  
(188) Yang, B.; Keum, J.; Ovchinnikova, O. S.; Belianinov, A.; Chen,  
2376 S.; Du, M.-H.; Ivanov, I. N.; Rouleau, C. M.; Geohegan, D. B.; Xiao, K.  
2377 Deciphering Halogen Competition in Organometallic Halide Perov-  
2378 skite Growth. *J. Am. Chem. Soc.* **2016**, *138*, 5028–5035. 2379  
(189) Binek, A.; Grill, I.; Huber, N.; Peters, K.; Hufnagel, A. G.;  
2380 Handloser, M.; Docampo, P.; Hartschuh, A.; Bein, T. Control of  
2381 Perovskite Crystal Growth by Methylammonium Lead Chloride  
2382 Templating. *Chem. - Asian J.* **2016**, *11*, 1199–1204. 2383  
(190) Ng, T.-W.; Chan, C.-Y.; Lo, M.-F.; Guan, Z. Q.; Lee, C.-S.  
2384 Formation Chemistry of Perovskites with Mixed Iodide/Chloride  
2385 Content and the Implications on Charge Transport Properties. *J.  
2386 Mater. Chem. A* **2015**, *3*, 9081–9085. 2387  
(191) Luo, P.; Liu, Z.; Xia, W.; Yuan, C.; Cheng, J.; Xu, C.; Lu, Y.  
2388 Chlorine-Conducted Defect Repairment and Seed Crystal-Mediated  
2389 Vapor Growth Process for Controllable Preparation of Efficient and  
2390 Stable Perovskite Solar Cells. *J. Mater. Chem. A* **2015**, *3*, 22949–  
2391 22959. 2392  
(192) Xie, F. X.; Zhang, D.; Su, H.; Ren, X.; Wong, K. S.; Grätzel, M.;  
2393 Choy, W. C. H. Vacuum-Assisted Thermal Annealing of  $\text{CH}_3\text{NH}_3\text{PbI}_3$   
2394 for Highly Stable and Efficient Perovskite Solar Cells. *ACS Nano* **2015**,  
2395 *9*, 639–646. 2396  
(193) Dar, M. I.; Arora, N.; Gao, P.; Ahmad, S.; Grätzel, M.;  
2397 Nazeeruddin, M. K. Investigation Regarding the Role of Chloride in  
2398 Organic-Inorganic Halide Perovskites Obtained from Chloride  
2399 Containing Precursors. *Nano Lett.* **2014**, *14*, 6991–6996. 2400  
(194) Williams, S. T.; Zuo, F.; Chueh, C.-C.; Liao, C.-Y.; Liang, P.-  
2401 W.; Jen, A. K. Y. Role of Chloride in the Morphological Evolution of  
2402

- 2403 Organo-Lead Halide Perovskite Thin Films. *ACS Nano* **2014**, *8*,  
2404 10640–10654.
- 2405 (195) Tidhar, Y.; Edri, E.; Weissman, H.; Zohar, D.; Hodes, G.;  
2406 Cahen, D.; Rybtchinski, B.; Kirmayer, S. Crystallization of Methyl  
2407 Ammonium Lead Halide Perovskites: Implications for Photovoltaic  
2408 Applications. *J. Am. Chem. Soc.* **2014**, *136*, 13249–13256.
- 2409 (196) Park, B.-W.; Philippe, B.; Gustafsson, T.; Steinbjörnsson, K.;  
2410 Hagfeldt, A.; Johansson, E. M. J.; Boschloo, G. Enhanced Crystallinity  
2411 in Organic–Inorganic Lead Halide Perovskites on Mesoporous TiO<sub>2</sub>  
2412 via Disorder–Order Phase Transition. *Chem. Mater.* **2014**, *26*, 4466–  
2413 4471.
- 2414 (197) Zhao, Y.; Zhu, K. CH<sub>3</sub>NH<sub>3</sub>Cl-Assisted One-Step Solution  
2415 Growth of CH<sub>3</sub>NH<sub>3</sub>PbI<sub>3</sub>; Structure, Charge-Carrier Dynamics, and  
2416 Photovoltaic Properties of Perovskite Solar Cells. *J. Phys. Chem. C*  
2417 **2014**, *118*, 9412–9418.
- 2418 (198) Docampo, P.; Hanusch, F. C.; Stranks, S. D.; Döblinger, M.;  
2419 Feckl, J. M.; Ehrenspurger, M.; Minar, N. K.; Johnston, M. B.; Snaith,  
2420 H. J.; Bein, T. Solution Deposition-Conversion for Planar Hetero-  
2421 junction Mixed Halide Perovskite Solar Cells. *Adv. Energy Mater.* **2014**,  
2422 *4*, 1400355.
- 2423 (199) Dualeh, A.; Tétreault, N.; Moehl, T.; Gao, P.; Nazeeruddin, M.  
2424 K.; Grätzel, M. Effect of Annealing Temperature on Film Morphology  
2425 of Organic-Inorganic Hybrid Perovskite Solid-State Solar Cells. *Adv.  
2426 Funct. Mater.* **2014**, *24*, 3250–3258.
- 2427 (200) Stranks, S. D.; Eperon, G. E.; Grancini, G.; Menelaou, C.;  
2428 Alcocer, M. J. P.; Leijtens, T.; Herz, L. M.; Petrozza, A.; Snaith, H. J.  
2429 Electron-Hole Diffusion Lengths Exceeding 1 Micrometer in an  
2430 Organometal Trihalide Perovskite Absorber. *Science* **2013**, *342*, 341–  
2431 344.
- 2432 (201) Im, J.-H.; Lee, C.-R.; Lee, J.-W.; Park, S.-W.; Park, N.-G. 6.5%  
2433 efficient perovskite quantum-dot-sensitized solar cell. *Nanoscale* **2011**,  
2434 *3*, 4088–4093.
- 2435 (202) Sharek, A.; Toney, M. F. Relationships between Lead Halide  
2436 Perovskite Thin-Film Fabrication, Morphology, and Performance in  
2437 Solar Cells. *J. Am. Chem. Soc.* **2016**, *138*, 463–470.
- 2438 (203) Xing, G. C.; Mathews, N.; Sun, S. Y.; Lim, S. S.; Lam, Y. M.;  
2439 Gratzel, M.; Mhaisalkar, S.; Sum, T. C. Long-Range Balanced Electron-  
2440 and Hole-Transport Lengths in Organic-Inorganic CH<sub>3</sub>NH<sub>3</sub>PbI<sub>3</sub>.  
2441 *Science* **2013**, *342*, 344–347.
- 2442 (204) Luo, S.; Daoud, W. Crystal Structure Formation of  
2443 CH<sub>3</sub>NH<sub>3</sub>PbI<sub>3-x</sub>Cl<sub>x</sub> Perovskite. *Materials* **2016**, *9*, 123.
- 2444 (205) Dong, Q.; Yuan, Y.; Shao, Y.; Fang, Y.; Wang, Q.; Huang, J.  
2445 Abnormal Crystal growth in CH<sub>3</sub>NH<sub>3</sub>PbI<sub>3-x</sub>Cl<sub>x</sub> Using a Multi-Cycle  
2446 Solution Coating Process. *Energy Environ. Sci.* **2015**, *8*, 2464–2470.
- 2447 (206) Mosconi, E.; Amat, A.; Nazeeruddin, M. K.; Grätzel, M.; De  
2448 Angelis, F. First-Principles Modeling of Mixed Halide Organometal  
2449 Perovskites for Photovoltaic Applications. *J. Phys. Chem. C* **2013**, *117*,  
2450 13902–13913.
- 2451 (207) Zheng, F.; Takenaka, H.; Wang, F.; Koocher, N. Z.; Rappe, A.  
2452 M. First-Principles Calculation of the Bulk Photovoltaic Effect in  
2453 CH<sub>3</sub>NH<sub>3</sub>PbI<sub>3</sub> and CH<sub>3</sub>NH<sub>3</sub>PbI<sub>3-x</sub>Cl<sub>x</sub>. *J. Phys. Chem. Lett.* **2015**, *6*, 31–  
2454 37.
- 2455 (208) Motta, C.; El-Mellouhi, F.; Sanvito, S. Charge carrier mobility  
2456 in hybrid halide perovskites. *Sci. Rep.* **2015**, *5*, 12746.
- 2457 (209) Lian, Z.; Yan, Q.; Gao, T.; Ding, J.; Lv, Q.; Ning, C.; Li, Q.;  
2458 Sun, J.-l. Perovskite CH<sub>3</sub>NH<sub>3</sub>PbI<sub>3</sub>(Cl) Single Crystals: Rapid Solution  
2459 Growth, Unparalleled Crystalline Quality, and Low Trap Density  
2460 toward 10<sup>8</sup> cm<sup>-3</sup>. *J. Am. Chem. Soc.* **2016**, *138*, 9409–9412.
- 2461 (210) Li, G.; Zhang, T.; Zhao, Y. Hydrochloric Acid Accelerated  
2462 Formation of Planar CH<sub>3</sub>NH<sub>3</sub>PbI<sub>3</sub> Perovskite With High Humidity  
2463 Tolerance. *J. Mater. Chem. A* **2015**, *3*, 19674–19678.
- 2464 (211) Yang, L.; Wang, J.; Leung, W. W.-F. Lead Iodide Thin Film  
2465 Crystallization Control for High-Performance and Stable Solution-  
2466 Processed Perovskite Solar Cells. *ACS Appl. Mater. Interfaces* **2015**, *7*,  
2467 14614–14619.
- 2468 (212) Pan, J.; Mu, C.; Li, Q.; Li, W.; Ma, D.; Xu, D. Room-  
2469 Temperature, Hydrochloride-Assisted, One-Step Deposition for  
2470 Highly Efficient and Air-Stable Perovskite Solar Cells. *Adv. Mater.*  
2471 **2016**, *28*, 8309–8314.
- 213) Chen, Y.; Zhao, Y.; Liang, Z. Non-Thermal Annealing 2472  
Fabrication of Efficient Planar Perovskite Solar Cells with Inclusion 2473  
of NH<sub>4</sub>Cl. *Chem. Mater.* **2015**, *27*, 1448–1451. 2474
- (214) Chen, Y.; Zhao, Y.; Liang, Z. Nonvolatile Chlorinated 2475  
Additives Adversely Influence CH<sub>3</sub>NH<sub>3</sub>PbI<sub>3</sub> Based Planar Solar 2476  
Cells. *J. Mater. Chem. A* **2015**, *3*, 9137–9140. 2477
- (215) Sun, C.; Xue, Q.; Hu, Z.; Chen, Z.; Huang, F.; Yip, H.-L.; Cao, 2478  
Y. Phosphonium Halides as Both Processing Additives and Interfacial 2479  
Modifiers for High Performance Planar-Heterojunction Perovskite 2480  
Solar Cells. *Small* **2015**, *11*, 3344–3350. 2481
- (216) Li, X.; Ibrahim Dar, M.; Yi, C.; Luo, J.; Tschumi, M.; 2482  
Zakeeruddin, S. M.; Nazeeruddin, M. K.; Han, H.; Grätzel, M. 2483  
Improved Performance and Stability of Perovskite Solar Cells by 2484  
Crystal Crosslinking with Alkylphosphonic Acid ω-Ammonium 2485  
Chlorides. *Nat. Chem.* **2015**, *7*, 703–711. 2486
- (217) Chen, Y.; He, M.; Peng, J.; Sun, Y.; Liang, Z. Structure and 2487  
Growth Control of Organic–Inorganic Halide Perovskites for 2488  
Optoelectronics: From Polycrystalline Films to Single Crystals. *Adv. 2489  
Sci.* **2016**, *3*, 1500392. 2490
- (218) Lv, S.; Pang, S.; Zhou, Y.; Padture, N. P.; Hu, H.; Wang, L.; 2491  
Zhou, X.; Zhu, H.; Zhang, L.; Huang, C.; et al. One-Step, Solution- 2492  
Processed Formamidinium Lead Trihalide (FAPbI<sub>(3-x)</sub>Cl<sub>x</sub>) for 2493  
Mesoscopic Perovskite-Polymer Solar Cells. *Phys. Chem. Chem. Phys.* 2494  
2014, *16*, 19206–19211. 2495
- (219) Wang, Z.; Zhou, Y.; Pang, S.; Xiao, Z.; Zhang, J.; Chai, W.; Xu, 2496  
H.; Liu, Z.; Padture, N. P.; Cui, G. Additive-Modulated Evolution of 2497  
HC(NH<sub>2</sub>)<sub>2</sub>PbI<sub>3</sub> Black Polymorph for Mesoscopic Perovskite Solar 2498  
Cells. *Chem. Mater.* **2015**, *27*, 7149–7155. 2499
- (220) Noh, J. H.; Im, S. H.; Heo, J. H.; Mandal, T. N.; Seok, S. I. 2500  
Chemical Management For Colorful, Efficient, and Stable Inorganic- 2501  
Organic Hybrid Nanostructured Solar Cells. *Nano Lett.* **2013**, *13*, 2502  
1764–1769. 2503
- (221) Gil-Escríg, L.; Miquel-Sempere, A.; Sessolo, M.; Bolink, H. J. 2504  
Mixed Iodide–Bromide Methylammonium Lead Perovskite-based 2505  
Diodes for Light Emission and Photovoltaics. *J. Phys. Chem. Lett.* 2506  
2015, *6*, 3743–3748. 2507
- (222) Sutter-Fella, C. M.; Li, Y.; Amani, M.; Ager, J. W.; Toma, F. 2508  
M.; Yablonovitch, E.; Sharp, I. D.; Javey, A. High Photoluminescence 2509  
Quantum Yield in Band Gap Tunable Bromide Containing Mixed 2510  
Halide Perovskites. *Nano Lett.* **2016**, *16*, 800–806. 2511
- (223) Cao, K.; Li, H.; Liu, S.; Cui, J.; Shen, Y.; Wang, M. 2512  
MAPbI<sub>3-x</sub>Br<sub>x</sub> Mixed Halide Perovskites for Fully Printable Mesoscopic 2513  
Solar Cells with Enhanced Efficiency and Less Hysteresis. *Nanoscale* 2514  
2016, *8*, 8839–8846. 2515
- (224) Kulkarni, S. A.; Baikie, T.; Boix, P. P.; Yantara, N.; Mathews, 2516  
N.; Mhaisalkar, S. Band-Gap Tuning of Lead Halide Perovskites Using 2517  
a Sequential Deposition Process. *J. Mater. Chem. A* **2014**, *2*, 9221– 2518  
9225. 2519
- (225) Aharon, S.; Cohen, B. E.; Etgar, L. Hybrid Lead Halide Iodide 2520  
and Lead Halide Bromide in Efficient Hole Conductor Free Perovskite 2521  
Solar Cell. *J. Phys. Chem. C* **2014**, *118*, 17160–17165. 2522
- (226) Fedeli, P.; Gazza, F.; Calestani, D.; Ferro, P.; Besagni, T.; 2523  
Zappettini, A.; Calestani, G.; Marchi, E.; Ceroni, P.; Mosca, R. 2524  
Influence of the Synthetic Procedures on the Structural and Optical 2525  
Properties of Mixed-Halide (Br,I) Perovskite Films. *J. Phys. Chem. C* 2526  
2015, *119*, 21304–21313. 2527
- (227) Misra, R. K.; Ciammaruchi, L.; Aharon, S.; Mogilyansky, D.; 2528  
Etgar, L.; Visoly-Fisher, I.; Katz, E. A. Effect of Halide Composition on 2529  
the Photochemical Stability of Perovskite Photovoltaic Materials. 2530  
*ChemSusChem* **2016**, *9*, 2572–2577. 2531
- (228) Jong, U.-G.; Yu, C.-J.; Ri, J.-S.; Kim, N.-H.; Ri, G.-C. Influence 2532  
of Halide Composition on the Structural, Electronic, and Optical 2533  
Properties of Mixed CH<sub>3</sub>NH<sub>3</sub>Pb(I<sub>1-x</sub>Br<sub>x</sub>)<sub>3</sub> Perovskites Calculated 2534  
Using the Virtual Crystal Approximation Method. *Phys. Rev. B:* 2535  
*Condens. Matter Mater. Phys.* **2016**, *94*, 125139. 2536
- (229) Brivio, F.; Caetano, C.; Walsh, A. Thermodynamic Origin of 2537  
Photoinstability in the CH<sub>3</sub>NH<sub>3</sub>Pb(I<sub>1-x</sub>Br<sub>x</sub>)<sub>3</sub> Hybrid Halide Perovskite 2538  
Alloy. *J. Phys. Chem. Lett.* **2016**, *7*, 1083–1087. 2539

- 2540 (230) De Wolf, S.; Holovsky, J.; Moon, S. J.; Loper, P.; Niesen, B.;  
 2541 Ledinsky, M.; Haug, F. J.; Yum, J. H.; Ballif, C. Organometallic Halide  
 2542 Perovskites: Sharp Optical Absorption Edge and Its Relation to  
 2543 Photovoltaic Performance. *J. Phys. Chem. Lett.* **2014**, *5*, 1035–1039.  
 2544 (231) Sadhanala, A.; Deschler, F.; Thomas, T. H.; Dutton, S. E.;  
 2545 Goedel, K. C.; Hanusch, F. C.; Lai, M. L.; Steiner, U.; Bein, T.;  
 2546 Docampo, P.; et al. Preparation of Single-Phase Films of  $\text{CH}_3\text{NH}_3\text{Pb}(\text{I}_{1-x}\text{Br}_x)_3$   
 2547 with Sharp Optical Band Edges. *J. Phys. Chem. Lett.* **2014**, *5*,  
 2548 2501–2505.  
 2549 (232) Yuan, Y.; Huang, J. Ion Migration in Organometal Trihalide  
 2550 Perovskite and Its Impact on Photovoltaic Efficiency and Stability. *Acc.  
 2551 Chem. Res.* **2016**, *49*, 286–293.  
 2552 (233) Bischak, C. G.; Hetherington, C. L.; Wu, H.; Aloni, S.;  
 2553 Ogletree, D. F.; Limmer, D. T.; Ginsberg, N. S. Origin of Reversible  
 2554 Photoinduced Phase Separation in Hybrid Perovskites. *Nano Lett.*  
 2555 **2017**, *17*, 1028–1033.  
 2556 (234) Hoke, E. T.; Slotcavage, D. J.; Dohner, E. R.; Bowring, A. R.;  
 2557 Karunadasa, H. I.; McGehee, M. D. Reversible Photo-Induced Trap  
 2558 Formation in Mixed-Halide Hybrid Perovskites for Photovoltaics.  
 2559 *Chem. Sci.* **2015**, *6*, 613–617.  
 2560 (235) Yang, X.; Yan, X.; Wang, W.; Zhu, X.; Li, H.; Ma, W.; Sheng,  
 2561 C. Light Induced Metastable Modification of Optical Properties in  
 2562  $\text{CH}_3\text{NH}_3\text{PbI}_{3-x}\text{Br}_x$  Perovskite Films: Two-Step Mechanism. *Org.  
 2563 Electron.* **2016**, *34*, 79–83.  
 2564 (236) Yoon, S. J.; Draguta, S.; Manser, J. S.; Sharia, O.; Schneider, W.  
 2565 F.; Kuno, M.; Kamat, P. V. Tracking Iodide and Bromide Ion  
 2566 Segregation in Mixed Halide Lead Perovskites during Photoirradiation.  
 2567 *ACS Energy Lett.* **2016**, *1*, 290–296.  
 2568 (237) Slotcavage, D. J.; Karunadasa, H. I.; McGehee, M. D. Light-  
 2569 Induced Phase Segregation in Halide-Perovskite Absorbers. *ACS  
 2570 Energy Lett.* **2016**, *1*, 1199–1205.  
 2571 (238) Snaith, H. J.; Abate, A.; Ball, J. M.; Eperon, G. E.; Leijtens, T.;  
 2572 Noel, N. K.; Stranks, S. D.; Wang, J. T.-W.; Wojciechowski, K.; Zhang,  
 2573 W. Anomalous Hysteresis in Perovskite Solar Cells. *J. Phys. Chem. Lett.*  
 2574 **2014**, *5*, 1511–1515.  
 2575 (239) Egger, D. A.; Rappe, A. M.; Kronik, L. Hybrid Organic-  
 2576 Inorganic Perovskites on the Move. *Acc. Chem. Res.* **2016**, *49*, 573–  
 2577 581.  
 2578 (240) Unger, E. L.; Kegelmann, L.; Suchan, K.; Sörell, D.; Korte, L.;  
 2579 Albrecht, S. Roadmap and Roadblocks for the Band Gap Tunability of  
 2580 Metal Halide Perovskites. *J. Mater. Chem. A* **2017**, *5*, 11401–11409.  
 2581 (241) Hu, M.; Bi, C.; Yuan, Y.; Bai, Y.; Huang, J. Stabilized Wide  
 2582 Bandgap  $\text{MAPbBr}_x\text{I}_{3-x}$  Perovskite by Enhanced Grain Size and  
 2583 Improved Crystallinity. *Adv. Sci.* **2016**, *3*, 1500301.  
 2584 (242) Rehman, W.; Milot, R. L.; Eperon, G. E.; Wehrenfennig, C.;  
 2585 Boland, J. L.; Snaith, H. J.; Johnston, M. B.; Herz, L. M. Charge-  
 2586 Carrier Dynamics and Mobilities in Formamidinium Lead Mixed-  
 2587 Halide Perovskites. *Adv. Mater.* **2015**, *27*, 7938–7944.  
 2588 (243) Zhang, M.; Yu, H.; Lyu, M.; Wang, Q.; Yun, J.-H.; Wang, L.  
 2589 Composition-Dependent Photoluminescence Intensity and Prolonged  
 2590 Recombination Lifetime of Perovskite  $\text{CH}_3\text{NH}_3\text{PbBr}_{3-x}\text{Cl}_x$  Films.  
 2591 *Chem. Commun.* **2014**, *50*, 11727–11730.  
 2592 (244) Niemann, R. G.; Kontos, A. G.; Palles, D.; Kamitsos, E. L.;  
 2593 Kaltzoglou, A.; Brivio, F.; Falaras, P.; Cameron, P. J. Halogen Effects  
 2594 on Ordering and Bonding of  $\text{CH}_3\text{NH}_3^+$  in  $\text{CH}_3\text{NH}_3\text{PbX}_3$  ( $X = \text{Cl}, \text{Br},$   
 2595 I) Hybrid Perovskites: A Vibrational Spectroscopic Study. *J. Phys.  
 2596 Chem. C* **2016**, *120*, 2509–2519.  
 2597 (245) Wei, M.; Chung, Y.-H.; Xiao, Y.; Chen, Z. Color Tunable  
 2598 Halide Perovskite  $\text{CH}_3\text{NH}_3\text{PbBr}_{3-x}\text{Cl}_x$  Emission via Annealing. *Org.  
 2599 Electron.* **2015**, *26*, 260–264.  
 2600 (246) Fang, Y.; Dong, Q.; Shao, Y.; Yuan, Y.; Huang, J. Highly  
 2601 Narrowband Perovskite Single-Crystal Photodetectors Enabled by  
 2602 Surface-Charge Recombination. *Nat. Photonics* **2015**, *9*, 679–686.  
 2603 (247) Zhang, T.; Yang, M.; Benson, E. E.; Li, Z.; van de Lagemaat, J.;  
 2604 Luther, J. M.; Yan, Y.; Zhu, K.; Zhao, Y. A Facile Solvothermal Growth  
 2605 of Single Crystal Mixed Halide Perovskite  $\text{CH}_3\text{NH}_3\text{Pb}(\text{Br}_{1-x}\text{Cl}_x)_3$ .  
 2606 *Chem. Commun.* **2015**, *51*, 7820–7823.  
 2607 (248) Edri, E.; Kirmayer, S.; Kulbak, M.; Hodes, G.; Cahen, D.  
 2608 Chloride Inclusion and Hole Transport Material Doping to Improve  
 Methyl Ammonium Lead Bromide Perovskite-Based High Open-  
 Circuit Voltage Solar Cells. *J. Phys. Chem. Lett.* **2014**, *5*, 429–433.  
 (249) Kitazawa, N.; Watanabe, Y.; Nakamura, Y. Optical Properties of  
 $\text{CH}_3\text{NH}_3\text{PbX}_3$  ( $X = \text{Halogen}$ ) and their Mixed-Halide Crystals. *J. Mater. Sci.* **2002**, *37*, 3585–3587.  
 (250) Yin, W.-J.; Yan, Y.; Wei, S.-H. Anomalous Alloy Properties in  
 Mixed Halide Perovskites. *J. Phys. Chem. Lett.* **2014**, *5*, 3625–3631.  
 (251) Tan, Z. K.; Moghaddam, R. S.; Lai, M. L.; Docampo, P.;  
 Higler, R.; Deschler, F.; Price, M.; Sadhanala, A.; Pazos, L. M.;  
 Credgington, D.; et al. Bright Light-Emitting Diodes Based on  
 Organometal Halide Perovskite. *Nat. Nanotechnol.* **2014**, *9*, 687–692.  
 (252) Zhang, F.; Zhong, H.; Chen, C.; Wu, X.-g.; Hu, X.; Huang, H.;  
 Han, J.; Zou, B.; Dong, Y. Brightly Luminescent and Color-Tunable  
 Colloidal  $\text{CH}_3\text{NH}_3\text{PbX}_3$  ( $X = \text{Br}, \text{I}, \text{Cl}$ ) Quantum Dots: Potential  
 Alternatives for Display Technology. *ACS Nano* **2015**, *9*, 4533–4542.  
 (253) Kim, Y.-H.; Cho, H.; Heo, J. H.; Kim, T.-S.; Myoung, N.; Lee, C.-L.;  
 Im, S. H.; Lee, T.-W. Multicolored Organic/Inorganic Hybrid  
 Perovskite Light-Emitting Diodes. *Adv. Mater.* **2015**, *27*, 1248–1254.  
 (254) Suarez, B.; Gonzalez-Pedro, V.; Ripolles, T. S.; Sanchez, R. S.;  
 Otero, L.; Mora-Sero, I. Recombination study of combined halides  
 $(\text{Cl}, \text{Br}, \text{I})$  perovskite solar cells. *J. Phys. Chem. Lett.* **2014**, *5*, 1628–1635.  
 (255) Zhao, Y.; Zhu, K. Efficient Planar Perovskite Solar Cells Based  
 on 1.8 eV Band Gap  $\text{CH}_3\text{NH}_3\text{PbI}_2\text{Br}$  Nanosheets via Thermal  
 Decomposition. *J. Am. Chem. Soc.* **2014**, *136*, 12241–12244.  
 (256) Chiang, C.-H.; Lin, J.-W.; Wu, C.-G. One-Step Fabrication of a  
 Mixed-Halide Perovskite Film for a High-Efficiency Inverted Solar Cell  
 and Module. *J. Mater. Chem. A* **2016**, *4*, 13525–13533.  
 (257) Beal, R. E.; Slotcavage, D. J.; Leijtens, T.; Bowring, A. R.;  
 Belisle, R. A.; Nguyen, W. H.; Burkhardt, G. F.; Hoke, E. T.; McGehee,  
 M. D. Cesium Lead Halide Perovskites with Improved Stability for  
 Tandem Solar Cells. *J. Phys. Chem. Lett.* **2016**, *7*, 746–751.  
 (258) Ma, Q.; Huang, S.; Wen, X.; Green, M. A.; Ho-Baillie, A. W. Y.;  
 Hole Transport Layer Free Inorganic  $\text{CsPbIBr}_2$  Perovskite Solar Cell  
 by Dual Source Thermal Evaporation. *Adv. Energy Mater.* **2016**, *6*,  
 1502202.  
 (259) Domanski, K.; Roose, B.; Matsui, T.; Saliba, M.; Turren-Cruz,  
 S. H.; Correa-Baena, J. P.; Carmona, C. R.; Richardson, G.; Foster, J.;  
 De Angelis, F.; et al. Migration of Cations Induces Reversible  
 Performance Losses Over Day/Night Cycling in Perovskite Solar  
 Cells. *Energy Environ. Sci.* **2017**, *10*, 604–613.  
 (260) Eperon, G. E.; Leijtens, T.; Bush, K. A.; Prasanna, R.; Green,  
 T.; Wang, J. T.-W.; McMeekin, D. P.; Volonakis, G.; Milot, R. L.; May,  
 R.; et al. Perovskite-Perovskite Tandem Photovoltaics with Optimized  
 Band Gaps. *Science* **2016**, *354*, 861–865.  
 (261) Rehman, W.; McMeekin, D. P.; Patel, J. B.; Milot, R. L.;  
 Johnston, M. B.; Snaith, H. J.; Herz, L. M. Photovoltaic Mixed-Cation  
 Lead Mixed-Halide Perovskites: Links Between Crystallinity, Photo-  
 Stability and Electronic Properties. *Energy Environ. Sci.* **2017**, *10*, 361–  
 369.  
 (262) Conings, B.; Babayigit, A.; Klug, M. T.; Bai, S.; Gauquelin, N.;  
 Sakai, N.; Wang, J. T.-W.; Verbeeck, J.; Boyen, H.-G.; Snaith, H. J. A  
 Universal Deposition Protocol for Planar Heterojunction Solar Cells  
 with High Efficiency Based on Hybrid Lead Halide Perovskite  
 Families. *Adv. Mater.* **2016**, *28*, 10701–10709.  
 (263) Leblebici, S. Y.; Leppert, L.; Li, Y.; Reyes-Lillo, S. E.;  
 Wickenburg, S.; Wong, E.; Lee, J.; Melli, M.; Ziegler, D.; Angell, D. K.;  
 et al. Facet-Dependent Photovoltaic Efficiency Variations in Single  
 Grains of Hybrid Halide Perovskite. *Nat. Energy* **2016**, *1*, 16093.  
 (264) Shallcross, R. C.; Zheng, Y.; Saavedra, S. S.; Armstrong, N. R.  
 Determining Band-Edge Energies and Morphology-Dependent  
 Stability of Formamidinium Lead Perovskite Films Using Spectroelec-  
 trochemistry and Photoelectron Spectroscopy. *J. Am. Chem. Soc.* **2017**,  
 139, 4866–4878.  
 (265) Bella, F.; Griffini, G.; Correa-Baena, J.-P.; Saracco, G.; Grätzel,  
 M.; Hagfeldt, A.; Turri, S.; Gerbaldi, C. Improving Efficiency and  
 Stability of Perovskite Solar Cells with Photocurable Fluoropolymers.  
*Science* **2016**, *354*, 203–206.

- 2677 (266) Tress, W.; Correa Baena, J. P.; Saliba, M.; Abate, A.; Graetzel, 2678 M. Inverted Current–Voltage Hysteresis in Mixed Perovskite Solar 2679 Cells: Polarization, Energy Barriers, and Defect Recombination. *Adv. 2680 Energy Mater.* **2016**, *6*, 1600396.
- 2681 (267) Abate, A.; Paek, S.; Giordano, F.; Correa-Baena, J.-P.; Saliba, 2682 M.; Gao, P.; Matsui, T.; Ko, J.; Zakeeruddin, S. M.; Dahmen, K. H.; 2683 et al. Silolothiophene-Linked Triphenylamines as Stable Hole 2684 Transporting Materials for High Efficiency Perovskite Solar Cells. 2685 *Energy Environ. Sci.* **2015**, *8*, 2946–2953.
- 2686 (268) Domanski, K.; Correa-Baena, J.-P.; Mine, N.; Nazeeruddin, M. 2687 K.; Abate, A.; Saliba, M.; Tress, W.; Hagfeldt, A.; Grätzel, M. Not All 2688 That Glitters Is Gold: Metal-Migration-Induced Degradation in 2689 Perovskite Solar Cells. *ACS Nano* **2016**, *10*, 6306–6314.
- 2690 (269) Zhang, L.; Tian, F.; Xie, Z.; Qin, G. Efficiency Evaluation on 2691  $Cs_x[NH_2CH = NH_2]_{1-x}Pb(I_{1-y}Br_y)_3$ /Crystalline Silicon Tandem Solar 2692 Cells. *Sol. Energy* **2017**, *147*, 432–438.
- 2693 (270) Philippe, B.; Saliba, M.; Correa-Baena, J.-P.; Cappel, U. B.; 2694 Turren-Cruz, S.-H.; Grätzel, M.; Hagfeldt, A.; Rensmo, H. Chemical 2695 Distribution of Multiple Cation ( $Rb^+$ ,  $Cs^+$ ,  $MA^+$ , and  $FA^+$ ) Perovskite 2696 Materials by Photoelectron Spectroscopy. *Chem. Mater.* **2017**, *29*, 2697 3589–3596.
- 2698 (271) Leijtens, T.; Bush, K.; Cheacharoen, R.; Beal, R.; Bowring, A.; 2699 McGehee, M. D. Towards Enabling Stable Lead Halide Perovskite 2700 Solar Cells; Interplay Between Structural, Environmental, and Thermal 2701 Stability. *J. Mater. Chem. A* **2017**, *5*, 11483–11500.
- 2702 (272) Leijtens, T.; Eperon, G. E.; Noel, N. K.; Habreutinger, S. N.; 2703 Petrozza, A.; Snaith, H. J. Stability of Metal Halide Perovskite Solar 2704 Cells. *Adv. Energy Mater.* **2015**, *5*, 1500963.
- 2705 (273) Peng, Y.; Jing, G.; Cui, T. High Performance Perovskite Solar 2706 Cells through Vapor Deposition with Optimized  $PbI_2$  Precursor Films. 2707 *RSC Adv.* **2015**, *5*, 95847–95853.
- 2708 (274) Dong, Q.; Song, J.; Fang, Y.; Shao, Y.; Ducharme, S.; Huang, J. 2709 Lateral-Structure Single-Crystal Hybrid Perovskite Solar Cells via 2710 Piezoelectric Poling. *Adv. Mater.* **2016**, *28*, 2816–2821.
- 2711 (275) Dong, Q.; Fang, Y.; Shao, Y.; Mulligan, P.; Qiu, J.; Cao, L.; 2712 Huang, J. Electron-Hole Diffusion Lengths  $> 175 \mu m$  in Solution- 2713 Grown  $CH_3NH_3PbI_3$  Single Crystals. *Science* **2015**, *347*, 967–970.
- 2714 (276) Schulz, P.; Edri, E.; Kirmayer, S.; Hodges, G.; Cahen, D.; Kahn, 2715 A. Interface Energetics in Organo-Metal Halide Perovskite-Based 2716 Photovoltaic Cells. *Energy Environ. Sci.* **2014**, *7*, 1377–1381.
- 2717 (277) Schulz, P.; Whittaker-Brooks, L. L.; MacLeod, B. A.; Olson, D. 2718 C.; Loo, Y.-L.; Kahn, A. Electronic Level Alignment in Inverted 2719 Organometal Perovskite Solar Cells. *Adv. Mater. Interfaces* **2015**, *2*, 2720 1400532.
- 2721 (278) Schulz, P.; Dowgiallo, A.-M.; Yang, M.; Zhu, K.; Blackburn, J. 2722 L.; Berry, J. J. Charge Transfer Dynamics between Carbon Nanotubes 2723 and Hybrid Organic Metal Halide Perovskite Films. *J. Phys. Chem. Lett.* 2724 **2016**, *7*, 418–425.
- 2725 (279) Endres, J.; Egger, D. A.; Kulbak, M.; Kerner, R. A.; Zhao, L.; 2726 Silver, S. H.; Hodges, G.; Rand, B. P.; Cahen, D.; Kronik, L.; et al. 2727 Valence and Conduction Band Densities of States of Metal Halide 2728 Perovskites: A Combined Experimental–Theoretical Study. *J. Phys. 2729 Chem. Lett.* **2016**, *7*, 2722–2729.
- 2730 (280) Endres, J.; Kulbak, M.; Zhao, L.; Rand, B. P.; Cahen, D.; 2731 Hodges, G.; Kahn, A. Electronic structure of the  $CsPbBr_3$ /polytriaryl- 2732 amine (PTAA) system. *J. Appl. Phys.* **2017**, *121*, 035304.
- 2733 (281) Emara, J.; Schnier, T.; Pourdavoud, N.; Riedl, T.; Meerholz, K.; 2734 Olthof, S. Impact of Film Stoichiometry on the Ionization Energy and 2735 Electronic Structure of  $CH_3NH_3PbI_3$  Perovskites. *Adv. Mater.* **2016**, 2736 *28*, 553–559.
- 2737 (282) Olthof, S.; Meerholz, K. Substrate-dependent electronic 2738 structure and film formation of  $MAPbI_3$  perovskites. *Sci. Rep.* **2017**, 2739 *7*, 40267.
- 2740 (283) Wang, Q. K.; Wang, R. B.; Shen, P. F.; Li, C.; Li, Y. Q.; Liu, L. 2741 J.; Duhm, S.; Tang, J. X. Energy Level Offsets at Lead Halide 2742 Perovskite/Organic Hybrid Interfaces and Their Impacts on Charge 2743 Separation. *Adv. Mater. Interfaces* **2015**, *2*, 1400528.
- 2744 (284) Li, C.; Wei, J.; Sato, M.; Koike, H.; Xie, Z.-Z.; Li, Y.-Q.; Kanai, 2745 K.; Kera, S.; Ueno, N.; Tang, J.-X. Halide-Substituted Electronic Properties of Organometal Halide Perovskite Films: Direct and 2746 Inverse Photoemission Studies. *ACS Appl. Mater. Interfaces* **2016**, *8*, 2747 11526–11531.
- (285) Liu, X. L.; Wang, C. G.; Lyu, L.; Wang, C. C.; Xiao, Z. G.; Bi, C.; Huang, J. S.; Gao, Y. L. Electronic Structures at the Interface between Au and  $CH_3NH_3PbI_3$ . *Phys. Chem. Chem. Phys.* **2015**, *17*, 2751 896–902.
- (286) Chen, S.; Goh, T. W.; Sabba, D.; Chua, J.; Mathews, N.; Huan, C. H. A.; Sum, T. C. Energy Level Alignment at the Methylammonium Lead Iodide/Copper Phthalocyanine Interface. *APL Mater.* **2014**, *2*, 2755 081512.
- (287) Wang, C. G.; Liu, X. L.; Wang, C. C.; Xiao, Z. G.; Bi, C.; Shao, Y. C.; Huang, J. S.; Gao, Y. L. Surface Analytical Investigation on Organometal Triiodide Perovskite. *J. Vac. Sci. Technol., B: Nanotechnol. Microelectron.: Mater., Process., Meas., Phenom.* **2015**, *33*, 032401.
- (288) Liu, P.; Liu, X. L.; Lyu, L.; Xie, H. P.; Zhang, H.; Niu, D. M.; Huang, H.; Bi, C.; Xiao, Z. G.; Huang, J. S.; et al. Interfacial Electronic Structure at the  $CH_3NH_3PbI_3/MoO_x$  Interface. *Appl. Phys. Lett.* **2015**, *106*, 193903.
- (289) Miller, E. M.; Zhao, Y. X.; Mercado, C. C.; Saha, S. K.; Luther, J. M.; Zhu, K.; Stevanovic, V.; Perkins, C. L.; van de Lagemaat, J. Substrate-Controlled Band Positions in  $CH_3NH_3PbI_3$  Perovskite Films. *Phys. Chem. Chem. Phys.* **2014**, *16*, 22122–22130.
- (290) Thibau, E. S.; Llanos, A.; Lu, Z. H. A simple rule for determining the band offset at  $CH_3NH_3PbI_3$ /organic semiconductor heterojunctions. *Appl. Phys. Lett.* **2016**, *108*, 021602.
- (291) Jiang, C.-S.; Yang, M.; Zhou, Y.; To, B.; Nanayakkara, S. U.; Luther, J. M.; Zhou, W.; Berry, J. J.; van de Lagemaat, J.; Padture, N. P.; et al. Carrier Separation and Transport in Perovskite Solar Cells Studied by Nanometre-Scale Profiling of Electrical Potential. *Nat. Commun.* **2015**, *6*, 8397.
- (292) Bergmann, V. W.; Weber, S. A. L.; Javier Ramos, F.; Nazeeruddin, M. K.; Grätzel, M.; Li, D.; Domanski, A. L.; Lieberwirth, I.; Ahmad, S.; Berger, R. Real-Space Observation of Unbalanced Charge Distribution Inside a Perovskite-Sensitized Solar Cell. *Nat. Commun.* **2014**, *5*, 5001.
- (293) Guerrero, A.; Juarez-Perez, E. J.; Bisquert, J.; Mora-Sero, I.; Garcia-Belmonte, G. Electrical Field Profile and Doping in Planar Lead Halide Perovskite Solar Cells. *Appl. Phys. Lett.* **2014**, *105*, 133902.
- (294) Chakraborty, S.; Xie, W.; Mathews, N.; Sherburne, M.; Ahuja, R.; Asta, M.; Mhaisalkar, S. G. Rational Design: A High-Throughput Computational Screening and Experimental Validation Methodology for Lead-Free and Emergent Hybrid Perovskites. *ACS Energy Lett.* **2017**, *2*, 837–845.
- (295) Kamat, P. V.; Bisquert, J.; Buriak, J. Lead-Free Perovskite Solar Cells. *ACS Energy Lett.* **2017**, *2*, 904–905.
- (296) Volonakis, G.; Filip, M. R.; Haghhighirad, A. A.; Sakai, N.; Wenger, B.; Snaith, H. J.; Giustino, F. Lead-Free Halide Double Perovskites via Heterovalent Substitution of Noble Metals. *J. Phys. Chem. Lett.* **2016**, *7*, 1254–1259.
- (297) Savory, C. N.; Walsh, A.; Scanlon, D. O. Can Pb-Free Halide Double Perovskites Support High-Efficiency Solar Cells? *ACS Energy Lett.* **2016**, *1*, 949–955.
- (298) Harikesh, P. C.; Mulmudi, H. K.; Ghosh, B.; Goh, T. W.; Teng, Y. T.; Thirumal, K.; Lockrey, M.; Weber, K.; Koh, T. M.; Li, S.; et al. Rb as an Alternative Cation for Templing Inorganic Lead-Free Perovskites for Solution Processed Photovoltaics. *Chem. Mater.* **2016**, *28*, 7496–7504.
- (299) Giustino, F.; Snaith, H. J. Toward Lead-Free Perovskite Solar Cells. *ACS Energy Lett.* **2016**, *1*, 1233–1240.
- (300) Gupta, S.; Bendikov, T.; Hodges, G.; Cahen, D.  $CsSnBr_3$ , A Lead-Free Halide Perovskite for Long-Term Solar Cell Application: Insights on  $SnF_2$  Addition. *ACS Energy Lett.* **2016**, *1*, 1028–1033.
- (301) Yokoyama, T.; Cao, D. H.; Stoumpos, C. C.; Song, T.-B.; Sato, Y.; Aramaki, S.; Kanatzidis, M. G. Overcoming Short-Circuit in Lead-Free  $CH_3NH_3SnI_3$  Perovskite Solar Cells via Kinetically Controlled Gas–Solid Reaction Film Fabrication Process. *J. Phys. Chem. Lett.* **2016**, *7*, 776–782.

- 2814 (302) Liao, W.; Zhao, D.; Yu, Y.; Grice, C. R.; Wang, C.; Cimaroli, A.  
2815 J.; Schulz, P.; Meng, W.; Zhu, K.; Xiong, R.-G.; et al. Lead-Free  
2816 Inverted Planar Formamidinium Tin Triiodide Perovskite Solar Cells  
2817 Achieving Power Conversion Efficiencies up to 6.22%. *Adv. Mater.*  
2818 **2016**, *28*, 9333–9340.
- 2819 (303) Yu, Y.; Zhao, D.; Grice, C. R.; Meng, W.; Wang, C.; Liao, W.;  
2820 Cimaroli, A. J.; Zhang, H.; Zhu, K.; Yan, Y. Thermally Evaporated  
2821 Methylammonium Tin Triiodide Thin Films for Lead-Free Perovskite  
2822 Solar Cell Fabrication. *RSC Adv.* **2016**, *6*, 90248–90254.
- 2823 (304) Vigneshwaran, M.; Ohta, T.; Iikubo, S.; Kapil, G.; Ripolles, T.  
2824 S.; Ogomi, Y.; Ma, T.; Pandey, S. S.; Shen, Q.; Toyoda, T.; et al. Facile  
2825 Synthesis and Characterization of Sulfur Doped Low Bandgap  
2826 Bismuth Based Perovskites by Soluble Precursor Route. *Chem.*  
2827 *Mater.* **2016**, *28*, 6436–6440.
- 2828 (305) Ogomi, Y.; Morita, A.; Tsukamoto, S.; Saitho, T.; Fujikawa, N.;  
2829 Shen, Q.; Toyoda, T.; Yoshino, K.; Pandey, S. S.; Ma, T. L.; et al.  
2830  $\text{CH}_3\text{NH}_3\text{Sn}_x\text{Pb}_{(1-x)}\text{I}_3$  Perovskite Solar Cells Covering up to 1060 nm. *J.*  
2831 *Phys. Chem. Lett.* **2014**, *5*, 1004–1011.
- 2832 (306) Xiao, Z. W.; Meng, W. W.; Wang, J. B.; Mitzi, D. B.; Yan, Y. F.  
2833 Searching for Promising New Perovskite-Based Photovoltaic Absorb-  
2834 ers: The Importance of Electronic Dimensionality. *Mater. Horiz.* **2017**,  
2835 *4*, 206–216.
- 2836 (307) Filip, M. R.; Eperon, G. E.; Snaith, H. J.; Giustino, F. Steric  
2837 engineering of metal-halide perovskites with tunable optical band gaps.  
2838 *Nat. Commun.* **2014**, *5*, 5757.
- 2839 (308) Filip, M. R.; Giustino, F. Computational Screening of  
2840 Homovalent Lead Substitution in Organic–Inorganic Halide Perov-  
2841 skites. *J. Phys. Chem. C* **2016**, *120*, 166–173.
- 2842 (309) Korbel, S.; Marques, M. A. L.; Botti, S. Stability and electronic  
2843 properties of new inorganic perovskites from high-throughput ab initio  
2844 calculations. *J. Mater. Chem. C* **2016**, *4*, 3157–3167.
- 2845 (310) Lee, B.; Stoumpos, C. C.; Zhou, N.; Hao, F.; Malliakas, C.;  
2846 Yeh, C.-Y.; Marks, T. J.; Kanatzidis, M. G.; Chang, R. P. H. Air-Stable  
2847 Molecular Semiconducting Iodosalts for Solar Cell Applications:  
2848  $\text{Cs}_2\text{SnI}_6$  as a Hole Conductor. *J. Am. Chem. Soc.* **2014**, *136*, 15379–  
2849 15385.
- 2850 (311) Park, B.-W.; Philippe, B.; Zhang, X.; Rensmo, H.; Boschloo, G.;  
2851 Johansson, E. M. J. Bismuth Based Hybrid Perovskites  $\text{A}_3\text{Bi}_2\text{I}_9$  (A:  
2852 Methylammonium or Cesium) for Solar Cell Application. *Adv. Mater.*  
2853 **2015**, *27*, 6806–6813.
- 2854 (312) Johansson, M. B.; Zhu, H.; Johansson, E. M. J. Extended  
2855 Photo-Conversion Spectrum in Low-Toxic Bismuth Halide Perovskite  
2856 Solar Cells. *J. Phys. Chem. Lett.* **2016**, *7*, 3467–3471.
- 2857 (313) Hamaguchi, R.; Yoshizawa-Fujita, M.; Miyasaka, T.; Kunugita,  
2858 H.; Ema, K.; Takeoka, Y.; Rikukawa, M. Formamidine and Cesium-  
2859 Based Quasi-Two-Dimensional Perovskites as Photovoltaic Absorbers.  
2860 *Chem. Commun.* **2017**, *53*, 4366–4369.
- 2861 (314) Vassilakopoulou, A.; Papadatos, D.; Zakouras, I.; Koutselas, I.  
2862 Mixtures of quasi-two and three dimensional hybrid organic-inorganic  
2863 semiconducting perovskites for single layer LED. *J. Alloys Compd.*  
2864 **2017**, *692*, 589–598.
- 2865 (315) Smith, I. C.; Hoke, E. T.; Solis-Ibarra, D.; McGehee, M. D.;  
2866 Karunadasa, H. I. A Layered Hybrid Perovskite Solar-Cell Absorber  
2867 with Enhanced Moisture Stability. *Angew. Chem.* **2014**, *126*, 11414–  
2868 11417.
- 2869 (316) Cao, D. H.; Stoumpos, C. C.; Farha, O. K.; Hupp, J. T.;  
2870 Kanatzidis, M. G. 2D Homologous Perovskites as Light-Absorbing  
2871 Materials for Solar Cell Applications. *J. Am. Chem. Soc.* **2015**, *137*,  
2872 7843–7850.
- 2873 (317) Slavney, A. H.; Smaha, R. W.; Smith, I. C.; Jaffe, A.; Umeyama,  
2874 D.; Karunadasa, H. I. Chemical Approaches to Addressing the  
2875 Instability and Toxicity of Lead-Halide Perovskite Absorbers. *Inorg.*  
2876 *Chem.* **2017**, *56*, 46–55.